

AD-A274 356  
■■■■■■■■■■

2

## Semiannual Technical Report

Interface Properties of Wide Bandgap  
Semiconductor Structures

DTIC  
ELECTE  
JAN 04 1994  
S B D

Supported under Grant #N00014-92-J-1477  
Office of the Chief of Naval Research  
Report for the period 7/1/93-12/31/93

Robert F. Davis, Salah Bedair,\* Jerry Bernholc,\*\*  
Jeffrey T. Glass and R. J. Nemanich\*\*  
c/o Materials Science and Engineering Department  
\*Electrical and Computer Engineering Department  
and \*\*Department of Physics  
North Carolina State University  
Campus Box 7907  
Raleigh, NC 27695-7907

DISTRIBUTION STATEMENT A  
Approved for public release  
Distribution Unlimited

December, 1993

94-00029  
■■■■■■■■■■

94 1 03 062

259300

**Best  
Available  
Copy**

# REPORT DOCUMENTATION PAGE

Form Approved  
OMB No. 0704-0188

Public reporting burden for this collection of information is estimated to average 1 hour per response, including the time for reviewing instructions, searching existing data sources, gathering and maintaining the data needed, and completing and reviewing the collection of information. Send comments regarding this burden estimate or any other aspect of this collection of information, including suggestions for reducing this burden to Washington Headquarters Services, Directorate for Information Operations and Reports, 1215 Jefferson Davis Highway, Suite 1204, Arlington, VA 22202-4302, and to the Office of Management and Budget Paperwork Reduction Project (0704-0188), Washington, DC 20503.

1. AGENCY USE ONLY (Leave blank)		2. REPORT DATE December, 1993	3. REPORT TYPE AND DATES COVERED Semiannual Technical 7/1/93-12/31/93	
4. TITLE AND SUBTITLE Interface Properties of Wide Bandgap Semiconductor Structures			5. FUNDING NUMBERS uri41114a-01 1114SS N00179 N66005 4B855	
6. AUTHOR(S) Robert F. Davis and R. J. Nemanich			8. PERFORMING ORGANIZATION REPORT NUMBER N00014-92-J-1477	
7. PERFORMING ORGANIZATION NAME(S) AND ADDRESS(ES) North Carolina State University Hillsborough Street Raleigh, NC 27695			10. SPONSORING/MONITORING AGENCY REPORT NUMBER	
9. SPONSORING/MONITORING AGENCY NAME(S) AND ADDRESS(ES) Sponsoring: ONR, 800 N. Quincy, Arlington, VA 22217-5660 Monitoring: Office of Naval Research Resider The Ohio State University Research Center 1960 Kenny Road Columbus, OH 43210-1063			11. SUPPLEMENTARY NOTES	
12a. DISTRIBUTION/AVAILABILITY STATEMENT Approved for Public Release; Distribution Unlimited			12b. DISTRIBUTION CODE	
13. ABSTRACT (Maximum 200 words) <p><i>Ab initio</i> molecular dynamics calculations have shown that the 1x1:2H and the 2x1:H surfaces of diamond(C)(100) have a (-) electron affinity(EA); the clean (100) surface has a (+) EA. This is in agreement with experiment. Biased nucleation of C on <math>\beta</math>-SiC(100) and Si(100) has been achieved but not on Cu(100). C nucleation densities on Hf, Ti, Ta, Ni and W were directly related to the carbide heat of formation. The precursors of chlorinated methylsilanes coupled with bias were used to deposit C films on Si(100). Textured C(III) films were also achieved using an oxyacetylene torch. Cu forms an epitaxial rectifying contact to diamond with a Schottky barrier height (SBH) of <math>\sim 1.1</math> eV. Hydrogen plasma was used to remove hydrocarbons from SiC surface at 400°C. Controlled growth of single crystal. <math>\beta</math>(3C)- and <math>\alpha</math>(6H)-SiC films has been achieved on <math>\alpha</math>(6H)-SiC wafers at 1050°C by gas source(GS) MBE. The growth mode of each polytype has been investigated. Rectifying Ti contacts with low ideality factors (<math>n &lt; 1.09</math>) and leakage currents (<math>5 \times 10^{-7}</math> A/cm<sup>2</sup> at 10V) and SBHs of 0.79-0.88 have been achieved. The three-dimensional nucleation and coalescence of islands of AlN on <math>\alpha</math>(6H)-SiC has been discerned via TEM. Multilayers and solid solutions of AlN and SiC have been achieved and characterized. Thin AlN crystals have been deposited on <math>\alpha</math>(6H)-SiC substrates by sublimation. Initial results using AlN as an insulator in an MIS structure have been obtained. Operation of this device at 300°C was successful. Chemical vapor deposition of AlN and GaN has been achieved and characterized. Contact studies involving Zn/Au and Cr/Au and Au, reactive ion etching and optical characterization of GaN and AlN have been initiated. Pure cubic BN has been achieved via ion assisted electron beam deposition. GaP films and In<sub>0.47</sub>Ga<sub>0.53</sub>P were epitaxially achieved on GaP(100) and GaAs substrates, respectively, at 200-260°C using GSMBE.</p>				
14. SUBJECT TERMS molecular dynamics, thin films, diamond, negative electron affinity, bias-enhanced nucleation, refractory metals, chlorinated methylsilanes, oxyacetylene torch, rectifying contacts, Schottky barrier height, hydrogen plasma, $\beta$ (3C)-SiC, $\alpha$ (6H)-SiC, gas source MBE, AlN, GaN, multilayers, solid solutions, reactive ion etching, optical characterization, c-BN, GaP, In <sub>0.47</sub> Ga <sub>0.53</sub> P.			15. NUMBER OF PAGES 208	
17. SECURITY CLASSIFICATION OF REPORT UNCLAS			15. PRICE CODE	
18. SECURITY CLASSIFICATION OF THIS PAGE UNCLAS		19. SECURITY CLASSIFICATION OF ABSTRACT UNCLAS		20. LIMITATION OF ABSTRACT SAR

## Table of Contents

I. Introduction	1
II. Surface Structures and Electron Affinities of Clean and Hydrogenated Diamond C(100) Surfaces <i>J. Bernholc</i>	3
III. Negative Electron Affinity Effects on the Diamond (100) Surface <i>J. van der Weide, Z. Zhang, P. K. Baumann, M. G. Wensell, J. Bernholc and R. J. Nemanich</i>	11
IV. Bias-enhanced Nucleation on Refractory Metal Substrates <i>S. D. Wolter, B. R. Stoner and J. T. Glass</i>	19
V. Diamond Nucleation using Halogenated Organosilicics <i>P. Goeller, D. Tucker and J. T. Glass</i>	27
VI. Growth of Diamond Films Using an Enclosed Combustion Flame <i>P. W. Morrison, Jr., A. Somashekhar, J. T. Glass and J. T. Prater</i>	33
VII. Epitaxial Cu Contacts on Semiconducting Diamond <i>P. K. Baumann, T. P. Humphreys, R. J. Nemanich, K. Ishibashi, N. R. Parikh, L. M. Porter and R. F. Davis</i>	67
VIII. Structure of Si(001) Surface with Monoatomic Steps <i>J. Bernholc</i>	75
IX. Surface Preparation of SiC Films <i>M. C. Benjamin and R. J. Nemanich</i>	80
X. Controlled Growth of the 3C and 6H Polytypes of SiC by Gas-Source Molecular Beam Epitaxy <i>S. Kern and R. F. Davis</i>	86
XI. Growth Mechanisms of SiC Film on 6H-SiC (0001) by Gas-source Molecular Beam Epitaxy <i>S. Tanaka and R. F. Davis</i>	90
XII. Chemistry, Microstructure and Electrical Properties at Interfaces between Thin Films of Titanium and $\alpha$ (6H) Silicon Carbide (0001) <i>L. M. Porter, R. F. Davis, J. S. Bow, M. J. Kim, R. W. Carpenter and R. C. Glass</i>	95
XIII. Initial Stage of AlN Film Growth on 6H-SiC by Plasma-Assisted Gas-source Molecular Beam Epitaxy <i>S. Tanaka and R. F. Davis</i>	121
XIV. Growth of Pseudomorphic Heterostructures and Solid Solutions in the AlN-SiC System by Plasma-Assisted, Gas-source Molecular Beam Epitaxy <i>S. Kern and R. F. Davis</i>	126
XV. Growth of Aluminum Nitride Crystals by Sublimation <i>C. Balkas and R. F. Davis</i>	131
XVI. Application of Epitaxial Aluminum Nitride (AlN) in Metal-Insulator Semiconductor Structures <i>C. Wang and R. F. Davis</i>	136
XVII. Metalorganic Chemical Vapor Deposition (MOCVD) of III-V <i>W. Weeks and R. F. Davis</i>	141



XVIII.	Development of a Photo- and Cathodoluminescence System for Optical Studies of III-V Nitride Films <i>W. Perry and R. F. Davis</i>	149
XIX.	Reactive Ion Etching of GaN and AlN <i>K. Gruss and R. F. Davis</i>	153
XX.	Contact Formation in GaN and AlN <i>L. Smith and R. F. Davis</i>	160
XXI.	Growth and Characterization of Cubic Boron Nitride Thin Films <i>D. J. Kester, K. S. Ailey, D. J. Lichtenwalner and R. F. Davis</i>	173
XXII.	Semi-insulating GaP and InGaP Films Grown at Low Temperatures by Gas Source Molecular Beam Epitaxy <i>Y. He, J. Ramdani and S. Bedair</i>	190
XXIII.	Distribution List	208

DTIC QUALITY INSPECTED 5

Accession For	
NTIS GRA&I	<input checked="" type="checkbox"/>
DTIC TAB	<input type="checkbox"/>
Unannounced	<input type="checkbox"/>
Justification	
By	
Distribution/	
Availability Codes	
Dist	Avail and/or Special
A-1	

## I. Introduction

Heteroepitaxy is the growth of a crystal (or a film) on a foreign crystalline substrate that determines its orientation. Such oriented growth requires that lattice planes in both materials have similar structure. In general, an epitaxial relationship is probable whenever the orientation of the substrate and overgrowth produces an interface with a highly coincident atomic structure having low interfacial energy relative to a random arrangement.

During the past decade, nonequilibrium techniques have been developed for the growth of epitaxial semiconductors, superconductors, insulators and metals which have led to new classes of artificially structured materials. In many cases, the films were deposited on substrates having a different chemistry from that of the film, and heteroepitaxy was achieved. Moreover, layered structures with a periodicity of a few atomic layers have also been produced by the sequential heteroepitaxial deposition of a film of one type on another. Metastable structures can be generated which possess important properties not present in equilibrium systems. A consideration of the materials under consideration for next generation electronic and optoelectronic devices, e.g., the III-V nitrides show that only a few of them can currently be grown in bulk, single crystal form having a cross-sectional area of  $>3\text{cm}^2$ . Thus other, commercially available substrates must be used. This introduces a new set of challenges for the successful growth of device quality films which are not present in homoepitaxial growth and which must be surmounted if these materials are to be utilized in device structures.

In addition to providing structures which do not exist in nature, applications of advanced heteroepitaxial techniques permit the growth of extremely high quality heterostructures involving semiconductors, metals, and insulators. These heterostructures offer the opportunity to study relationships between the atomic structure and the electrical properties of both the film itself and the interface between the two dissimilar materials. They also allow the study of epitaxial growth between materials exhibiting very different types (ionic, covalent, or metallic) of bonding.

While the potential of heteroepitaxial deposition has been demonstrated, significant advances in theoretical understanding, experimental growth and control of this growth, and characterization are required to exploit the capabilities of this process route. It is particularly important to understand and control the principal processes which control heteroepitaxy at the atomic level. It is this type of research as well as the chemistry of dry etching via laser and plasma processing which forms the basis of the research in this grant.

The materials of concern in this report are classified as wide bandgap semiconductors and include diamond, the III-V nitrides, SiC, GaP and AlP. The extremes in electronic and thermal properties of diamond and SiC allow the types and numbers of current and

conceivable applications of these materials to be substantial. However a principal driving force for the interest in the III-V nitrides and GaP and AlP is their potential for solid-state optoelectronic devices for light emission and detection from the visible through the far ultraviolet range of the spectrum.

The principal objectives of the research program are the determination of (1) the fundamental physical and chemical processes ongoing at the substrate surface and substrate/film interface during the heteroepitaxial deposition of both monocrystalline films of the materials noted above, as well as metal contacts on these materials, (2) the mode of nucleation and growth of the materials noted in (1) on selected substrates and on each other in the fabrication of multilayer heterostructures, (3) the resulting properties of the individual films and the layered structures and the effect of interfacial defects on these properties, (4) the development and use of theoretical concepts relevant to the research in objectives (1-3) to assist in the fabrication of improved films and structures and (5) the determination of process chemistry which leads to the laser assisted and plasma etching of these wide bandgap compound semiconductors.

This is the third bi-annual report since the initiation of the project. The following sections introduce each topic, detail the experimental approaches, report the latest results and provide a discussion and conclusion for each subject. Each major section is self-contained with its own figures, tables and references.

## II. Surface Structures and Electron Affinities of Clean and Hydrogenated Diamond C(100) Surfaces

### A. Introduction

The (100) surface is a CVD epitaxial growth surface [1]. According to experimental results, a  $1\times 1$  LEED pattern appears when C(100) surface is heated from 500 to 700 K and at temperatures above 1300 °K a  $2\times 1$  LEED pattern is observed. It is believed that a  $2\times 1$  reconstructed monohydride or bare surface is responsible for the  $2\times 1$  LEED pattern [2]. While no consensus has been reached on the observed  $1\times 1$  LEED pattern, the surface has been suggested as either a dihydride or a disordered phase consists of patches of  $(2n+1)\times 1$  structures [3]. Previous theoretical studies on these surfaces have used empirical or semiempirical methods [4, 5] but no consensus has been reached.

Certain diamond surfaces may exhibit negative electron affinity (NEA), thus electrons at the conduction band edge can be emitted into vacuum. NEA for diamond surfaces has been observed in photoemission spectra when a distinct peak appears at low energy end of the valence band [6]. For C(111) diamond surfaces, negative electron affinities were found to be associated with the  $1\times 1$  phase, whereas the  $(2\times 1)$  reconstructed phase exhibited a positive electron affinity [7]. Recently in their UV photoemission experiments, van der Weide and Nemanich [8] found that the hydrogenated C(100) $2\times 1$  surface exhibits negative electron affinity while the C(100) $1\times 1$  does not. In general, the measured electron affinities may have contributions from two relatively different mechanisms—band bending and surface dipole adjustment. Band bending occurs over a range of about  $1000\text{\AA}$  around the surface and is due to the occupation of the surface states by the impurity carriers in the solid [9, 10]. Surface dipole adjustment is a variable on the atomic scale and strongly depends on the surface structures and adsorptions. In our work, we have studied the role hydrogen plays with the negative electron affinity and electron states at the diamond C(100) surface, but we have not addressed issues on band bending which are dependent on bulk doping. The NEA effect could potentially make diamond useful in applications such as cold cathode emitters and detectors.

### B. Methodology

The theoretical calculations were performed using Local Density Approximation (LDA) and the Car-Parrinello formalism [11]. Soft-core, norm-conserving pseudopotentials for hydrogen and carbon were generated by a modified Hamann procedure [12, 13]. The energy cutoff in the plane wave expansion was 35 Rydbergs. The diamond surfaces were modeled by using supercells containing ten layers of diamond. The slabs were separated by  $10\text{\AA}$  of vacuum in order to avoid interactions between slab surfaces. Since both sides of the slab have the same surface, it is equivalent to five layers of the actual surface. We believe that this is a more accurate choice than passivating one side of the slab with hydrogen (a method often

used to model a thicker slab), because it avoids the dipole interactions between the surfaces due to differences in their workfunctions. The clean C(100)2×1 surface supercell contains total 80 carbon atoms with eight atoms on each layer. The monohydride C(100)2×1:H surface was modeled by a supercell containing ten layers of diamond with twelve carbon atoms on each layer. One hydrogen atom was attached to every surface carbon atom according to the C(100)2×1:H stoichiometry. For the C(100)1×1:2H dihydride surface, two hydrogen atoms were attached to each of the nine surface carbon atoms. Due to the supercell size, only  $\Gamma$  point sampling was used. Starting from an estimated structure, the zero temperature geometries were obtained by steepest descents and/or fast-relax methods of ion dynamics [14].

### C. Surface Geometry and Binding Energies

In Table I, we present the calculated geometries of the clean, monohydride, and dihydride surfaces. The results are qualitatively in agreement with the published works [4, 5, 15, 16], but quantitative differences exist. Both the clean and the monohydride surfaces can have stable 2×1 structures, but the C-C dimer bond length was shorter on a clean surface (1.38Å) than on a monohydride surface (1.63Å). The difference is expected when compared to typical C-C double and single bond lengths. Much larger vertical relaxations were found for the clean surface than for the hydrogenated surfaces. For all three surfaces, spacing between the first and second layers was compressed (by -26%, -10% and -6.7% respectively), while spacing between second and third layers was stretched (+5.6%, +1.1% and +2.2%). However, only small displacements (less than 0.02Å) from the ideal bulk positions were found on the third and fourth layers—an indication that the ten-layer slab used in the calculation is adequate for studying the physics of these surfaces. Due to steric repulsions, the hydrogen atoms tend to avoid each other. This is the reason for the change in angle between the C-H bond and the surface normal on the monohydride surface from its starting value 54.7° to 23.1°, as a result of the relaxation. On the dihydride surface the steric repulsion is even stronger.

Table I. Diamond Surface Geometries

	2×1:clean	2×1:H	1×1:2H (sym)	1×1:2H (canted)
$r_{\text{dimer}}(\text{\AA})$	1.377	1.628	-	-
$r_{\text{CH}}(\text{\AA})$	-	1.112	1.056	1.04 - 1.13 *
$\alpha(\text{dimer-H})$	-	113.1°	-	-
$\theta(\text{H-C-H})$	-	-	84.72°	93° - 96° *
$\Delta x_1(\text{\AA})$	.65	.80	.83	-
$\Delta x_2(\text{\AA})$	.94	.90	.91	-
$\Delta x_3(\text{\AA})$	.87	.89	.89	-

\*Fluctuation range during finite temperature simulation

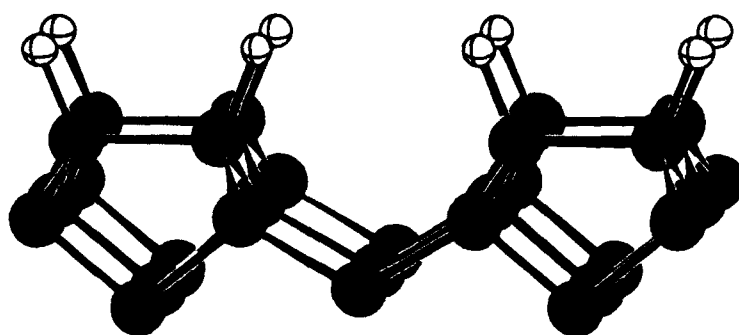


Figure 1. Hydrogenated C(100) diamond surface.

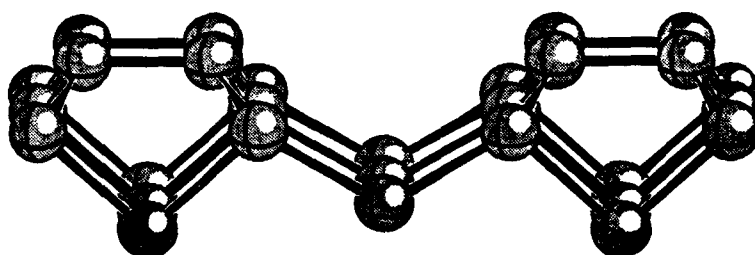


Figure 2. The clean C(100) diamond surface.

The hydrogen desorption from the surfaces was analyzed by using the following end-point energetics:

$$\delta E = (E_{\text{substrate}} + E_{\text{H atom}}) - E_{\text{system}}$$

Here,  $E_{\text{system}}$  and  $E_{\text{substrate}}$  are the energies of the fully relaxed hydrogenated surfaces (C:(100)2×1:H or C(100)1×1:2H) and surfaces with less hydrogen (clean C(100)2×1 or C(100)2×1:H).  $E_{\text{H atom}}$  is the energy of a free hydrogen atom, 13.03 eV within the LDA approximation. The  $\delta E$  then reflects the strength of hydrogen binding. In Table II, we compare our calculated  $\delta E$ 's with existing works.

Table II. Energetics of Hydrogen Binding

Surface	Zheng, <i>et al.</i>	Mehandru, <i>et al.</i>	Yang, <i>et al.</i>	Yang	This work
$\delta E_{\text{mono}}(\text{eV})$	6.32	6.63	3.27	6.18	5.49
$\delta E_{\text{di}}(\text{eV})$	4.11	-	1.19	-	1.13

Large differences (4.36 eV/ H atom) in the  $\delta E$ 's were found between the monohydride and dihydride surfaces. Experimentally, in their time-of-flight mass spectroscopy, Hamza and co-workers [2] found two distinct velocity distributions ("fast" and "slow") in the TDS from the  $2\times 1$  diamond surface at around 1300K. The fast ions were attributed to the desorption from  $\text{CH}_2$  dihydride surface species and the slower component, which persists to higher temperatures ( $\sim 1530\text{K}$ ), was believed to be due to the monohydride units. The much smaller  $\delta E$  for dihydride surface implies a lower desorption energy than the monohydride surface. However the true binding energy should be defined as the energy required to remove a single atom from the surface. This depends on the specific surface site and surface coverage. Moreover, there will be energy barriers for the various desorption paths, therefore dynamic simulations [11] are necessary to make quantitative correlations to the measured desorption temperatures.

Several unanswered questions remain for the C(100) surface. First, what is the surface atomic structure for the  $1\times 1$  surface and is a dihydride phase responsible for it? Second, for the  $(2\times 1)$  surface, what is the hydrogen coverage? Based on the present calculation, the dihydride surface is energetically unfavorable (by 2.3 eV/ $\text{H}_2$ ) with respect to the  $\text{H}_2$  desorption although it is still favored relative to atomic H (-1.13 eV). We have examined the stability of the dihydride surface by using a finite temperature simulation where the surface was heated to 300K for about 0.02 ps ( $\sim 3$  times the period of C-H vibrations). The hydrogen atoms deviated from the symmetric positions but no hydrogen dissociation from the surface was observed. The subsequent steepest decent calculation led to a canted and twisted structure which has a total energy of 0.12 eV per  $1\times 1$  unit lower than the symmetric structure. Similar twisting of the dihydride pairs was found by Yang and D'Evelyn [17, 18]. Due to the prohibitive computational cost, we did not attempt higher temperature simulations or a search for a global minimum for the dihydride surface.

Accurate experimental measurements of hydrogen coverage on diamond (100) surfaces are not currently available, possibly due to experimental difficulties [2, 18]. In the cases of Si(100) surfaces, Cheng and Yates found a saturation coverage of 1.9ML (1 ML is defined as one H per surface Si atom) and suggested that the Si(100) $1\times 1$  surface was a disordered phase containing monohydride, dihydride, and trihydride species. However, we have an alternate interpretation of the TPD data. The Si(100) $1\times 1$  phase contains mainly dihydride species, while the monohydride species (the  $\beta_1\text{-H}_2$ ) appeared after the  $2\times 1$  reconstruction during the heating [3]. Compared to silicon, the diamond lattice is 34% smaller. Thus, the larger steric repulsions will inhibit high coverage density. Yang and D'Evelyn [17, 18] suggested that a disordered dihydride with local  $(2n+1)\times 1$  structure will most likely give rise to a  $1\times 1$  LEED pattern [2]. This model eliminates the large repulsion between two adjacent dihydride units

and implies a maximum coverage of 1.33 ML at which a  $3\times 1$  structure results. In principle the fully covered surface (the dihydride) can exist at zero temperature. Although the repulsion is the highest, the calculations indicate that it is still lower in energy relative to the free atom and bare surface, and that a barrier exists for  $H_2$  desorption. However, the conditions required for this phase to occur may be very different from normal laboratory conditions.

#### D. Electronic Structure

The electronic wavefunctions were analyzed by examining their Milliken populations and plane-averaged square modulus. The information on the charge distribution and the bond orientations could be determined from the Milliken populations. Surface states could be identified by the wavefunctions being heavily weighted at the surface region. Figure 3 and Fig. 4 describe the electronic structures of the clean and monohydride surfaces. The bare surface is characterized by having both filled and empty surface states in the forbidden gap. They mainly consist of  $\pi$  bonding and antibonding orbitals on the dimer atoms. The energy separation between the filled and empty surface states is 1.5 eV. This is in qualitative agreement with the tight-binding results ( $\sim 2$  eV) of Davidson *et al* [16]. However, Yang *et al.* [5] and Mehandru *et al.* [4] found the bare surface to be metallic.

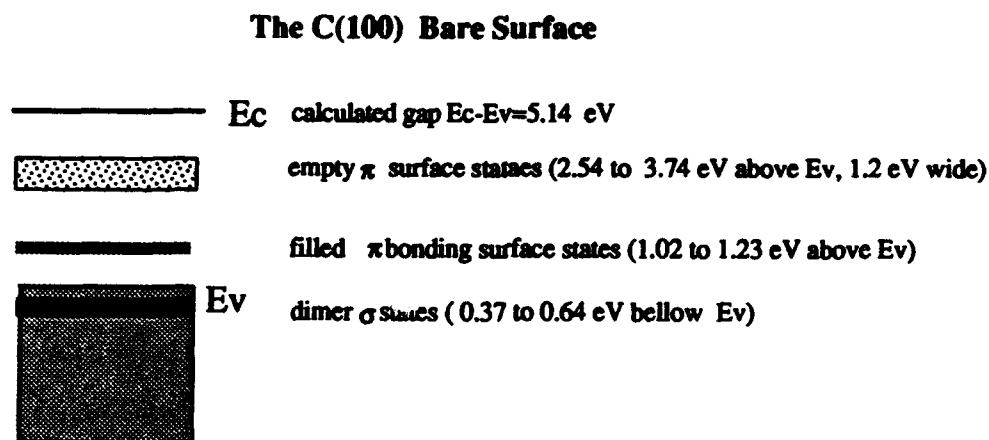


Figure 3. Electronic structure of bare C(100)( $2\times 1$ ) diamond surface.

For the monohydride surface, no occupied surface states were found in the band gap. The C-H bonding states lie about 4eV below VBM. However, a broad band of unoccupied states, which are related to the C-H antibonding, were found to be between 1.5 to 2.5 eV below the conduction band edge. While this disagrees with another theoretical calculation [4], where an



empty gap was found for the monohydride surface, it is very similar to theoretical and experimental findings on monohydride silicon (100) surface (Si(100)2×1:H). In their STM spectroscopy, Hammers *et al.* [19] attributed the peak 1.0 eV above  $E_f$  to the Si-H antibonding states that were computed by the empirical tight-binding method by Ciraci *et al.* [20]. Although a strong C-H bond means large separation between bonding and antibonding states (typically ~9 eV in small molecules such as CH<sub>4</sub>), the interactions on the surface may broaden the band so that the empty states drop below the bulk the conduction band edge. Due to the well known inadequacy of LDA in describing the excited states, the position of these states cannot be precisely determined. Experimentally for the 2×1 diamond surface, Hamza *et al.* [2] found occupied states over a 1.5eV range of the energies above the valence band maximum (VBM) and no empty states from 1.2 to 5.5 eV above the Fermi level. Neither of the present calculations for the ideal 2×1 surface (clean and monohydride) have an electronic structure that exactly matches experiment. Since there is a clear indication of occupied gap states, we conclude that the actual surface is at least partially bare. Based on their tight-binding calculations, Davidson *et al.* [16] have shown that a half-hydride structure, which has partially filled gap states, would best fit the photoemission data. Recently Lee and Pai using EELS measurements found that hydrogen easily desorbs from C(100) surface upon heating to 1473K[21]. We should not expect the calculations for the perfect surfaces to exactly correlate with the measurements on the samples which have defects and steps. Therefore, the actual hydrogen coverage is still unknown. More study will be necessary to resolve this problem.

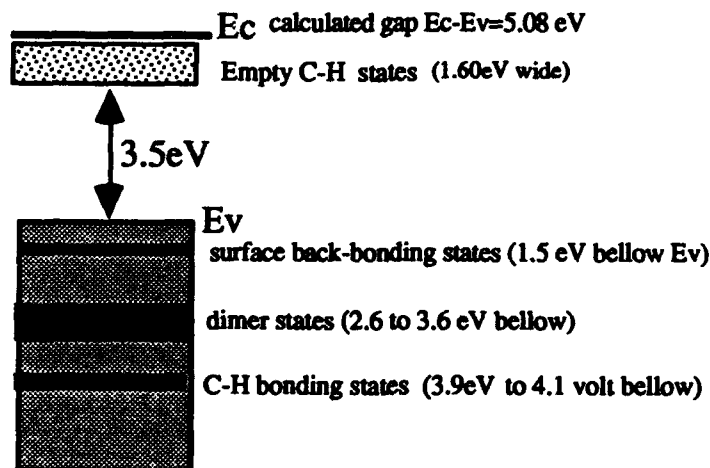


Figure 4. Electronic structure of monohydride C(100)(2×1):H surface.

#### E. Electron Affinity

The electron affinity of a semiconductor surface is defined as the energy separation between the conduction band minimum inside the solid and the vacuum level. Normally, two

factors may affect the electron affinity value: the surface dipole moment at the first few atomic layers of the surface and the space-charge due to the occupation of the surface states by impurity carriers in the bulk. The effect of hydrogen adsorption on the positions of bulk energy levels relative to the vacuum level can be directly analyzed using the present calculations. However the space-charge, which extends hundreds of angstroms from the surface and depends on bulk doping, must be studied by a different formalism.

In order to determine the position of the vacuum level relative to the electron states of the system, we plot the plane-averaged self-consistent potential versus the distance normal to the surface. As one can see from Fig. 5, the effective potential has flattened out in the vacuum region, indicating that there is enough vacuum between the slabs in the calculation. To ensure good convergence, the position of the valence band maximum (VBM) was computed via a bulk diamond calculation, where the separation between the VBM and the average potential was found to be 25.84 eV. It is well known that Local Density Approximation (LDA) can only give an accurate description of the occupied states. Therefore, for the present purpose, the position of the conduction band edge was determined by adding the experimental value of band gap (5.47 eV) to the VBM. The conduction band is 2.2 eV above the vacuum level for the 2×1 monohydride surface, while it is 0.8 below the vacuum level for the clean surface. The difference in the electron affinities (-2.2 and +0.8) between the monohydride and clean surfaces can be explained by the hydrogen-induced surface dipoles. By definition, the workfunction is

$$\begin{aligned}\Phi &= [v(\infty) + E_{N-1}] - E_N \\ &= v(\infty) - \mu - V_{\text{bulk}} + V_{\text{bulk}} \\ &= D - E_f.\end{aligned}$$

Here,  $E_f = \mu - V_{\text{bulk}}$  is the chemical potential of electrons in the bulk relative to the averaged electron static potential ( $V_{\text{bulk}}$ ) inside the solid and it is purely a property of the bulk. And  $D = v(\infty) - V_{\text{bulk}}$  can be defined as the surface dipole strength. Since the model surfaces have two dimensional periodicity, the electrostatic potentials and the barriers ( $D$ ) across the surfaces can be calculated by integrating the one dimensional Poisson's equation:

$$d^2V/dz^2 = -4\pi\rho(z)$$

where  $\rho(z)$  is the total charge averaged in the plane at  $z$ . Due to the fact that the hydrogen atoms have saturated the dangling bonds, the monohydride surface has less electronic charge spread out into the vacuum than the bare surface; thus the surface barrier is reduced. From the solution of the Poisson's equation, we found that the difference in the dipole strength is exactly 3.0 eV (0.8+2.2).

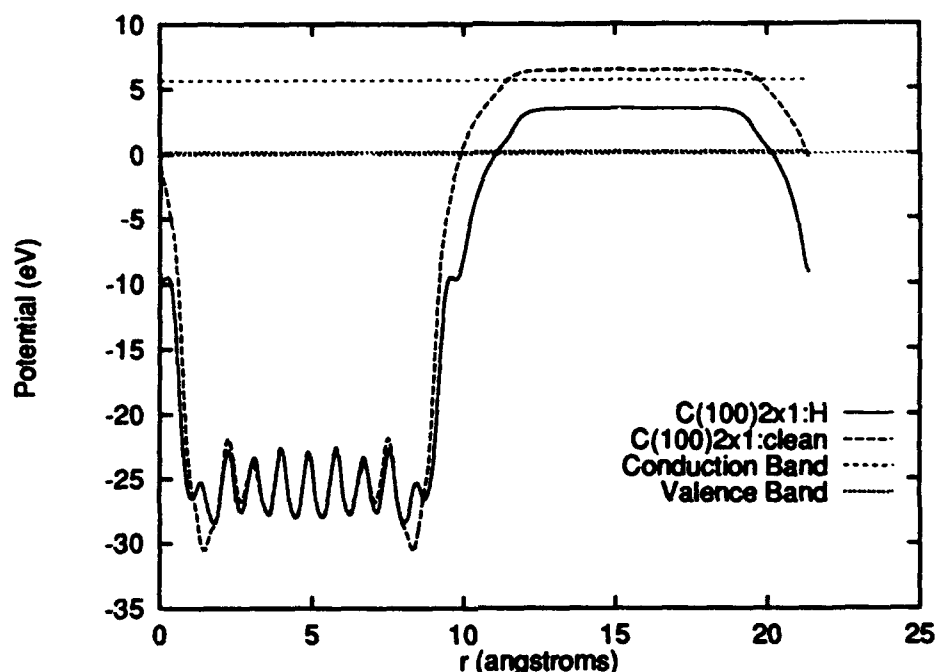


Figure 5. Plane-averaged self-consistent potential.

#### F. References

1. T. Tsuno, T. Imai, Japanese Journal of Applied Physics **30**(5) (1991).
2. A. V. Hamza, G. D. Kubiak, and R. H. Stulen, Surf. Sci. **237** (1990) 35.
3. C. Cheng and J. G. Yates, Phys. Rev. B **43** (1991) 4041.
4. S. P. Mehandru and A. B. Anderson, Surf. Sci. **248** (1991) 369.
5. S. H. Yang, D. A. Drabold and J. B. Adams, Phys. Rev. B **48**(8) (1993) 5261.
6. F. J. Himpsel, *et al.*, Phys. Rev. B **20**(2) (1979) 624.
7. B. B. Pate, Sur. Sci. **165** (1985) 83.
8. J. van der Weide, *et al.*, to be submitted to PRL, 1993.
9. C. G. B. Garrett and W. H. Brattain, Physical Review **99**(2) (1955) 376.
10. B. B. Pate, *et al.*, J. Vac. Sci. Technol. **17**(5) (1980) 1087.
11. R. Car, Phys. Rev. Lett. **55** (1985) 2471.
12. D. R. Hamann, M. Schluter, and C. Chiang, Phys. Rev. Lett. **43** (1979) 1494.
13. G. B. Bachelet, D. R. Hamann, and M. Schluter, Phys. Rev. B **26** (1982) 4199.
14. C. Wang, Q.-M. Zhang, and J. Bernholc, PRL **69**(26) (1992) 3789.
15. X. M. Zheng and P. V. Smith, Surf. Sci. **256** (1991) 1.
16. B. N. Davidson and W. E. Pickett, preprints, (1993).
17. Y. L. Yang and M. D'Evelyn, J. Vac. Sci. Technol. A, **10**(4) (1991) 978.
18. Y. L. Yang, *et al.*, Thin Solid Films **225** (1993) 203.
19. R. P.J. Hamers, P. Avouris, and F. Bozso, Phys. Rev. Lett. **59**(18) (1987) 2071.
20. S. Ciraci, *et al.*, Phys. Rev. B **30**(2) (1984) 711.
21. S.-T. Lee and G. Apai, Phys. Rev. B **48** (1993) 9556.

### **III. Negative Electron Affinity Effects on the Diamond (100) Surface**

**J. van der Weide, Z. Zhang, P. K. Baumann, M. G. Wensell,  
J. Bernholc and R. J. Nemanich**

**Department of Physics and Department of Materials Science and Engineering,  
North Carolina State University,  
Raleigh, North Carolina 27695-8202**

#### **Abstract**

A negative electron affinity (NEA) was found both experimentally by photoemission spectroscopy and theoretically by *ab initio* calculations for the  $2\times 1$  reconstructed diamond (100) surface. This surface is the dominant growth surface for diamond thin films and can be obtained by chemical vapor deposition. Various surface preparation methods which result in a NEA are described. Theoretical results indicate that the observed NEA is associated with a monohydride terminated surface, while the hydrogen-free surface exhibits a positive electron affinity.

---

Submitted to Physical Review Letters, PACS numbers: 73.30.+y, 79.60.Eq, 81.60.Cp

Negative electron affinity (NEA) surfaces are semiconductor surfaces that have a work function such that the vacuum level lies below the conduction band edge. Electrons that are present in the conduction band can therefore readily escape the surface. The NEA surfaces are utilized in a number of important applications, such as photocathodes, secondary electron emitters, and cold-cathode emitters. In general, wide bandgap semiconductors are particularly suitable candidates for NEA emitters, since the conduction band minimum is likely to be close to the vacuum level. Diamond, which has a 5.5 eV bandgap, can be grown as high quality homoepitaxial and heteroepitaxial films with (100) oriented surfaces [1]. We have investigated the possibility of inducing a NEA on the diamond (100) surface and have found several surface preparation methods which led to this effect. *Ab initio* calculations were used to compute the electron affinity of different surface structures, and to identify the structure of the NEA surface and the origin of the NEA effect.

Photoemission is a highly sensitive tool to determine the presence of a NEA. Electrons that are excited in the photoemission process from the valence band into various conduction band energy levels lose energy through inelastic collision processes and accumulate in levels at the conduction band minimum. At a NEA surface, the vacuum level lies below the conduction band and the electrons accumulated at the conduction band minimum can be emitted into the vacuum. These electrons appear in the photoemission spectra as a sharp peak at low electron energies. The position of the peak can be correlated with other features in the photoemission spectra to verify that the emission originates from the conduction band minimum.

A NEA has been demonstrated for the diamond (111) surface [2] and has been associated with the presence of hydrogen bonded to the surface [3, 4]. The bulk terminated diamond (100) surface has two unsatisfied bonds which would in principle allow the formation of a dihydride terminated surface. The existence of the dihydride terminated surface has been subject to some debate [5-9]. Recent large scale *ab initio* calculations indicate that this surface is locally stable, but it is preferred only at very high values of hydrogen chemical potential [10]. It is, therefore, uncertain whether a stable dihydride terminated surface can be achieved. Diamond thin films, grown at 700-1000°C in a hydrogen rich environment, typically exhibit a 2×1 reconstruction. This surface is found to be stable in air [11], and is presumed to be a monohydride terminated surface [7]. A 2×1 reconstructed surface can also be obtained by annealing the diamond surface to ~1000°C. Temperature programmed desorption studies indicate that at these temperatures the monohydride evolves from the surface [7, 12], and it has been suggested that this surface is free of hydrogen [7].

In this study natural diamond wafers with a (100) surface orientation were polished with diamond grit, etched in chromic acid and *aqua regia* and introduced into the vacuum system. The wafers measured  $3 \times 3 \times 0.5 \text{ mm}^3$ , and were type IIb (p-type semiconducting) with

resistivities of  $10^3$ – $10^4$   $\Omega\text{cm}$ . Photoemission was excited with 21.21 eV light from a helium discharge lamp. The photoemission spectra, shown in Fig. 1, were obtained after the diamond surface had been annealed to temperatures ranging from 545°C to 1070°C. The spectra exhibited small, random shifts on the order of 0.2 eV with respect to each other. This is attributed to charging effects. The spectra were therefore aligned according to a bulk feature indicated by the line in Fig. 1 to allow comparison between them. As can be seen in the figure, the low energy onset of the spectra shifts by as much as 1 eV towards lower energies as the annealing temperature is increased. This is indicative of a lowering of the work function of the surface since electrons with lower energies are able to escape from the surface. After a 1035°C anneal the spectrum exhibits a peak at low energies which becomes more pronounced after a 1070°C anneal. As mentioned above, the appearance of this peak indicates that the vacuum level lies below the conduction band edge and that the surface has a NEA. The peak is positioned  $\sim 7.5$  eV below the bulk feature indicated by the solid line in Fig. 1. An identical peak at  $\sim 7.5$  eV below this bulk feature can be observed in the spectra of NEA diamond (111) surfaces [13–15]. The appearance of the peak on the (100) surface coincided with the appearance of a  $2\times 1$  surface reconstruction.

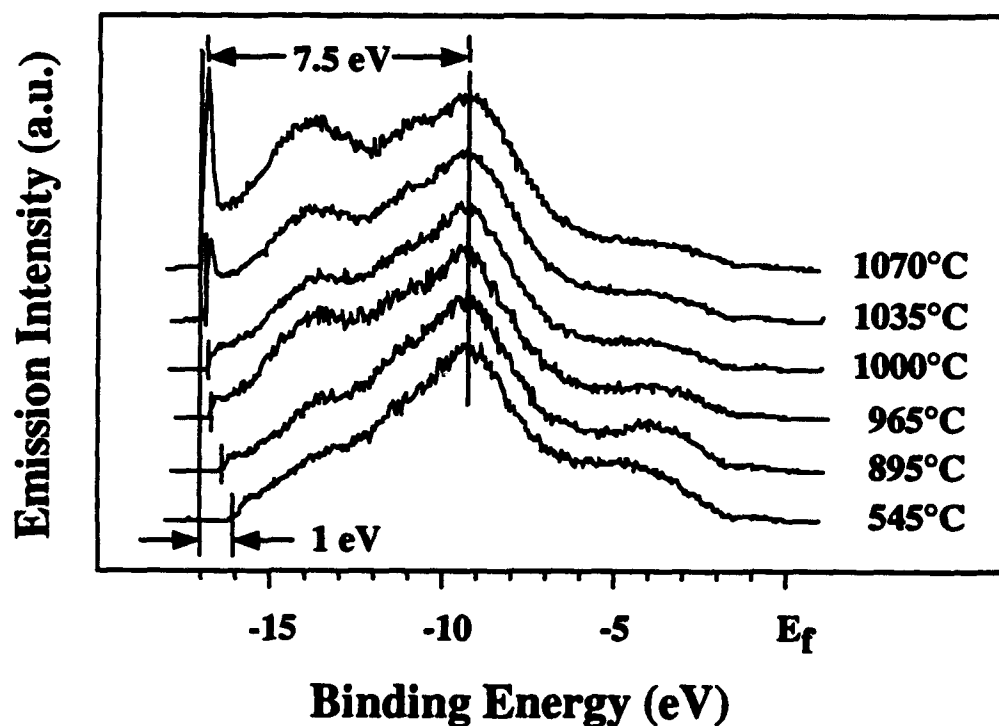


Figure 1. Photoemission spectra showing the effects of annealing on the diamond (100) surface. The shift in the back edge is indicative of a lowering of the work function and the presence of the sharp peak indicates a NEA. The spectra have been aligned according to the peak at  $\sim 9$  eV below the Fermi level.

Auger electron spectra, shown in Fig. 2, indicate the presence of oxygen on the as-loaded surface which remained present after various anneals ranging from 500°C to 900°C. A reduction in the oxygen signature was observed after repeated anneals to 900°C. No oxygen could be detected after the diamond had been annealed to 1050°C. The surface was observed to transform from a 1×1 structure to a 2×1 structure, coincident with the removal of oxygen from the surface. The presence of hydrogen on the 1×1 and 2×1 surfaces cannot be determined from these measurements since AES is not sensitive to hydrogen. However, since no special efforts were made to obtain a strictly oxygen terminated surface, it is likely that hydrogen was also present on the surface.

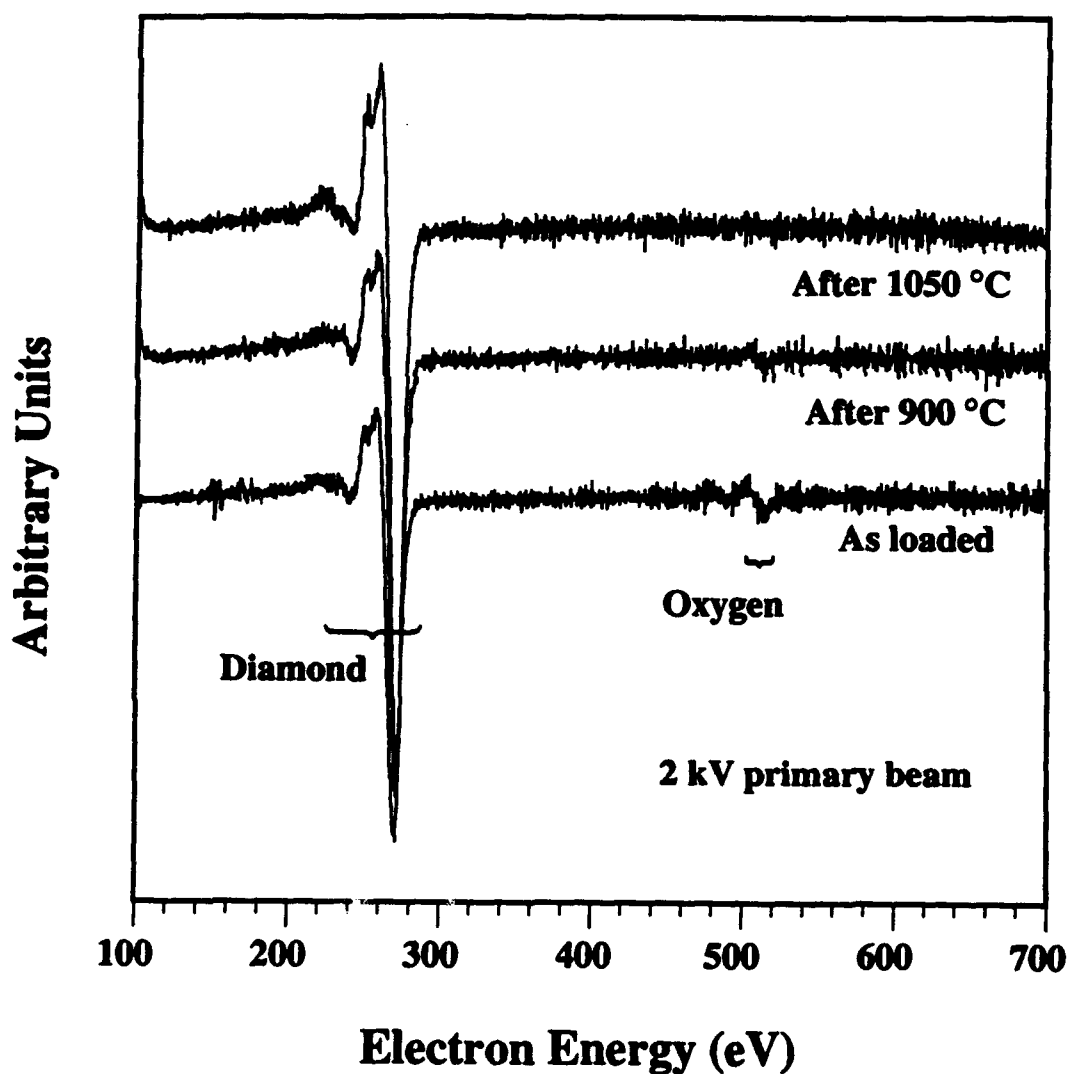


Figure 2. Auger spectra, obtained from the diamond (100) surface, as a function of annealing temperature. Oxygen, which is present on the surface after sample preparation, is observed to evolve at ~900°C, and removed after a 1050°C anneal. The removal of oxygen coincides with the transformation of the surface from a 1×1 to a 2×1 reconstructed surface.

Neither LEED nor AES can be used to determine whether the observed  $2\times 1$  reconstructed surface is a hydrogen-free or a monohydride terminated surface. In order to resolve that we have carried out *ab initio* calculations for both the bare and the hydrogen terminated  $2\times 1$  reconstructed diamond surfaces. The calculations were based on the Local Density Approximation (LDA) and the Car-Parrinello formalism [16]. The hydrogen-free (100) surface was modeled by a supercell consisting of a slab of ten layers of diamond with twelve carbon atoms on each layer. The slabs were separated by 10 Å of vacuum. One hydrogen atom was attached to every surface carbon atom to model the monohydride surface. Due to the size of the supercell, only  $\Gamma$  point sampling was used. Starting from an approximate structure, the ground state geometry was obtained by steepest descents and/or fast relaxation methods [17]. The vacuum level of the surface was determined from the plane-averaged, self-consistent potential in the vacuum region. Since calculations based on the local density approximation do not reproduce well the experimentally measured bandgap [18], the position of the conduction band minimum is determined by adding the experimental value for the bandgap (5.47 eV) to the position of the valence band maximum. The position of the valence band maximum was found by adding the energy difference between the average self-consistent potential in the bulk and the highest occupied energy level in bulk calculations to the average self-consistent potential inside the slab.

The calculations indicated that the monohydride terminated surface relaxes to a  $2\times 1$  reconstructed surface. The plane-averaged, self-consistent potential for this surface is shown as a function of the distance to the surface in Fig. 3. As can be seen in the figure, the effective potential has flattened out in the vacuum region, which indicates that the slab separation used in the calculations is sufficiently large to avoid interactions between the slabs. The flat region is representative of the vacuum level. The conduction band minimum is found at  $\sim 2.2$  eV above the vacuum level, resulting in a  $\sim 2.2$  eV NEA for C(100)- $2\times 1$ :H surface.

The bare C(100) surface also relaxes to a  $2\times 1$  reconstruction, with a geometry similar to that obtained by other authors [9, 19]. Substantial displacements from the ideal bulk positions were found in the surface layers. The plane-averaged self-consistent potential for this surface is also shown in Fig 3. A  $\sim 0.8$  eV positive electron affinity was found for this surface. We also find that occupied surface states exist inside the bandgap near the valence band maximum, in agreement with photoemission studies [20]. The calculations indicate that these states are related to dangling bond orbitals on the dimer atoms. The electronic charge in these dangling orbitals results in a stronger dipole layer of the bare surface when compared to the hydrogenated surface. The differences in work function and electron affinities between these two surfaces are due to this dipole layer.

The CVD grown diamond (100) surface is known to exhibit a  $2\times 1$  reconstruction, which has been shown to be stable in air [11]. This  $2\times 1$  reconstruction has been attributed to the



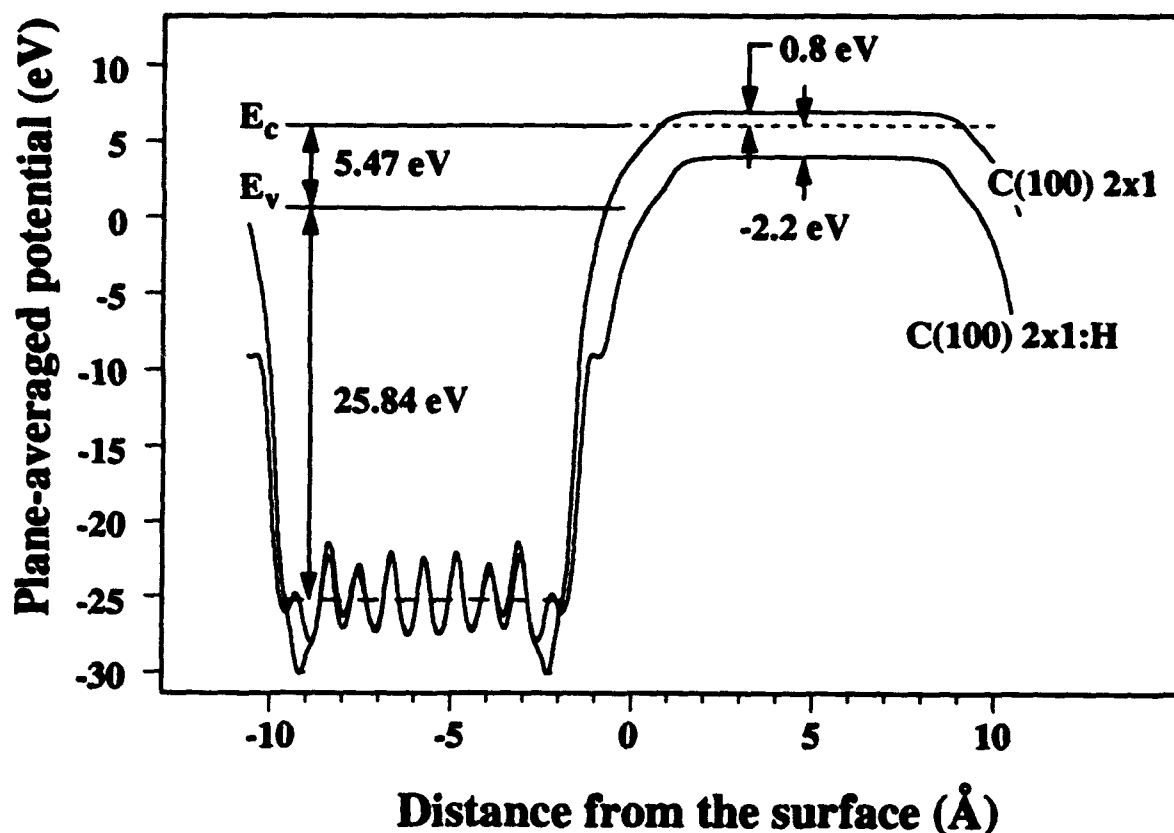


Figure 3. Calculated plane-averaged, self-consistent potentials of a hydrogen-free and monohydride terminated  $2\times 1$  reconstructed diamond (100) surface.

presence of a monohydride structure [5–7]. Based on the results described above it is expected that the CVD growth surface would exhibit a NEA. Diamond was deposited on a (100) oriented, type IIb wafer, resulting in a homoepitaxial film. After transport in air a faint pattern associated with the  $2\times 1$  reconstruction could be discerned. The film was etched to remove a dark discoloration which was due to the deposition process. After the etch, the  $2\times 1$  reconstruction could not be discerned but the  $1\times 1$  bulk pattern remained. Photoemission spectra, shown in Fig. 4, exhibited a clear peak at 7.3 eV below the bulk feature indicating the presence of a NEA. This result suggests that the (100) oriented growth surface exhibits a NEA which is unaffected by exposure to air and various etches.

Typical diamond growth conditions consist of surface temperatures ranging from 700°C to 1000°C and exposure to a hydrogen plasma with a small (< 5%) amount of a carbon containing gas mixed in. To emulate growth conditions, natural diamond wafers were exposed to a pure hydrogen plasma while heated to 350°C and 500°C. It was found that under these conditions a NEA could be induced as well. This result supports the conclusion that the growth surface exhibits a NEA which is related to hydrogen termination.

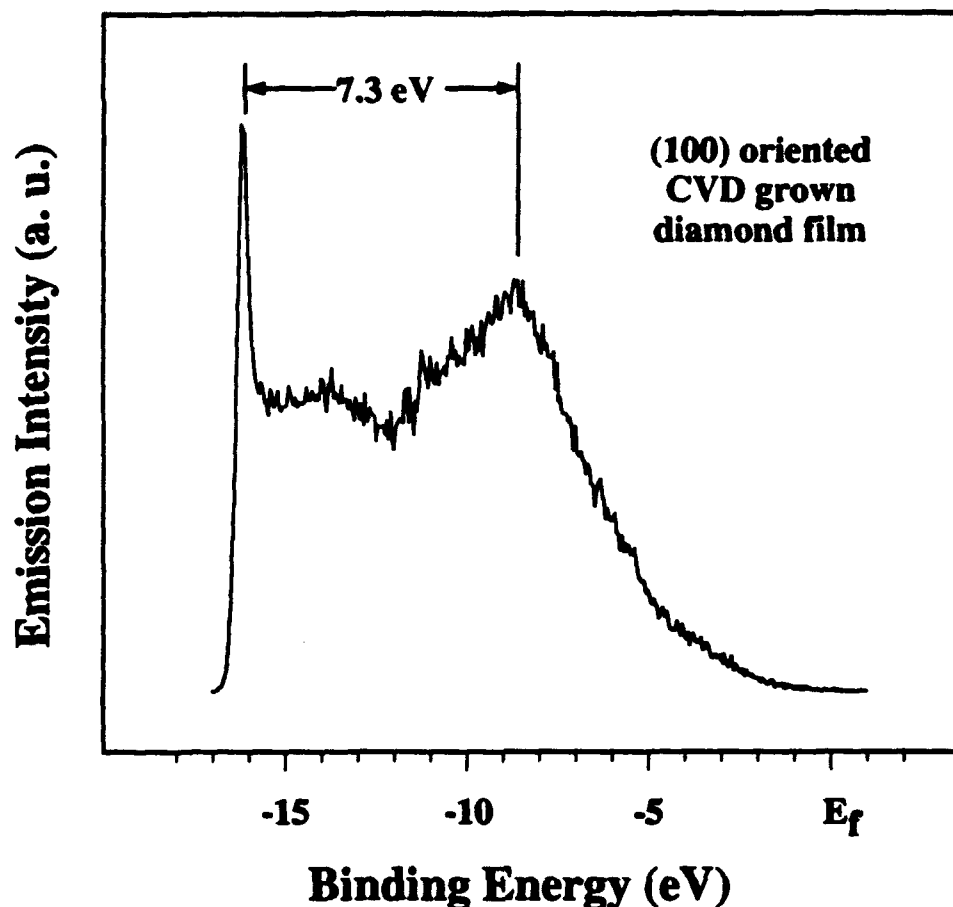


Figure 4. Photoemission obtained from a CVD grown, (100) oriented diamond film indicates the presence of a NEA.

In summary, a NEA was obtained on the diamond (100) by annealing a polished and chemically cleaned surface to  $\sim 1000^\circ\text{C}$ . This resulted in the desorption of oxygen and the appearance of a  $2\times 1$  reconstruction. Theoretical calculations indicate that the NEA is associated with a monohydride terminated surface. It was found that CVD-grown diamond film, which results in a similar surface structure, exhibits a NEA. A NEA can also be induced by exposing a surface heated to  $350\text{--}500^\circ\text{C}$  to a hydrogen plasma, supporting the conclusion that the growth surface exhibits a NEA. Many more NEA emitters are likely to be found as the methods for growth of wide bandgap semiconductors are improved. Local-density-based calculations, when corrected for bandgap effect, appear to predict correctly the occurrence of the NEA effect. These calculations can thus be used to identify other promising passivant-semiconductor combinations for NEA emitters, and to establish trends in dipole strength and sign. Photoemission experiments provide unambiguous evidence of the existence of NEA, and can be used both to calibrate the theoretical findings and to verify the actual occurrence of NEA.

The authors would like to acknowledge L.S. Plano and K. Das of Kobe Research for diamond film growth and polishing. This work was supported in part by the Office of Naval Research through grants N0014-92-J-1477 and N0014-92-J-1604 and the National Science Foundation through grants DMR-9204285 and DMR-9100063.

## References

1. S. D. Wolter, B. R. Stoner, J. T. Glass, P. J. Ellis, D. S. Buhaenko, C. E. Jenkins and P. Southworth, *Appl. Phys. Lett.* **62**, 1215 (1993).
2. F.J. Himpsel, J. A. Knapp, J. A. van Vechten and D. E. Eastman, *Phys. Rev. B* **20**, 624 (1979).
3. B. B. Pate, *Surf. Sci.* **165**, 83 (1986).
4. B. B. Pate, M.H. Hecht, C. Binns, I. Lindau and W.E. Spicer, *J. Vac. Sci. Technol.* **21**, 364 (1982).
5. Y. L. Yang and M. P. D'Evelyn, *J. Vac. Sci. Technol., A* **10**, 978 (1992).
6. Y. L. Yang and M. P. D'Evelyn, *J. Am. Chem. Soc.* **114**, 2796 (1992).
7. Y. L. Yang, L. M. Struck, L. F. Sutcu and M. P. D'Evelyn, *Thin Solid Films* **225**, 203 (1993).
8. B. N. Davidson and W. E. Pickett, preprint
9. S. H. Yang, D. Drabold and J. B. Adams, *Phys. Rev. B* **48**, 5261 (1993).
10. M. G. Wensell, Z. Zhang and J. Bernholc, to be published.
11. T. Tsuno, T. Imai and Y. Nishibayashi, *Jap. J. Appl. Phys.* **30**, 1063 (1991).
12. R. E. Thomas, R. A. Rudder and R. J. Markunas, *J. Vac. Sci. Technol. A* **10**, 2451 (1992).
13. J. van der Weide and R. J. Nemanich, submitted to *J. Appl. Phys.*
14. J. van der Weide and R. J. Nemanich, *J. Vac. Sci. Technol. B* **10**, 1940 (1992).
15. J. van der Weide and R. J. Nemanich, *Appl. Phys. Lett.* **62**, 1878 (1993).
16. R. Car and M. Parrinello, *Phys. Rev. Lett.* **55**, 2471 (1985).
17. C. Wang, Q.-M. Zhang and J. Bernholc, *Phys. Rev. Lett.* **69**, 3798 (1992).
18. D. Hamman, M. Schluter and C. Chiang, *Phys. Rev. Lett.* **43**, 1494 (1979).
19. S. P. Mehandru and A. B. Anderson, *Surf. Sci.* **248**, 369 (1991).
20. A. V. Hamza, G. D. Kubiak and R. H. Stulen, *Surf. Sci.* **237**, 1 (1990).

## IV. Bias-enhanced Nucleation on Refractory Metal Substrates

### A. Introduction

The first attempts to produce synthetic diamond relied upon the fact that diamond is composed entirely of carbon. Therefore, to form diamond it is essential that for the case of low pressure CVD, for example, a carbon containing gas source is utilized. In this high temperature process environment it is likely that carbide phases will be produced if the substrates are capable of forming them. These carbide phases have been observed via x-ray diffraction (XRD) [1] and surface sensitive techniques [2, 3] such as x-ray photoelectron spectroscopy (XPS) and Auger electron spectroscopy (AES).

The understanding how the formation of a carbide influences the diamond nucleation process is important. Joffreau *et al.* [1] have observed an influence on diamond nucleation pertaining to refractory metal substrates. These substrates are known carbide formers and their formation was confirmed via XRD. Also, surface analytical studies on scratched silicon have indicated the formation of a carbide prior to detecting the presence of diamond [2, 3]. It should be noted though that very early during nucleation the presence of diamond may be difficult to observe since the diamond present is possibly below the sensitivity of the analytical instrumentation. To enhance the nucleation density on these and other non-carbide forming substrates the typical pretreatment involves scratching the substrates with diamond grit. Researchers suggest that diamond residue from this pretreatment routine is important for diamond nucleation [4, 5]. This diamond residue may act as nucleation sites and/or may provide surface carbon that is ideal for diamond nucleation. The form of the surface carbon may be relevant for diamond nucleation; therefore, much work has been directed toward observing the influence of nucleation on the form of the surface carbon [5-7]. It appears that the form of the surface carbon and the formation of a carbide play a role in the diamond nucleation process.

This study was undertaken to investigate the influence of bias-enhanced nucleation (BEN) on the refractory metals. BEN has been observed to enhance the diamond nucleation density on unscratched silicon substrates [8, 9]. This process involves applying a negative bias to the substrate holder in order to promote diamond nucleation. The carbide forming nature of silicon has been speculated to be an important attribute of this material [8, 10]. Thus, the varying degrees of the carbide forming nature of the refractory metals may indicate a correlation with the nucleation phenomena via BEN. This should make it possible to gain further insight into the BEN phenomena as well as investigating potential heteroepitaxial substrates using this pretreatment technique.

## B. Experimental

Bias-enhanced nucleation of diamond and diamond deposition was performed in a microwave plasma CVD chamber purchased from Applied Science and Technology, Inc. The growth system and BEN apparatus has been discussed previously [8]. Table I indicates the BEN and growth conditions utilized in this study. The refractory metals used in this study were hafnium, titanium, tantalum, niobium, and tungsten. These substrates were chosen as arbitrary representations of carbide formers with the exception to hafnium in which this substrate was used to confirm possible correlations as explained in the Discussion section. The substrates were highly polished down to 0.05 $\mu$ m alumina grit suspended in deionized water.

Table I. The BEN and growth conditions utilized in this study

Process Parameters	Bias Conditions	Growth Conditions
Microwave Power	900 Watts	900 Watts
CH <sub>4</sub> /H <sub>2</sub>	5%	1%
Pressure	15 Torr	25 Torr
Substrate Temperature	~725°C	~700°C
Bias Voltage	-250VDC	Floating
Bias Current	~100mA	N/A
Sample Position	Immersed	Immersed

Alumina was used in the final polishing procedure to ensure that very little residual diamond would be present on the substrates which was used in the preceding polishing steps. The substrates were then solvent cleaned using TCE, acetone, methanol, and 2-propanol, consecutively. A deionized water rinse was performed on the substrates just prior to entering into the growth chamber. As discussed briefly, BEN was used as an *in situ* pretreatment technique to promote diamond nucleation. A negative potential was applied to the molybdenum holder containing the substrate. The positive potential was applied to the chamber wall. The refractory metal substrates were subjected to various bias times followed by 30 minutes of growth to obtain a plot of nucleation density versus bias time. The short growth period enabled an accurate account of all the diamond nuclei that was later determined by scanning electron microscopy (SEM). X-ray diffraction (XRD) was used to determine the phases present following BEN and the short growth period. Table II lists the carbide phases observed via XRD in addition to their carbide heat of formation values [11].

Table II. This table indicates the metal-carbides observed in this study using XRD. Along with this data are the carbide heat of formation for each.

Possible Carbides	$\Delta H_f$ (kcal/mole-metal)	Observed in this study
$\beta$ -SiC	-15.6	Not studied
HfC	-60.1	Yes
TiC	-44.1	Yes
TaC	-35.0	Yes
Ta <sub>2</sub> C	-24.9	Yes
NbC	-33.2	Yes
Nb <sub>2</sub> C	-23.3	Yes
WC	-9.69	Yes
W <sub>2</sub> C	-3.2	Yes

### C. Results

The plot of nucleation density versus bias time for the refractory metals referenced to silicon and copper is shown in Fig. 1. A study of copper versus silicon revealed that the substrate choice did influence the nucleation density during BEN [10]. This is obvious as indicated in this plot. The individual plots for the refractory metals were fit with correlation coefficients greater than 0.85. The influence that BEN had on these substrates was determined by denoting the nucleation densities at 60 minutes of biasing. At this time the nucleation densities were approximately constant with any further biasing. The nucleation densities at these times are plotted in Fig. 2 according to there position in the refractory metal portion of the periodic table. This plot suggests that there is a correlation established among these materials. The metals in parenthesis are estimated positions as related to the substrates studied in this report.

The materials under investigation as discussed earlier were hafnium, titanium, tantalum, niobium, and tungsten. The hafnium, though, was studied following the work on the other metals to verify the possible correlation existing among these metals as was indicated in Fig. 2. It was determined in research conducted by Joffreau *et al.* [1] that the substrate may influence diamond nucleation. In their study refractory substrates displayed a correlation to the incubation time (i.e. the time prior to the onset of nucleation) and the nucleation rate. Therefore, it is not unlikely that the refractory metals in this study also show a correlation. The correlation to the material properties of these metals referenced to the nucleation density via BEN will be discussed in the next section.

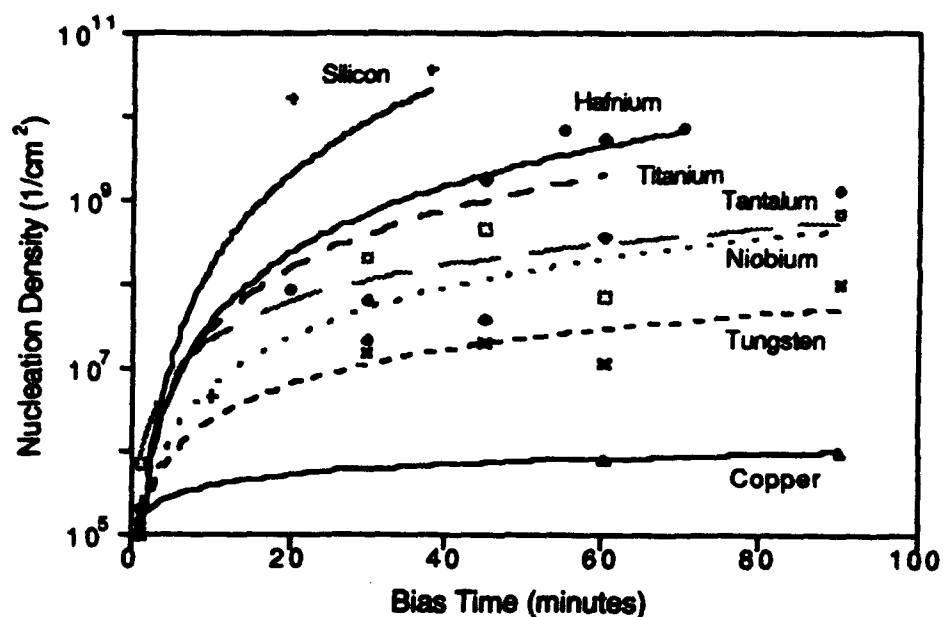


Figure 1. This plot illustrates the relative influence of BEN on the refractory metal substrates referenced to silicon and copper.

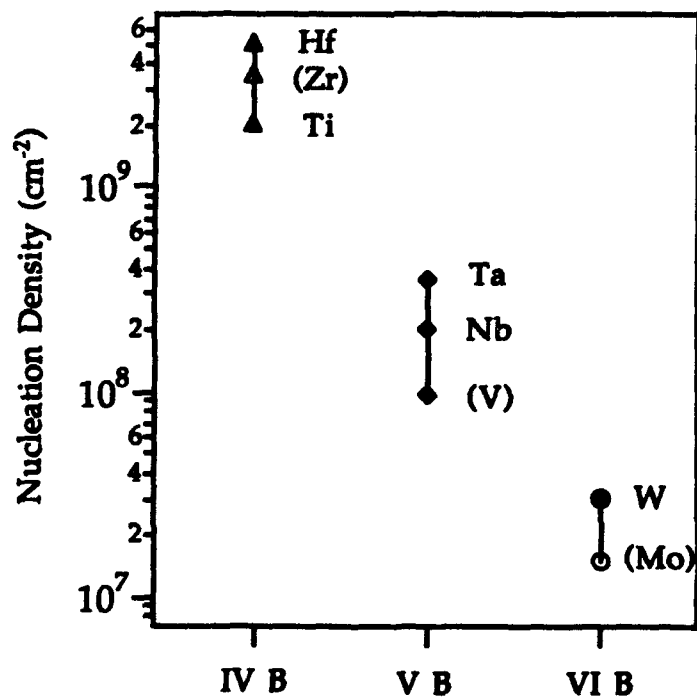


Figure 2. This graphic shows the nucleation density at 60 minutes of biasing according to the relative positions of the refractory metals in the periodic table.

The refractory metals that were targeted are shown in Fig. 3 as they are situated in the periodic table. These materials were chosen because of their carbide forming nature. A previous study of copper versus silicon indicated a substrate effect [10]; the carbide forming nature of silicon was believed to be a key factor. The choice of these metals also allowed a group of materials to be studied with the possibility of observing other properties of these substrates which could enhance the effects of BEN. The study of refractory metals and refractory metal carbides have been undertaken for decades with the intent to investigate their high temperature material characteristics. Figure 4 shows a trend established between the activation energy for carbon diffusion in the refractory metal substrates and the melting points of these refractory metals [11].

IV B	VB	VIB
Ti	V	Cr
Zr	Nb	Mo
Hf	Ta	W

Figure 3. The refractory metals used in this study are indicated in their respective position in the periodic table.

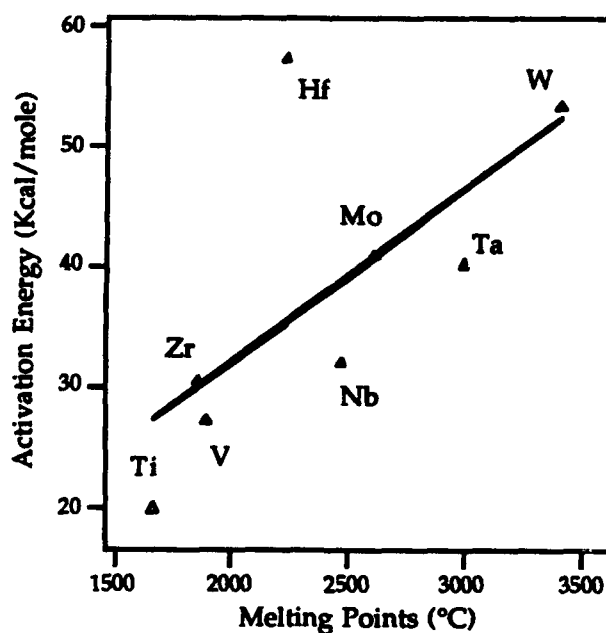


Figure 4. This figure notes the trend between the activation energy for diffusion of carbon in the refractory metal substrates versus their melting points [11].



Also, Fig. 5 shows a correlation between the carbide heat of formation and the ratio of the melting points of the metal to that of the metal carbide [11]. This later figure was based on the work by Worrel *et al.* [12] It can be assumed then that in reference to Fig. 4 the carbon diffusivity in the refractory metals is related to the melting points of these metals. Also, the thermodynamic relationship presented by Worrel gives some indication as to the metal-carbon bonding nature. The carbide heat of formation related to the refractory metals in their respective groups in the periodic table are shown in Fig. 6. This data shows the distinct correlation among the refractory metals for this thermodynamic property. The carbide data obtained from the literature are difficult to determine and the data in some instances are still not well established. Therefore, the overall trends presented in this work are emphasized with little emphasis placed on the specific values. Figure 7 indicates the trend established in the present study between the carbide heat of formation and the nucleation density at 60 minutes of biasing.

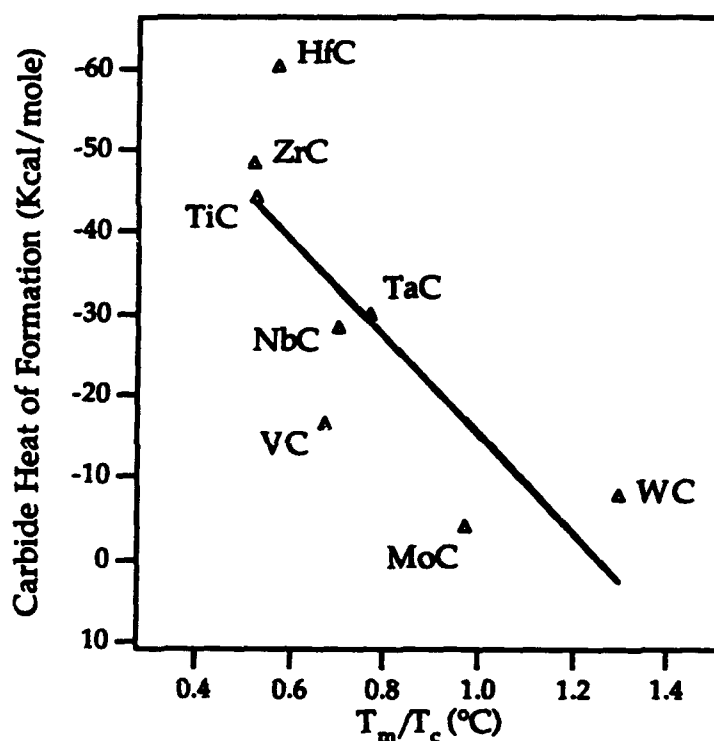


Figure 5. This graphic indicates a correlation between the carbide heat of formation and the ratio of the metal to metal-carbide melting points.

#### E. Conclusions

BEN has lead to heteroepitaxy on  $\beta$ -SiC [13, 14] and Si(100) [15]. A BEN study conducted on copper showed a slight influence for enhancing the nucleation density [10].

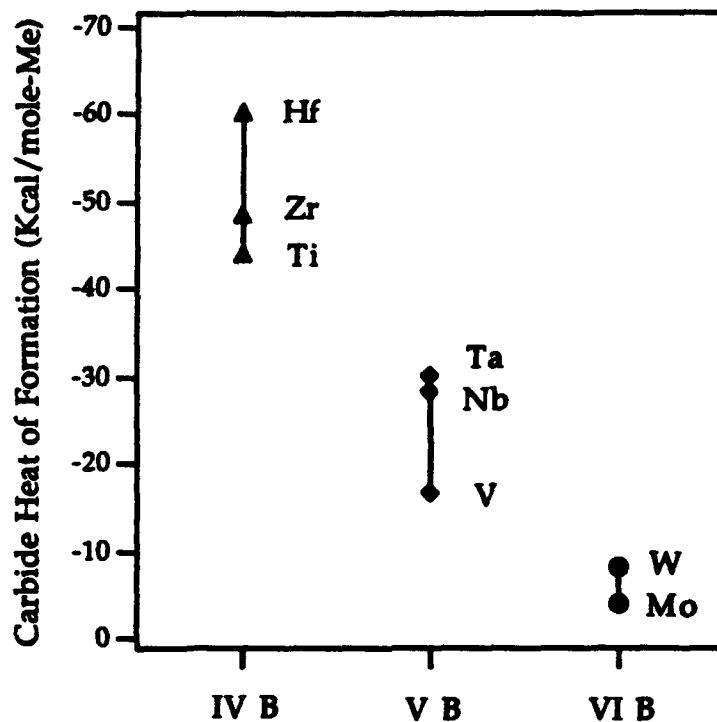


Figure 6. Material properties such as the carbide heat of formation as is shown here illustrates a correlation among the refractory metals.

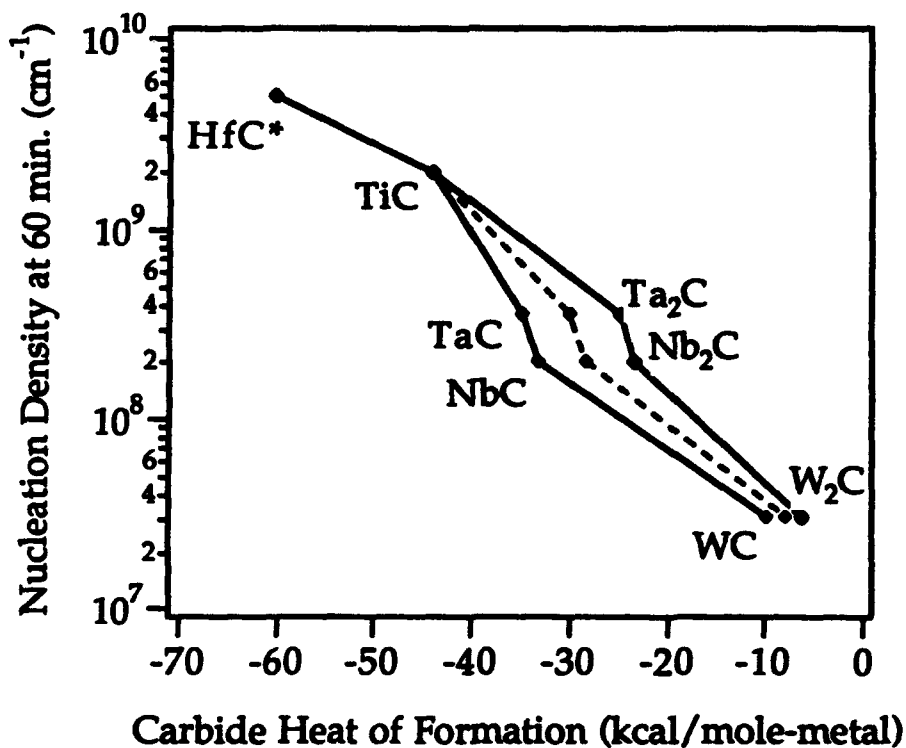


Figure 7. The trend established in the present study between the carbide heat of formation and the nucleation density at 60 minutes of biasing.

Therefore, the carbide forming nature of silicon appears to be an important attribute. Thus, the motivation for studying the refractory metals is linked to their carbide forming traits. These substrates offer a class of potential heteroepitaxial substrates and also provide a group of metals that because they possess different material properties are ideal for gaining an understanding of BEN. The refractory metals did show a correlation to the carbide heat of formation. This property have been discussed to be related to other refractory material properties. The thermodynamic data referenced to the nucleation density at 60 minutes of biasing indicates very strongly that the substrates are influencing the nucleation mechanisms, as was the case in the study of BEN on copper. Also, the relatively high nucleation densities (with no scratching pretreatment) reveals that, provided a high quality carbide may be formed, these substrates are potential candidates for BEN of heteroepitaxial diamond.

#### F. Acknowledgments

The authors wish to acknowledge the financial support of this research which was provided in part by BMDO/IST through ONR and the Kobe Steel, Ltd. Professorship at NCSU.

#### G. References

1. P. O. Joffreau, R. Haubner and B. Lux, *Int. J. of Ref. Hard Metals*, **7** (1988) 186.
2. D. N. Belton, S. J. Harris, S. J. Schmieg, A. M. Wiener and T. A. Perry, *Appl. Phys. Lett.*, **54** (1989) 416.
3. B. E. Williams, B. R. Stoner, D. A. Asbury and J. T. Glass, presented at *NATO Advanced Study Institute on Diamond and Diamond-Like Films and Coatings*, Castelveccchio Pascoli, Italy, 1990.
4. P. K. Bachmann, W. Drawl, D. Knight, R. Weimer and R. F. Messier, presented at *Diamond and Diamond-Like Materials Synthesis*, 1988, Materials Research Society, p. 99.
5. J. C. Angus, Z. Li, M. Sunkara, R. Gat, A. B. Anderson, S. P. Mehandru and M. W. Geis, *Proceedings of the Second International Symposium on Diamond Materials*, Electrochemical Society Meeting, Washington, DC, May 5-10, 1991.
6. J. J. Dubray, C. G. Pantano, M. Meloncelli and E. Bertran, *J. Vac. Sci. Technol. A*, **9** (1991) 3012.
7. Y. Avigal, *Diamond and Related Materials*, **1** (1992)
8. B. R. Stoner, G.-H. M. Ma, S. D. Wolter and J. T. Glass, *Phys. Rev. B*, **45** (1991) 11067.
9. S. Yugo, T. Kanai, T. Kimura and T. Muto, *Appl. Phys. Lett.*, **58** (1991) 1036.
10. S. D. Wolter, B. R. Stoner and J. T. Glass, *Diamond and Related Materials*, (1994), in press.
11. *CRC Handbook of Chemistry and Physics*, CRC Press, Inc., Boca Raton, 1983-1984.
12. W. L. Worrell, *J. Phys. Chem.*, **68** (1964) 954.
13. B. R. Stoner and J. T. Glass, *Appl. Phys. Lett.*, **60** (1992) 698.
14. B. R. Stoner, G. H. Ma, S. D. Wolter, W. Zhu, Y.-C. Wang, R. F. Davis and J. T. Glass, *Diamond and Related Materials*, **2** (1993) 142.
15. S. D. Wolter, B. R. Stoner, J. T. Glass, P. J. Ellis, D. S. Buhaenko, C. E. Jenkins and P. Southworth, *Appl. Phys. Lett.*, **62** (11) (1993) 1215.

## V. Diamond Nucleation Using Halogenated Organosilicics

### A. Introduction

This report describes recent experiments involving the use of chlorine substituted organosilicic reagents for use as precursors in the atomic layer nucleation of diamond. In these experiments, four halogenated species,  $(\text{CH}_3)_{4-x}\text{SiCl}_x$  ( $x = 0$  to 3), are introduced onto cleaned and passivated single crystal silicon  $\langle 111 \rangle$  substrates in a hot filament chemical vapor deposition (HFCVD) reactor in order to observe the effect of the increasing halogenation on subsequent diamond nucleation. After diamond nucleation, the resulting films are characterized by SEM and Raman spectroscopy.

### B. Experimental Procedure

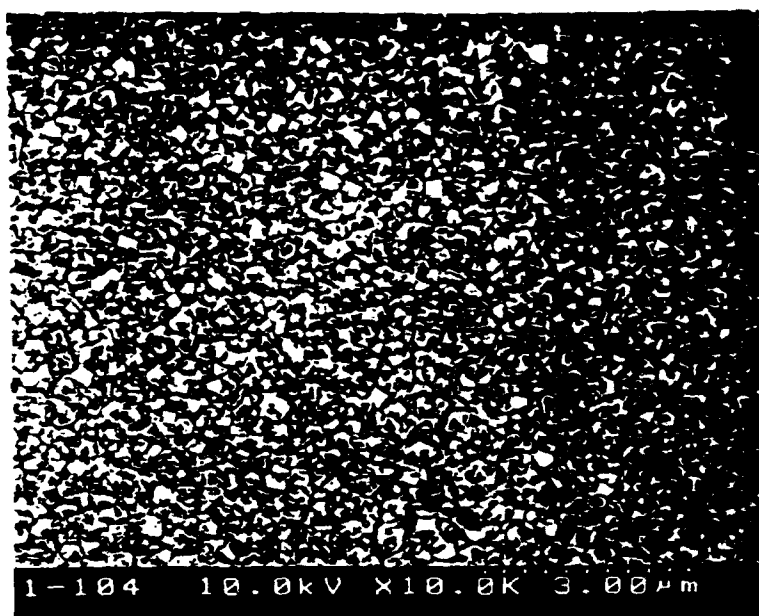
Single crystal Si  $\langle 111 \rangle$  wafers are spin etched[1] and loaded into a HFCVD chamber fitted with a resistively heated sample stage. The chamber is purged with argon and quickly pumped down to  $5 \times 10^{-5}$  torr. Helium carrier gas flow is started and the chamber pressure is maintained typically at 5 torr. The sample is then heated with the stage to 600 °C. Five microliters of reagent are injected into the carrier gas flow via a syringe injection system. Sufficient time is allowed for the species to react with the substrate. Then the helium flow is terminated and bias enhanced HFCVD of diamond using 2%  $\text{CH}_4/\text{H}_2$  is performed on the treated substrate for a period of 20 minutes. SEM and Raman spectroscopy are used to evaluate the diamond nucleation density and quality.

### C. Results

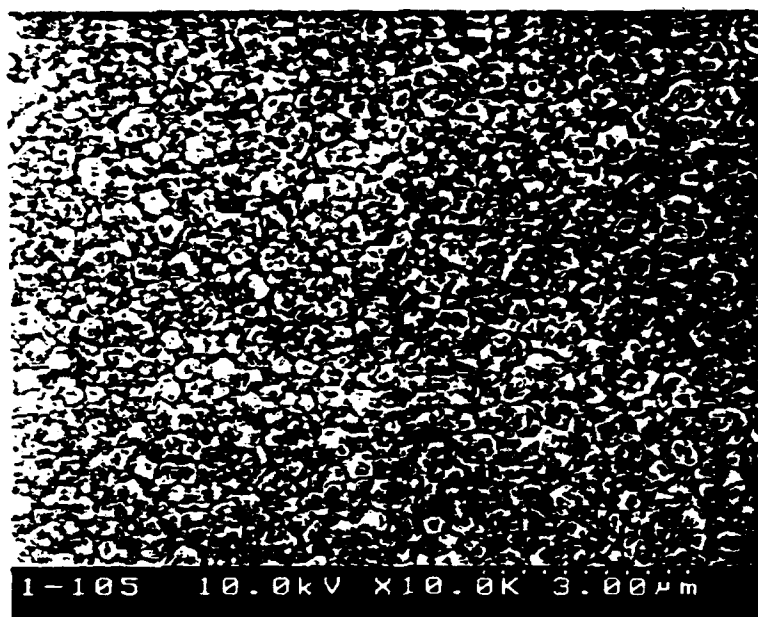
Figure (1a) and (1b) show scanning electron micro graphs of diamond films grown on Si wafers treated with  $(\text{CH}_3)_2\text{SiCl}_2$  and  $\text{CH}_3\text{SiCl}_3$ , respectively. The nucleation densities of these films were measured to be  $2.6 \times 10^9 \text{ cm}^{-2}$  in (1a) and  $1.0 \times 10^9 \text{ cm}^{-2}$  in (1b). The films grown on wafers treated with  $(\text{CH}_3)_4\text{Si}$  and  $(\text{CH}_3)_3\text{SiCl}$  were similar in morphology and texture. Table I lists the measured diamond nucleation densities for the films grown with the four precursors.

Table I. Diamond nucleation densities for treated substrates.

Precursor	particles/cm <sup>2</sup>
$(\text{CH}_3)_4\text{Si}$	$2.0 \times 10^9$
$(\text{CH}_3)_3\text{SiCl}$	$3.0 \times 10^9$
$(\text{CH}_3)_2\text{SiCl}_2$	$2.6 \times 10^9$
$\text{CH}_3\text{SiCl}_3$	$1.0 \times 10^9$



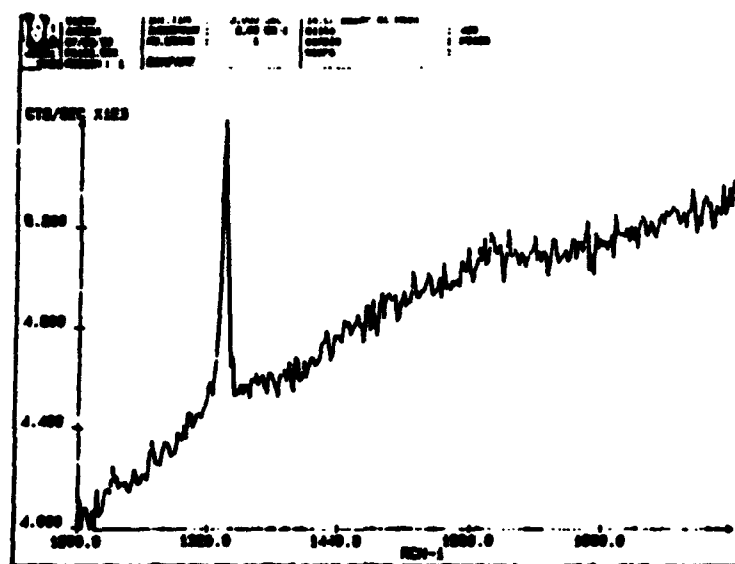
(a)



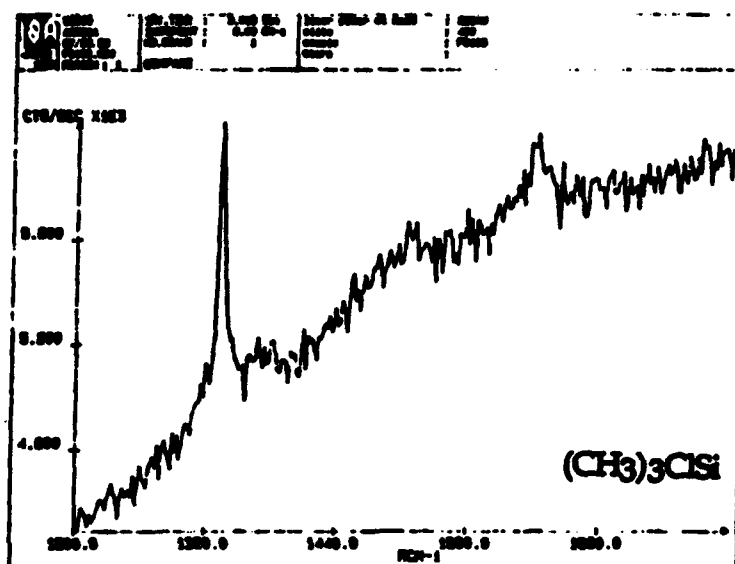
(b)

Figure 1. SEM micrographs of diamond films on Si  $\langle 111 \rangle$  substrates treated with (a)  $(\text{CH}_3)_2\text{SiCl}_2$  and (b)  $\text{CH}_3\text{SiCl}_3$ .

Fig. 2 shows the Raman spectra for the four films. The spectrum for the  $(\text{CH}_3)_2\text{SiCl}_2$  treated wafer shows a sharp peak at  $1334 \text{ cm}^{-1}$ , slightly shifted from the characteristic diamond peak at  $1332 \text{ cm}^{-1}$ . There are sharp peaks at  $1332 \text{ cm}^{-1}$  for the other three films, however, a large graphitic component is present in all four spectra.



$(\text{CH}_3)\text{Cl}_3\text{Si}$



$(\text{CH}_3)_3\text{ClSi}$

Figure 2. Raman spectra of diamond films on treated Si <111> substrates.

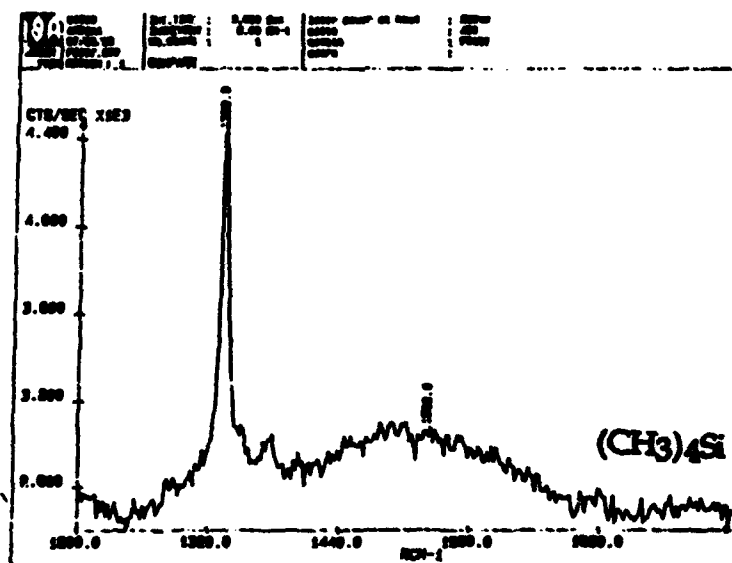
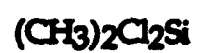
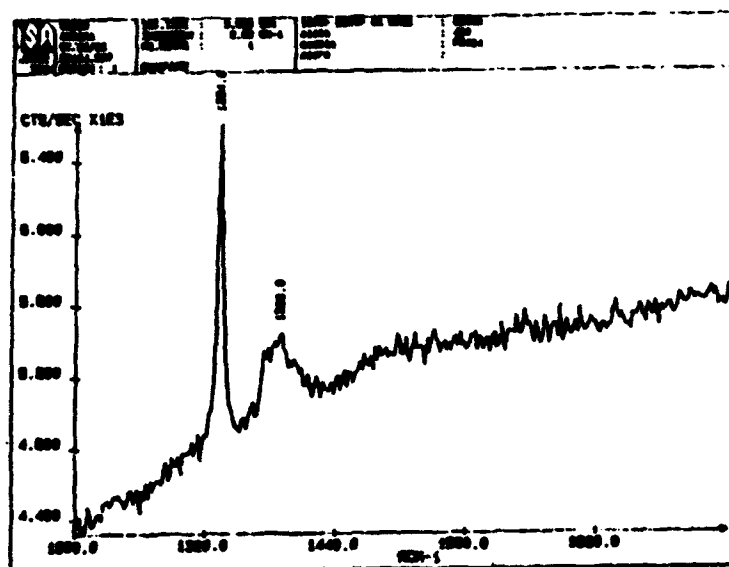


Figure 2. Continued: Raman spectra of diamond films on treated Si <111> substrates.

#### D. Discussion

These experiments were designed to investigate the influence on diamond nucleation of decreasing the number of methyl groups on the  $(\text{CH}_3)_4\text{Si}$  molecule by substituting chlorine for methyl groups. Since the Si-Cl bond energy (406 kJ/mol) is less than the Si-CH<sub>3</sub> bond energy (451 kJ/mol), Cl will leave before the methyl group. We expected that the more highly Cl substituted molecules would bond more easily with the Si substrate surface since the loss of the chlorine's would leave Si dangling bonds available to bond with the Si substrate. The results indicated, however, that there was no significant difference in subsequent diamond nucleation density. One reason for this result may be that the methyl hydrogen's are leaving, allowing methyl carbons to bond to the silicon substrate resulting in an amorphous carbon surface. This reasoning is supported by the amorphous peaks in the Raman spectra. Another reason may be contamination by oxygen during the syringe injection procedure since it is difficult to completely remove oxygen from the interior of the gas syringe and the halogenated methyl silanes are getter oxygen [2].

#### E. Conclusions

Experiments investigating the use of chlorinated methylsilanes as diamond precursors were conducted. These precursors were introduced onto cleaned and passivated Si <111> substrates, which were then subjected to bias enhanced HFCVD diamond growth conditions. Characterization by SEM and Raman spectroscopies revealed no significant difference in diamond nucleation density or quality between precursor species. Two possible causes of this result are the unintentional cleavage of methyl hydrogen's resulting in the methyl carbon bonding to the substrate and oxygen contamination during syringe injection of the liquid organometallics.

#### F. Future Work

A solution to both of the above mentioned difficulties is to use methyl silane,  $\text{CH}_3\text{SiH}_3$ , as a precursor. Since methyl silane is gaseous, it will be possible to introduce it into the HFCVD chamber without the possibility of oxygen contamination. Secondly, the H-SiH<sub>2</sub>CH<sub>3</sub> bond energy (375 kJ/mol) is significantly less than either the H-CH<sub>2</sub> bond strength (460 kJ/mol), or the Si-CH<sub>3</sub> bond strength (451 kJ/mol). This lower bond energy will allow the molecule to decompose via dehydrogenation of the H-Si hydrogen's, without allowing the methyl hydrogen's to leave and cause carbon to bond to the substrate surface. A cylinder of methyl silane has been purchased, and we are now in the process of installing the required piping into our HFCVD chamber.



## **G. References**

1. D. B. Fenner, D. K. Biegelsen, and R. D. Bringans, *Journal of Applied Physics* **66** (1), 419 (1989).
2. L. H. Dubois, R. G. Nuzzo, *Surface Science* **149**, 133 (1985).

## **VI. Growth of Diamond Films Using an Enclosed Combustion Flame**

**Philip W. Morrison, Jr. <sup>\*</sup>, Ambika Somashekhar, and Jeffrey T. Glass**

**Department of Materials Science and Engineering  
North Carolina State University  
Raleigh, NC 27695-7919**

**John T. Prater**

**US Army Research Office  
Materials Science Division  
P.O. Box 12211  
Research Triangle Park, NC 27709-2211**

**\* Present Address:**

**Department of Chemical Engineering  
Case Western Reserve University  
10900 Euclid Avenue  
Cleveland, OH 44106-7217**

This paper discusses the growth of diamond thin films using an enclosed oxyacetylene torch. Using statistical experimental design techniques, we have systematically explored the parameter space to construct maps of nucleation density, film quality, growth rate, and orientational texture as functions of conditions. The deposition process has been broken down into a nucleation enhancement step and a growth step, and each step is optimized separately. In the study of the nucleation enhancement, we vary the flow ratio =  $O_2/C_2H_2$  ( $R$ ), substrate-flame distance ( $z$ ), and pretreatment time ( $t$ ) while holding substrate temperature ( $T_{sub}$ )  $\leq 550$  °C and flow rate ( $F$ ) = 4 slm. Scanning electron microscopy determines the nucleation density and nucleation uniformity. The best nucleation enhancement occurs at  $R = 0.91$ ,  $z = 50\%$  of the feather length, and  $t = 5$  minutes. For the growth study, the variables are  $R$ ,  $z$ , and  $T_{sub}$  ( $F = 4$  slm), and we employ two different Raman scattering measurements to assess film quality. In one case, we determine quality using a quantity called  $\beta$  = diamond peak/(diamond peak + nondiamond peak); the second indicator is the luminescence ( $L$ ) determined from the baseline of the spectrum and is related to defects in the film. the highest quality films appear at high  $R$  (0.95-0.97),  $z = 1$  mm, and high  $T_{sub}$  (900-1000 °C). We have also determine the growth rate as a function of conditions using infrared spectroscopy and find that the growth rate is a factor of 10 less than in the atmospheric flame. Films grown for one hour show orientational texturing predominantly in the  $\langle 111 \rangle$  direction.

## I. INTRODUCTION

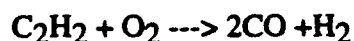
Unlike many other methods of depositing diamond films, the combustion flame method does not require vacuum and can operate in the open atmosphere. For this reason, the apparatus is quite simple, usually comprising of a commercial oxyacetylene torch and a water cooled substrate. Studying and controlling this chemical vapor deposition (CVD) process, however, can be frustrating because the interaction of the flame chemistry with its environment is beyond the control of the researcher. The typical torch flame consists of a premixed flame, a transition region where deposition occurs (called the feather), and an outer (or secondary) flame formed by air diffusing into the feather region. The outer flame is highly oxidizing, and as a result, it limits the deposition area to a relatively small region in the center of the flame. In addition, the entrained air brings  $N_2$  into the flame, and the nitrogen appears as an unwanted dopant in the films. [1-4] Furthermore, controlled doping of the films with noxious materials would be safer if the flame were enclosed. Most importantly, enclosing the flame allows one to improve the properties of the diamond film by varying the operating pressure or the atmospheric composition (e.g. replace air with  $H_2$ ). At present, the literature contains very little systematic work in this area. [4-7]

This work represents the first step in understanding the interaction of the flame with its environment. The goals for this work are to 1) develop the necessary apparatus for safely enclosing a torch flame, 2) identify the optimal conditions for depositing diamond films on Si(100) at  $\sim 1$  atm, and 3) compare those results to experiments using the atmospheric (open air) torch. To facilitate the optimization process, we have divided the deposition process into a nucleation step and a growth step and have optimized each step separately using statistical experimental design (SED). When studying nucleation, scanning electron microscopy provides information on the number density and uniformity of nuclei. To analyze the film growth, we first employ Raman spectroscopy to determine the quality of the diamond film and then use Fourier transform infrared spectroscopy to measure the film thickness. We then focus on the most important deposition variables to optimize the process further and also measure the orientational texture of the films.

## II. BACKGROUND

### A. Previous experiments using enclosed flames

Researchers have investigated enclosed flames in conjunction with 1) attempts to coat large areas by scanning an atmospheric (open air) flame across a substrate and 2) attempts to grow at low pressures. During scanning experiments in the atmosphere, researchers have discovered that the geometry of a conventional atmospheric torch prevents coating areas larger than  $\sim 5$  mm. A typical deposition flame operating in air consists of an inner cone, a feather, and an outer flame (Fig. 1). The inner cone forms where the acetylene-oxygen mixture leaving the torch burns to form CO and  $H_2$  via the reaction



(1)

To deposit diamond, the torch must operate slightly fuel rich ( $R = \text{O}_2/\text{C}_2\text{H}_2 \sim 1$ ), which forms the feather region downstream of the inner cone where diamond can grow if a cooled substrate is present. Outside the feather, the outer flame appears as air from the atmosphere diffuses into the flame. The air oxidizes the CO, H<sub>2</sub>, and excess carbon to form CO<sub>2</sub> and H<sub>2</sub>O. For scanning techniques, the presence of the outer flame is fatal: as the torch moves across the substrate, the trailing edge of the outer flame oxidizes the diamond film deposited by the leading edge of the feather. [8, 9]

Enclosing the flame overcomes this limitation by excluding the air and eliminating the outer flame. Murakawa et al [5] are the first to demonstrate the feasibility of this adaptation. In their work, they cover the flame to trap CO and H<sub>2</sub> around the entire substrate and thus eliminate the outer flame. With this modification, they are able to coat an area of 40 mm x 40 mm using a cutting torch. At the ratio  $R = 0.89$ , the Raman spectrum shows an amorphous carbon (1600 cm<sup>-1</sup>) peak of similar magnitude to the diamond peak. The authors have not reported any systematic studies of their enclosed flame and have not compared it to an atmospheric flame.

Murakawa and Takeuchi [6] have investigated both enclosed flames as well as a low pressure, enclosed flame and have compared them to an atmospheric (open air) torch system. When operated at 760 torr, the enclosed flame has several important differences from the atmospheric flame. First, the heat load on the substrate decreases substantially: the heat of reaction of Eq. 1 is only  $\sim 1/3$  of the heat of reaction of burning C<sub>2</sub>H<sub>2</sub> completely to CO<sub>2</sub> and H<sub>2</sub>O. Second, the deposition area increases  $\sim 20\%$ , and the size of individual grains decrease from a range of 2-20  $\mu\text{m}$  to a range of 2-8  $\mu\text{m}$ ; the roughness also decreases, and there are fewer inclusions. Finally, unlike atmospheric depositions, the optical emission spectrum of an enclosed flame has no CN features, and the films grown in an enclosed flame have no nitrogen features in their Auger electron spectra. Comparing atmospheric and low pressure flames, they find that lowering the chamber pressure to 360 torr increases area by 50% compared to the open air torch, but the grain morphology is similar to the enclosed flame at 760 torr. The authors do not present Raman spectra of their films, so assessing the quality of the diamond is difficult.

Enclosing the flame is also possible by shrouding the flame with a flow of gas. Doverspike et al [4] have used this technique to grow films by flowing Ar or O<sub>2</sub> and then compared the films to those grown in the atmosphere. Their system consists of a torch in a chamber with a pump to evacuate the system prior to growth; during growth, however, the system exhausts to the atmosphere and thus operates slightly above one atmosphere. The authors grow the films on Mo at 900 °C using a total torch flow of 7 slm. To achieve similar growths in Ar and O<sub>2</sub>, the authors must use more O<sub>2</sub> for flames in Ar ( $R = 1.1$ ) than for flames in O<sub>2</sub> ( $R = 1.03$ ); for comparison, high quality growths in the open air need  $R = 1.04$  as observed by Hanssen et al using a similar torch. [10] In the flowing Ar experiments, the lack of an outer flame produces several expected results: the feather is long and slender compared to the open air flame, no water condenses on the walls of the chamber, and the substrate temperature is lower for same cooling rate. The films have smooth (100) faces, but the Raman spectra of the films shows more amorphous carbon (a-

C), more fluorescence, and a wider full width at half maximum for the diamond peak (FWHM =  $7.0 \text{ cm}^{-1}$ ) when compared to atmospheric films. When deposited under flowing  $\text{O}_2$ , the films have a Raman spectrum similar to atmospheric films (FWHM of diamond peak =  $4.7 \text{ cm}^{-1}$ ), and photoluminescence shows much smaller peaks due to nitrogen defects than found in films grown in the open air. When the films cool down under flowing Ar, the diamond facets are smooth, but if the film cools under  $\text{O}_2$ , etch pits form.

Other authors note similar results when they place a flow of Ar around a torch and scan the flame. [7] The Ar sheath gas moves the outer flame downstream, doubles the length of the feather, and increases the deposition area.

## B. Statistical experimental design methodology

Statistical experimental design (SED) is an efficient means to search a multidimensional parameter space for optimum conditions using a small number of experiments. As a first step, we identify the various properties to be measured (responses). In the present case, these responses could be nucleation density or the full width at half maximum of the diamond Raman line. The magnitudes of these responses depend on various experimental parameters called factors; each of these factors has an upper and lower limit set by practical or physical limitations. In the case of flame CVD, factors include  $\text{O}_2/\text{C}_2\text{H}_2$  ratio, substrate temperature, distance between the substrate and inner cone, etc. Each response ( $Y_j$ ) is related to the factors ( $X_i$ ) by some specific function  $f_j$ ; for a three factor experimental problem

$$Y_j = f_j(X_1, X_2, X_3) \quad \text{where} \quad \begin{aligned} X_{1\min} &\leq X_1 \leq X_{1\max} \\ X_{2\min} &\leq X_2 \leq X_{2\max} \\ X_{3\min} &\leq X_3 \leq X_{3\max} \end{aligned} \quad (2)$$

The SED approach does not determine the exact form of  $f_j$  but rather approximates  $f_j$  with a generic model that captures most of the major features of the data. After fitting the model to the data, the model can then predict the location of the optimal operating conditions. Since the model is a simplified version of reality, further experiments at the predicted conditions will test the accuracy of the prediction. The advantage of this approach is that the number of initial experiments is significantly reduced because the model has a limited number of adjustable parameters. For example, the results described in later sections use a quadratic model for 3 factors to approximate  $f_j$ :

$$Y'_j = B_{j0} + B_{j1}X_1 + B_{j2}X_2 + B_{j3}X_3 + B_{j12}X_1X_2 + B_{j13}X_1X_3 + B_{j23}X_2X_3 + B_{j11}X_1^2 + B_{j22}X_2^2 + B_{j33}X_3^2 \quad (3)$$

where  $Y'_j$  is the predicted value of  $Y_j$ . The quadratic model is applicable to a broad class of phenomena because it can approximate functions with either a saddle shaped response (all  $B_{jii} = 0$ ) as well as functions with a maximum or minimum somewhere in the interior of the parameter space ( $B_{jii} \neq 0$ ). Since the three factor model has 10 adjustable B values, at least 10 different experimental conditions are necessary; in this work, however, we use 13 different experimental conditions and a total of 15 experiments. We have chosen these experimental conditions by

normalizing the parameter space so that it becomes a cube and then selecting (normalized) conditions corresponding to the midpoint of each edge of the cube and the center of the cube (uniform shell design). To determine confidence limits on the predicted values  $Y'_j$ , we also run two additional experiments at the center point conditions. We have implemented the above approach using a software package called STRATEGY (The Experiment Strategies Foundation, Seattle, WA). Given the necessary inputs, the software will generate a list of experiments to perform, regress the model to the measured results, calculate confidence limits, search the parameter space for optimum conditions, and present contour plots of the model results.

### III. EXPERIMENTAL APPARATUS

#### A. Enclosed flame reactor

The enclosed flame reactor consist of a cylindrical vacuum chamber, mass flow controllers, a throttle valve and pump, and a temperature control system (Fig. 2). The chamber is stainless steel and contains various ports for gas inlet, pumping, electrical connections, operator access, and optical access. The view ports for the operator have secondary shields to deflect flying glass in the event of an explosion. Acetylene and ox<sup>2</sup>/gen pass through mass flow controllers (MKS 1259C, 0-10 slm) and enter the chamber through a modified welders torch. A personal computer controls the set points to the mass flow controllers via a digital to analog converter (Keithly DASCON1) and an MKS power supply/readout unit (model 247C); the computer also logs flow data from the flow controllers as a function of time. The modified torch is a standard welders nozzle from Victor (tip size #2, 1.17 mm orifice) which is cut in half and connected to either side of a gas feed through fitting. This torch design is advantageous because it retains the gas mixing already incorporated in the torch handle. The tip of the nozzle points downward in the center of the chamber. Please note that the neutral flame condition (no feather) occurs at  $R = \text{O}_2/\text{C}_2\text{H}_2 = 1.03$  when this system operates in the atmosphere. A ballasted mechanical pump (Edwards E2M80, 1500 liter/min) exhausts the combusted gases through a motorized butterfly valve (MKS 253A). The butterfly valve has an o-ring seal to provide a positive seal. Using pressure measurements from a capacitance manometer (MKS 122AA, 0-1000 torr), the valve controller (MKS 252C) varies the valve position to maintain a constant operating pressure.

The substrate holder consists of a 1/4 NPT brass plug screwed into a brass female run tee. The run tee is attached to a vertical translation stage so that the distance between the torch tip and the substrate is variable between 0-3 cm. Anti-seize compound (Fel-Pro C5-A) on the threads of the plug keeps the plug from sticking in the tee after a deposition. The Si(100) substrates are attached to the plug using colloidal silver paste (Ted Pella). Cooling fluids (either air or water) pass up through the tee to maintain the substrate temperature. Flowing water through the tee delivers maximum cooling power while flowing air provides essentially no cooling. To reach a desired temperature, the temperature controller switches between water and air cooling in response to the temperature measured by the pyrometer. Practically speaking, this approach works well because the low mass of the tee keeps the thermal response of the system short (30-40 seconds). Fig. 3 shows a temperature profile for a typical deposition at 900 °C. Heating rates of at least 350 °C/min are possible, and the temperature variation around the set point can be very

small at steady state ( $\pm 20^\circ\text{C}$ ).

The temperature control system consists of a pyrometer and a temperature controller. The pyrometer is a 2 color model (2.1  $\mu\text{m}$  and 2.4  $\mu\text{m}$ ) manufactured by Williamson (model 8220). The pyrometer stares down onto the substrate through a 4 1/2 inch quartz window mounted on the top of the chamber. To clear the torch nozzle, the angle of incidence on the substrate is  $12\text{--}13^\circ$ . This angle is small enough that re-alignment of the pyrometer is not necessary if the sample is not moved more than 2 cm. The pyrometer sends its temperature measurements to a proportional-integral-derivative controller manufactured by Eurotherm (model 818). The Eurotherm in turn issues on/off commands to the water and air flows to maintain the desired temperature (Fig. 3). The personal computer sends commands to the Eurotherm to change the set point and also logs the temperature data as a function of time.

The final feature of the enclosed flame reactor is the flame ignitor. The ignitor consists of a sharpened wire located  $\sim 1$  cm radially from the torch tip and  $\sim 1$  cm downstream. This wire connects to a high voltage (30 kV) electrical feed through. Touching a tesla coil to the electrical feed though draws a large, continuous spark between the wire and the torch tip which ignites the flame. The spark is long enough that the wire does not interfere with the motion of the substrate.

A typical deposition employs the following procedure. After mounting a Si(100) substrate on a plug, the substrate is scratched with 1 micron diamond paste and cleaned with acetone. The plug is then screwed into the run tee, and the pump evacuates the reactor. On the computer, the operator programs the desired conditions for pretreatment step (flow ratio, substrate temperature, and time) and the growth step (flow ratio). For all the pretreatment and growth experiments described below, the total flow is fixed at 4 slm. After backfilling the reactor with Ar, the operator then sets the throttle valve controller to 700 torr and starts the  $\text{O}_2$  flow. As soon as the pressure and  $\text{O}_2$  flow stabilize, the  $\text{C}_2\text{H}_2$  flow is started, and the flame is ignited. After ignition, the operator moves the substrate to the desired position in the flame. If the flame does not ignite after 10 seconds of  $\text{C}_2\text{H}_2$  flow, the operator aborts the ignition and pumps out the chamber before trying again. Pumping out the reactor prevents accumulated gases from reaching the explosion limit. After the pretreatment ends, the computer automatically switches the flow ratio to the growth conditions, and the operator readjusts the sample position in the flame and resets the substrate temperature. Once the growth is complete, opening the throttle valve full open quickly extinguishes the flame as the pressure falls.

## B. Film characterization

The films have been analyzed using four different techniques: scanning electron microscopy (SEM), Raman spectroscopy, infrared reflectance spectroscopy, and x-ray diffraction (XRD). The SEM is a field emission microscope made by Philips (EM 400). Analysis of SEM images yields a relative measure of the nucleation density and the morphology of the films. The Raman spectrometer is a SPEX 1250M operating at a wavelength of 514.5 nm and a power of 100 mW prior to entering the microscope. The magnification of the microscope is  $100\times$  yielding a spot size of 1  $\mu\text{m}$ . A multichannel charged coupled detector array records the Raman scattering at a

resolution of  $1.2 \text{ cm}^{-1}$ . In this research, the integration time is kept small (3 seconds) so that we can perform all Raman measurements on a given set of samples with as little instrumental drift and sample degradation as possible. This is necessary because we have observed that the luminescence baseline of the spectra of poor films can decrease with the time of exposure to the laser. Presumably, the laser is partially oxidizing the sample and burning off the luminescing material.

We measure the thickness of the diamond films using specular reflectance spectroscopy in the mid-infrared region. The spectrometer for these measurements is a Fourier transform infrared (FTIR) instrument made by Analect (Model FX6260). The FX6260 scans the region between  $4398\text{-}500 \text{ cm}^{-1}$  ( $2.27\text{-}20 \mu\text{m}$ ) at roughly  $4 \text{ cm}^{-1}$  resolution (the resolution varies slightly across the spectrum). We use a  $30^\circ$  specular reflectance accessory from Pike Technologies. Finally, XRD measurements of thick films provide a rough indication of texture in the polycrystalline films. The diffractometer for these measurements is a Rigaku using a step size =  $0.1^\circ$  and a 5 second integration. The range of the measurements spans the five x-ray peaks of diamond shown in Table I. The texture ratios are calculated first by normalizing the peak intensities to the  $\{111\}$  intensity and then ratioing the normalized intensity to the powder pattern intensity. Thus a texture ratio  $\ll 1$  indicates little orientation in that crystallographic direction while a ratio  $\gg 1$  indicates significant orientation of the crystallites.

Table I - Location of x-ray diffraction peaks and their relative intensities in a powder pattern.

X-ray Diffraction Peak	2 $\theta$ Position	Powder Pattern Intensity
$\{111\}$	$43.9^\circ$	100%
$\{220\}$	$75.3^\circ$	25%
$\{311\}$	$91.5^\circ$	16%
$\{400\}$	$119.5^\circ$	8%
$\{331\}$	$140.6^\circ$	16%

#### IV. RESULTS OF PARAMETER SEARCH

Experiments with the enclosed flame have proceeded in three distinct steps. The first step is to discover the optimum conditions for nucleating diamond at high density with good uniformity. In the second step, we survey a three dimensional parameter space to determine roughly the conditions for high quality diamond growth and also measure the deposition rate. Finally, in the third step, we further optimize the diamond quality on a two dimensional parameter space and also examine the growth of orientational texture in the films. We have employed SED techniques during each of these steps.

##### A. Nucleation pretreatment

In atmospheric flames, diamond nucleates extremely slowly on silicon unless the substrate is



scratched. Even with scratching, however, the nucleation density is not very high and varies with radial position, typically producing an annular ring of diamond film. [11, 12] To improve the nucleation densities and uniformity on the scratched silicon, many researchers pretreat the silicon by lowering the O<sub>2</sub>/C<sub>2</sub>H<sub>2</sub> ratio and moving the substrate away from the inner cone; after a few minutes, they then reset the O<sub>2</sub>/C<sub>2</sub>H<sub>2</sub> ratio and distance back to the growth conditions. [13-20] Exploratory experiments also show a similar need for such a nucleation enhancement step in the enclosed flame. To discover the optimum conditions for enhancing nucleation, we have performed a series of experiments in which we scratch Si(100) with diamond paste and then pretreat the substrate at various conditions. After the pretreatment, we grow at a fixed set of growth conditions to decorate the nucleation sites and then use the SEM to measure the nucleation density and uniformity.

For the nucleation study, there are five potential variables to consider: flow ratio ( $R_{nuc}$ ), distance between the substrate and the inner cone ( $z_{nuc}$ ), pretreatment time ( $t$ ), substrate temperature ( $T_{sub}$ ), and total flow rate ( $F$ ). We have restricted the SED to the three factors  $R_{nuc}$ ,  $z_{nuc}$ , and  $t$ . Although  $T_{sub}$  should have an important effect on nucleation density, it depends so heavily on the other parameters that controlling it independently is very difficult. For example, at small  $z_{nuc}$ , high  $R_{nuc}$ , and long  $t$ , the heat input to the substrate is high and any temperature between 500-800 °C is possible. However, at large  $z_{nuc}$ , low  $R_{nuc}$ , and short  $t$ , the heat input is too low for the substrate to rise much above 500 °C. Since  $T_{sub}$  is not sufficiently independent of the other variables, we arbitrarily set the temperature controller to 550 °C (the pyrometer cannot measure below 500 °C) and drop  $T_{sub}$  from the SED. The SED also does not include flow rate since nucleation density ought to be a weak function of  $F$ . Reducing the number of factors from four to three decreases the number of experiments from 23 to 15. In all the nucleation experiments,  $F = 4$  slm.

The responses for the nucleation SED are nucleation density and nucleation uniformity as determined from SEM micrographs of the surface. We have chosen two ways to quantify the nucleation density. In one case, we can determine a relative number density ( $N$ ) by counting the number of diamond crystals in the field of view at a fixed magnification ( $\times 10k$ ). In the second method, we determine the fractional area ( $f$ ) of the field of view covered with diamond as determined by the method of lineanalysis. The first technique yields a value proportional to the number of nucleation sites per area while the second method yields a value that depends on the number of sites per area and the size of the crystallites per site. The values of  $N$  and  $f$  reported below are actually averages ( $\bar{N}$  and  $\bar{f}$ ) of values measured in the center and the edge of the film. To determine an indicator for uniformity, we also calculate the quantities (center - edge)/average for both the number density and the fractional coverage ( $\Delta N / \bar{N}$  and  $\Delta f / \bar{f}$ ).

The range of values for the pretreatment conditions appears in Table II. The choices for the upper and lower limits are the result of a few exploratory growths which showed reasonable nucleation density and uniformity at  $R_{nuc} = 0.89-.91$ ,  $z_{nuc} = 50\%$  of the feather length, and  $t = 2-5$  minutes. The initial study began with a lower  $z_{nuc}$  limit = 50%, but analysis of the SED shows this value is close to the optimum value, so we added four new experiments at  $z_{nuc} = 30\%$ . Thus the total number of experiments expanded from 15 to 21 (which includes 2 additional

replicates). Table II also shows the growth conditions employed to decorate the nucleation sites.

The results of the SED analysis appear in Fig. 4. Fig. 4 contains the contours for the average number density ( $\bar{N}$ ), the average fractional area covered ( $\bar{f}$ ), the uniformity in  $N$  ( $\Delta N / \bar{N}$ ), and the uniformity fractional area ( $\Delta f / \bar{f}$ ) as a function of ratio and time near the optimal distance  $z = 50\%$ . Other distances are not shown. The predicted optimal conditions determined from these contours appear in Table II, and micrographs of the surface deposited at those conditions appear in Fig. 5.

The statistical tests on the regression for  $\bar{N}$  and  $\bar{f}$  (Fig. 4a and 4b) show that the quadratic model is a reasonable approximation for these two responses. For  $\bar{N}$ , all the residuals fall with 1.2 standard deviations; in the case of  $\bar{f}$ , all the residuals fall with 2 standard deviations. The indices for uniformity, however, do not fit the quadratic model well and must be viewed with some caution (Fig. 4c and 4d). In both cases, 20-30% of the predicted values lie outside the 95% confidence limits. Examining the residuals more closely, one finds the greatest deviations between the model and data occur at the short pretreatment times (1 and 3 minutes). This result is not unexpected: at short pretreatment times, the conditions at the substrate are continually in transition and the nucleation is sporadic and inconsistent. However, since the most uniform nucleation occurs at 4-5 minutes, the model results of Fig. 4c and 4d are sufficiently accurate to proceed without further refinement of the SED.

Table II - Torch conditions explored for the study of nucleation enhancement for the enclosed flame.

Parameter	Range of Values for Pretreatment	Fixed Growth Conditions	Optimized Pretreatment Conditions
O <sub>2</sub> /C <sub>2</sub> H <sub>2</sub> Ratio (R <sub>nuc</sub> )	0.87 - 0.93	0.93	0.91
Total Flow Rate (F)	4 slm (fixed)	4 slm	4 slm
Distance (z <sub>nuc</sub> )	30-90% of feather length	1-2 mm	50%
Time (t)	1 - 5 minutes	5 minutes	5 minutes
Substrate Temperature	≤ 550 °C (fixed)	750 °C	≤ 550 °C

#### B. Initial survey of the parameter space for diamond growth

In these experiments, we nucleate diamond on a substrate of scratched Si(100) using the conditions shown in Table II and then grow at various deposition conditions for 15 minutes. To assess the quality of the films, we employ two responses determined from Raman spectroscopy. We have also determined the growth rate by measuring film thickness with FTIR spectroscopy.

The factors to consider for the survey study are similar to the nucleation study, and they include

flow ratio ( $R_g$ ), distance ( $z_g$ ), substrate temperature ( $T_{\text{sub}}$ ), and flow rate ( $F$ ). Again, we hold  $F$  constant at 4 slm because flow rate should be relatively unimportant and the savings in the number of experiments is considerable. The range of values for these factors appear in Table III.

We determine the quality of a film from its Raman spectra taken in the center of the film. Consider the Raman spectrum in Fig. 6. In general, the diamond and nondiamond features superimpose themselves on top of a broad band photoluminescence spectrum. One index of film quality is the magnitude of the luminescence ( $L$ ): lower values of  $L$  correlate with less defects and higher film quality. We can determine  $L$  (in counts) from the average value of the baseline correction necessary to remove the luminescence from the spectrum. A more typical way to assess the film quality is to construct an index from the amplitude of the diamond  $1332 \text{ cm}^{-1}$  peak ( $D$ ) to some nondiamond peak ( $ND$ ) at some fixed wavenumber (for example, graphite at  $1580 \text{ cm}^{-1}$  or amorphous carbon at  $1340\text{-}1350 \text{ cm}^{-1}$ ). [10, 21] In this study, however, the relative amounts of the nondiamond component varies among the spectra, so we substitute an averaged value for  $ND$  calculated by taking the baseline corrected spectrum, removing the diamond feature, summing the intensities between  $1075 \text{ cm}^{-1}$  and  $1725 \text{ cm}^{-1}$ , and dividing by the number of data points. From the diamond peak and the averaged nondiamond "peak", we can calculate the quality ratio,  $Q = D/ND$ . Under most circumstances, the quality ratio works very well as long as  $ND$  does not approach zero (pure diamond). When that occurs, small changes in  $ND$  produce large changes in  $Q$ , and  $Q \rightarrow \infty$ . A simple way to resolve this problem is to construct an index that does not approach infinity as the film approaches pure diamond. One such index is the following:

$$\beta = \frac{D}{D + ND} = \frac{Q}{Q + 1} \quad (4)$$

$\beta$  is the Raman fraction of diamond in the film and ranges from zero when nondiamond is present to one when only diamond is found. This definition weights the Raman intensities of the diamond and nondiamond components equally even though diamond scatters very inefficiently compared to other forms of carbon. Thus a value of  $\beta > 0.9$  represents a very high quality film. The SED quadratic model fits the  $\beta$  index much better than the  $Q$  index, so this is the measure we use. Assessing film quality using the full width at half maximum is not possible in this study because the width of the  $1332 \text{ cm}^{-1}$  feature is similar in all the spectra.

Determining the film thickness is possible using FTIR spectroscopy. For thin films, the reflectance spectrum of the film contains interference fringes due to the film thickness as shown in Fig. 7. The amplitude of the fringes decays at high wavenumbers due to scattering by the diamond crystallites, but a fit is still possible using the positions of the maxima and minima (smooth curve in Fig. 7). As long as films are thin enough ( $< 10 \mu\text{m}$ ), this method works quite well.

The results for the SED analysis of the Raman spectra appear in Fig. 8 ( $\beta$ ) and Fig. 9 ( $L$ ). Each figure presents the results as contour plots at three different deposition distances:  $z = 1, 3$ , and  $5 \text{ mm}$ . The highest quality diamond appears at  $z = 1 \text{ mm}$ ,  $T_{\text{sub}} = 900^\circ\text{C}$ , and  $R = 0.93\text{-}0.97$ . A

comparison of the Raman spectra for experiments at these conditions appear in Fig. 10. The predicted results of Fig. 8 and 9 all lie within 1.1-1.2 standard deviations of the observed values. Fig. 11 contains the contour plots for the deposition rate ( $r$ ) at the same conditions as Fig. 8-9. The quadratic model in Fig. 11 fits all the data points to within 1.25 standard deviations.

Table III - Torch conditions explored for the survey study for the enclosed flame.

Parameter	Range of Values for Growth	Optimized Growth Conditions
$O_2/C_2H_2$ Ratio ( $R_g$ )	0.89 - 0.97	0.95-0.97
Total Flow Rate (F)	4 slm (fixed)	4 slm
Distance	1-5 mm from inner cone	1 mm
Substrate Temperature	600-900 °C	900 °C
Time	15 minutes (fixed)	

### C. Study of thick films and the measurement of texture

The goal of this study is to map the quality of thick films grown in the region of the parameter space near the optimum and to observe whether growth conditions influence the orientational texture of the films. The deposition time in this parametric study is one hour instead of 15 minutes.

Results from the survey study indicate that the best quality films grow at the distance  $z = 1$  mm (Fig. 8). Consequently, this study is a two factor design using only  $R_g$  and  $T_{sub}$  as variables and  $z$  is constant at 1 mm. This decreases the number of factors from three to two and the required number of experiments from 15 to 9. The experimental design includes a deposition at  $R_g = 0.95$  and 1000 °C where the survey study predicts high quality growth to occur. The survey study also indicates that high  $T_{sub}$  is desirable, so we have increased the upper limit of  $T_{sub}$  to 1000 °C. This represents the upper limit of the reliability of the silver paste and the temperature controller. Table IV summarizes the parameter space as well as the optimal conditions from the SED analysis.

In this study, we assess the Raman film quality using  $\beta$  and  $L$  as defined above. The orientational texture measurements come from analysis using texture factors for the {220}, {311}, {400}, and {331} directions. In some cases, the films are thin enough that an IR measurement of the thickness is also possible. The Raman results appear in Fig. 12 while Fig. 13 shows the texture factor contours.

Table IV - Torch conditions explored for diamond quality and x-ray texturing.

Parameter	Range of Values for Growth	Optimized Growth Conditions
O <sub>2</sub> /C <sub>2</sub> H <sub>2</sub> Ratio	0.89 - 0.97	0.95-0.97
Total Flow Rate (F)	4 slm (fixed)	
Distance	1 mm from inner cone (fixed)	
Substrate Temperature	650-1000 °C	900-1000 °C
Time	60 minutes (fixed)	

## V. DISCUSSION

### A. General observations of flame

As reported in the literature, [4, 7] excluding secondary O<sub>2</sub> sources causes the outer flame to disappear and the feather to become longer; there is also no condensation of water on the walls of the chamber. If the chamber does contain secondary O<sub>2</sub> prior to ignition, the outer flame appears for a few minutes and water condenses on the walls until the flame consumes the secondary O<sub>2</sub>. Once this occurs, the enclosing gas is 2 parts CO and 1 part H<sub>2</sub> as shown by Eq. 1. Interestingly, the conditions for a neutral flame at 700 torr changes as the composition of the enclosing gas composition changes. In flowing air, the neutral flame condition (no feather) at 700 torr is  $R_{\text{neutral}} = (\text{O}_2/\text{C}_2\text{H}_2)_{\text{no feather}} = 1.03$  which is the same for a flame in the open atmosphere. Similarly, if the flame is ignited in a chamber filled with air (not flowing),  $R_n$  is also 1.03 after one minute but eventually falls to 1.01-1.02 after 10 minutes. When the chamber initially contains Ar rather than air,  $R_n$  begins at a low value of 1.01-1.02 and creeps up to 1.02 after 10 minutes. The time constants for these changes are consistent with the residence time of the chamber given by  $(\text{volume})/(\text{exit flow rate}) = 25 \text{ liters}/6 \text{ lpm} = 4.2 \text{ minutes}$ .

Clearly, the composition of the enclosing gas determines the length of the feather. Since eliminating the secondary O<sub>2</sub> increases the length of the feather, one would expect a greater flow of O<sub>2</sub> (larger R) would be necessary to pull the feather back to zero length. Apparently, the outer flame alters the concentration of excited species that form the luminous feather either by reducing the production of excited species or by more efficiently quenching those species than either Ar or CO + H<sub>2</sub>. Of course, we also expect the temperature in the enclosed flame to be lower at the edge of the feather, and this may also play a significant role.

### B. Nucleation

The various nucleation responses show very different dependences on pretreatment conditions. As shown in Fig. 4, the average of the nucleation density at the center and the edge ( $\bar{N}$ ) increases as both  $R_{\text{nuc}}$  and  $t_{\text{nuc}}$  increase; this is true for all pretreatment distances. For  $z_{\text{nuc}} = 30\%$ , the highest  $\bar{N}$  is ~ 10% higher than shown in Fig. 4a while for  $z_{\text{nuc}} = 90\%$ , it is ~ 10% lower. Uniformity in  $\bar{N}$  ( $\Delta N / \bar{N}$ ), however, varies strongly with all three parameters. For  $z_{\text{nuc}} = 90\%$ ,

the "sweet spot" for best uniformity ( $\Delta N / \bar{N} = \pm 10\%$ ) occurs at low values of  $R_{\text{nuc}}$  and  $t_{\text{nuc}}$ , and its size is fairly small. As shown in Fig 4c, the size of the sweet spot broadens considerably at intermediate values of  $z_{\text{nuc}}$  and centers on high values of  $R_{\text{nuc}}$ . Further decreasing  $z_{\text{nuc}}$  to 30% again narrows the sweet spot and it moves to the middle range of  $R_{\text{nuc}}$  and long times.

A different kind of behavior occurs for the fractional coverage ( $\bar{f}$ ) and the coverage uniformity ( $\Delta f / \bar{f}$ ). At  $z_{\text{nuc}} = 90\%$ ,  $\bar{f}$  improves as  $R_{\text{nuc}}$  decreases and time increases while for  $z_{\text{nuc}} = 30\%$ ,  $\bar{f}$  increases as  $R_{\text{nuc}}$  increases and time increases. The behavior at mid range values of  $z_{\text{nuc}}$  (Fig. 4b) is intermediate to these two:  $\bar{f}$  increases with time but is fairly independent of  $R_{\text{nuc}}$ . In this case, the uniformity across the substrate does not vary with conditions as greatly as does  $\Delta N / \bar{N}$ . The broadest sweet spot ( $\Delta f / \bar{f} = \pm 10\%$ ) occurs at an intermediate value of  $z_{\text{nuc}}$  (Fig. 4d) and gets smaller as  $z_{\text{nuc}}$  increases or decreases. At  $z_{\text{nuc}} = 90\%$ , the sweet spot occurs at the lowest values of  $R_{\text{nuc}}$  and in the mid range of pretreatment time whereas at  $z_{\text{nuc}} = 30\%$  the best uniformity is still at intermediate values of time but is roughly independent of  $R_{\text{nuc}}$ .

Since the optimal pretreatment conditions occur when  $\bar{N}$  and  $\bar{f}$  are high and their uniformities are low ( $\pm 10\%$ ), one finds that the overall sweet spot for pretreatment in the enclosed flame occurs near  $z_{\text{nuc}} = 50\%$ , time = 5 minutes, and  $R_{\text{nuc}} = 0.91-0.93$ . After performing two further experiments, we find that pretreating at  $R_{\text{nuc}} = 0.91$  produces better nucleation density and uniformity than  $R_{\text{nuc}} = 0.93$ . Even though the predictions of Fig. 4 indicate better conditions may lie at longer times and higher values of  $R_{\text{nuc}}$ , we have not performed additional investigations because pretreatment times longer than 5 minutes or  $R_g > 0.93$  would exceed the standard growth time used to decorate the nucleation sites. Thus one could not distinguish between effects due to pretreatment and effects due to the standard growth. A separate study would be required.

These optimal pretreatment conditions for the enclosed flame are similar to previous pretreatments described in the atmospheric flame literature for Si substrates. [16, 17, 20] Furthermore, where direct comparisons are possible, the trends in the data are also consistent. Von Windheim and Glass [16] use a pretreatment of  $R = 0.93$  for 2-5 minutes to enhance nucleation and improve uniformity and then grow at  $R = 0.97$ . They conclude that the low  $R$  pretreatment performs two functions: 1) it enhances nucleation by etching native oxide and reducing the formation of  $\text{SiO}_2$  ( $\text{SiO}_2$  inhibits diamond nucleation) and 2) it deposits a carbonaceous layer that enhances nucleation. Later studies by McClure et al [17, 20] using Auger electron and x-ray photoelectron spectroscopies confirm this interpretation. In addition, one set of their experiments demonstrates that nucleation density increases by a factor of  $\sim 3$  as the pretreatment time increases from 1 to 3 minutes. For both the atmospheric and enclosed flames, the pretreatment is shifted down a similar amount from the typical growth conditions:  $R_{\text{nuc}} = R_g - 0.04$ . Apparently the flame chemistry shifts when the flame is enclosed, and both  $R_{\text{nuc}}$  and  $R_g$  shift with it to maintain a fixed offset between the carbon chemical potential that produces good nucleation and the chemical potential that grows diamond best.

### C. Deposition Rate

Enclosing the flame also has a significant impact on the deposition rate of diamond. In general, the deposition area in the atmospheric flame is roughly 5 mm wide while in the enclosed flame is approximately 8 mm. But although the deposition area increases by a factor of  $\sim 2.5$ , the deposition rates in the enclosed flame shown Fig. 11 are roughly an order of magnitude less than rates reported for atmospheric flames (8-100  $\mu\text{m/hr}$ ). [10] Direct experimental comparison of the growth rate of the enclosed flame to the atmospheric flame under two nearly identical conditions verifies this observation (Table V). The cause for the change the change in  $r$  is unknown. If the lack of an outer flame significantly reduces the gas temperature, then one could expect lower growth rates since the growth rate in diamond CVD generally increases with gas temperature. [22] Adiabatic flame calculations on the enclosed flame do not predict temperature shifts of more than 100-200 K, however. On the other hand, these temperature shifts do cause significant changes in the species concentrations which could explain the decrease in  $r$ . A more systematic theoretical study is required.

Table V - Comparison of growth rates for growth in the enclosed flame and an atmospheric flame.

		Atmospheric	Enclosed	Atmospheric	Enclosed
Pretreatment	$R_{\text{nuc}}$	0.91	0.91	0.93	0.91
	$T_{\text{sub}}$	550 °C	$\leq 550$ °C	550 °C	$\leq 550$ °C
	$t$	5 minutes	5 minutes	3 minutes	5 minutes
Growth	$R_g$	0.95	0.95	0.97	0.97
	$T_{\text{sub}}$	900 °C	900 °C	750 °C	750 °C
	Rate	28 $\mu\text{m/hr}$	3.5 $\mu\text{m/hr}$	13 $\mu\text{m/hr}$	1.5 $\mu\text{m/hr}$

The contour plots of Fig. 11 show that the growth rate is a moderate function of  $R_g$ ,  $T_{\text{sub}}$ , and  $z_g$ , and generally follows similar trends as observed for atmospheric flames. Overall, for both atmospheric and enclosed flames, the growth rate increases by roughly the same factor (2-3) as  $T_{\text{sub}}$  increases and  $R_g$  decreases. [23] On the other hand, in the enclosed flame, the growth rate does not decrease appreciably as  $z$  increases unlike the behavior in atmospheric flames. [24, 25] This difference is somewhat expected because if the outer flame has any effect at all, it should have its largest impact on growth species in the axial direction. However, the strong dependence of growth rate on  $z$  in the atmospheric flame may be an experimental artifact. The above authors estimate growth rate using crystal size, and they do not use a pretreatment step to minimize the run to run variation in induction period for nucleation. In other atmospheric flame research, Schermer et al [26] avoid this difficulty by measuring thick films with Nomarski differential contrast microscopy. Unfortunately, their temperature range lies completely above 900 °C, and direct comparison with this work is not possible. The rate data also do not show any Arrhenius dependence on  $T_{\text{sub}}$  as observed in atmospheric turbulent flames. [27] In turbulent flames, the growth rate data can be fit using one activation energy above 750 °C and another below 750 °C.

The range of  $T_{\text{sub}}$  in the present study spans this transition temperature, however, and any Arrhenius dependence may not be observable.

In some cases, we have been able to measure the thickness of films grown for one hour, and these data show a higher average growth rate than measured in Fig. 11. For high values of  $R_g$ , a one hour growth can be as much as twice as thick as predicted from the growth rates of Fig. 11. Clearly even with a nucleation pretreatment, there is still an induction period for diamond nucleation before growth begins.

#### D. Raman results

As shown in Fig. 10, the best quality films have a full width at half maximum (FWHM) of  $\sim 5\text{-}6\text{ cm}^{-1}$ ; when the  $1332\text{ cm}^{-1}$  peak appears for a poor film, its FWHM is  $\sim 10\text{-}12\text{ cm}^{-1}$ . This result agrees quite well with the results of Doverspike et al [4] in which films grown in a flow of Ar have a FWHM of  $7.0\text{ cm}^{-1}$  compared to a FWHM  $= 4.7\text{ cm}^{-1}$  if grown in air or a flow of  $\text{O}_2$ . The Raman spectra of these films are also similar to spectra of films deposited by cycling the growth ratio in an atmospheric torch. [19, 28] The trend of the spectra with the  $R_g$  shown in Fig. 10 is somewhat expected since larger values of  $R_g$  ought to increase the amount of oxidation in the flame and suppress the deposition of nondiamond components. On the other hand, these films are fairly thin ( $0.5\text{-}2\text{ }\mu\text{m}$ ), and the Raman spectra may also include scattering from the nucleation enhancement layer. If this were the case, the improvement in film quality would also arise because the flame etches away some of the nondiamond component of the pretreatment layer. However, the trends shown in Fig 12 for one hour growths are nearly the same as the trends observed in both Fig. 8a and 9a.

At any deposition distance  $z_g$ , the best quality films ( $\beta \sim 1$  and  $L \sim 0$ ) appear under conditions where both  $R_g$  and  $T_{\text{sub}}$  are high (Fig. 8). For higher values of  $z_g$  (3 mm and 5 mm),  $\beta$  varies between 0 and 1 while at  $z_g = 1\text{ mm}$ , all films show a  $\beta \geq 0.4$ . Interestingly, the contour plot predicts  $\beta \rightarrow 1$  at  $900\text{ }^\circ\text{C}$  and  $R_g = 0.97$  for either  $z_g$  equal to 1 mm or 5 mm; over all the parameter space, however, the film quality is best when  $z_g = 1\text{ mm}$ . Thus, the subsequent texture study has focused only on conditions where  $z_g = 1\text{ mm}$ ; those results (Fig 10) reproduce the results of Fig. 8a and 9a. The variations in  $L$  with  $R_g$  and  $T_{\text{sub}}$  generally follow the same trends as  $\beta$ , and the lowest luminescence levels come from high  $\beta$  films (Fig. 9). The luminescence also shows the same sort of trends with  $z$  (at high  $R_g$  and  $T_{\text{sub}}$ ,  $L$  is lowest at  $z_g = 1$  and  $z_g = 5\text{ mm}$ ), although in this case the maximum value for  $L$  is slightly lower at  $z_g = 5\text{ mm}$  than  $z_g = 1\text{ mm}$  (probably because there is less diamond in the film).

The above trends for the enclosed flame results are fairly consistent with the results found for atmospheric flames. Researchers [10, 21] have construct maps of the  $R_g$ - $T_{\text{sub}}$  parameter space using Raman spectroscopy. For the center of the films, [10] the diamond peak increases with higher  $R_g$  and lower  $T_{\text{sub}}$  while the graphite peak behaves just the opposite; amorphous carbon (a-C) is present in virtually all depositions but tends to increase at lower  $T_{\text{sub}}$ . Thus quality improves with  $R_g$  and is optimal at some intermediate temperature ( $\sim 900\text{ }^\circ\text{C}$ ). Other authors also report a optimum temperature for good growth near that temperature as well. [29] As shown



in Fig. 9 and 12, however, the enclosed flame has its optimum at the highest temperatures and ratios. On the other hand, better quality films appear at the edge of the films, [21] and in this case, films deposited at high  $R_g$  and  $T_{sub}$  have a very large diamond peak and virtually no graphite nor a-C peaks. The fluorescence also decreases as the substrate temperature increases. In the case of turbulent flames, [30] film quality also degrades with decreasing  $R_g$ . Thus, the enclosed flame is more akin to films grown near the interface between the feather and outer flame. To explain this result, we note that successful diamond CVD requires deposition precursor(s), etchant species, and some surface mobility. In the case of atmospheric flames, these conditions are met at slightly fuel rich conditions, at the boundary between the feather and the outer flame, and at high substrate temperature. Turbulence in an atmospheric flame blurs the edge of the flame [31] and generates these conditions in the center of the flame as well as the edge. For an enclosed flame, however, high quality growth may also occur throughout the flame because of the extra atomic H generated when  $H_2$  is entrained from the chamber atmosphere.

#### E. XRD results

In general, the orientational texture of diamond films will depend on growth conditions because the relative growth rates in the  $\langle 100 \rangle$  and  $\langle 111 \rangle$  directions vary with gas composition and substrate temperature. Determining a map of the texturing of the combustion films will aid the growth of smooth oriented films. [32]

Fig. 13 clearly shows that the orientational texture of the diamond films is predominantly  $\{111\}$  since the other texture factors are relatively small. In the case of the  $\{220\}$  and  $\{331\}$  textures, the changes in amount of texture are relatively insensitive to  $R_g$  and  $T_{sub}$  (Fig. 13a and 13d) while the  $\{311\}$  texture depends mostly on  $R_g$  rather than  $T_{sub}$  (Fig 13b). The  $\{400\}$  texture, however, depends on both the ratio and temperature, and under some conditions can disappear completely (Fig. 13c). Further reducing the texture factors for directions other than  $\{400\}$  would require growing films much longer than one hour. In addition, please note that improving the texture in any other direction than  $\{111\}$  is not possible given the parameter space explored.

There are very few x-ray studies of films grown in an atmospheric flame, and none of them systematically explore the parameter space. Unlike the enclosed flame, films grown in air show a variety of textures including  $\{100\}$  texture, [33] bipolar texture along  $\{114\}$  and  $\{221\}$ , [34]  $\{220\}$  texture, [35-37] and  $\{111\}$  texture. [38, 39] The only systematic trend in the data appears in the work of Choi and Shin who find that the  $\{220\}$  texture increases with  $T_{sub}$  at  $R_g = 0.9$ . This result is consistent with the trend of Fig. 13a. The variety of observed textures does suggest two conclusions: a) the relative growth rates of the crystal planes may be more sensitive to conditions than the enclosed flame or b) the higher growth rate of the atmospheric torch allows the texture to evolve quickly with film thickness and thus one can inadvertently observe different textures if the film thickness is not properly considered.

#### F. Scatter Plots

To help uncover correlations among the responses, the STRATEGY software also presents

scatter plots of the various responses comparing one another. From these scatter plots, there are two major observations. First, there is a distinct linear relationship between  $\beta$  and  $L$ , and it appears in both the survey and the texture studies as long as  $\beta > 0.2$ . Fig. 14 displays the scatter plot for the texture study. In both studies, the correlation coefficient is quite high ( $\sim 0.95$ ), and  $\beta$  approaches one as  $L \rightarrow 0$ . This relationship can arise if the luminescence is directly proportional to the nondiamond Raman scattering and if the ratio of the volume fraction of nondiamond material to diamond material is small. To see this, rewrite  $\beta$  in terms of volume fractions ( $\phi$ ) and Raman scattering cross sections ( $\sigma$ ):

$$\beta = \frac{D}{D + ND} = \frac{\sigma_D \phi_D}{\sigma_D \phi_D + \sigma_{ND} \phi_{ND}} = \frac{1}{1 + \frac{\sigma_{ND}}{\sigma_D} \cdot \frac{\phi_{ND}}{\phi_D}} \approx 1 - \frac{\sigma_{ND}}{\sigma_D} \cdot \frac{\phi_{ND}}{\phi_D} \quad (5)$$

where the subscripts  $D$  and  $ND$  refer to diamond and nondiamond respectively. Since the ratio  $\frac{\sigma_{ND}}{\sigma_D}$  is large ( $\sim 50$ ), the ratio  $\frac{\phi_{ND}}{\phi_D}$  is small for values of  $\beta > 0.2$ , and the approximation appearing in Eq. 5 is valid. Thus, if  $L \propto \phi_{ND}$ , then Eq. 5 predicts a\* linear relationship between  $\beta$  and  $L$  as long as  $\beta$  is not too close to zero, and it also has an intercept of 1.

The other scatter plots show no obvious relationships among diamond quality, growth rate, and the various texture factors. Most unexpectedly, there is no relationship between growth rate and film quality. Generally speaking, most researchers observe an inverse relationship between growth rate and diamond quality. Of course, the inverse relationship may be obscured if the measured  $\beta$  also contains contributions from the nucleation enhancement layer. More study on thicker films will be necessary to settle this question.

## V. CONCLUSIONS

This research has systematically studied the growth of diamond films in an enclosed oxyacetylene torch. The primary tool in this research is statistical experimental design which allows us to map the parameter space with a relatively small number of experiments. The experiments are divided into three separate studies, and we have performed a SED for each: nucleation enhancement, a survey of growth conditions, and a study of texturing in thick films. The optimal conditions for high nucleation density and good uniformity on Si(100) occur when  $R_{nuc} = 0.91$ ,  $z_{nuc} = 50\%$  of the feather length, and  $t_{nuc} = 5$  minutes;  $T_{sub}$  and flow rate are fixed at  $\leq 550$  °C and 4 slm respectively. Pretreatment times  $> 5$  minutes may further improve the nucleation, but they were not included in this work. Since long pretreatment times are the most effective, future studies should also include  $T_{sub}$  in the SED. During the survey study, we have mapped the growth rate and Raman quality of the films as functions of  $R_g$ ,  $z_g$ , and  $T_{sub}$ . In general, the growth rate is approximately a factor of 10 less than rates observed in atmospheric torches, but the deposition area is  $\sim 2.5\times$  larger. We judge the quality of the film using the Raman ratio  $\beta$  and the luminescence  $L$ . The highest quality films ( $\beta \rightarrow 1$  and  $L \rightarrow 0$ ) occur when the growth conditions are  $R_g = 0.95-0.97$ ,  $z_g = 1$  mm, and  $T_{sub} = 900-1000$  °C; other results

from the texture study confirm this observation. The quality of these films is similar to films grown by cycling the growth ratio in an atmospheric torch. There is also a linear correlation between  $\beta$  and  $L$  which may imply that the luminescing defect is directly proportional to the nondiamond component in the film. In the final study, we have determined the variation of orientational textures as functions of  $R_g$  and  $T_{\text{sub}}$  ( $z_g = 1$  mm). After one hour of growth, all the films have predominantly  $\{111\}$  texture although small amounts of  $\{220\}$ ,  $\{311\}$ ,  $\{400\}$ , and  $\{331\}$  are present. Eliminating the  $\{400\}$  texture is possible under some conditions, but longer growth times would be necessary to eliminate the other texture directions.

## VI. ACKNOWLEDGMENTS

The authors gratefully acknowledge funding from the Ballistic Missile Defense Office/Innovative Science and Technology (BMDO/IST) through the Office of Naval Research (ONR) and the University Research Initiative through ONR. Additional funding also comes from the Army Research Office. The authors have also received much assistance with the various measurements reported here. The Kobe Steel Electronic Materials Center (EMC) has provided access to its scanning electron microscope and Raman spectroscopy facilities. Glenn Tessmer of Kobe Steel EMC has also helped acquire the Raman spectra. At North Carolina State University, Prof. Robert Nemanich has also provided Raman analyses, and Scott Wolter has performed the x-ray diffraction measurements. Finally, the authors thank the following people for their helpful discussions: from North Carolina State University, Firmy Sivazlian, Shane Trent, and Denise Tucker; from Kobe Steel EMC, Dr. Brian Stoner and Dr. Jesko von Windheim.

## REFERENCES

1. J. A. Freitas Jr., J. E. Butler, and U. Strom, *J. Mater. Res.* **5**, 2502 (1990).
2. J. A. Freitas Jr., U. Strom, J. E. Butler, and K. A. Snail, in *MRS International Conference Proceedings Series: New Diamond Science and Technology (Proceedings of the Second International Conference on New Diamond Science and Technology)*, edited by R. Messier, J. T. Glass, J. E. Butler, and R. Roy (Materials Research Society, Pittsburgh, PA, 1991), p. 723.
3. J. A. Freitas Jr., U. Strom, K. Doverspike, C. M. Marks, and K. A. Snail, in *Materials Research Society Symposium Proceedings: Wide Band Gap Semiconductors*, edited by T. D. Moustakas, J. I. Pankove, and Y. Hamakawa (Materials Research Society, Pittsburgh, PA, 1992), Vol. 242, p. 139.
4. K. Doverspike, J. E. Butler, and J. A. Freitas Jr., in *Materials Research Society Symposium Proceedings: Wide Band Gap Semiconductors*, edited by T. D. Moustakas, J. I. Pankove, and Y. Hamakawa (Materials Research Society, Pittsburgh, PA, 1992), Vol. 242, p. 37.
5. M. Murakawa, S. Takeuchi, and Y. Hirose, *Surf. Coat. Technol.* **43-44**, 22 (1990).
6. M. Murakawa and S. Takeuchi, *Surf. Coat. Technol.* **54/55**, 403 (1992).

7. D. Y. Wang, Y. H. Song, J. J. Wang, and R. Y. Cheng, *Dia. Related Mater.* **2**, 304 (1993).
8. M. Murakawa, S. Takeuchi, and Y. Hirose, *Surf. Coat. Technol.* **39-40**, 235 (1989).
9. Y. Tzeng, R. Phillips, C. C. Tin, Y. Chen, T. Srivinyunon, and C. Cutshaw, in *Materials Research Society Symposium Proceedings: Diamond, Silicon Carbide and Related Wide Bandgap Semiconductors*, edited by J. T. Glass, R. Messier, and N. Fujimori (Materials Research Society, Pittsburgh, PA, 1990), Vol. 162, p. 145.
10. L. M. Hanssen, K. A. Snail, W. A. Carrington, J. E. Butler, S. Kellogg, and D. B. Oakes, *Thin Solid Films* **196**, 271 (1991).
11. J. E. Butler, F. G. Celii, D. B. Oakes, L. M. Hanssen, W. A. Carrington, and K. A. Snail, *High Temp. Sci.* **27**, 183 (1990).
12. D. B. Oakes and J. E. Butler, *J. Appl. Phys.* **69**, 2602 (1991).
13. Y. Tzeng, C. Cutshaw, R. Phillips, and T. Srivinyunon, *Appl. Phys. Lett.* **56**, 134 (1990).
14. K. V. Ravi and C. A. Koch, *Appl. Phys. Lett.* **57**, 348 (1990).
15. K. V. Ravi, C. A. Koch, H. S. Hu, and A. Joshi, *J. Mater. Res.* **5**, 2356 (1990).
16. J. A. von Windheim and J. T. Glass, *J. Mater. Res.* **7**, 2144 (1992).
17. M. T. McClure, J. A. von Windheim, J. T. Glass, and J. T. Prater, in *Materials Research Society Symposium Proceedings: Novel Forms of Carbon*, edited by C. L. Renschler, J. J. Pouch, and D. M. Cox (Materials Research Society, Pittsburgh, PA, 1992), Vol. 270, p. 323.
18. M. A. Golozar, I. R. McColl, D. M. Grant, and J. V. Wood, *Dia. Related Mater.* **1**, 262 (1992).
19. J. A. von Windheim, F. Sivazlian, M. T. McClure, and J. T. Glass, *Dia. Related Mater.* **2**, 438 (1993).
20. M. T. McClure, J. A. von Windheim, J. T. Glass, and J. Prater, *Dia. Related Mater.* **submitted** (1993).
21. K. A. Snail, D. B. Oakes, J. E. Butler, and L. M. Hanssen, in *MRS International Conference Proceedings Series: New Diamond Science and Technology (Proceedings of the Second International Conference on New Diamond Science and Technology)*, edited by R. Messier, J. T. Glass, J. E. Butler, and R. Roy (Materials Research Society, Pittsburgh, PA, 1991), p. 503.
22. P. K. Bachmann, D. Leers, and H. Lydtin, *Dia. Related Mater.* **1**, 1 (1991).
23. Y. Matsui, H. Yabe, and Y. Hirose, *Jpn. J. Appl. Phys.* **29**, 1552 (1990).
24. Y. Morinishi and T. Suzuki, in *MRS International Conference Proceedings Series: New Diamond Science and Technology (Proceedings of the Second International Conference*

- on *New Diamond Science and Technology*, edited by R. Messier, J. T. Glass, J. E. Butler, and R. Roy (Materials Research Society, Pittsburgh, PA, 1991), p. 517.
25. W.-S. Lee, Y.-J. Baik, and K. Y. Eun, in *MRS International Conference Proceedings Series: New Diamond Science and Technology (Proceedings of the Second International Conference on New Diamond Science and Technology*, edited by R. Messier, J. T. Glass, J. E. Butler, and R. Roy (Materials Research Society, Pittsburgh, PA, 1991), p. 593.
  26. J. J. Schermer, J. E. M. Hogenkamp, G. C. J. Otter, G. Janssen, W. J. P. van Enckevort, and L. J. Giling, *Dia. Related Mater.* **2**, 1149 (1993).
  27. K. A. Snail and C. M. Marks, *Appl. Phys. Lett.* **60**, 3135 (1992).
  28. F. R. Sivazlian, J. A. von Windheim, and J. T. Glass, in *Materials Research Society Symposium Proceedings: Novel Forms of Carbon*, edited by C. L. Renschler, J. J. Pouch, and D. M. Cox (Materials Research Society, Pittsburgh, PA, 1992), Vol. 270, p. 329.
  29. K. S. Harshavardhan, M. N. Vijayaraghavan, N. Chandrabhas, and A. K. Sood, *J. Appl. Phys.* **68**, 3303 (1990).
  30. K. A. Snail, R. G. Vardiman, J. P. Estrera, C. Merzbacher, C. J. Craigie, C. M. Marks, J. W. Glesener, R. Glosser, and J. A. Freitas Jr., *J. Appl. Phys.* **submitted** (1993).
  31. C. M. Marks, H. R. Burris, J. L. Grun, and K. A. Snail, *J. Appl. Phys.* **73**, 755 (1993).
  32. C. Wild, P. Koidl, W. Muller-Sebert, H. Walcher, R. Kohl, N. Herres, R. Locher, R. Samlenski, and R. Brenn, *Dia. Related Mater.* **2**, 158 (1993).
  33. R. G. Vardiman, C. L. Vold, K. A. Snail, J. E. Butler, and C. S. Pande, *Mat. Lett.* **8**, 468 (1989).
  34. H. A. Hoff, A. A. Morrish, J. E. Butler, and B. B. Rath, *J. Mater. Res.* **5**, 2572 (1990).
  35. S. J. Choi and Y. S. Shin, in *Materials Science Monographs, 73: Applications of Diamond Films and Related Materials*, edited by Y. Tzeng, M. Yoshikawa, M. Murakawa, and A. Feldman (Elsevier Science Publishers, Amsterdam, 1991), p. 527.
  36. W. Zhu, J. Ahn, H. S. Tan, and B. H. Tan, *J. Cryst. Growth* **125**, 649 (1992).
  37. W. Zhu, B. H. Tan, J. Ahn, and H. S. Tan, *Dia. Related Mater.* **2**, 491 (1993).
  38. Y. Tzeng and R. Phillips, in *Materials Science Monographs, 73: Applications of Diamond Films and Related Materials*, edited by Y. Tzeng, M. Yoshikawa, M. Murakawa, and A. Feldman (Elsevier Science Publishers, Amsterdam, 1991), p. 189.
  39. R. Phillips, J. Wei, and Y. Tzeng, *Thin Solid Films* **212**, 30 (1992).

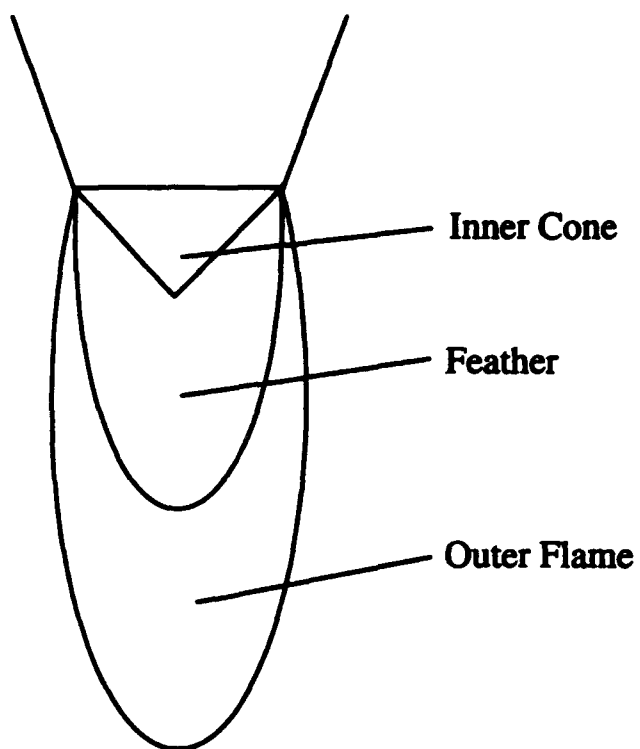


FIG. 1 - Schematic diagram of a torch flame.

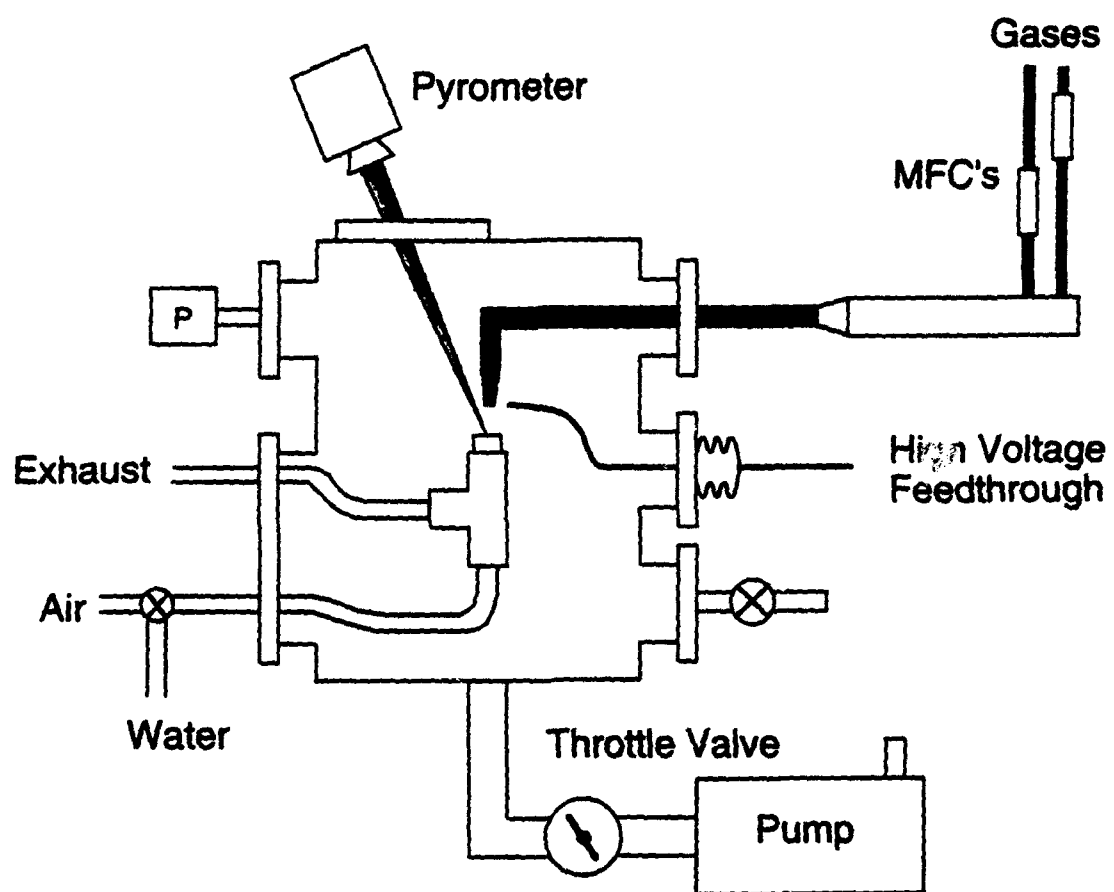


FIG. 2 - Diagram of the enclosed flame reactor.

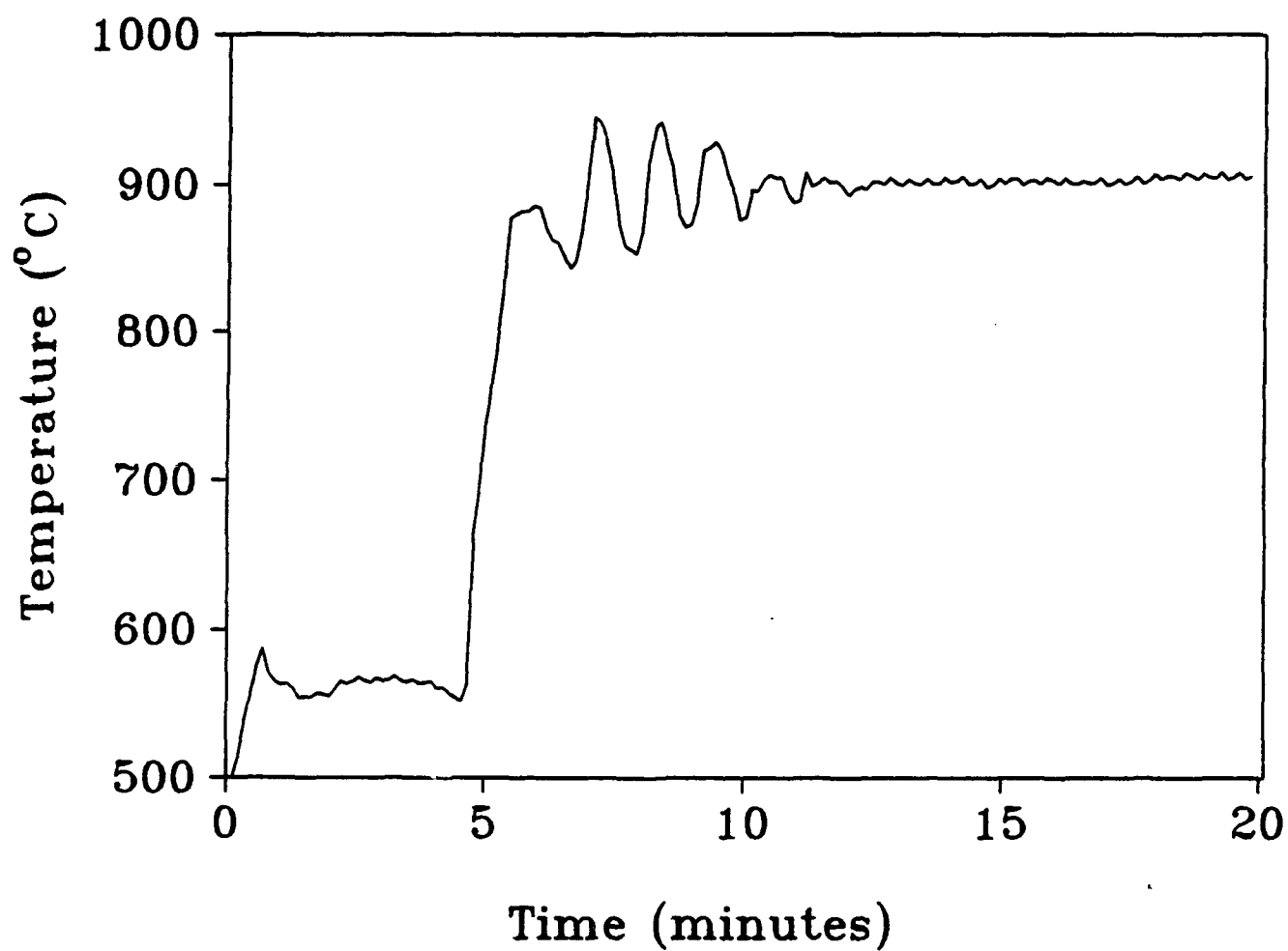


FIG. 3 - Measured temperature profile for a deposition. During pretreatment (0-5 minutes), the set point is 550 °C ( $R = 0.91$  and distance = 50 % of the feather length) while during growth the set point is 900 °C ( $R = 0.95$  and distance = 1 mm from inner cone).



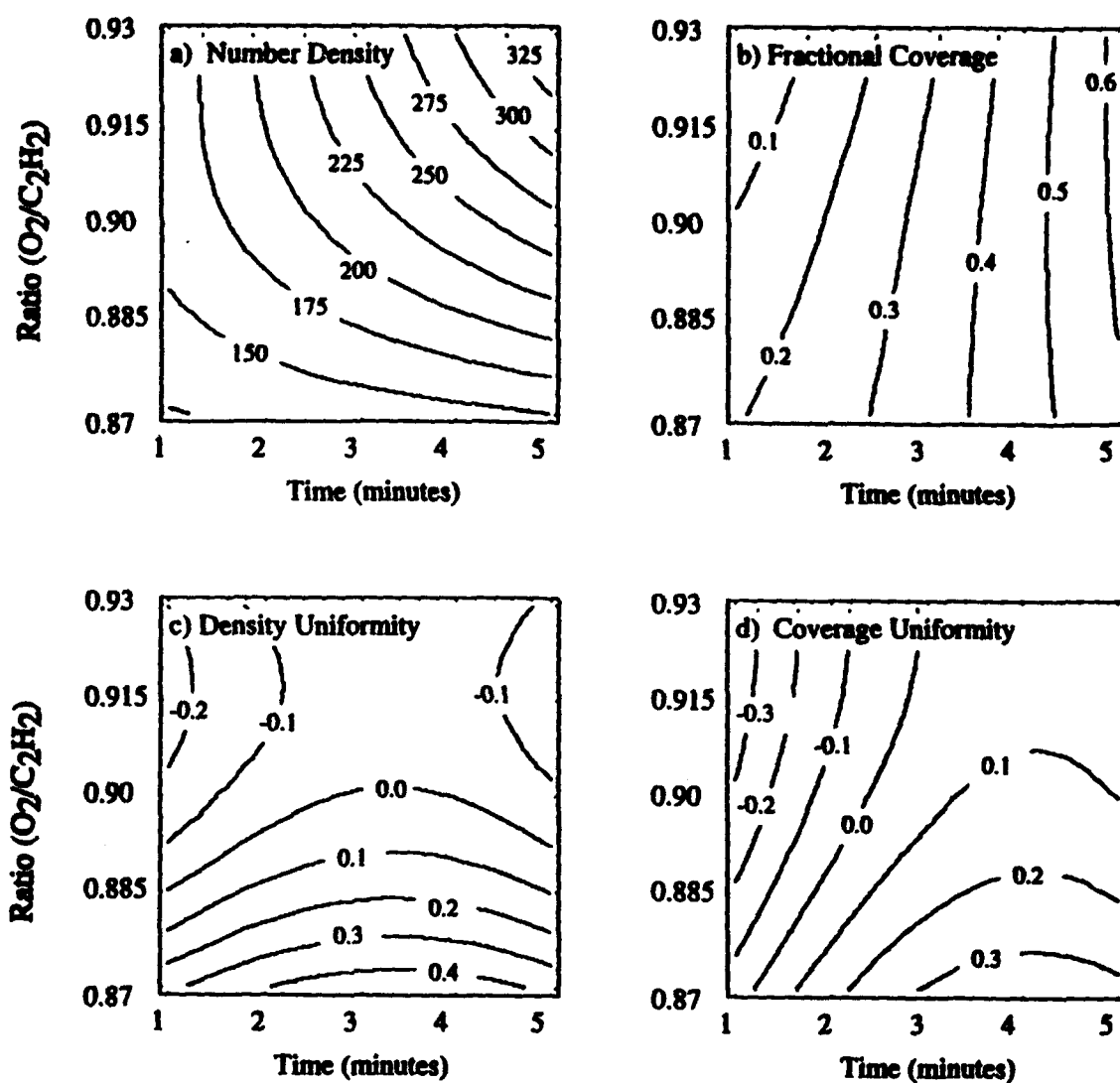


FIG. 4 - Contours of (a) average number density ( $\bar{N}$ ), (b) average fractional area coverage ( $\bar{f}$ ), (c) uniformity in number density ( $\Delta N / \bar{N}$ ), and (d) uniformity in fractional area coverage ( $\Delta f / \bar{f}$ ) at a distance of  $z_{nuc} = 50\%$  of the feather length.

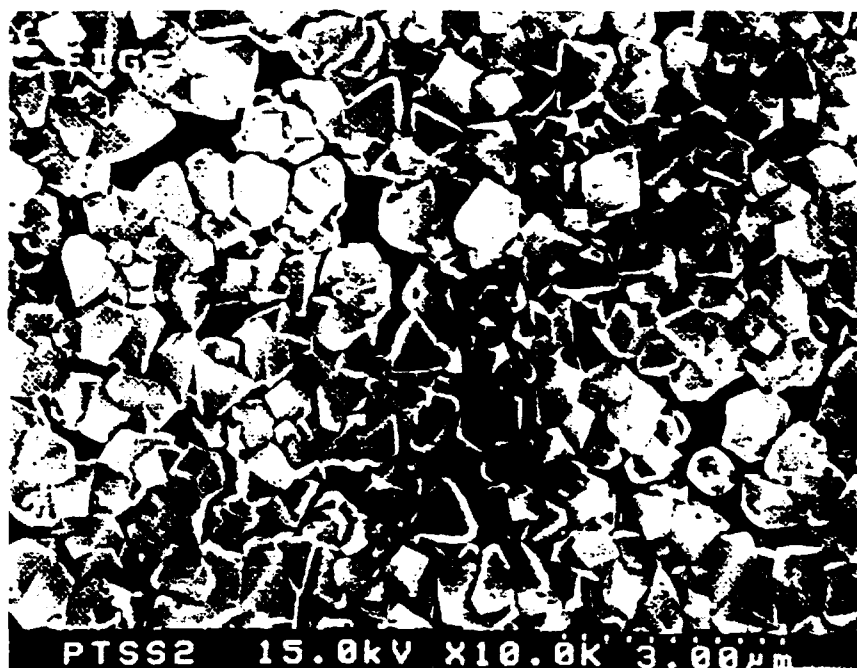


FIG. 5 - Scanning electron micrographs of a Si(100) surface pretreated at the optimized conditions of Table II. a) center of the film, b) edge of the film. The magnification is  $\times 10k$ .

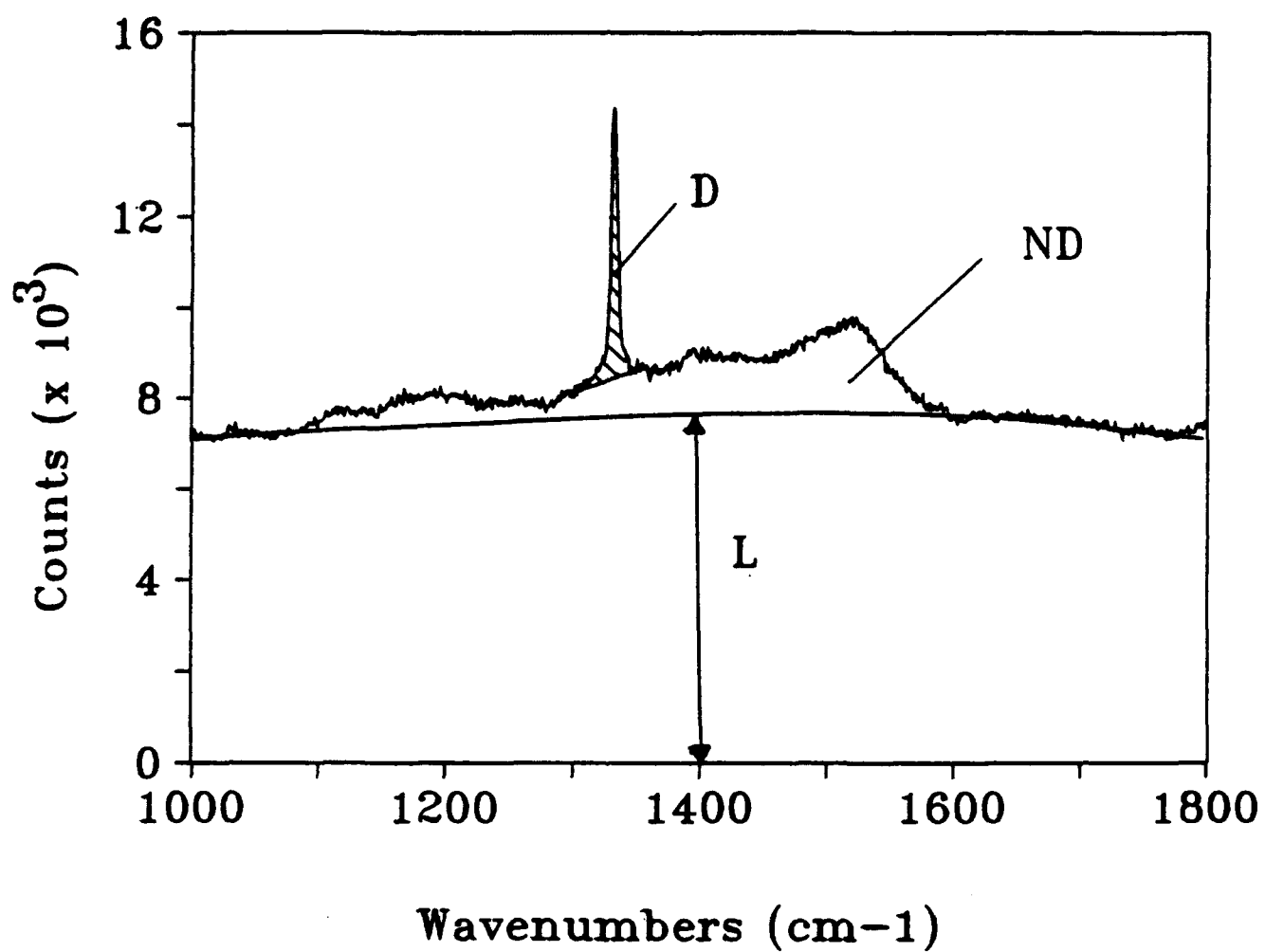
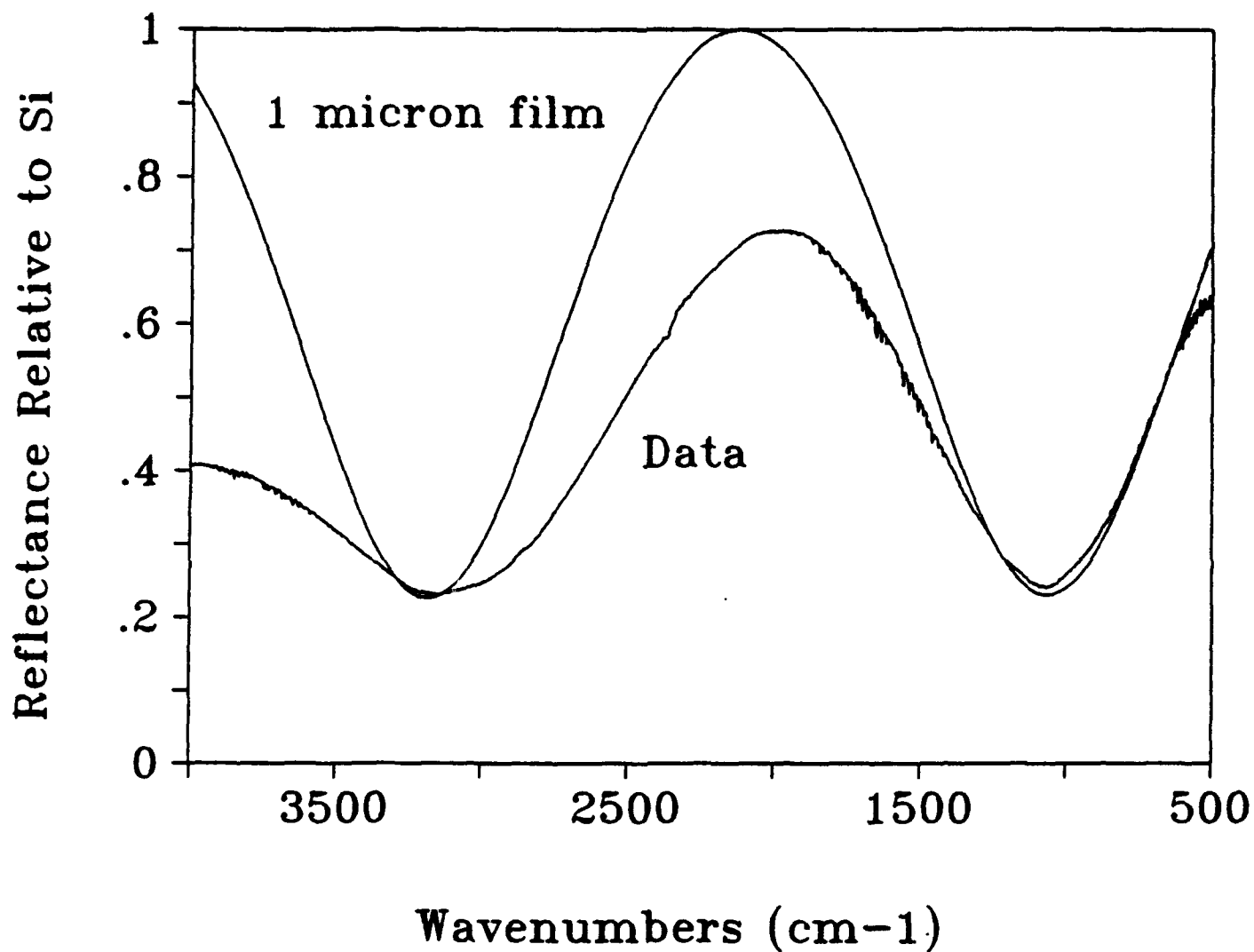


FIG. 6 - Description of the analysis of a sample Raman spectrum.



diathik1

FIG. 7 - Specular reflectance of a diamond film on Si(100) at an angle of incidence of  $30^\circ$ . The smooth curve is the predicted spectrum of a diamond film on silicon using literature values for the indices of refraction ( $n_{\text{dia}} = 2.41$  and  $n_{\text{Si}} = 3.42$ ) and a thickness of  $1 \mu\text{m}$ .

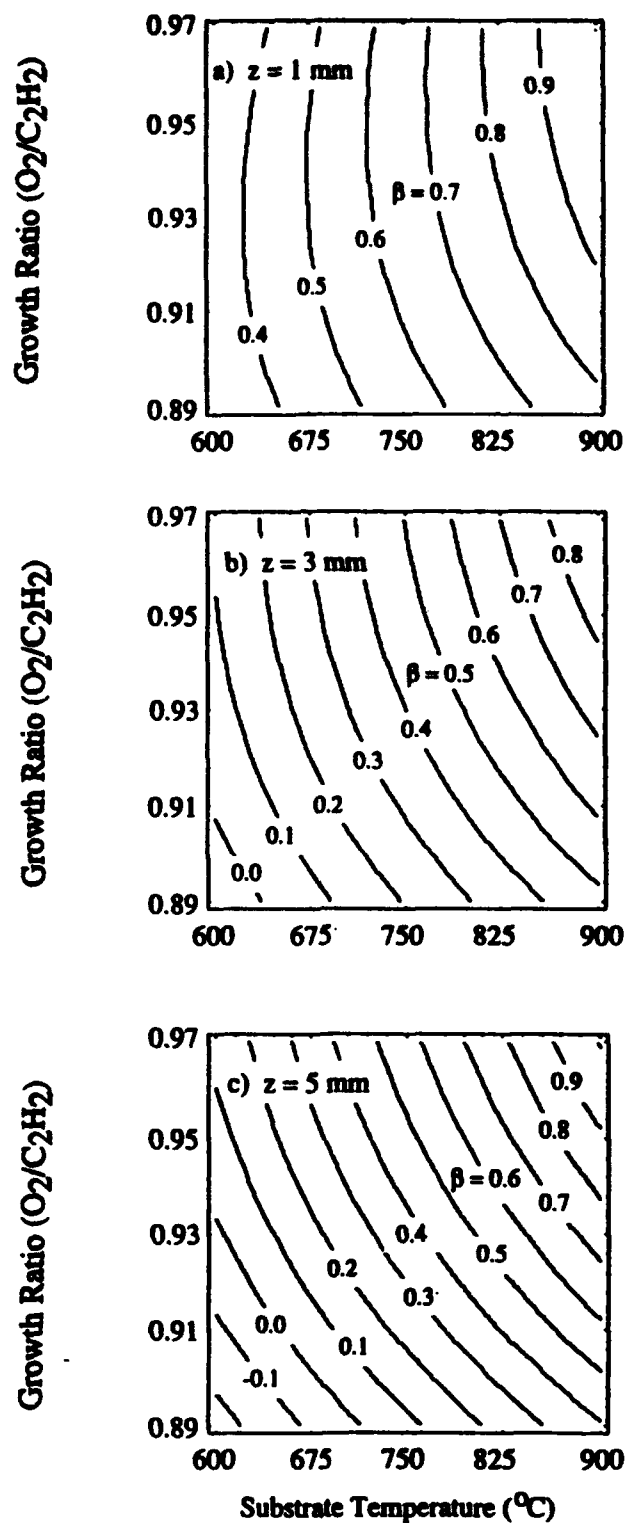


FIG. 8 - Contour plots of  $\beta$  as a function of growth ratio ( $R_g$ ) and substrate temperature ( $T_{sub}$ ) at three different deposition distances: (a)  $z = 1$  mm, (b)  $z = 3$  mm, and (c)  $z = 5$  mm. The units for  $\beta$  are dimensionless;  $\beta \rightarrow 1$  indicates pure diamond.

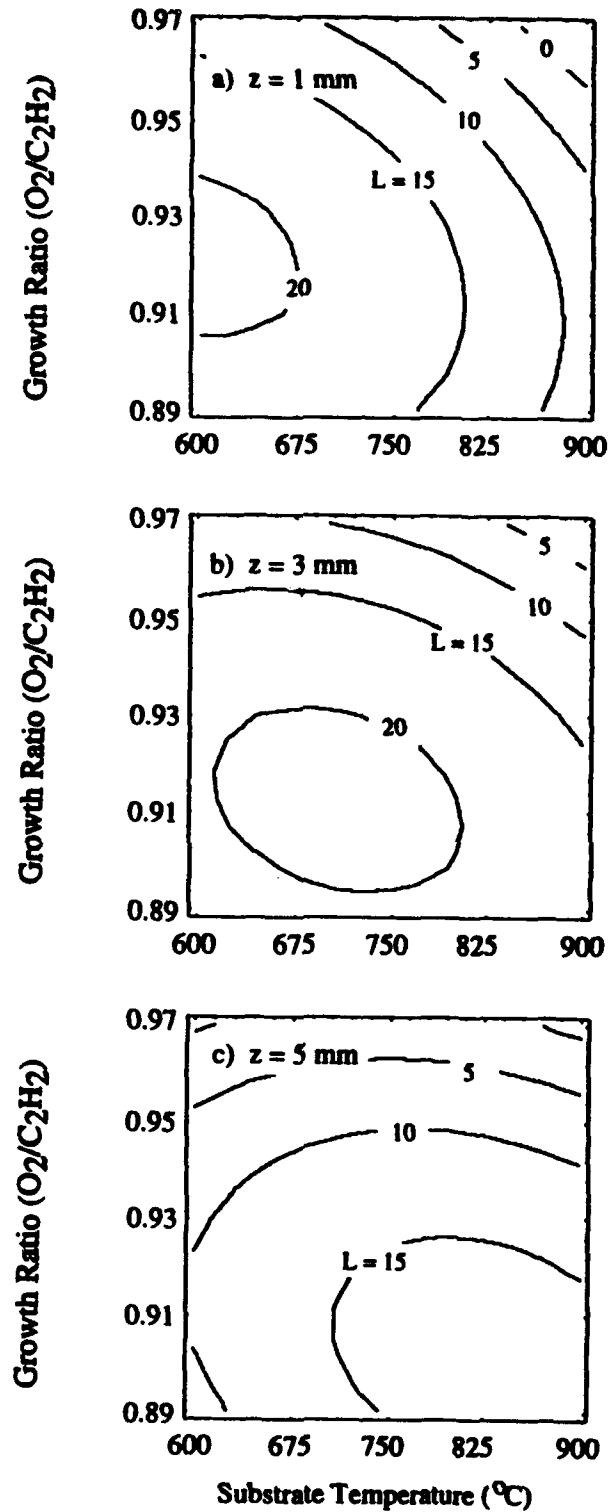


FIG. 9 - Contour plots of luminescence ( $L$ ) as a function of growth ratio ( $R_g$ ) and substrate temperature ( $T_{sub}$ ) at three different deposition distances: (a)  $z = 1$  mm, (b)  $z = 3$  mm, and (c)  $z = 5$  mm. The units for  $L$  are thousands of counts;  $L \rightarrow 0$  indicates diamond free of photoluminescing defects.

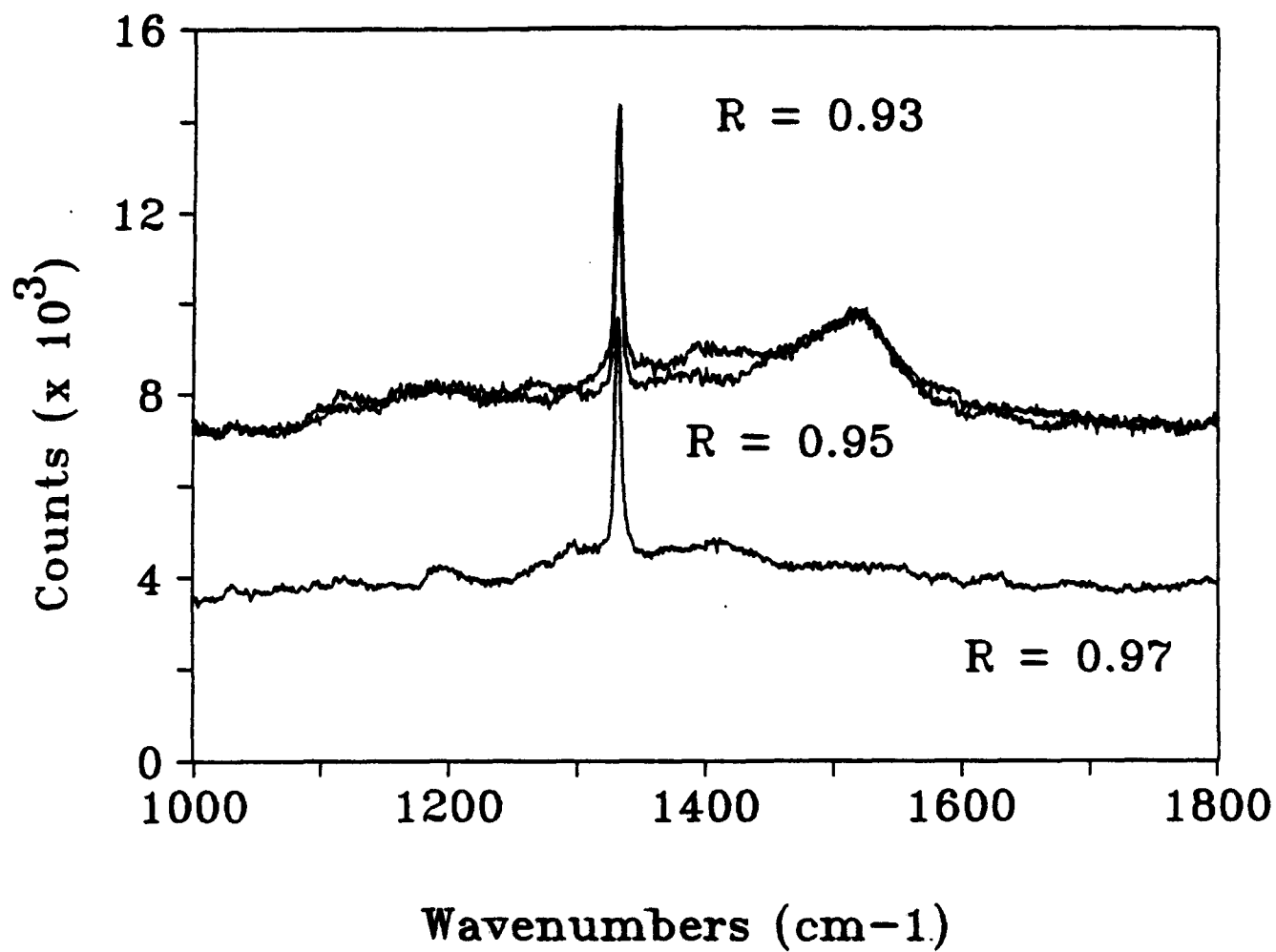


FIG. 10 - Comparison of Raman spectra of films grown near the optimal conditions. (a)  $R = 0.93$ ,  $R = 0.95$ , (b)  $R = 0.97$ . The other deposition parameters are the same for each sample:  $z = 1$  mm and  $T_{\text{sub}} = 900$  °C.

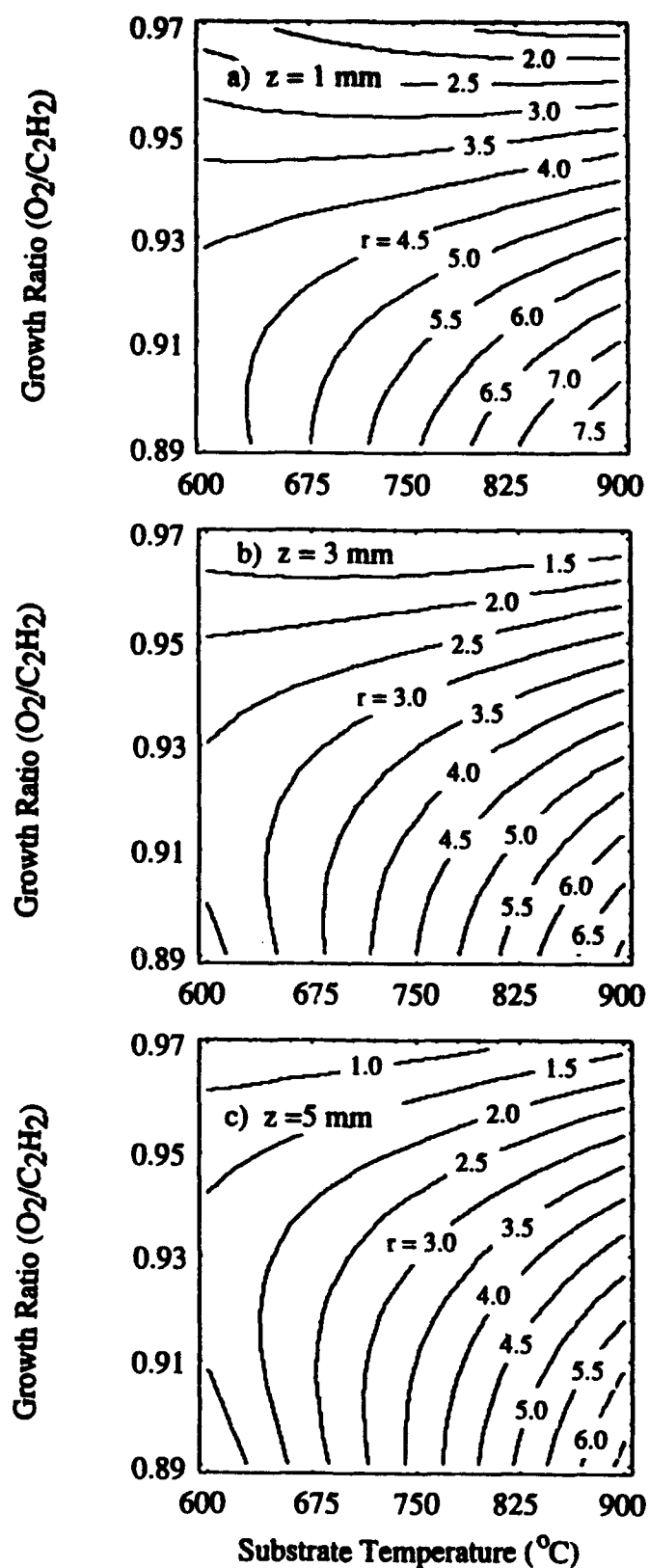


FIG. 11 - Contour plots of deposition rate ( $r$ ) as a function of growth ratio ( $R_g$ ) and substrate temperature ( $T_{\text{sub}}$ ) at three different deposition distances: (a)  $z = 1 \text{ mm}$ , (b)  $z = 3 \text{ mm}$ , and (c)  $z = 5 \text{ mm}$ . The units on deposition rate are  $\mu\text{m/hr}$ .



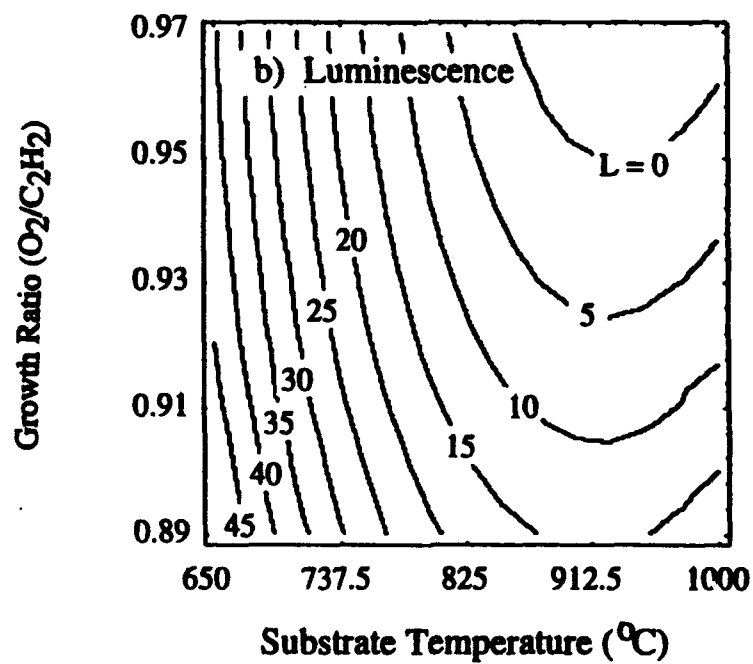
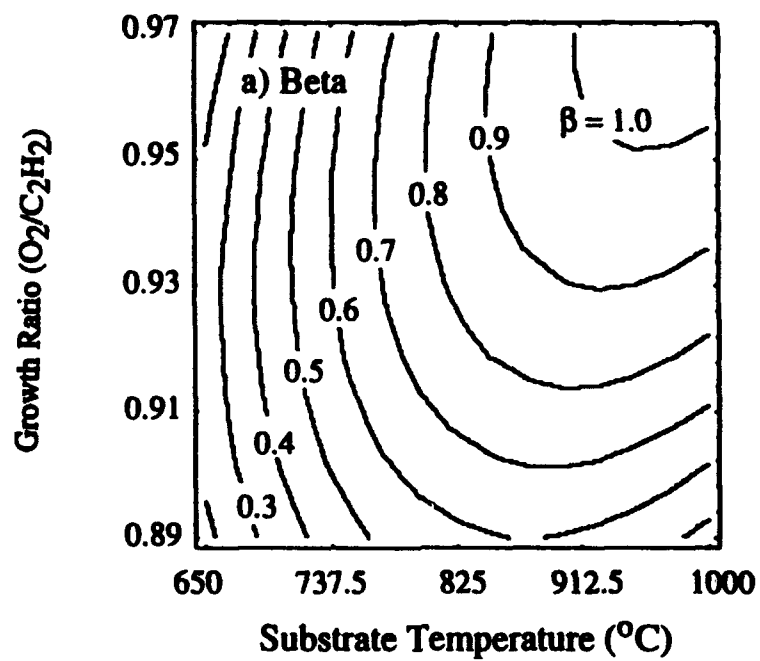


FIG. 12 - Contour plots of  $\beta$  (a) and luminescence (b) as functions of growth ratio ( $R_g$ ) and substrate temperature ( $T_{sub}$ ).

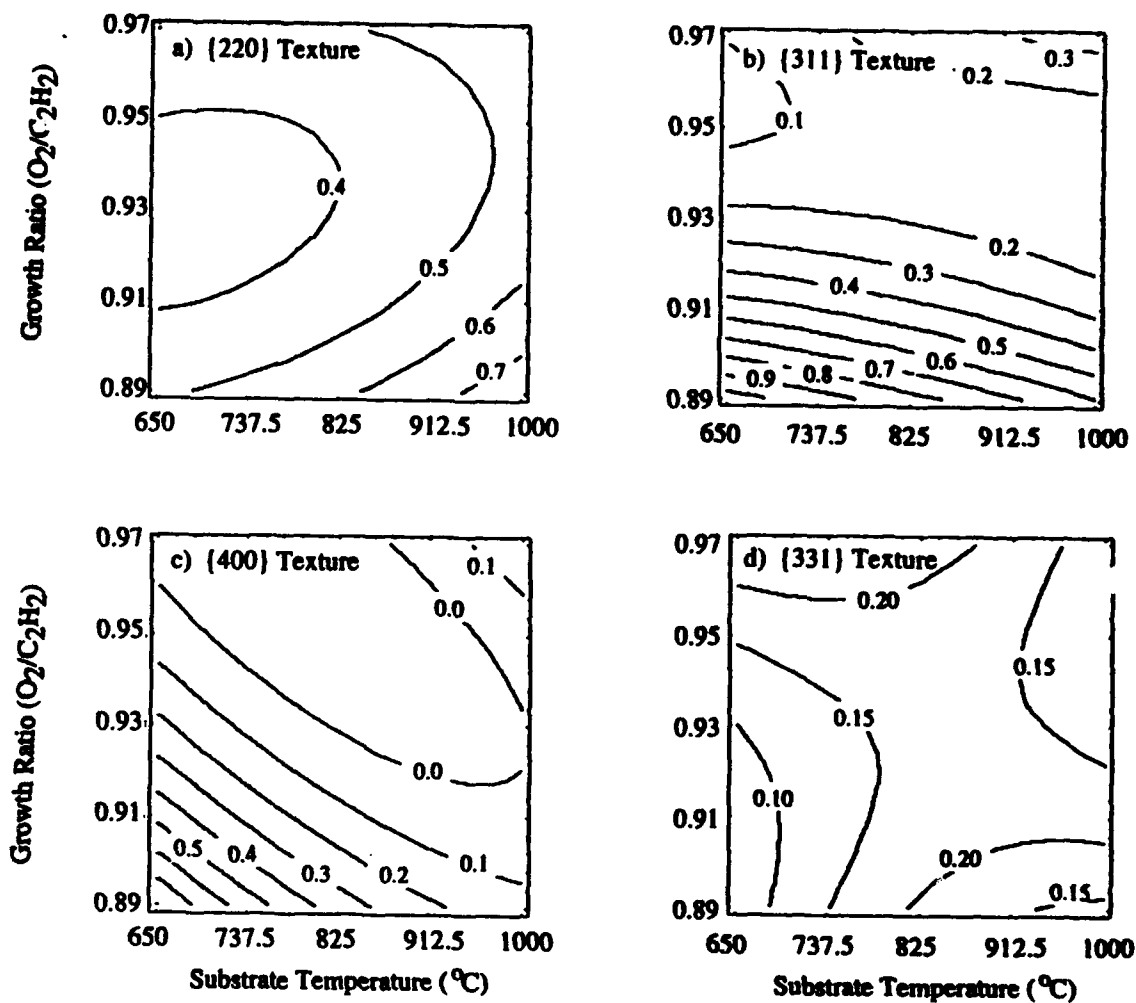


FIG. 13 - Contour plots of texture factors for the (a) {220}, (b) {311}, (c) {400}, and (d) {331} directions as functions of growth ratio ( $R_g$ ) and substrate temperature ( $T_{sub}$ ).

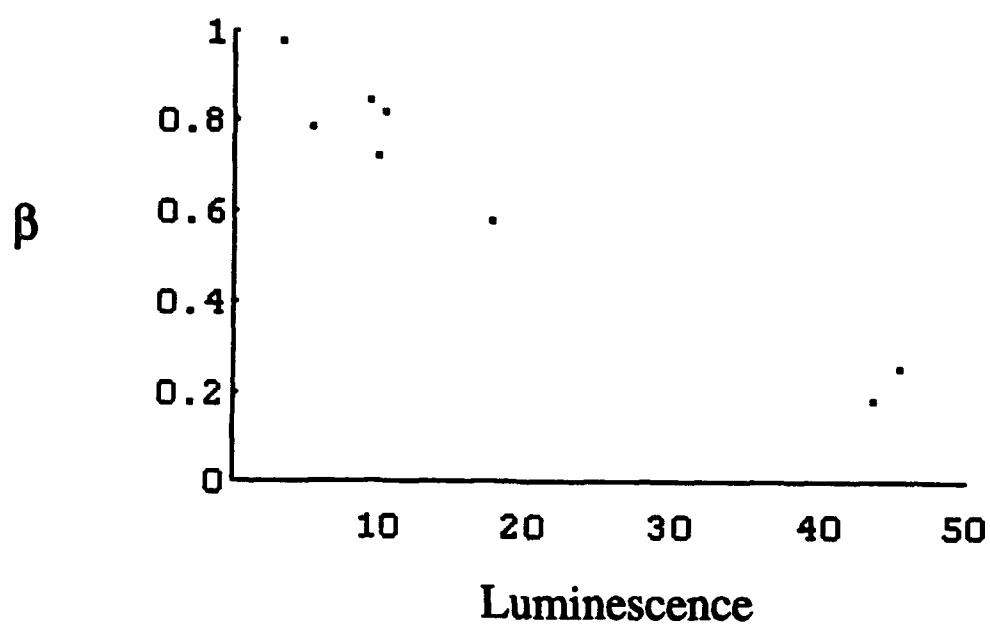


FIG. 14 - Scatter plot of  $\beta$  versus luminescence  $L$  using data taken from the texture study.

## VII. Epitaxial Cu Contacts on Semiconducting Diamond

### A. Introduction

There is a significant scientific and technological interest in the fabrication of rectifying and ohmic contacts for future diamond-based electronic devices. In particular, metal, silicide and semiconductor contacts have been investigated [1, 2, 3]. Recent publications have established excellent mechanical adhesion for polycrystalline Si and SiGe contacts [2, 3]. To date, the majority of rectifying metal contacts exhibit polycrystalline morphology and appear to have poor adhesion properties [1]. In contrast, Ni is the only epitaxially grown metal contact on diamond exhibiting rectifying behavior at both room- and elevated temperatures [4]. In this study Cu has been selected as a suitable contact metal, since Cu has a near-lattice match to diamond similar to Ni. Furthermore, no stable Cu carbides exist in the binary Cu-C phase diagram [5]. Therefore Cu is expected to form a physically and chemically abrupt interface with diamond.

In this paper we report the first results regarding heteroepitaxially grown Cu films on diamond C(001). The microstructure and electrical characteristics for these contacts are presented.

### B. Experimental Details

Several (3×3 and 4×4 mm) natural type IIb semiconducting diamond C(001) crystals (supplied by D. Drucker & ZN.N.V.) were used in this study. Two independent chemical cleaning processes were employed to remove the non-diamond carbon from the surface of the diamond substrates. The first approach was a conventional chemical clean using chromic acid ( $\text{CrO}_3\text{:H}_2\text{SO}_4$ ) (boiling for 15 min), aqua regia ( $3\text{HCl:1HNO}_3$ ) (boiling for 15 min) followed by deionized (DI) water (rinsing). The other procedure involved an electrochemical etch [6]. Therefore the samples were mounted on a Teflon™ holder and placed between two Pt electrodes in DI water as electrolyte. A DC-voltage of 350 V was applied between the two electrodes. Typical etch times were 3 hours. To assess and compare the effectiveness of these two cleaning processes *in situ* low-energy diffraction (LEED) was used. A comparable unreconstructed (1×1) LEED pattern was observed from crystals cleaned by either approach. Following chemical cleaning the diamond crystals were blown dry with  $\text{N}_2$  and mounted on a Mo sample block and transferred into the vacuum system. In order to desorb adsorbed gas contaminants all samples were annealed to 750°C for 15 minutes in ultra-high vacuum (UHV). Prior to growth 5.0 nm of Cu was evaporated from the solid source to liberate any foreign material which may have collected on its surface between depositions. Both large area films and contacts (625  $\mu\text{m}$  in diameter) were grown by electron-beam evaporation. The contact dots were fabricated by employing a Mo shadow mask.

Two independent growth chambers were employed. One system had a base pressure of  $\sim 5 \times 10^{-9}$  Torr and featured a Thermionics, model 100-0010, single source evaporator. Due to the small dimensions of this deposition chamber the pressure rose to  $\sim 2 \times 10^{-7}$  Torr during growth. In this system, Cu layers of 30 nm and 200 nm thickness were deposited on substrates that were chemically cleaned by chromic acid. A deposition rate of 2.0–2.5 nm/min was used. The second chamber (base pressure  $\sim 1.2 \times 10^{-10}$  Torr) was equipped with a dual source,  $270^\circ$  HM<sup>2</sup> evaporator made by Thermionics. To commence the deposition a deposition rate of 1.0–1.2 nm/min. was stabilized, and the shutter was removed from the front of the sample. After 20 nm was deposited, the rate was increased to 2.5–3.0 nm/min to give a final thickness of 200 nm. Electrochemically etched crystals were used here. Throughout the deposition ( pressure  $\sim 3 \times 10^{-8}$  ) the substrate was rotated to ensure uniform thickness across the sample. In both experiments a growth temperature of  $500^\circ\text{C}$  was used and the thickness of the Cu layers was determined by a quartz crystal oscillator.

Several techniques were employed to analyze the samples including *in situ* low-energy diffraction (LEED), Rutherford backscattering (RBS)/channeling, atomic force microscopy (AFM) and current-voltage (I-V) measurements.

### C. Results and Discussion

The technique of LEED was employed to establish that the as-deposited films were epitaxial as shown in Fig. 1a. In particular, an unreconstructed (1×1) LEED pattern was seen from the as-annealed C(001) substrates (Fig. 1b). This (1×1) pattern was retained after Cu deposition. RBS/channeling has been performed using 2 MeV He<sup>+</sup> ions with a scattering angle of  $110^\circ$ . This gave a depth resolution of 6.7 nm for the Cu film. As shown in Fig. 2, the epitaxial quality of the Cu films grown under higher pressure ( $2 \times 10^{-7}$  Torr) has been determined by channeling along the  $\langle 110 \rangle$  directions of the diamond substrate.  $\chi_{\min}$  is the ratio of the aligned to nonaligned backscattering ion yields and gives the degree of crystallinity for the sample. Values of  $\chi_{\text{Dia}} = 33\%$  and  $\chi_{\text{Cu}} = 49\%$  have been established for the diamond substrate and the overgrown Cu film, respectively. Furthermore, RBS analysis has shown the presence of oxygen impurities in these Cu films (peak near 950 keV). In addition the random spectrum shows a step in the carbon signal at 760 keV, indicating a non uniform thickness of the Cu layer.

The value of  $\chi_{\text{Cu}}$  appears to be fairly high. But considering  $\chi_{\text{Dia}}$ , the crystalline quality of the Cu film is actually quite reasonable.

The non uniformity in the deposited Cu layers has been attributed to island morphology for all samples as evidenced by AFM. The samples grown in a vacuum of  $2 \times 10^{-7}$  Torr exhibited well separated islands. For the Cu contacts of 30 nm thickness oriented islands of



Fig. 1a. (1x1) LEED pattern from type IIb C(001) substrate after chemical clean by  $\text{CrO}_3 + \text{H}_2\text{SO}_4$  and  $3\text{HCl} + 1\text{HNO}_3$  and following anneal at  $750^\circ \text{C}$  in UHV,  $E_B = 180\text{eV}$ .



Fig. 1b. (1x1) LEED pattern from 30 nm thick Cu film deposited on type IIb C(001) substrate (see Fig. 1a.) at  $500^\circ \text{C}$  in UHV:  $3 \times 10^{-8} \text{Torr}$  during growth,  $E_B = 180\text{eV}$ .

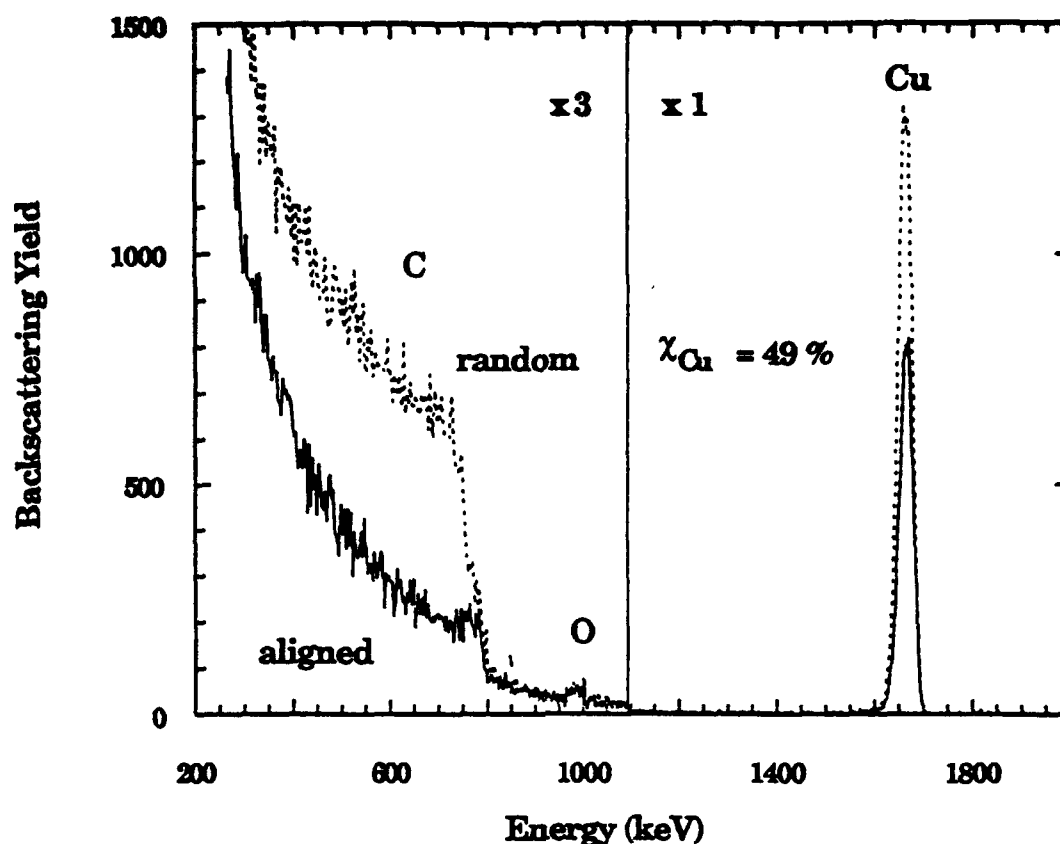


Figure 2. RBS/channeling aligned (solid line) and random (dashed line) spectrum for Cu (001) grown on C(001) substrates (cleaned by  $\text{CrO}_3 + \text{H}_2\text{SO}_4$  and  $3\text{HCl} + \text{HNO}_3$ ) in UHV:  $2 \times 10^{-7}$  Torr during growth.

~ 50 nm were observed. However, films of 200 nm thickness grew as well defined islands of ~ 1000 nm x 500 nm in size with smooth morphologies, as shown in Fig 3a. These islands were found to be oriented in the  $\langle 110 \rangle$  crystallographic directions. Therefore, coalescence of these islands was evident for increasing Cu coverage. However, no continuous layer was formed. Electrical measurements for these samples showed a lack of current transport across one Cu dot. This interesting phenomenon may be attributed to the observed islanding behavior of these Cu films.

In comparison, AFM images of the 200 nm thick Cu films deposited under better vacuum ( $3 \times 10^{-8}$  Torr) showed a fairly smooth and contiguous surface structure. However, the presence of numerous pinholes was observed (Fig. 3b). Corresponding I-V measurements between a dot and a large area back contact showed rectifying behavior. In addition, a reverse bias leakage current of ~ 40 nA was observed at 5 V as shown in Fig. 4. This corresponds to a current density of  $13 \times 10^{-6}$  A/cm<sup>2</sup>. To remove any highly conductive surface contaminants that could contribute to the reverse bias leakage current, another electrochemical etch was employed. Prior to etching the Cu dots were covered with wax

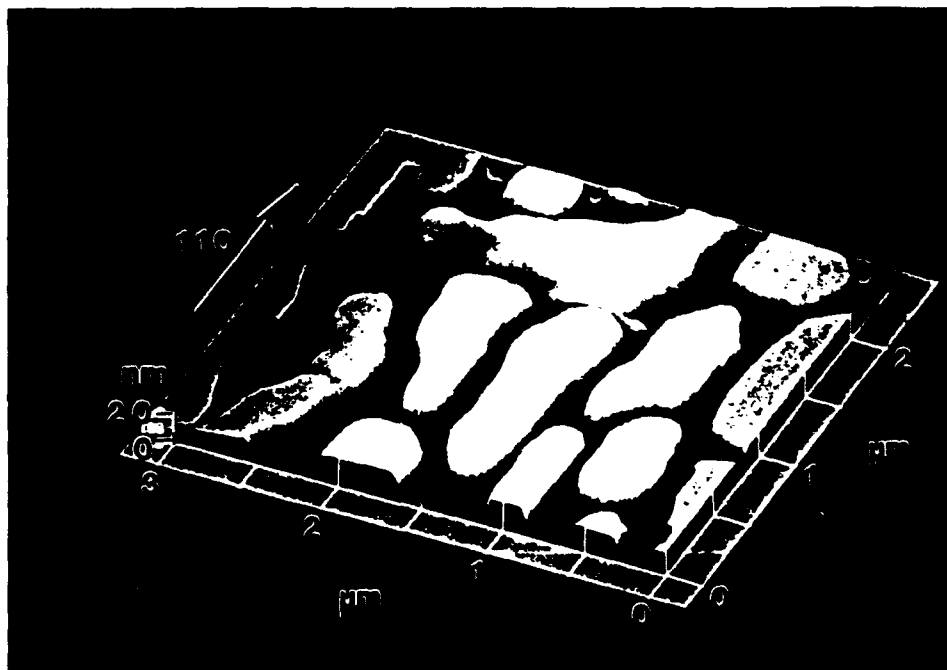


Fig. 3a. AFM micrograph of 200 nm thick epitaxial Cu film deposited on type IIb C(001) substrates (cleaned by  $\text{CrO}_3 + \text{H}_2\text{SO}_4$  and  $3\text{HCl} + 1\text{HNO}_3$ ) in UHV:  $2 \times 10^{-7}$  Torr during growth.

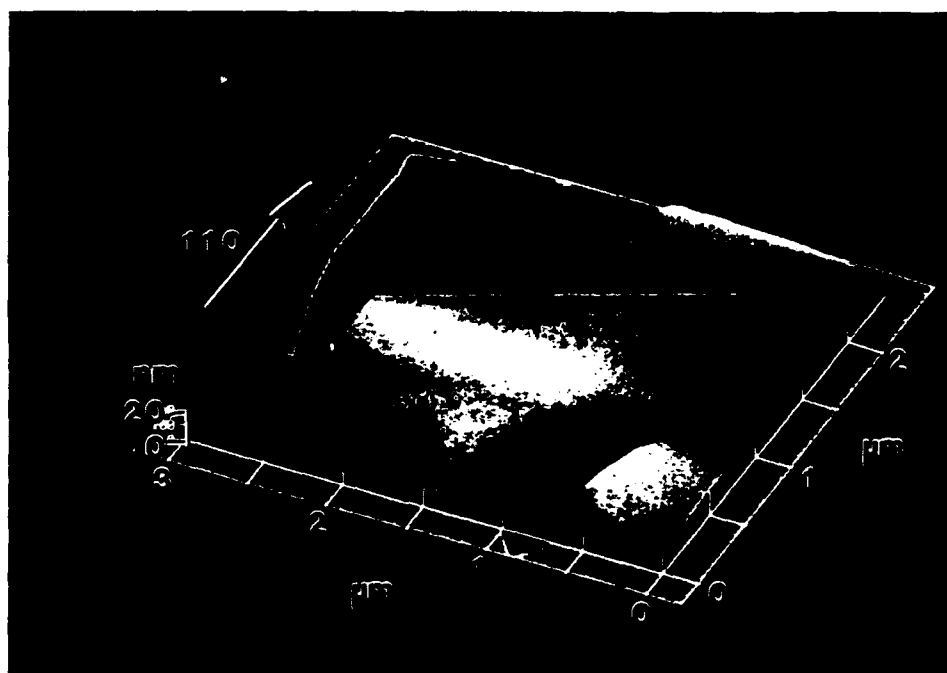


Fig. 3b. AFM micrograph of 200 nm thick epitaxial Cu film deposited on type IIb C(001) substrates (cleaned by electrochemical etch) in UHV:  $3 \times 10^{-8}$  Torr during growth.



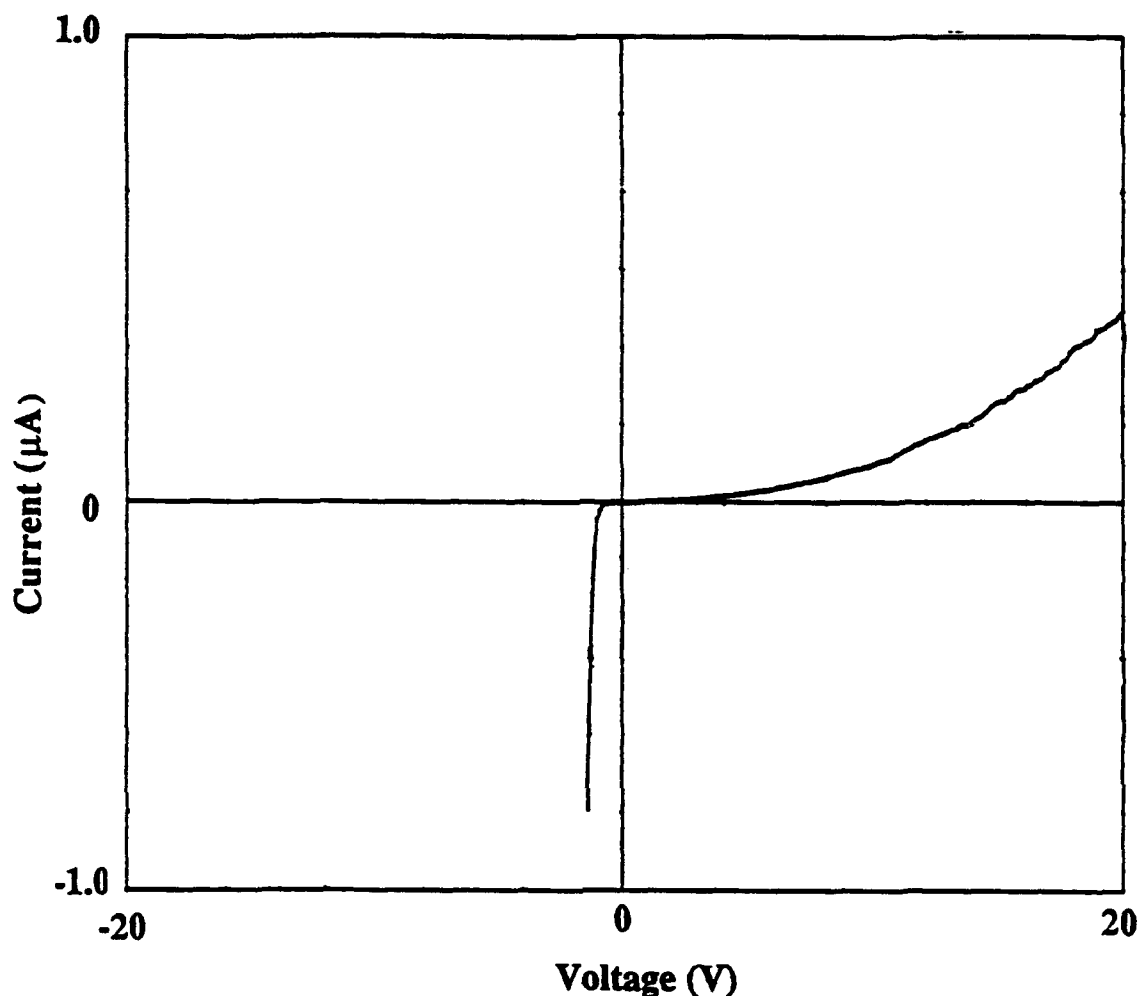


Figure 4. Linear plot of the room temperature I-V characteristics of heteroepitaxial Cu contacts deposited on type IIb (001) substrates in  $3 \times 10^{-8}$  Torr.

while the diamond surface was kept exposed. Following the etch process the wax was readily removed with acetone. Indeed, in separate experiments investigating electrochemical etching it has been demonstrated that besides graphite also various metals could be removed from the surface by this etching process [7, 8]. However, the I-V characteristics remained unchanged. Therefore it is reasonable to conclude that non diamond carbon and possible metal contaminants have been effectively removed from the diamond surface already in the first place. Consequently, the observed turn-on voltage and corresponding leakage current are believed to be intrinsic to the Cu/C(001) interface. However it will have to be established why Cu contacts display such a high reverse leakage current. Indeed, further studies are necessary to investigate the Cu/diamond interface structure.

Because of the nonlinearity in the semi-logarithmic I-V plot, an independent method to measure the Schottky barrier height  $\Phi_B$  had to be employed. A value of  $\Phi_B \cong 1.1$  eV has been established from ultraviolet photoemission spectroscopy (UPS). Furthermore, the UPS spectra showed that deposition of Cu on diamond C(001) induced a negative electron affinity (NEA) on the surface [9].

It is reasonable to assume that these observations are due to a 3-dimensional (3D) growth mechanism featuring larger nucleation area and better coalesation of the islands compared to the samples deposited under higher pressure. As shown in Fig. 2, RBS/channeling clearly demonstrated the presence of oxygen impurities in latter films. The oxygen contamination is expected to be lower for the system with better vacuum. Therefore samples deposited under lower pressure are expected to exhibit better microstructure. No significant effect on the morphology of the Cu films is expected due to the two different chemical cleaning procedures since they appear to be comparable. Therefore it is reasonable to conclude that the differences in microstructure for the epitaxial Cu layers were mainly due to a change in oxygen contamination.

Further improvement pertaining to a more uniform growth however, could be accomplished by using higher deposition rates. Also, a higher substrate temperature should increase the surface mobility of Cu on diamond and result in smoother epitaxial layers. With respect to the reports on Ni, even 2-dimensional (2D) growth could be possible [4]. This needs to be object of future work.

Consistent results from all samples clearly indicated that various processing steps including thermal annealing, electrical probing and ultrasonic cleaning did not degrade the excellent mechanical adhesion of the Cu contacts with the underlying diamond substrates.

#### D. Conclusions

Epitaxial Cu films have been deposited on p-type semiconducting natural diamond C(001) substrates using electron-beam evaporation techniques. For all samples 3-dimensional (3D) growth has been observed. However, differences in the nucleation area and the degree of coalesation for the Cu islands have been correlated to the quality of vacuum in the UHV growth chamber. Excellent mechanical adhesion properties have been established for the Cu films throughout. I-V measurements showed rectifying behavior at room temperature. Furthermore, a Schottky barrier height of  $\Phi_B \cong 1.1$  eV has been determined by means of UPS. Suggestions regarding future work to further assess and improve microstructure as well as electrical behavior have been made.

#### E. Acknowledgements

We gratefully acknowledge support from the Office of Naval Research (Contract No. N000114-92-J-1477) for the University Research Initiative. PKB and TPH thank K. Das (Kobe Steel USA, Inc.), R. G. Alley and J. B. Posthill (both: Research Triangle Institute) for technical assistance.

#### F. References

1. K. Das, V. Venkatesan, K. Miyata, D. L. Dreifus and J. T. Glass, *Thin Solid Films*, 212 (1992) 19-24.
2. V. Venkatesan, D. G. Thompson and K. Das, *Symp. Mater. Res. Soc.* 270 (1992).
3. T. P. Humphreys, P. K. Baumann, K. F. Turner, R. J. Nemanich, R. G. Alley, D. P. Malta and J. B. Posthill, accepted for publication in the *Proceed. 3rd. Internat. Conf. Symp. on Dia. Mat.*, Honolulu, Hawaii, May, 1993.
4. T. P. Humphreys, J. V. La Brasca, R. J. Nemanich, K. Das and J. B. Posthill, *Jpn. J. Appl. Phys.* 30 (1991) L1409.
5. *Binary Alloy Phase Diagrams*, ed. T. B. Massalski (American Society for Metals, Metals Park, OH, 1990) Vol. 1, p. 839.
6. M. Marchywka, P. E. Pehrsson, S. C. Binari, and D. Moses, *J. Electrochem. Soc.*, Vol. 140, No. 2 (1993).
7. M. Marchywka, private communication (1993).
8. P. K. Baumann, T. P. Humphreys, R. J. Nemanich, to be published (1993).
9. P. K. Baumann, R. J. Nemanich, to be published (1993).

## VIII. Structure of Si(001) Surface with Monoatomic Steps

### A. Introduction

Successful epitaxial growth requires control of both the surface of the substrate and of processes of deposition with the precision at the atomic level. In particular, the presence of monoatomic steps at the free surface may decisively influence the morphology of the epilayer. For instance, in the case of silicon, high quality crystals are obtained for the step-flow mode of growth, when deposited adatoms are incorporated at step edges. Also, a device-quality heteroepitaxy of III-V semiconductors on Si occurs when the miscut angle of the substrate exceeds about 4 degrees, and all steps are bilayer high. Before initializing the calculations for the surface of wide bandgap materials with monoatomic steps, we performed calculations of the electronic structure and atomic-scale configurations for the stepped Si(001). This study, reported below, tested our methods, and gave us both satisfactory results and experience. Calculations of the energetics and the electronic structure of flat SiC are in progress

### B. Computational Details

The calculations were based on the *ab initio* molecular dynamics scheme and non-local atomic pseudopotentials. We used the repeated-slab geometry, where each slab had 7 Si layers, two bottom layers were kept fixed at ideal bulk sites, and slabs were separated by 7 layers of vacuum. The dangling bonds of the bottom surface were saturated with H atoms. The in-plane unit cell period was  $6 \times 4$ , resulting in about 160 Si atoms and 48 H atoms in the unit cell. Due to the large size of the cell, summations over the Brillouin Zone were approximated by one ( $\Gamma$ ) point. The kinetic energy cutoff for the plane wave basis set was 8 Ry. This set was used for both flat and stepped surfaces.

### C. Flat Surfaces

We begin with the analysis of the flat surface, which will provide reference results for stepped configurations. The considered reconstructions are  $s(2 \times 1)$  and  $b(2 \times 1)$  with symmetric and buckled dimers, respectively, and  $p(2 \times 2)$  and  $c(2 \times 4)$  with alternating buckled dimers. Our results are summarized in Table I.

In agreement with previous calculations [1,2,3,4], we find that symmetric dimers represent an unstable configuration of Si(001). The computed ground state configuration for the flat Si(001) surface is the  $c(2 \times 4)$  reconstruction, which induces an energy gain of 0.24 eV per surface dimer, and a buckling of 0.72 Å. The  $p(2 \times 2)$  reconstruction is nearly energetically degenerate with  $c(2 \times 4)$ , since its energy is higher by only about 8 meV per surface dimer.

Table I. Reconstruction energies, buckling, and band gaps for the considered reconstructions of flat Si(001).

	$\Delta E$ (eV)	tilt ( $\text{\AA}$ )	gap (eV)
s(2 $\times$ 1)	0	0	metallic
b(2 $\times$ 1)	-0.1	0.51	0.1
p(2 $\times$ 2)	-0.24	0.71	0.3
c(2 $\times$ 4)	-0.24	0.72	0.5

The electronic structure of the flat Si(001) surface was studied in Refs. [1,2,4,5]. It was found that the s(2 $\times$ 1) surface is metallic, while the buckling of dimers is accompanied by the increase of the band gap and by the charge transfer from the “down” to the “up” atoms. According to the most exact results obtained within the GW approximation [2], the direct gap is 0.9 eV, and the indirect one is about 0.3 eV. A direct comparison of our results with other data is somewhat difficult, since we compute the band structure at the  $\Gamma$  point only. (Strictly speaking, the band gap values reported here are direct band gaps at  $\Gamma$  of the 6 $\times$ 4 folded Brillouin Zone.) However, the results of Table I are in qualitative agreement with the trend emerging from the works of Ref. [1,2,4,5].

#### D. Configuration and Energetics of Stepped Surfaces

We will now consider the stepped Si(001). Because of the geometry of the diamond lattice, there are two types of monolayer steps, denoted by SA and SB [6]. In the case of SA, the dimers on the upper terrace are perpendicular to the step edge, and for SB they are parallel to the edge. Further, the SB step may be terminated either by a rebonded or a non-rebonded edge. Thus, when the dimers are symmetric, there are three non-equivalent configurations. The buckling of dimers substantially increases the number of possible stepped configurations. First, the reconstructions at the upper and the lower terrace may be different. In consequence, considering only two reconstruction of terraces, p(2 $\times$ 2) and c(2 $\times$ 4), one obtains 12 possible configurations. Second, a further increase of possible configurations comes from the various possible reconstructions of the step edges. For instance, as we indicate below, there are two possible variants of the SA edge. Due to the computational constraints we have not investigated all possibilities.

In the case of the step SA, there are two possible variants. The first one, called here SA1, is observed experimentally. In this variant, the “up” atoms at the edge of the upper plane are aligned with the center of the dimer in the lower plane, while the “down” atoms are aligned

with the gap between the dimer rows in the lower plane. (In the second variant, denoted here by SA2, the tilt has the opposite sign.) As a result, the configuration with symmetric dimers is unstable, and the  $c(2\times 4)$  reconstruction of the upper terrace is induced by the geometry of the step edge. The edge is not strongly reconstructed, i.e., the geometry on both terraces is close to that of the flat surface. We find that  $c(2\times 4)$  and  $p(2\times 2)$  reconstructions of the lower terrace are energetically degenerate within the accuracy of the calculations. The buckling energy is 0.14 eV per surface dimer, which is less than for the flat surface, 0.24 eV per surface dimer. Also the buckling of the lower plane, about 0.62 Å for both reconstructions, is smaller than that found for flat surfaces. The energy gaps for  $c(2\times 4)$  and  $p(2\times 2)$  are 0.5 eV and 0.6 eV, compared to 0.5 eV and 0.3 eV for the flat surfaces, respectively. The second step geometry SA2 has the total energy equal to that of SA1 within the accuracy of the calculations. This is unexpected, since this configuration was not observed experimentally.

The step SB may exist in two variants, rebonded and non-rebonded, and both variants are observed in STM experiments. We considered both possibilities, and both  $c(2\times 4)$  and  $p(2\times 2)$  reconstructions. In contrast to the case of SA, the edge of the step SB is strongly reconstructed. In fact, the bond angles of the edge atoms are substantially different from the ideal tetrahedral value, which implies a substantial change of the bond character. In the case of the rebonded edge, the reconstruction is less pronounced. The reconstructions of edges are driven by the buckling of dimers from the upper terrace, and thus are of electronic origin. The results for the step SB may be summarized as follows: (i) For the rebonded edge, the  $p(2\times 2)$  reconstruction is more stable than  $c(2\times 4)$  by 80 meV per surface dimer. This agrees with the high-resolution images of Ref. [7], where the  $p(2\times 2)$  periodicity is seen. The band gap is significantly reduced, to 0.1 eV for  $c(2\times 4)$ , and 0.25 eV for  $p(2\times 2)$ . (ii) For the non-rebonded edge with  $p(2\times 2)$  periodicity, the buckling of the upper terrace is 0.74 Å at the edge, which is more than for flat surfaces, and 0.6 Å for the middle row. The row of dimers at the lower terrace is buckled by 0.69 Å. The band gap of this system is 0.5 eV, which is larger than the result 0.3 eV for the flat surface, and two times larger than that for the non-rebonded edge. The increase of the band gap is consistent with the increase of buckling. (iii) The energy difference between the rebonded and non-rebonded edges strongly depends on the surface reconstruction. For the  $b(2\times 1)$  reconstruction on both terraces we obtain 0.8 eV per edge atom, while for  $c(2\times 4)$  we find 0.3 eV per edge atom.

#### E. Simulated STM Images

In the last part of this paper we will verify our results by simulating STM images, and comparing them with the experimental data. According to Tersoff and Hamann [8], the intensity of the tunneling current is proportional to the square of the wave function. We used an energy window of 0.3 eV centered at -0.5 eV below the top of the valence band for the

filled state image, and at +0.8 eV for empty state image. This analysis was performed for most of the studied geometries. In all cases we find the same qualitative differences between the filled and empty state images. On filled-state images, the positions of the maxima of the isosurface along the  $z$  axis coincide to a good approximation with the positions of the “up” atoms, while the “down” atoms are nearly not seen. In fact, the apparent buckling is about 1.2 Å, which is much more than the actual value of 0.7 Å. In contrast, on the empty state image shown in Fig. 2b, the dimers appear to be nearly symmetric. The above results can be understood by analyzing the wave functions contributing to STM images. For flat surfaces with  $b(2\times 1)$  periodicity, surface states form two bands with energies in the vicinity of the band gap [4]. The lower band, resonant with the top of the bulk valence band, is occupied, and its wave function at  $\Gamma$  is built up mainly from the  $p_z$  orbital of the “up” atom. The upper surface band, which is in the upper part of the gap, is empty, and its wave function is the dangling bond of the “down” atom. Note that for  $p(2\times 2)$  and  $c(2\times 4)$  surfaces, both bands are further split into doublets due to the doubling of the in-plane period [2]. This charge transfer, accompanying the buckling of the surface dimer, is universal for  $b(2\times 1)$ ,  $p(2\times 2)$ , and  $c(2\times 4)$  reconstructions on both flat and stepped surfaces. Consequently, the filled state image, which displays the occupied states of the “up” atom, has the tendency to overestimate the apparent buckling. In the empty state image, tunneling occurs to the dangling bond of the “down” atom, which makes the dimer to appear symmetric.

We end this Section by pointing out that the difference between the filled and the empty state images has been measured and discussed by Kochanski and Griffith [7]. Their interpretation of this effect assumes that the electric field between the tip and the sample is strong enough to drive the reconstruction from buckled to symmetric dimers. Our results provide an alternative interpretation of experiment, based on the calculated electronic structure of filled and empty states only, and not requiring any changes in the positions of the surface atoms.

## F. Conclusions

In summary, we have studied the stepped Si(001) surface using *ab initio* molecular dynamics. We considered monolayer SA and SB steps, and  $s(2\times 1)$ ,  $b(2\times 1)$ ,  $p(2\times 2)$ , and  $c(2\times 4)$  reconstructions. To display the influence of steps, the results were discussed in reference to the ideal flat surface. Considering the atomic structure, we find that the symmetric dimers are unstable with respect to buckling for all configurations considered here. The buckling amounts to about 0.7 Å, i.e., is comparable to the interlayer spacing, and it leads to an energy gain of  $\sim 0.2$  eV per dimer. In general,  $c(2\times 4)$  and  $p(2\times 4)$  are energetically close. However, the ground-state configuration depends on the type of the step. For SA, the  $c(2\times 4)$  reconstruction is induced by the edge geometry, while for the SB step, the  $p(2\times 2)$  is

more stable than  $c(2\times 4)$  by 80 meV per dimer. All of the studied stepped systems in an equilibrium configuration are insulating, which implies that there are no edge-induced states in the gap. Finally, we simulated STM images and compared them with experiment. The observed qualitative differences between filled- and empty-state images are explained by topology of surface states, without assuming tip-induced reconstructions.

#### G. References

1. J. Dabrowski and M. Scheffler, *Appl. Surf. Sci.* **56-58**, 15 (1992).
2. J. E. Northrup, *Phys. Rev. B* **47**, 10032 (1993).
3. N. Roberts and R. J. Needs, *Surf. Sc.* **236**, 112 (1990).
4. J. Pollmann, P. Kruger, and A. Mazur, *J. Vac. Sc. Technol.* **B5**, 945 (1987).
5. D.J. Chadi, *Phys. Rev. Lett.* **59**, 1691 (1987).
6. J. D. Chadi, *Phys. Rev. Lett.* **43**, 43 (1979).
7. G. P. Kochanski and J. E. Griffith, *Surf. Sci.* **249**, L293 (1991).
8. J. Tersoff and D. R. Hamann, *Phys. Rev. Lett.* **50**, 1998 (1983).



## IX. Surface Preparation of SiC Films

### A. Introduction

SiC has properties which make it an attractive material for electronic devices used in high temperature and power applications. In order to make useful devices we need to be able to characterize the surfaces and be able to control surface properties. One parameter we wish to measure is the Schottky barrier height which results from a thin metal layer on a semiconductor. In the Schottky-Mott model, the barrier depends only on the work function of the metal and the electron affinity of the semiconductor. However, for most practical situations there will be a dependence on electronic states at the interface. These surface states result in a dipole at the interface and will substantially affect the Schottky barrier.

The Schottky barrier height (SBH) in diamond has been shown to depend significantly on surface preparation [1]. The same trend can be expected to hold for SiC. Thus, we focus on surface preparation of SiC as a means to control the SBH. Independent of model, the SBH for an n-type semiconductor is the difference between the metal Fermi level and the conduction band minimum, while for a p-type semiconductor the SBH is the difference between the Fermi level of the metal and the valance band edge.

The SBH can be deduced from Ultraviolet Photoemission Spectroscopy (UPS) measurements. The measurements involve directing 21.2 eV light (the He I resonance line) to the surface of the sample and counting the photo excited electrons as a function of electron kinetic energy. The measurement gives a profile of the valance band (VB) since the light promotes electrons from the VB to the conduction band (CB) by shifting the energy by 21.2 eV. From the spectra the VB edge can be determined from the onset of electron emission. A thin metal layer can be then deposited on the semiconductor, and we can determine the Fermi level. Thus, the SBH for a p-type semiconductor can be measured directly. For an n-type semiconductor, the SBH is given by the bandgap energy minus the measured p-type barrier.

Before deposition of metals on the substrate, it is necessary to insure that a clean surface without defects or graphitization is obtained. We will examine cleaning both by *ex situ* wet chemical etch (HF spin) and *in situ* remote hydrogen plasma processing. Previous work dealing with *in situ* annealing indicated damage to the surface and an imbalance in the stoichiometry. [2] The analytical tools used will be low energy electron diffraction (LEED), Auger electron spectroscopy (AES), Ultraviolet photoemission spectroscopy (UPS), and X-ray photoemission spectroscopy (XPS).

### B. Experimental Procedure

The SiC samples used in this study were vicinal 6H n-type wafers supplied by Cree Research, Inc. The samples have doping concentrations of  $\sim 10^{15}$  to  $10^{16}$  /cm<sup>3</sup>. All work done

has been on the Si-terminated (0001) face which is oriented 3-4° towards [1120]. Prior to loading in the UHV system, the samples were prepared with an *ex situ* cleaning technique. The process included an HF spin etch with a solution of HF:H<sub>2</sub>O:ethanol at 1:1:10. This technique was developed for the cleaning of Si wafers.

The surface analysis and *in situ* cleaning processes were carried out in an integrated surface processing/characterization system. The backbone of the system is a ~35ft. long UHV sample transfer system with eight stations. The eight stations include remote plasma cleaning, uv-photoemission, XPS, AES, LEED, Raman spectroscopy, temperature programmed desorption, and epitaxial metal deposition MBE.

After the *ex situ* surface preparation, additional surface cleaning was performed in the remote plasma chamber. The processing parameters were a pressure of 18 mTorr and a power output of 20 Watts; a flow of 10 sccm of hydrogen gas was employed and a plasma was excited by a rf-coupled source. The sample was heated to 400 °C prior to the plasma clean and held at that temperature for a one minute plasma cleaning. An earlier sample had been processed for ninety minutes. These two samples define limits for our process.

UPS measurements have been done on SiC samples as loaded, and after anneals of 700 °C and 1000 °C. The UPS chamber has a base pressure of 10<sup>-10</sup> Torr. Operating conditions involve pressures up to 1×10<sup>-8</sup> Torr, but the higher pressure is due to the helium inflow and does not contaminate the sample. As mentioned earlier, the UPS system utilizes a helium resonance lamp (the He I line) to provide a source of 21.2 eV light. The light is directed to the surface and electrons in the valence band can be promoted to the conduction band. Electrons from the conduction band can migrate to the surface and escape. Emitted electrons then are energy analyzed by a 50 mm radius hemispherical photomultiplier. Some low energy electrons are unable to overcome the electron analyzer work function and, thus, are not detected. A bias is applied to the sample to enable the low energy electrons to be detected.

In addition, X-ray photoemission spectroscopy was performed before and after plasma cleaning. XPS is similar to UPS but uses higher energy photons (~1487 eV). Due to the higher energies involved, the electrons detected originate from the core levels instead of the valence band. In principal, XPS is somewhat more sensitive to chemical composition than AES, and it displays chemical shifts which can be related to bonding configurations.

### C. Results

Auger Electron Spectroscopy (AES) and Low Energy Electron Diffraction (LEED) were obtained immediately after loading the wafers into UHV and after a one minute H-plasma exposure at 400 °C. The AES spectra are compared in Fig. 1. As shown in the figure, the plasma processing sharply reduces the carbon and roughly halves the oxygen present at the surface. LEED measurements obtained immediately after loading showed no detectable

diffraction spots. In contrast, after the H-plasma exposure, a  $1\times 1$  hexagonal pattern was observed at an electron energy of 80 eV. The observation of a  $1\times 1$  pattern at this low electron energy indicates that the surface order has been substantially improved with the low temperature H-plasma clean.

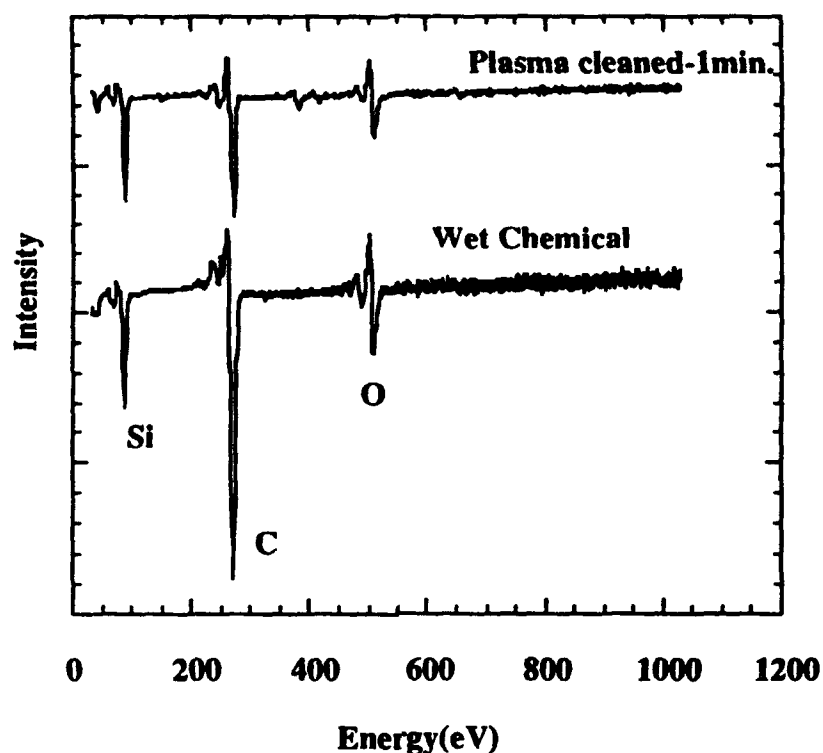


Figure 1. AES for SiC prepared with an *ex situ* chemical etch compared to a sample prepared with an *ex situ* etch plus an *in situ* H plasma clean. Spectra were normalized to the Si peak.

The XPS data also demonstrates the utility of the H-plasma cleaning. Figure 2 shows the Si 2s and 2p bands for the initial surface preparation and after H-plasma cleaning for a short and extended time. We note the Si lines are essentially unchanged in the process. The XPS spectra were also used to examine the C 1s transitions. The spectra are shown in Figure 3. The carbon 1s signal indicates two peaks present after the *ex situ* clean. After a short H-plasma exposure, the relative intensity of the higher energy feature is substantially reduced, and extended exposure results in complete removal of the feature. Recognizing that contamination due to hydrocarbon molecules at the surface is pervasive, we attribute this spectral change to hydrocarbon removal by the H-plasma.

The extended H-plasma exposure apparently also results in the removal of oxygen contamination. The results of the XPS measurements are summarized in Fig. 4. The spectra of the O 1s peak shows a doublet after the initial *ex situ* clean. After H-plasma exposure, one

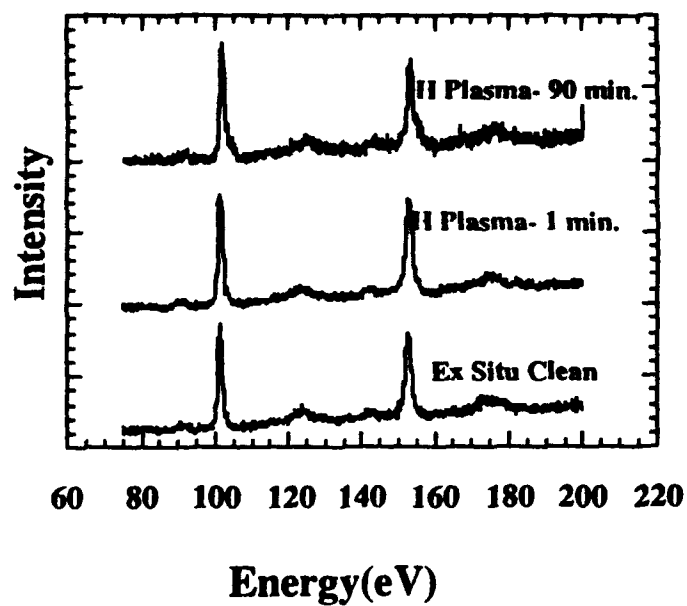


Figure 2. XPS data for the Si 2s and 2p peaks.

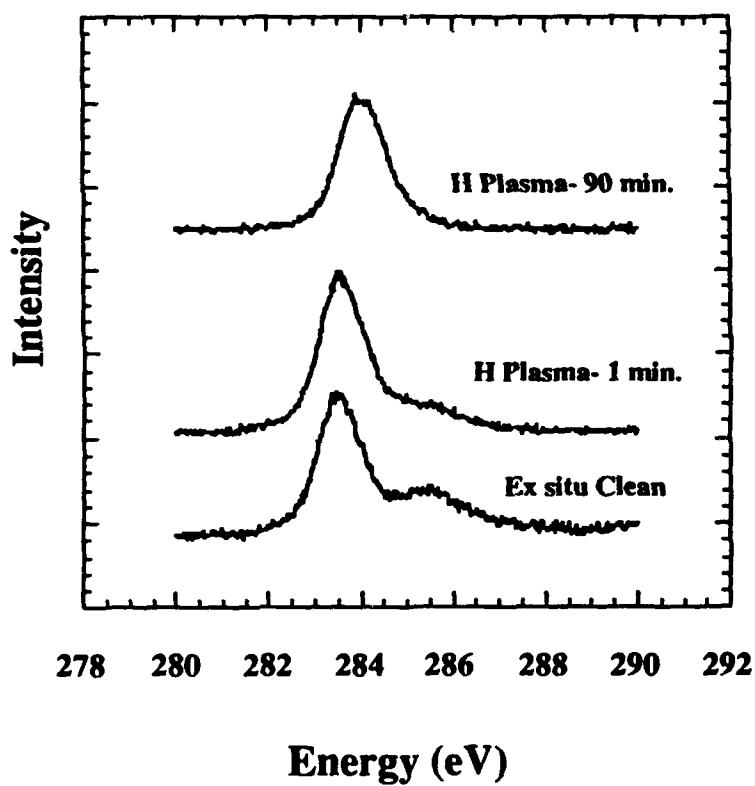


Figure 3. Carbon 1s peak.

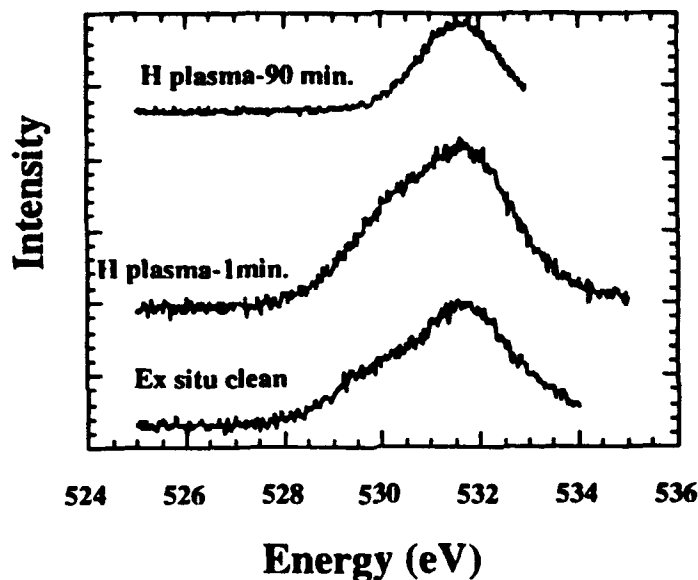


Figure 4. Oxygen 1s peak.

component of the doublet is substantially reduced. The origin of this doublet is not yet determined and will be the subject of future studies.

While annealing in UHV has previously been used to obtain clean surfaces, our previous UPS have shown that the processes tend to damage or disorder the surface. In contrast, the low temperature H-plasma cleaning procedure demonstrated here indicates that improved surface cleaning can be obtained with highly ordered surface structures.

#### D. Conclusions

Low temperature H-plasma processing for one minute has been shown to remove a significant amount of carbon and to remove 50% of the oxygen present on the SiC surface after HF etching. In light of these results, plasma cleaning appears as an attractive alternative to the standard annealing process of UHV annealing. It is projected that a five-minute plasma exposure will optimize the cleaning process. The 90-minute clean is considered too long to be practical. At present, we consider UHV annealing at elevated temperatures ( $\sim 700$  °C) to be undesirable, due to the formation of surface defects and damage.

#### E. Future Plans

The plasma chamber is being modified to use silane as a source gas. This will allow us to avoid preferential silicon evaporation at high temperature. The sample can then be heated, in a silane flow, to elevated temperature, giving off Si while Si is deposited and an equilibrium can be reached. With the results presented in this report, the interpolation is that a five-minute plasma exposure would optimize surface cleaning while keeping processing time short. UPS will be used to ensure that plasma processing has not damaged the surface. The *in situ* Raman

system mentioned in previous reports is operational and will be incorporated into the characterization of the SiC surface.

The Schottky barrier height (SBH) in diamond has been shown to depend significantly on surface preparation. The same trend can be expected to hold for SiC. Given this expectation, we will work further on surface preparation and cleaning. We will further investigate plasma cleaning of a bare SiC wafer and use the aforementioned silane treatment to try to arrive at a stoichiometric surface with defect and impurity concentrations of less than  $10^{12} \text{ cm}^{-2}$ . Preliminary XPS data have been taken and we will incorporate XPS into future studies.

The last report focused on determining the electron affinity of AlN grown on SiC. This work continues in collaboration with Scott Kern.

#### F. References

1. J. van der Weide, R. J. Nemanich, Appl. Phys. Lett. **62**, 1878 (1993).
2. M. C. Benjamin, R. J. Nemanich ONR Semiannual Technical Report, June 1993.

## **X. Controlled Growth of the 3C and 6H Polytypes of SiC by Gas-source Molecular Beam Epitaxy**

### **A. Introduction**

Silicon carbide (SiC) is a wide band gap material that exhibits polytypism, a one-dimensional polymorphism arising from the various possible stacking sequences of, e. g., the silicon and carbon layers along the directions of closest packing. There are approximately 250 SiC polytypes [1]. Included in these is one cubic polytype. This single cubic polytype,  $\beta$ -SiC, crystallizes in the zincblende structure, has a room temperature band gap of 2.3 eV, and is commonly referred to as 3C-SiC. (In the Ramsdell notation, the three (3) refers to the number of Si and C bilayers necessary to produce a unit cell and the C indicates its cubic symmetry.) The other rhombohedral and hexagonal polytypes are classed under the heading of  $\alpha$ -SiC. The most common of these latter polytypes is 6H-SiC with a room temperature band gap of  $\approx 3.0$  eV.

Since the 1950's, monocrystalline single crystals of 6H-SiC have been grown at using the Lely sublimation process [2]. However, nucleation was uncontrolled using this process and control of resultant polytypes was difficult. SiC single crystals inadvertently formed during the industrial Acheson process have also been used as substrates for SiC growth. However, neither these nor those formed using the Lely process are large enough for practical device applications. Recently, using a seeded sublimation-growth process, boules of single polytype 6H-SiC of  $>1$  inch diameter of much higher quality of that obtained using the Lely process have been grown. The use of single crystals of the 6H polytype cut from these boules has given a significant boost to SiC device development.

SiC epitaxial thin film growth on hexagonal SiC substrates has been reported since the 1960's. The use of nominally on-axis SiC substrates has usually resulted in growth of 3C-SiC films. Films of 3C-SiC(111) grown by CVD have been formed on 6H-SiC substrates less than  $1^\circ$  off (0001) [3]. Films of 3C-SiC on 6H-SiC substrates have typically had much lower defect densities than those grown on Si substrates. The major defects present in  $\beta$ -SiC/6H-SiC films have been double positioning boundaries (DPB) [4]. Despite the presence of DPBs, the resultant material was of sufficient quality to further device development of SiC. The use of off-axis 6H-SiC(0001) substrates has resulted in growth of high-quality monocrystalline 6H-SiC layers with very low defect densities [5].

In addition, the use of more advanced deposition techniques, such as molecular beam epitaxy (MBE), has been reported for SiC in order to reduce the growth temperature and from about 1400–1500 °C on 6H-SiC substrates. Si and C electron-beam sources have been used to epitaxially deposit SiC on 6H-SiC (0001) at temperatures of 1150 °C [6]. Previous reports by all investigators have documented 3C-SiC growth only on 6H-SiC(0001) by MBE.

Ion-beam deposition of epitaxial 3C-SiC on 6H-SiC has also been obtained at the temperature of 750 °C using mass-separated ion beams of  $^{30}\text{Si}^+$  and  $^{13}\text{C}^+$ .

Reflection high-energy electron diffraction (RHEED) at 10 kV and high-resolution transmission electron microscopy (HRTEM) were used for structure and microstructure analyses. Samples were prepared for HRTEM using standard techniques [7]. An Akashi EM 002B high-resolution transmission electron microscope was used at 200 kV for the HRTEM analysis.

### B. Experimental Procedure

Thin, epitaxial films of SiC were grown on the Si and C faces of 6H-SiC(0001) substrates supplied by Cree Research, Inc. These vicinal 6H-SiC(0001) wafers oriented  $3-4^\circ$  towards  $[11\bar{2}0]$  contained a 0.8  $\mu\text{m}$  epitaxial 6H-SiC layer deposited via CVD and a thermally oxidized 50 nm layer to aid in wafer cleaning. A novel *in situ* cleaning procedure has been developed using reaction and desorption of the silicon-containing precursor ( $\text{Si}_2\text{H}_6$ ). This new procedure involves cleaning with 10% HF and a 10-minute anneal at 1050 °C in UHV, as well as a disilane exposure and boil-off. This additional cleaning step, intended to remove any residual oxygen, fluorine other contaminant and create a silicon terminated surface, exposes the substrate to 0.1 sccm  $\text{Si}_2\text{H}_6$  for 2 minutes at 1050 °C until the surface undergoes a reconstruction from the  $1\times 1$  to  $3\times 3$  as observed by RHEED. This  $3\times 3$  reconstruction is indicative of a Si-rich surface. (For a description of the various surface reconstructions of SiC, please refer to Kaplan [9].) The  $3\times 3$  reconstructed samples were annealed at 1200 °C for 10 minutes causing them to revert to the  $1\times 1$  pattern.

All growth experiments were carried out in the gas-source molecular beam epitaxy system detailed in previous reports. The new heater assembly, designed for high temperature attainment and described in the previous report, has been installed and operates as expected allowing for substrate temperatures as high as 1400 °C. The sources of Si and C were  $\text{Si}_2\text{H}_6$  and  $\text{C}_2\text{H}_4$  (both 99.99% pure), respectively. Flow ratios of  $\text{Si}_2\text{H}_6$  and  $\text{C}_2\text{H}_4$  were varied from 1:2 to 1:1. Typical base pressures of  $10^{-9}$  Torr were used.

### C. Results and Discussion

All prior growth conditions have resulted, to this point, in monocrystalline, epitaxial layers of 3C-SiC with rough surfaces and the appearance of three-dimensional growth originating at the terraces of the vicinal substrates. The resulting films are generally cubic and have double positioning boundaries as evidenced by the RHEED and HRTEM. These results have been detailed in previous reports.

Single crystal layers of both 3C- and 6H-SiC have been grown on  $\alpha$ (6H)-SiC(0001) by MBE (Fig. 1 shows a 6H- on 6H-SiC film. For a 3C- on 6H-SiC, please refer to previous



reports.) using a slightly modified procedure. Part of the new procedure involves the new cleaning procedure described in the previous section. Figures 2a and 2b show the  $1\times 1$  to  $3\times 3$  reconstructions, respectively.



Figure 1. HRTEM micrograph showing a homoepitaxial film containing a mixture of 3C- and 6H-SiC on  $\alpha(6H)$ -SiC(0001).

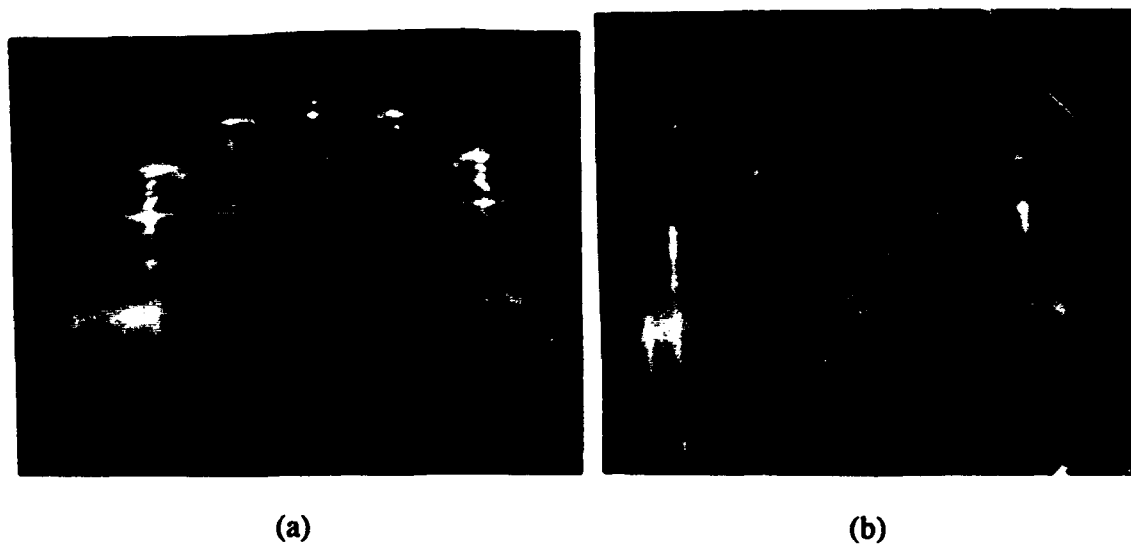


Figure 2. RHEED photographs showing the reconstructions of the  $\alpha(6H)$ -SiC(0001) surface (a) before exposure to disilane and after boil-off at  $1200^\circ\text{C}$  and (b) after exposure.

Since all previous growth of SiC was done with 2-to-1 or higher  $\text{C}_2\text{H}_4$ -to- $\text{Si}_2\text{H}_6$  flow ratios and resulted in 3C-SiC films, the flow ratio was moved to 1-to-1 and the resulting films

are 6H. The film shown in Fig. 1 was grown at 1050 °C using the previously described pretreatment and flows of 0.1 sccm C<sub>2</sub>H<sub>4</sub> and 0.1 sccm Si<sub>2</sub>H<sub>6</sub> for 4 hours. This film has some regions of 3C-SiC, but the reason of formation is not yet known; however, other films grown under similar circumstances show no phase mixtures.

#### D. Conclusions

Preliminary studies into the surface science and growth conditions have been performed. The initial results indicate that the single most important factor in SiC polytype control (3C versus 6H) is the ratio of the precursor gases. Flow ratios of 1:1 lead to 6H-SiC films while carbon-rich ratios give 3C-SiC films. Another ongoing study involves the surface reconstruction phenomenon and its relation to film growth.

#### E. Future Research Plans/Goals

A new gas delivery system intended to allow for very low flow rates of an NH<sub>3</sub>/Ar gas mixture is being installed so that an n-type dopant can be used easily. A study on both n- and p-type (with solid Al from a standard MBE effusion cell) is also underway. Further study of the effects of temperature, flow ratios and the role of surface reconstructions is also ongoing.

#### F. References

1. G. R. Fisher and P. Barnes, *Philos. Mag. B* **61**, 217 (1990).
2. J. A. Lely, *Ber. Deut. Keram. Ges.* **32**, 229 (1955).
3. H. S. Kong, J. T. Glass, and R. F. Davis, *Appl. Phys. Lett.* **49**, 1074 (1986).
4. H. S. Kong, B. L. Jiang, J. T. Glass, G. A. Rozgonyi, and K. L. More, *J. Appl. Phys.* **63**, 2645 (1988).
5. H. S. Kong, J. T. Glass, and R. F. Davis, *J. Appl. Phys.* **64**, 2672 (1988).
6. S. Kaneda, Y. Sakamoto, T. Mihara, and T. Tanaka, *J. Cryst. Growth* **81**, 536 (1987).
7. S. P. Withrow, K. L. More, R. A. Zuhr, and T. E. Haynes, *Vacuum* **39**, 1065 (1990).
8. J. C. Bravman and R. Sinclair, *J. Electron Microsc. Tech.* **1**, 53 (1987).
9. R. Kaplan, *Surface Sci.* **215**, 111 (1989).

## XI. Growth Mechanisms of SiC Film on 6H-SiC (0001) by Gas-source Molecular Beam Epitaxy

### A. Introduction

The growth mechanisms for the SiC film on 6H-SiC by chemical vapor deposition (CVD) is well-established [1, 2]. The 6H polytype of SiC has been obtained on off-axis 6H-SiC substrate under certain conditions. Step flow mechanisms were proposed to explain the homoepitaxial growth of 6H-SiC [1, 2]. According to the model, the stacking sequence of 6H, ABCACB..., can be retained due to the lateral growth which is initiated at the step site on the off-axis substrate. The use of on-axis substrate, therefore, causes the cubic (3C) SiC formation.

Molecular beam epitaxy has been used for the deposition of SiC thin films in order to reduce the growth temperature from that used in CVD (1450–1600°C) on 6H-SiC substrates [3, 4]. Although there has been many successful growth of SiC films in our group [5], the growth mechanisms are unknown. It is significantly important to study growth mechanisms in order to obtain very thin, smooth and defect free films, and to form other polytypes such as 2H- and 4H-SiC.

In this study an attempt has been made to clarify the growth mechanisms through the observation of the initial stage of growth by HRTEM and *in situ* RHEED oscillation.

### B. Experimental Procedure

SiC films were typically grown on Si-faces of 6H-SiC (0001) substrates. The substrates used in this study were either on-axis or off-axis (3–4° off from (0001) toward  $\langle 11\bar{2}0 \rangle$ ) provided by Cree Research, Inc. Films were all grown by GSMBE method under several conditions. The typical growth conditions are listed in Table I. The details of the deposition process can be seen in the accompanying report. During the growth of films, a RHEED pattern was monitored by the use of CCD camera and video recorder.

---

Table I. Typical Growth Conditions for the SiC films

---

Temperature	1050 °C
Si <sub>2</sub> H <sub>6</sub> flow rate	0.1, 0.3 sccm
C <sub>2</sub> H <sub>4</sub> flow rate	0.1–0.3 sccm
Si <sub>2</sub> H <sub>6</sub> /C <sub>2</sub> H <sub>4</sub> flow ratio	1.0, 0.5
Growth rate	50–100 Å/hr

---

After growing the film, the sample was cut and glued face to face to make a cross-sectional TEM sample, followed by the thinning processes of grinding, dimpling and ion milling. Finally the sample was examined by a Topcon EM-002B operated at 200kV acceleration voltage.

### C. Results

Figure 1 shows the cross-sectional image of the SiC film on off-axis (vicinal) 6H-SiC (0001) substrate. The substrate was oriented  $3-4^\circ$  off-axis towards  $\langle 11\bar{2}0 \rangle$  as indicated by the arrow in the figure. Thus, there are periodical steps on the surface. The resulting film was generally cubic (3C) in structure and had a rough surface morphology due to three dimensional growth under the condition of a  $\text{Si}_2\text{H}_6/\text{C}_2\text{H}_4$  ratio of 0.5. The magnified image of the island region can be seen in Fig. 2. The two islands (3C) which nucleated on the different terrace sites and are separated by a step can be clearly seen.

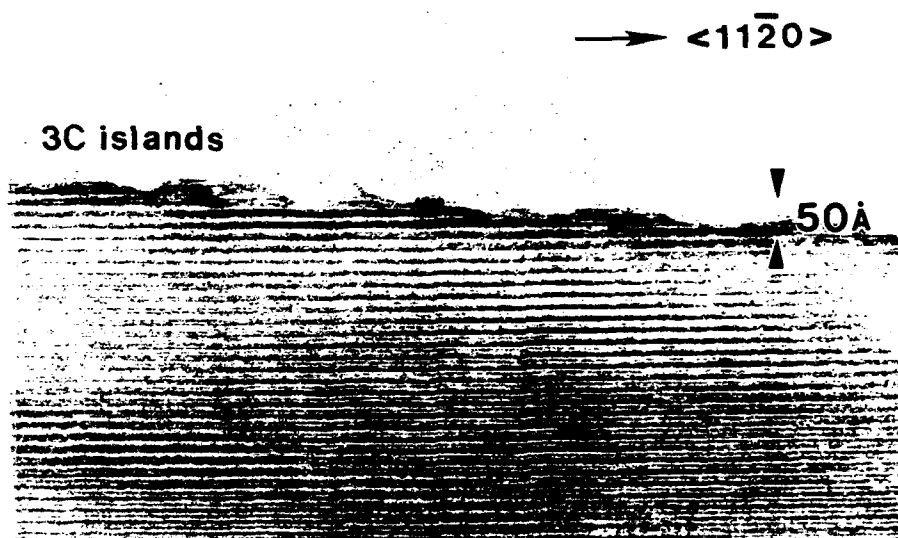


Figure 1. Cross sectional TEM image of 3C SiC islands on a 6H-SiC substrate off-axis towards  $\langle 11\bar{2}0 \rangle$ .

The effects of vicinal orientation on film morphology were examined with the use of a substrate which was tilted  $3-4^\circ$  off (0001) towards  $\langle 10\bar{1}0 \rangle$ . Figure 3 shows the result of growth under the same conditions as above on this substrate. A smoother surface can be observed compared with the material grown on the  $\langle 11\bar{2}0 \rangle$  substrate, suggesting that steps play a role in affecting film growth. The exact mechanism is unknown but the differences in step geometry and chemistry appear to affect the film growth. The  $\langle 11\bar{2}0 \rangle$  and  $\langle 10\bar{1}0 \rangle$

substrates have a zig-zag and a straight geometry of steps, respectively. Accordingly, each substrate may have a different bonding configuration at the steps. It should be addressed that investigating growth mechanisms in conjunction with substrate orientations will be done in the future.

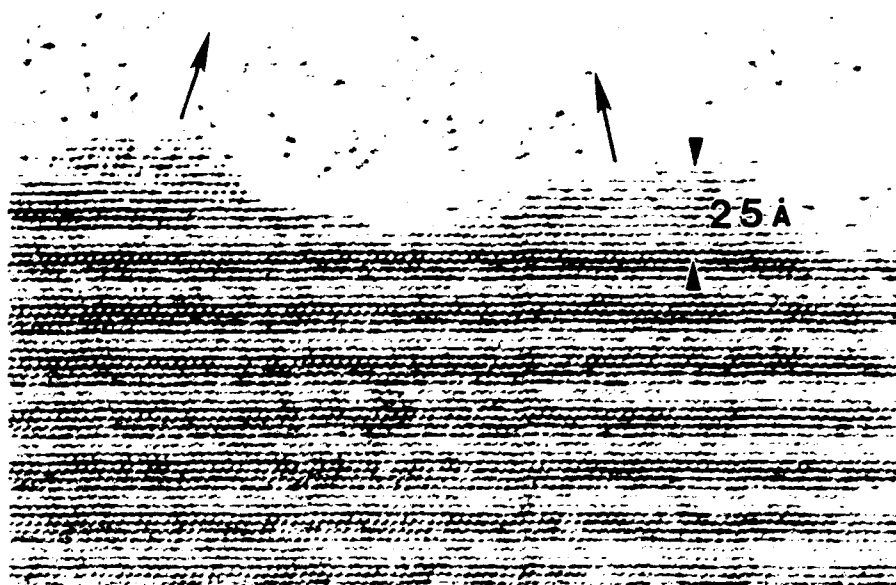


Figure 2. HRTEM image of 3C SiC islands on a 6H-SiC substrate off-axis towards  $\langle 11\bar{2}0 \rangle$ .

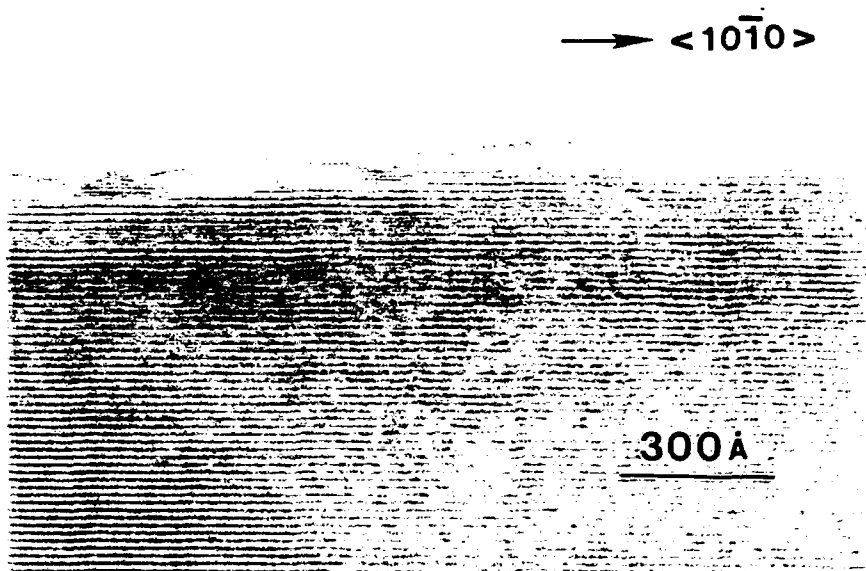


Figure 3. Cross sectional TEM image of 3C SiC on a 6H-SiC substrate off-axis towards  $\langle 10\bar{1}0 \rangle$ .

Under the different conditions in which the  $\text{Si}_2\text{H}_6/\text{C}_2\text{H}_4$  ratio was 1.0 and the total flow rate was 6.0 sccm, a drastic change in film growth was observed. Figure 4 shows 6H-SiC film growth with a fairly smooth surface (almost identical to the substrate). It could be inferred the film thickness is  $\sim 120\text{\AA}$  based on the previous study for the growth rates. However, it should be necessary to obtain the presence of a film by other techniques.

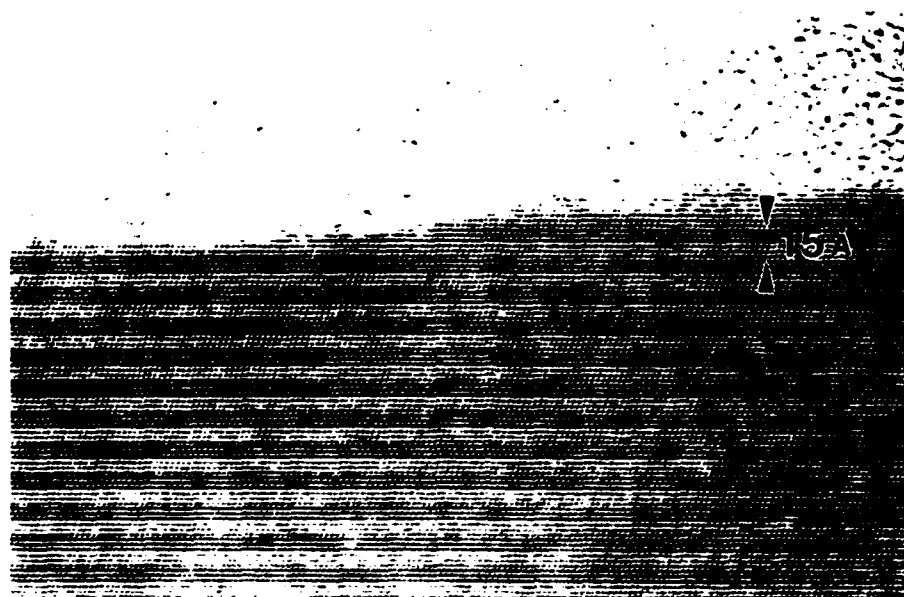


Figure 4. HRTEM image of 6H-SiC film on an off-axis 6H-SiC substrate.

#### D. Discussion

The drastic change in growth mode from three dimensional growth to two dimensional growth has been observed with the variation of the  $\text{Si}_2\text{H}_6$  to  $\text{C}_2\text{H}_4$  gas flow ratio from 0.5 to 1.0. The resulting film microstructures were also changed from 3C to 6H accordingly. The step flow type of growth might be enhanced. The possible scenario is that the surface migration distance of adatoms (or precursors) may be increased because of the change in surface chemistry as the film grows. It could be attributed to the Si terminated surface. At present the exact growth mechanisms under different growth parameters are continuing to be investigated through a combination of using a RHEED oscillation technique and HRTEM.

#### E. Conclusion

The growth mechanisms of SiC films under several growth conditions have been discussed. The vicinal orientation of the substrate may play some role in the growth mode due to geometrical and chemistry related effects of the steps. Interestingly, the growth modes and polytype of films can be altered with the variations of feed gas ratio such as  $\text{Si}_2\text{H}_6/\text{C}_2\text{H}_4$ .

Pure homoepitaxial growth of 6H-SiC was observed for the first time. The step flow type of mechanisms are considered to be plausible for explaining the results. However, the proof of the presence of the films and further studies should be made to elucidate the growth mechanisms.

#### F. Future Research Plans

Several more depositions will be conducted under the different growth conditions. Gas flow rates and ratios will be especially to be focused on. The proof of the film existence should also be made with various techniques. *In-situ* RHEED study will continue to be used in studying the growth mechanisms. Since the importance of initial surface chemistry and structure is obvious, an attempt to better understand the nature of the substrate surfaces will be performed through XPS, TPD (temperature programmed desorption) and LEED methods. Finally, the control of polytype formation (2H and 4H) will be challenged on the basis of the theory obtained in this study.

#### G. References

1. H. S. Kong, J. T. Glass, and R. F. Davis, *J. Appl. Phys.* **64** (5), 2672 (1988).
2. T. Ueda, H. Nishino, and H. Matsunami, *J. Cryst. Growth* **104**, 695 (1990).
3. S. Nishino, H. Matsunami, and T. Tanaka, *J. Cryst. Growth* **45**, 144 (1978).
4. H. S. Kong, B. L. Jiang, J. T. Glass, G. A. Rozgonyi, and K. L. More, *J. Appl. Phys.* **63**, 2645 (1988).
5. L. B. Rowland, R. S. Kern, S. Tanaka, and R. F. Davis, *J. Mater. Res.* **8**, 2753 (1993).

## **XII. Chemistry, Microstructure, and Electrical Properties at Interfaces Between Thin films of Titanium and $\alpha(6H)$ Silicon Carbide (0001)\***

**L. M. Porter and R. F. Davis**

*Department of Materials Science and Engineering, North Carolina State University, Raleigh,  
NC 27695-7907*

**J. S. Bow, M. J. Kim, and R. W. Carpenter**

*Center for Solid State Science, Arizona State University, Tempe, AZ 85287-1704*

**R. C. Glass**

*Westinghouse Science and Technology Center, Westinghouse Corporation, Pittsburgh, PA*

### **Abstract**

Thin films ( $4 - 1000\text{\AA}$ ) of Ti contacts deposited via UHV electron beam evaporation at room temperature on monocrystalline, n-type,  $\alpha(6H)$ -SiC (0001) were epitaxial. Current-voltage (I-V) measurements showed that the Ti contacts were rectifying with low ideality factors ( $n < 1.09$ ) and typical leakage currents of  $5 \times 10^{-7} \text{ A/cm}^2$  at  $-10 \text{ V}$ . The Schottky barrier heights (SBH's) calculated from x-ray photoelectron spectroscopy and I-V and C-V measurements were between 0.79 and 0.88 eV.

The interfacial chemistry and microstructure, electrical properties, and SBH's were investigated after annealing at  $700^\circ\text{C}$  up to 60 min. High resolution TEM analyses indicated that the reaction zones consisted of  $\text{Ti}_5\text{Si}_3$  and  $\text{TiC}$ . The corresponding electrical properties exhibited considerable stability except after an initial 20 min. anneal.

---

\*Paper submitted to Journal Materials Research



## A. Introduction

The extreme thermal, mechanical, and electronic properties of SiC has allowed its use for both structural applications and high-power, -temperature, -speed, and -frequency electronic and optoelectronic devices. The chemistry at annealed Ti/SiC interfaces has been investigated for structural applications by many groups, as discussed below. However, no integrated study has been found which has examined the Ti/SiC interface in terms of the chemistry, microstructure, and electrical properties for the purpose of contacts in semiconductor devices.

The increased use of (6H)-SiC for many types of semiconductor devices is challenged by the difficulty of controlling the properties of the metal contact/SiC interface, including uniformity and thickness of the interfacial region, stability at high temperatures ( $\sim 600^\circ\text{C}$ ), and most importantly, the Schottky barrier height (SBH), or the energy barrier for electrons traversing the interface. It is important to understand the chemistry and microstructure at the interface between the metal contact and the SiC substrate before and after annealing at temperatures at or above which devices may be operated so that the resulting phases may be correlated with the electrical properties.

In this study, analytical techniques have been employed to investigate the interfacial chemistry and microstructure on both an atomic scale and a microscopic ( $<1\ \mu\text{m}$ ) scale between Ti and n-type 6H-SiC (0001) before and after annealing at  $700^\circ\text{C}$ . In addition, the chemically-cleaned SiC surface was characterized in terms of chemistry, structure, and amount of band bending. The results of these studies have been correlated with the electrical properties and SBH's of the Ti contacts.

## B. Experimental Procedure

*SiC Material & Preparation.* Vicinal, single crystal, nitrogen-doped, n-type ( $\approx 10^{18}\ \text{cm}^{-3}$ ) wafers of 1" diameter 6H-SiC (0001) containing  $0.5\text{--}1.5\ \mu\text{m}$  thick, n-type ( $\approx 10^{16}\text{--}10^{17}\ \text{cm}^{-3}$ ) homoepitaxial films thermally oxidized to a thickness of  $500\text{--}1000\ \text{\AA}$  in dry oxygen at  $1300^\circ\text{C}$  were provided by Cree Research, Inc. The epitaxial layers were unintentionally-doped. The Si-terminated (0001) surface, tilted  $3^\circ\text{--}4^\circ$  towards  $[1\bar{2}0]$  was used for all depositions and analyses.

The substrates were simultaneously cleaned and the oxide layer etched from the surface using a 10 min. dip in either an ethanol / hydrofluoric acid / water (10:1:1) or 10% hydrofluoric acid solution. This was followed by a quick rinse in deionized water. The substrates were loaded immediately into a vacuum system transfer tube (base pressure  $\approx 10^{-9}$  Torr), thermally desorbed at  $700^\circ\text{C}$  for 15 min. to remove any residual hydrocarbon contamination, and transferred to the metal deposition chamber.

*Metal Deposition.* A UHV electron beam evaporation system was used to deposit various metal films having thicknesses ranging from  $4\text{--}1000\ \text{\AA}$  onto the substrates described above.

A substrate manipulator allowed for both heating and rotation and contained a manual shutter directly below the position of an inverted Mo substrate block located in the upper part of the chamber. The contact metals were evaporated using a dual source 270°, 10 cc electron beam evaporator made by Thermionics Corporation. A 330 l/s turbomolecular pump was used for roughing the system and during processing. A 500 l/s diode ion pump and a titanium sublimation pump were employed to achieve and maintain UHV base pressures of  $<2 \times 10^{-10}$  Torr.

Prior to deposition, approximately 25–50 Å was typically evaporated from the source to liberate any foreign material which may have collected on its surface. Each substrate was covered by the shutter during this operation. To commence the deposition, the emission current was increased very slowly until a deposition rate of 10–12 Å/min was stabilized according to the XTC thickness monitor, and the shutter subsequently removed from in front of the sample. The pressure during the depositions was between  $5 \times 10^{-9}$  and  $5 \times 10^{-8}$  Torr. The Ti acted as a pump during evaporations such that the pressure dropped slowly. After  $\sim 100$  Å was deposited, the rate was typically increased to  $\sim 20$  Å/min. Throughout each deposition the substrates were rotated to ensure uniform thickness across the sample. The substrates were not intentionally heated.

*Analysis Techniques.* Patterned contact structures consisting of 500  $\mu\text{m}$  (0.02") and 750  $\mu\text{m}$  (0.03") diameter circular contacts of 100 nm thickness were created by depositing the metal through a Mo mask in contact with the SiC epitaxial layer for electrical characterization. Silver paste served as the large area back contact. All subsequent annealing was conducted in UHV. Current-voltage (I-V) measurements were taken with a Rucker & Kolls Model 260 probe station in tandem with an HP 4145A Semiconductor Parameter Analyzer. Capacitance-voltage (C-V) measurements were taken with a Keithley 590 CV Analyzer using a measurement frequency of 1 MHz.

Titanium/SiC samples were prepared in cross-section for analysis by transmission electron microscopy (TEM). High resolution (HR) images were obtained with an ISI EM 002B operating at 200 kV with an interpretable resolution limit of 0.18 nm. These images were typically recorded at an electron-optical magnification of 490,000 to 590,000. Some of the HRTEM micrographs were digitized using a 512 $\times$ 512 camera and the resulting images analyzed by using the SEMPER program [1]. Lattice spacings (d-spacings) and interplanar angles were measured from optical digital diffraction patterns and used to identify the reaction product phases. The values of the lattice spacings were calculated using the (0006) d-spacing in 6H-SiC measured near the phase to be identified as a baseline. Thus, the change in d-spacing due to different focusing conditions was negligible. A data base of d-spacings for each possible reaction product phase was compared to the experimentally-determined d-spacings. The d-spacings from the data base which were within 2% of the measured values were compared with interplanar angles for the identification of phases. Most of the measured

values were within 1% of the theoretical values. Unknown phases were identified uniquely by these procedures.

Analytical electron microscopy was performed using a Gatan 666 parallel electron energy loss spectrometer (PEELS) with spatial resolution of approximately 3 nm attached to a Philips 400 FEG operating at 100 kV. Energy dispersive spectrometry (EDS) was performed using a JEOL 2000 FX operating at 200 kV with a probe size of approximately 40 nm. For fixed position PEELS and EDS, the probe position was adjusted in the diffraction mode by monitoring the shadow image in the Bragg disk of the transmitted beam. The image was created by defocusing the second condenser lens. A liquid nitrogen cooled double-tilted holder was used for all analytical experiments to minimize specimen contamination and local specimen heating.

Surface chemistry was studied using a Riber x-ray photoelectron spectroscopy (XPS) system. This system consists of a Mac2 semi-dispersive electron energy analyzer and is accessible by UHV transfer from the deposition chamber. Using Mg K $\alpha$  (1253.6 eV) x-rays, the x-ray source was operated at 14 kV with an emission-controlled current of 15 mA. This technique also allowed the calculation of the Schottky barrier height for thin films of Ti on SiC.

Analyzing samples usually consisted of three different types of spectra. Survey scans, which were important for fingerprinting elements present at the surface, contained 2000 data points from 0 to 1000 eV and were obtained 2.0 eV resolution and a counting rate of 100 ms. Scans of individual photoelectron peaks at higher resolution (0.8 eV) contained 500–750 data points and a 20–30 eV binding energy range. Valence spectra contained 500 data points from 0 to 20 eV and contained 500 data points at a resolution of 0.8 eV.

### C. Results and Discussion

*Surface Chemistry.* Comparison of the XPS C 1s and Si 2p peak areas divided by their atomic sensitivity factors revealed that chemically-cleaned, *non*-thermally oxidized SiC substrates contained C-rich surfaces. Thermal oxidation and subsequent etching solved this problem. This indicates that the excess C was present only at the surface and occurred during the cessation of the growth process. As such, all as-received SiC substrates used in this research contained a thermally-grown oxide.

X-ray photoelectron spectroscopy was also used to monitor the surface chemistry after cleaning. Figure 1 shows survey spectra after three different cleaning procedures. All cleaning procedures consisted of etching the oxide in a hydrofluoric acid solution followed by either a chemical or thermal process to remove hydrocarbon contamination. The top spectrum represents a sample which was etched for 10 min. in a 10% HF aqueous solution, quickly rinsed in deionized water, and heated to 700°C for 15 min.

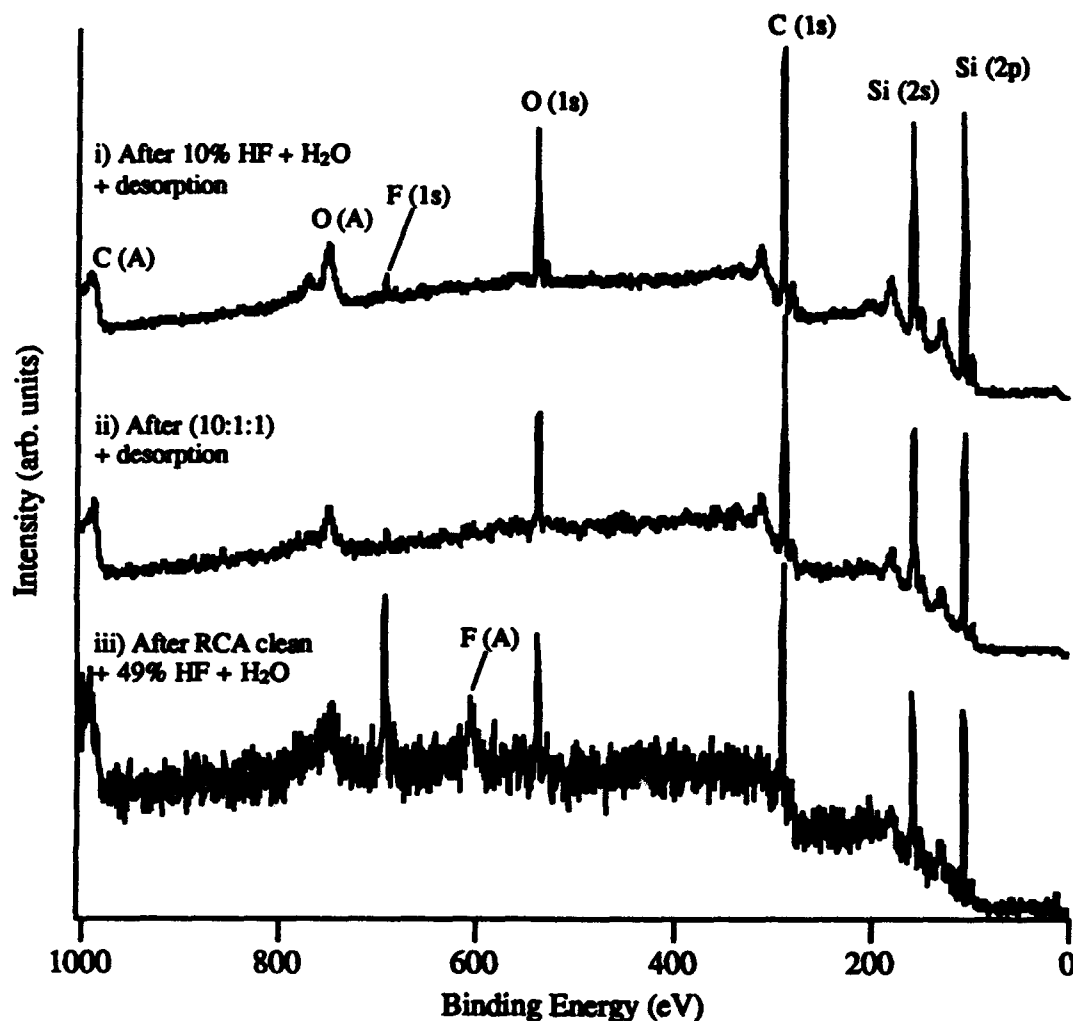


Figure 1. XPS survey spectra of the (0001) SiC surface after i) 10 min. in 10% HF and a quick deionized water rinse followed by a 15 min. UHV desorption at 700°C, ii) 10 min. in a (10:1:1) solution of ethanol / HF / deionized water followed by a 15 min. UHV desorption at 700°C, and iii) a modified RCA clean followed by 10 min. in 49% HF and 5 min. rinse in deionized water.

The spectrum shows that residual oxygen and, to a lesser extent, fluorine remained on the surface. The peaks marked with '(A)' are Auger peaks. A comparison of the relative concentrations of the elemental constituents requires incorporating both the peak area and the peak area sensitivity, or atomic sensitivity factor. The relative concentrations of the elements comprising the photoelectron signal can be estimated from the following expression [2]:

$$C_x = \frac{I_x / S_x}{\sum_i I_i / S_i}, \quad (1)$$

where  $I$  is the integrated peak area and  $S$  is the atomic sensitivity factor. However, this

expression does not take into account the fact that top portion of a film contributes to more of the signal than the portion underneath. The concentrations are relative to the total signal and not to an actual volume at the surface. The atomic sensitivity factors are 0.205 for C 1s, 0.63 for O 1s, 1.00 for F 1s, and 0.17 for Si 2p [2]. Using Eq. 1, the relative concentrations calculated from these sensitivity factors with their respective peak areas were ( $\pm 1\%$ ) 49.7% Si, 40.0% C, 9.3% O, and 0.9% F. It is believed that the higher concentration of Si as compared to C is representative of a Si-terminated surface. Waldrop et al. [3] calculated the amount of O on the same type of substrates to be  $\approx 3/4$  monolayer in addition to a trace amount of F ( $F/O < 0.05$ ).

The middle spectrum represents a sample which was prepared by the same procedure noted above except a (10:1:1) ethanol / hydrofluoric acid / deionized water solution was used in place of the 10% HF solution. Descriptions of using this solution for cleaning Si can be found in Ref. 4. The survey spectrum does not show any significant change in the amounts of O and F. The relative concentrations in this case were 45.8% Si, 44.8% C, 8.9% O, and 0.5% F. The C concentration is higher than in the case above because the sample was not thermally oxidized before surface treatment.

Results from a third cleaning procedure are shown in the bottom spectrum. This sample was first RCA cleaned, the sequence of which consisted of a 5 min. dip in a (1:1:5) solution of  $NH_4OH / H_2O_2 / H_2O$  (70°C), a 5 min. rinse in deionized water, a 5 min. dip in a (1:1:5) solution of  $HCl / H_2O_2 / H_2O$  (70°C), and a 5 min. rinse in deionized water. The sample was then etched in a 49% HF aqueous solution for 10 min. and rinsed in deionized water for 5 min. The survey shows that the higher concentrated HF solution resulted in a substantial increase in the amount of F left on the surface. The relative concentrations were 41.2% Si, 42.9% C, 8.5% O, and 7.3% F. It should also be mentioned that although this cleaning procedure did not consist of a thermal desorption, no significant changes in the amounts of O and F were found before and after the thermal desorptions for the preceding two procedures. Because of these results, the solutions containing lower HF concentrations were used for samples prior to metal deposition.

Figure 2 shows XPS Si 2p and C 1s spectra of a SiC surface that has been treated in 10% HF. Spectra of the surface before and after desorption at 700°C are compared. The Si 2p peaks before and after desorption appear to be virtually identical. Deconvolution of these peaks revealed both the main Si (bound to C) peak at 101.58 eV and a small peak at 102.98 eV, which is attributed to  $SiO_x$  [5]. The C peak does show significant change after desorption. The main peak at 283.78 eV is due to C bound to Si in SiC [6]. Before desorption a significant peak exists on the high binding energy side of the main peak and is attributed to adventitious carbon, which has a binding energy of 285.0 eV [7].

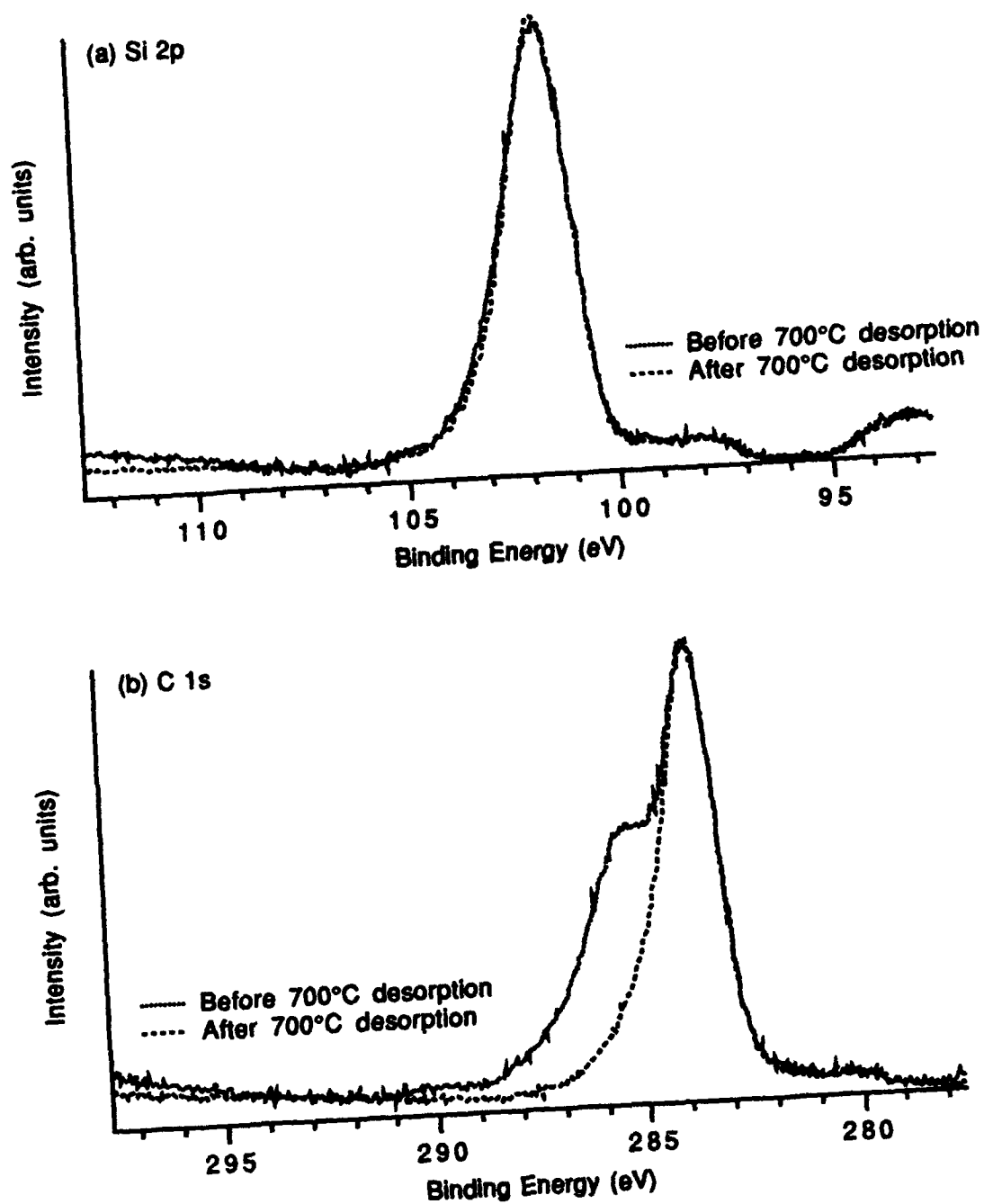


Figure 2. XPS spectra of 6H-SiC (0001) after 10 min. in 10% HF followed by a deionized water rinse. The (a) Si 2p and (b) C 1s peaks before and after a 700°C desorption are shown.

*Surface Structure.* The surface structure was monitored by low energy electron diffraction (LEED). For all samples examined treated by the various cleaning procedures noted above, a  $1 \times 1$  unreconstructed surface was displayed. This result is in agreement with that of Waldrop *et al.* [3] where  $3/4$  monolayer O and trace F was left on the Si-terminated surface of 6H-SiC.

As suggested by Kaplan [8], a  $1\times 1$  surface probably corresponds to a range of structures which do not have long range order. The  $1\times 1$  patterns in this case are most likely due to adsorbed O and F.

*Titanium/Silicon Carbide Interfaces. Electrical Properties.* Current-voltage measurements of Ti contacts deposited at room temperature on n-type SiC (0001) were rectifying with low ideality factors ( $n < 1.09$ ) and with typical leakage currents of  $5 \times 10^{-7}$  A/cm<sup>2</sup> at -10 V. Figure 3 shows a representative I-V characteristic of an as-deposited,  $2.0 \times 10^{-3}$  cm<sup>2</sup> Ti contact. The reverse bias characteristics of the same contact did not show hard breakdown to 100V, which is the voltage limit of the equipment. Instead, the leakage steadily increased to  $\approx 35$   $\mu$ A. This 'soft breakdown' is expected from high fields at the contact edges due to the geometry of the contact structure. It is not believed that inhomogeneities in the interface structure are the cause of the increasing leakage [9] because of the nature of this interface, which is described in the following section.

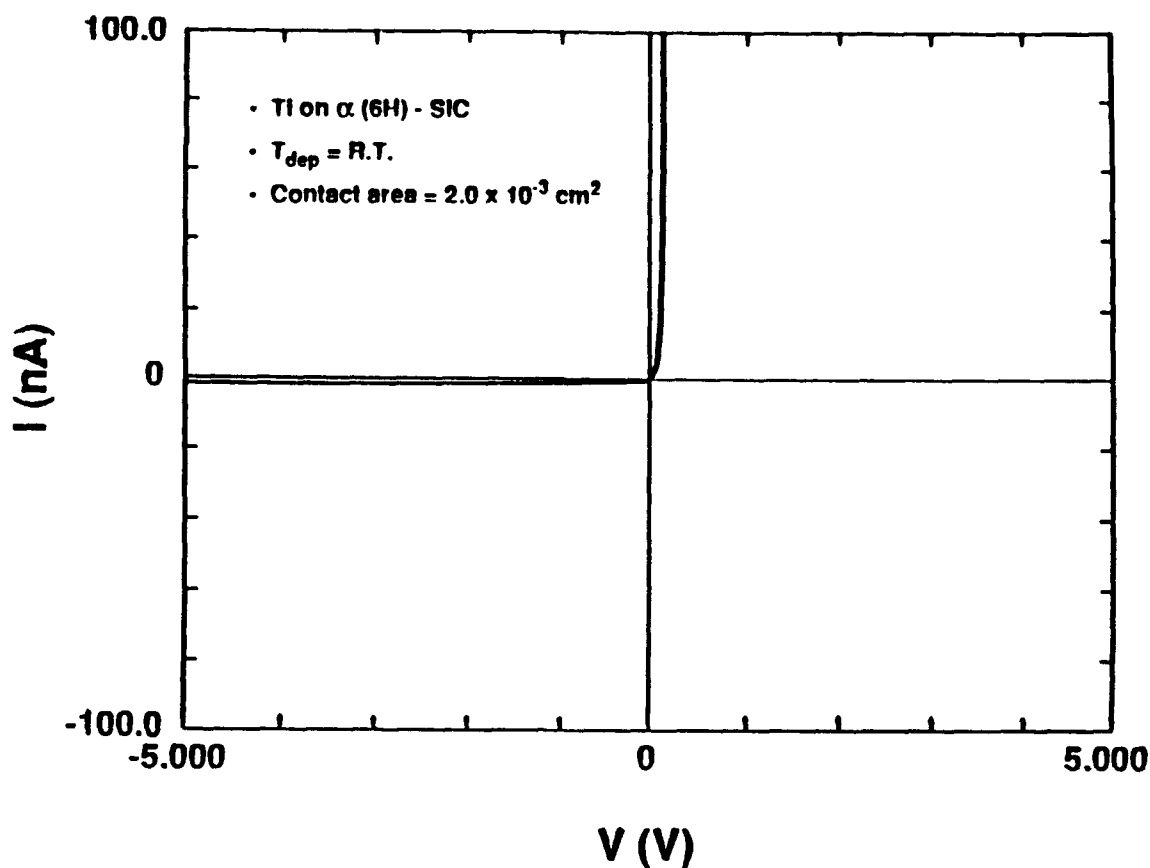


Figure 3. Current-voltage characteristics of Ti deposited on 6H-SiC at room temperature. (contact area =  $2.0 \times 10^{-3}$  cm<sup>2</sup>).

For values of applied voltage,  $V$ , greater than  $3kT/q$ , the current density can be expressed as

$$J = J_s \exp\left(\frac{qV}{nkT}\right), \quad (2)$$

where  $J_s$  is the extrapolated current density at zero voltage or saturation current density, and  $n$  is the ideality factor. Therefore, the ideality factor can be calculated from the linear region of a semi-logarithmic plot of current vs. voltage, as displayed in Fig. 4. The linear region in this case extends over approximately four decades of current. The reduced slope at higher voltages is due to the resistance of the substrate material. The low ideality factors were taken as evidence that thermionic emission theory may be applied for calculating the SBH.

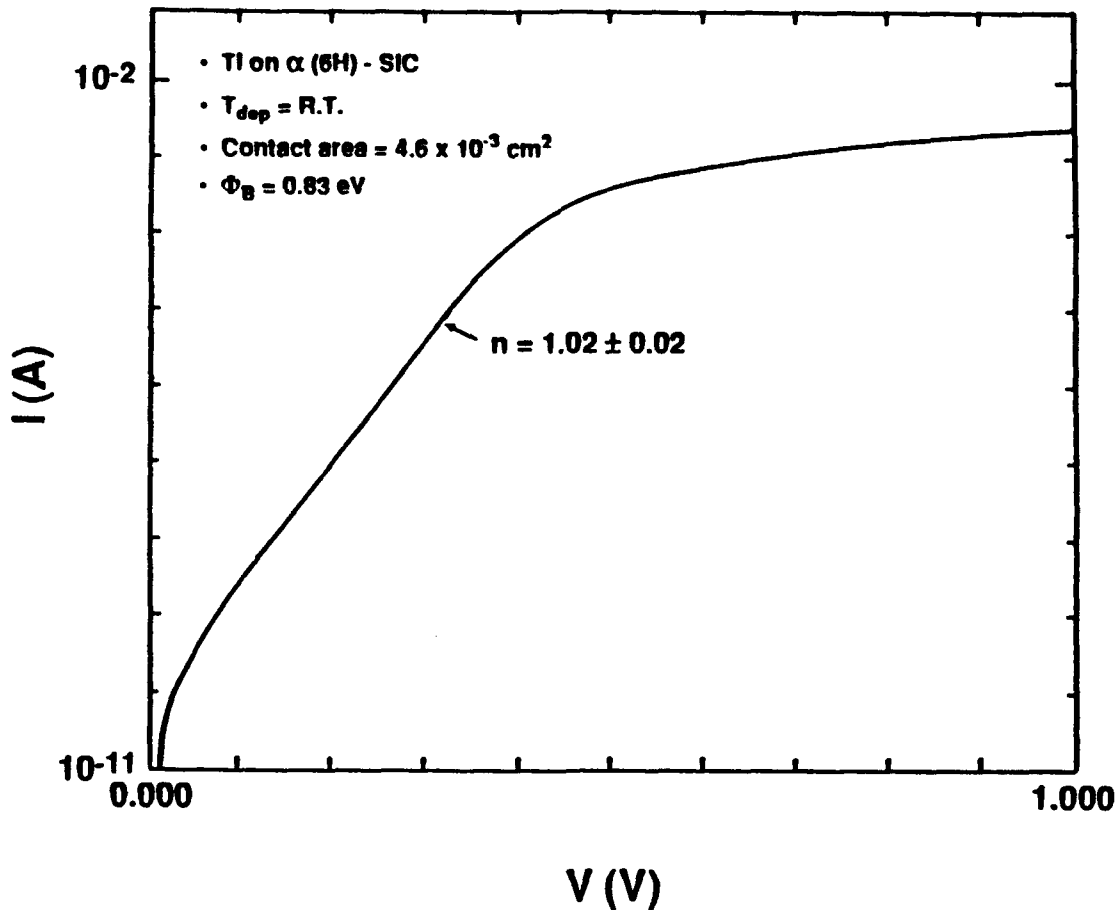


Figure 4. Semi-logarithmic I-V plot of Ti deposited on 6H-SiC. (contact area =  $4.6 \times 10^{-3} \text{ cm}^2$ )



Following Eq. 2 the SBH can then be determined from the equation

$$\Phi_B = \frac{kT}{q} \ln \left( \frac{A^* T^2}{J_s} \right), \quad (3)$$

where  $A^*$  is the effective Richardson constant. The value of  $A^*$  for 6H-SiC is  $194.4 \text{ A/cm}^2/\text{K}^2$  [10]. The accuracy of  $A^*$  is not usually critical, since, at room temperature, doubling its value only increases  $\Phi_B$  by 0.018 eV [11]. Using this equation with  $J_s = 2.0 \times 10^{-7} \text{ A/cm}^2$ , a SBH of 0.83 eV was calculated for unannealed Ti contacts.

The barrier heights were also determined from C-V measurements. Plotting  $1/C^2$  vs.  $V$  allows the barrier height to be determined from the equation

$$\Phi_B = V_i + \xi + \frac{kT}{q} - \Delta\Phi, \quad (4)$$

where  $V_i$  is the voltage intercept;  $\xi$ , is the difference between the conduction band and the Fermi level in the bulk of the material and is a function of the carrier concentration; and  $\Delta\Phi$  is the image force lowering. Figure 5 shows  $1/C^2$  vs.  $V$  of an as-deposited Ti/SiC contact biased from 0 to -5 V. Extrapolating the linear region gives an intercept of 0.67 V, indicating a SBH of 0.88 V.

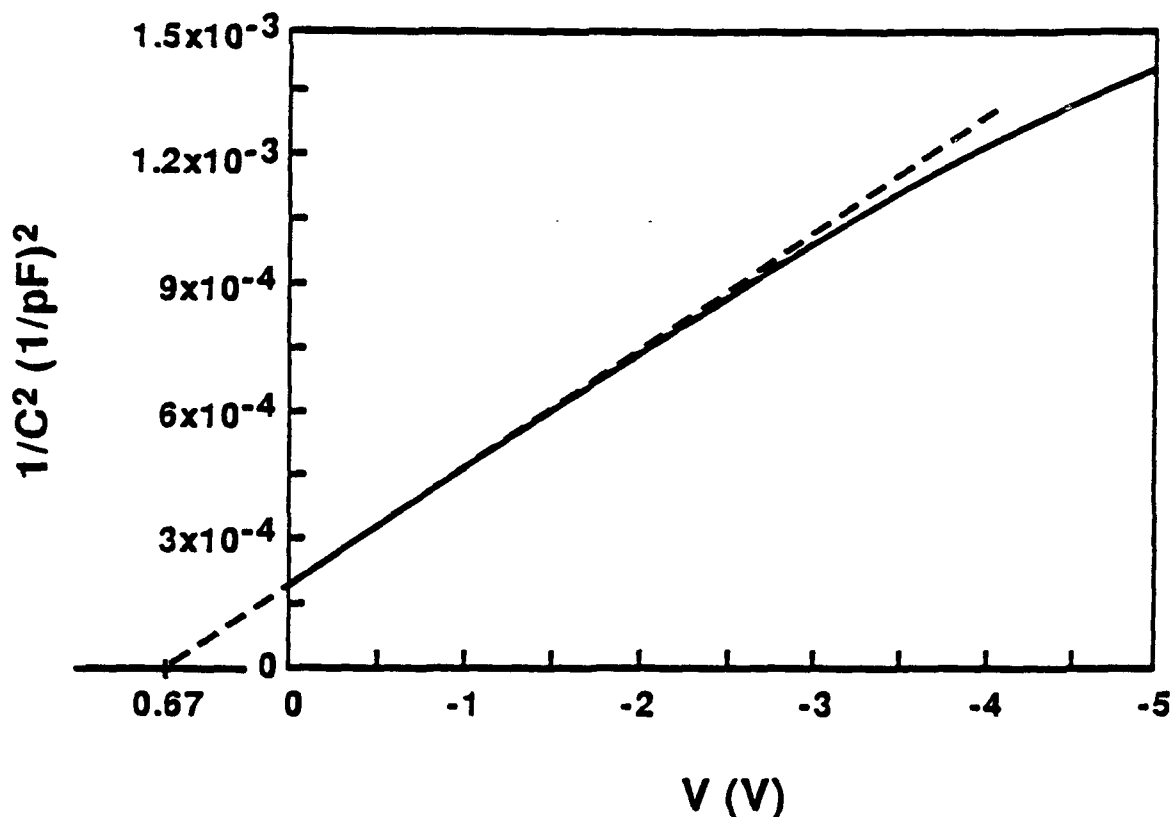


Figure 5.  $1/C^2$  vs.  $V$  plot of as-deposited Ti/SiC. (contact area =  $2.0 \times 10^{-3} \text{ cm}^2$ )

After annealing at 700°C for 20 minutes, the leakage increased; however, after further annealing to 60 minutes the characteristics in terms of leakage and ideality factors again improved. The I-V characteristics through the annealing series are plotted in Fig. 6. It can be seen from the corresponding semi-logarithmic plot (Fig. 7) that there was no linear region after annealing for 20 min. However, the ideality factors returned to low values ( $n < 1.09$ ) after further annealing. The barrier heights after annealing for 40 and 60 min. were 0.86 and 0.90 eV, respectively. The SBH after annealing for 60 min. was calculated from C-V measurements to be 1.04 eV.

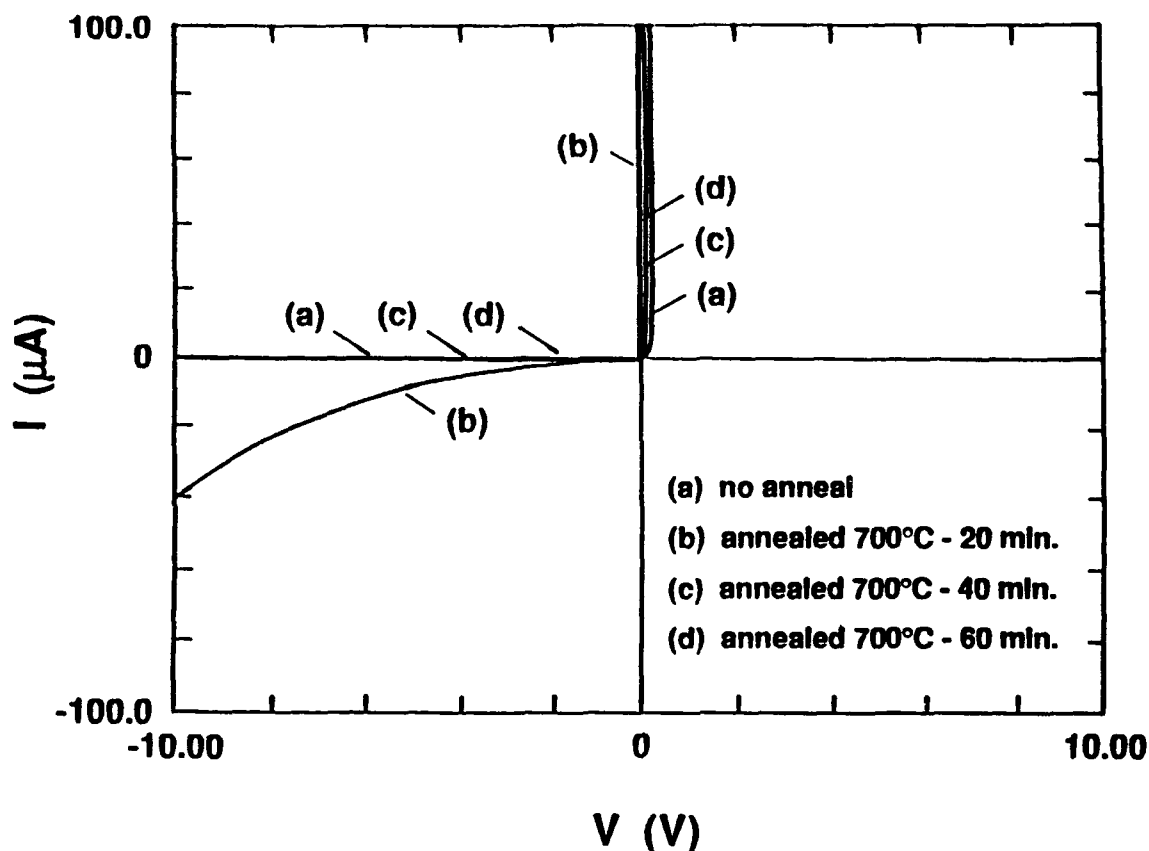


Figure 6. Current-voltage characteristics of Ti/SiC after annealing at 700°C.  
(contact area =  $2.0 \times 10^{-3} \text{ cm}^2$ )

The Schottky barrier height was also calculated from XPS spectra by careful comparison of core level peaks before and after deposition of very thin Ti films. In these experiments core level and valence band spectra were obtained of the SiC surface after chemical and thermal cleaning and prior to metal deposition. Immediately following the SiC surface analysis, a sequence of metal depositions was performed, which resulted in films of total thicknesses between 4 and 12 Å.

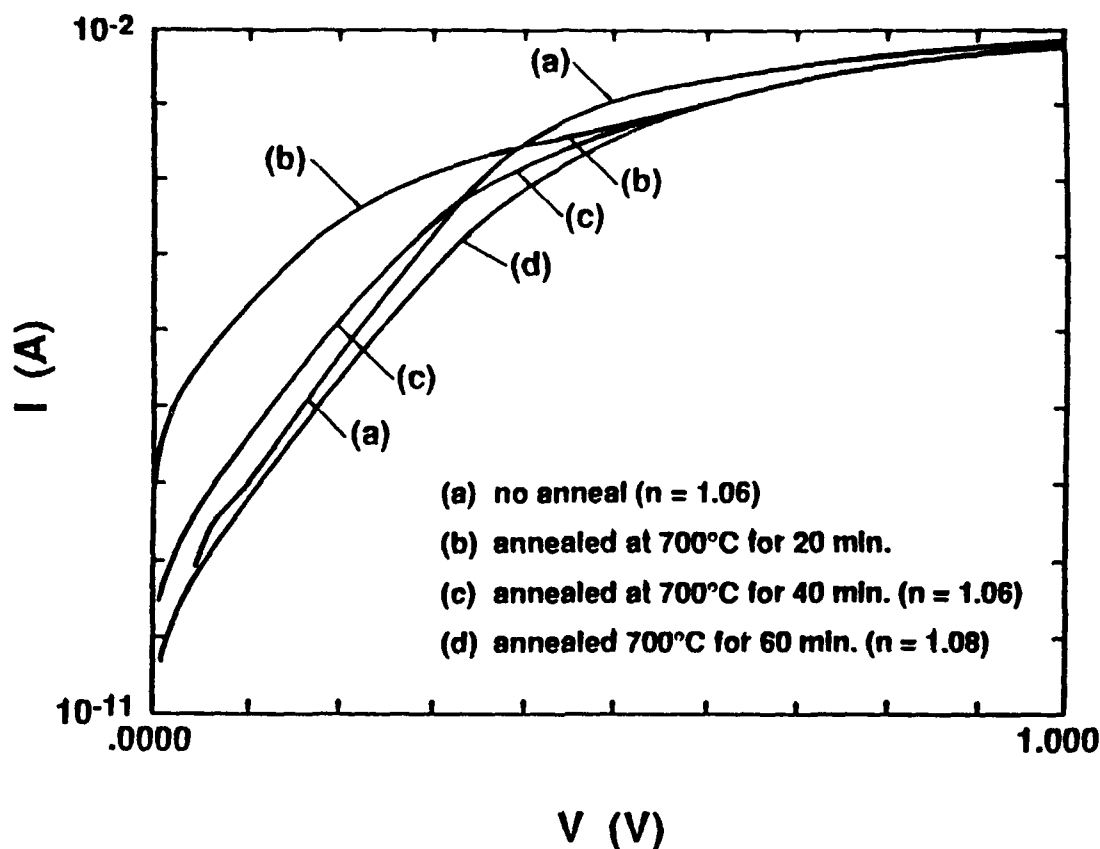


Figure 7. Semi-logarithmic I-V plot of Ti/siC after annealing at 700°C. (contact area =  $2.0 \times 10^{-3} \text{ cm}^2$ )

The binding energy (BE) of a photoelectron is related to its kinetic energy (KE) by the following relationship:

$$E_B = h\nu - E_K - \Phi_S, \quad (5)$$

where  $h\nu$  is the energy of the x-ray photons,  $E_K$  is the kinetic energy of the emitted electrons, and  $\Phi_S$  is the work function of the spectrometer (analyzer). The value of binding energy which is obtained directly from an XPS scan is actually equal to the true binding energy, BE, plus  $\Phi_S$ . Because binding energies are defined with respect to the Fermi level, it is important to use a known standard to define the Fermi level position. If the work function of the spectrometer tends to drift, a standard should be used with each collection of data. In these experiments a piece of Au foil was used as a standard with each new series of data. The Au 4f<sub>7/2</sub> peak has a known binding energy of 84.00 eV. The measured value of the Au 4f<sub>7/2</sub> peak is equal to 84.00 eV plus the work function of the spectrometer. Therefore, the measured binding energies of all core levels are corrected by the work function of the spectrometer determined from the Au standard. In this system the spectrometer work function was usually  $4.0 \pm 0.2 \text{ eV}$  (Au 4f<sub>7/2</sub> at  $\approx 88.0 \text{ eV}$ ).

The relationship between the SBH and the values measured by XPS is shown in Figure 8. This diagram shows energy bands in 6H-SiC which bend upward at the surface due either to surface states or to the metal contact. In nominally-doped material, which was used in these experiments, the depth over which band bending ( $>1000 \text{ \AA}$ ) occurs is much larger than the photoelectron escape depth ( $\approx 20 \text{ \AA}$ ); therefore, the XPS spectra effectively represent the position of energy bands at the surface.

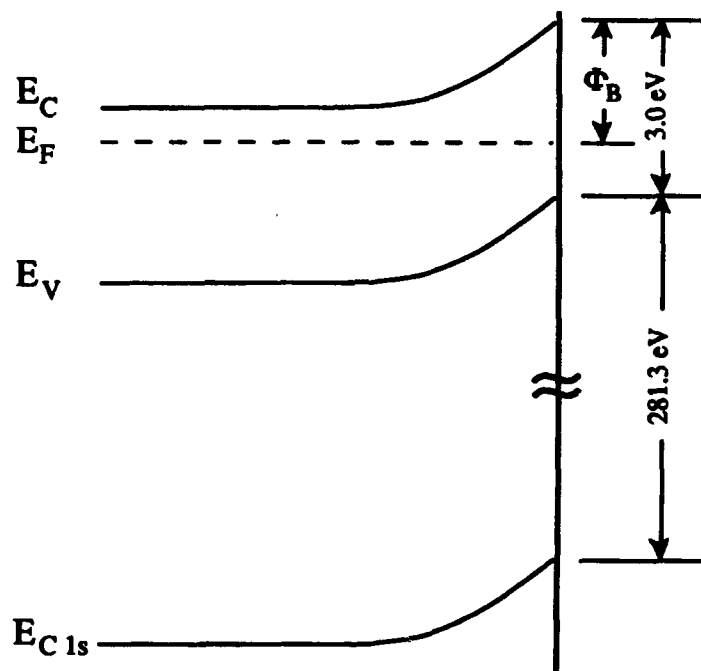


Figure 8. Energy band diagram of 6H-SiC showing the relationship between  $\Phi_B$  and binding energies measured by XPS.

Referring to Fig. 8, the SBH can be determined by the following expression:

$$\Phi_B = [(E_{C1s} - E_V) + E_g] - E_{C1s}, \quad (6)$$

where  $E_{C1s}$  is the C 1s binding energy originating at the SiC surface,  $(E_{C1s} - E_V)$  is the C 1s to valence band maximum binding energy difference (constant for a given material), and  $E_g$  is the band gap. A value of  $E_{C1s} - E_V = 281.30 \text{ eV}$  was obtained from the SiC surface prior to metal deposition by extrapolating the leading edge of the valence band spectra to zero intensity. This value agrees very well with the  $281.26 \pm 0.1 \text{ eV}$  value determined by Waldrop *et al.* [12]. Substituting values into Eq. 6, the expression can be rewritten as

$$\Phi_B = 284.3 - E_{C1s} (\text{eV}). \quad (7)$$

Therefore, the amount of band bending at the SiC surface prior to metal deposition is determined by the position of the C 1s peak. After deposition of the metal, shifts in core levels are used to calculate the SBH.

A deconvolution procedure was used to separate effects due to changes in chemical bonding and changes in band bending. One or more peaks, which typically were 20–30% Gaussian and 70–80% Lorentzian, were fit to the core levels of interest. The peaks were located by the midpoints of their full widths at half maximum (FWHM), which were 0.78–0.80 eV. The Si-bound-to-C part of the Si 2p peak and the C-bound-to-Si part of the C 1s peak were used to determine band shifting before and after the Ti depositions.

Table I lists the binding energies of the Si 2p (Si-bound-to-C) and C 1s (C-bound-to-Si) peaks after depositing 0, 4, 8, and 12 Å of Ti. The total band bending at the SiC surface before deposition of Ti was determined by subtracting the C 1s binding energy from 284.30 eV (see Eq. 7). These results indicated that the energy difference between the conduction band minimum and Fermi level at the surface was  $0.40 \pm 0.1$  eV.

Table I. Binding energies of Si 2p and C 1s peaks from SiC with various thicknesses of Ti. These binding energies have been corrected according to the Au 4f<sub>7/2</sub> peak. Units are in electron-volts.

XPS peak	0 Å Ti	4 Å Ti	8 Å Ti	12 Å Ti
Si 2p	101.74	101.40	101.38	101.34
C 1s	283.90	283.62	283.56	283.52

Because these layers were so thin, it was important to make sure that complete coverage was achieved. Two-dimensional layer-by-layer growth, or Frank-van der Merwe growth, results in greater reduced intensities of the peaks originating from the substrate than three-dimensional island growth (a.k.a. Volmer-Weber growth). An expression for the reduced intensities of the substrate peaks for layer-by-layer growth is expressed by the following relationship [13, 14]:

$$I_{red} = (1 - \Theta) \exp\left(\frac{-(n-1)m}{\lambda}\right) + \Theta \exp\left(\frac{-nm}{\lambda}\right), \quad (8)$$

where  $\Theta$  equals the covered monolayer fraction,  $n$  is the number of monolayers,  $m$  is the thickness of one monolayer, and  $\lambda$  is the attenuation length of the emitted electrons. The attenuation length is relatively independent of the particular material but is a function of the energy of the electrons. For C 1s and Si 2p peaks,  $\lambda$  is equal to approximately 7 monolayers

[7]. Between integer numbers of monolayer coverage (e.g.,  $n = 1$ ,  $\Theta = 1$  to  $n = 2$ ,  $\Theta = 1$ ), the reduced intensity decreases linearly with  $\Theta$ . At integer numbers of monolayer coverage, where  $\Theta = 1$ , Eq. 4.2-4 becomes

$$I_{red} = \exp\left(\frac{-nm}{\lambda}\right). \quad (9)$$

The reduced intensity (of either C 1s or Si 2p peaks) according to the layer-by-layer growth model is plotted vs. Ti thickness in Figure 9. The thickness of one monolayer,  $m$ , was approximated to be  $1/2 c = 2.34 \text{ \AA}$  for Ti, which has an hcp structure with  $a=2.95 \text{ \AA}$  and  $c=4.68 \text{ \AA}$ . The C 1s and Si 2p reduced intensities calculated and normalized from the peak areas are also plotted vs. Ti thickness in Fig. 9. The data points follow the theoretical curve for two-dimensional growth very closely.

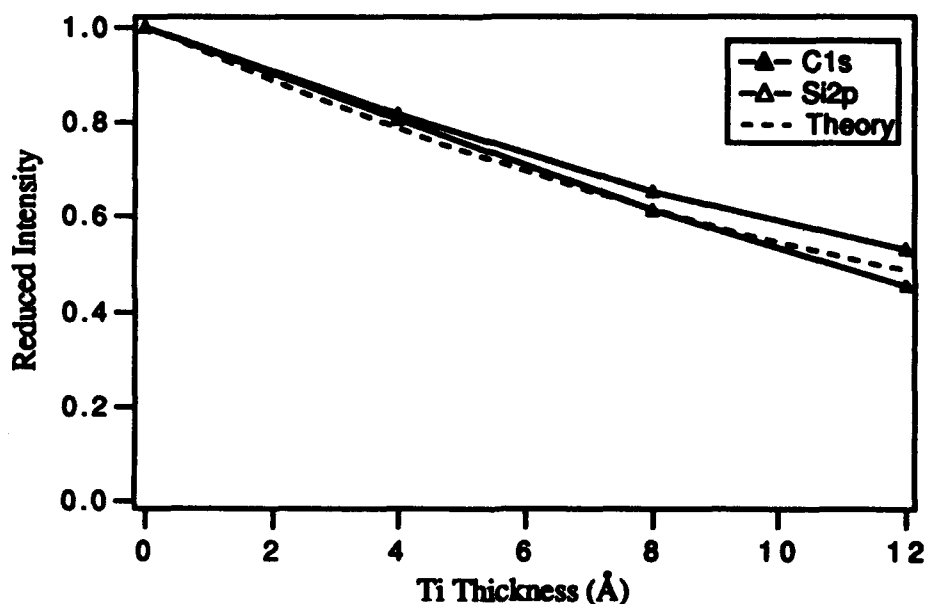


Figure 9. Plot of the reduced intensities of the C 1s and Si 2p peaks vs. Ti overlayer thickness as measured by the quartz deposition (film thickness) monitor. The theoretical curve represents layer-by-layer (Frank-van der Merwe) growth.

After depositing  $4 \text{ \AA}$  of Ti, the Si 2p and C 1s binding energies (Table 1) were reduced by 0.34 and 0.28 eV, respectively, which corresponds to an increase in band bending. Most of the band bending occurred with the deposition of the first  $4 \text{ \AA}$  of Ti. With  $12 \text{ \AA}$  of Ti the total reduction in binding energies of the Si 2p and C 1s peaks were 0.40 and 0.38 eV, respectively. The difference in the binding energy shifts was within experimental error. The reduction in binding energies corresponded to an increase in the barrier height. Taking the average of the binding energy reductions and adding it to the initial amount of band bending gave a barrier height of  $0.79 \pm 0.1 \text{ eV}$ .

The SBH's of Ti contacts on SiC calculated from I-V, C-V, and XPS measurements are summarized in Table II. The XPS analyses were performed only on as-deposited contacts, and C-V data was not obtained for samples annealed at 700°C for 40 min. However, of the data collected, the agreement is very good, within 0.15 eV, between the three measurement techniques.

Table II. Barrier heights of unannealed and annealed Ti contacts on SiC measured by I-V, C-V, and/or XPS.

anneal condition	$\Phi_B^{I-V}$ (eV)	$\Phi_B^{C-V}$ (eV)	$\Phi_B^{XPS}$ (eV)
unannealed	0.83	0.88	0.79
700°C / 40 min.	0.86	—	—
700°C / 60 min.	0.90	1.04	—

**Interface Structure.** The room temperature deposition of Ti on 6H-SiC (0001) resulted in epitaxial films. Both Ti ( $a = 2.95 \text{ \AA}$ ,  $c = 4.68 \text{ \AA}$ ) and 6H-SiC ( $a = 3.08 \text{ \AA}$ ,  $c = 15.11 \text{ \AA}$ ) have hexagonal crystal structures, corresponding to a -4% lattice mismatch between  $(1\bar{1}00)_{Ti}$  and  $(1\bar{1}00)_{SiC}$ . The first indication of epitaxial growth was a  $1 \times 1$  LEED pattern, similar to that of the SiC substrate, which was obtained from a deposited film of Ti ( $\approx 200 \text{ \AA}$ ). Diffraction patterns of 6H-SiC and the Ti/6H-SiC interface are compared in Figure 10. Figure 10(a) shows a diffraction pattern of the 6H-SiC substrate along the zone axis  $[11\bar{2}0]$ , which is perpendicular to the  $[0001]$  direction. In Fig. 10(b) the diffraction pattern was obtained from an area which includes the interface of a cross-sectional Ti/SiC sample. The arrows mark spots from the Ti film. The other spots which are not present in (a) also originate from the Ti film. The fact that the Ti spots lie outside the SiC spots shows that the lattice parameter of the Ti film is smaller than that of the SiC substrate. The crystallographic relationships are  $(0001)_{Ti} \parallel (0001)_{SiC}$  and  $(1\bar{1}00)_{Ti} \parallel (1\bar{1}00)_{SiC}$ .

The integrity of the interface structure is represented well by the HRTEM image shown in Figure 11. The top part of the figure shows a high resolution image of the Ti/SiC interface region. The enclosed area is magnified in the bottom part of the figure. The image shows a nearly perfect interface. The arrow at the interface shown in Fig. 11 marks a location which was initially thought to be a misfit dislocation but was later found to be a step at the SiC surface.

Also marked in the magnified image are the nearest plane spacings perpendicular to the interface. In Ti, which has a 2-layer periodicity, the nearest-neighbor planes are  $(0002)$  along the  $[0001]$  direction. The corresponding nearest-neighbor planes in 6H-SiC are  $(0006)$ .

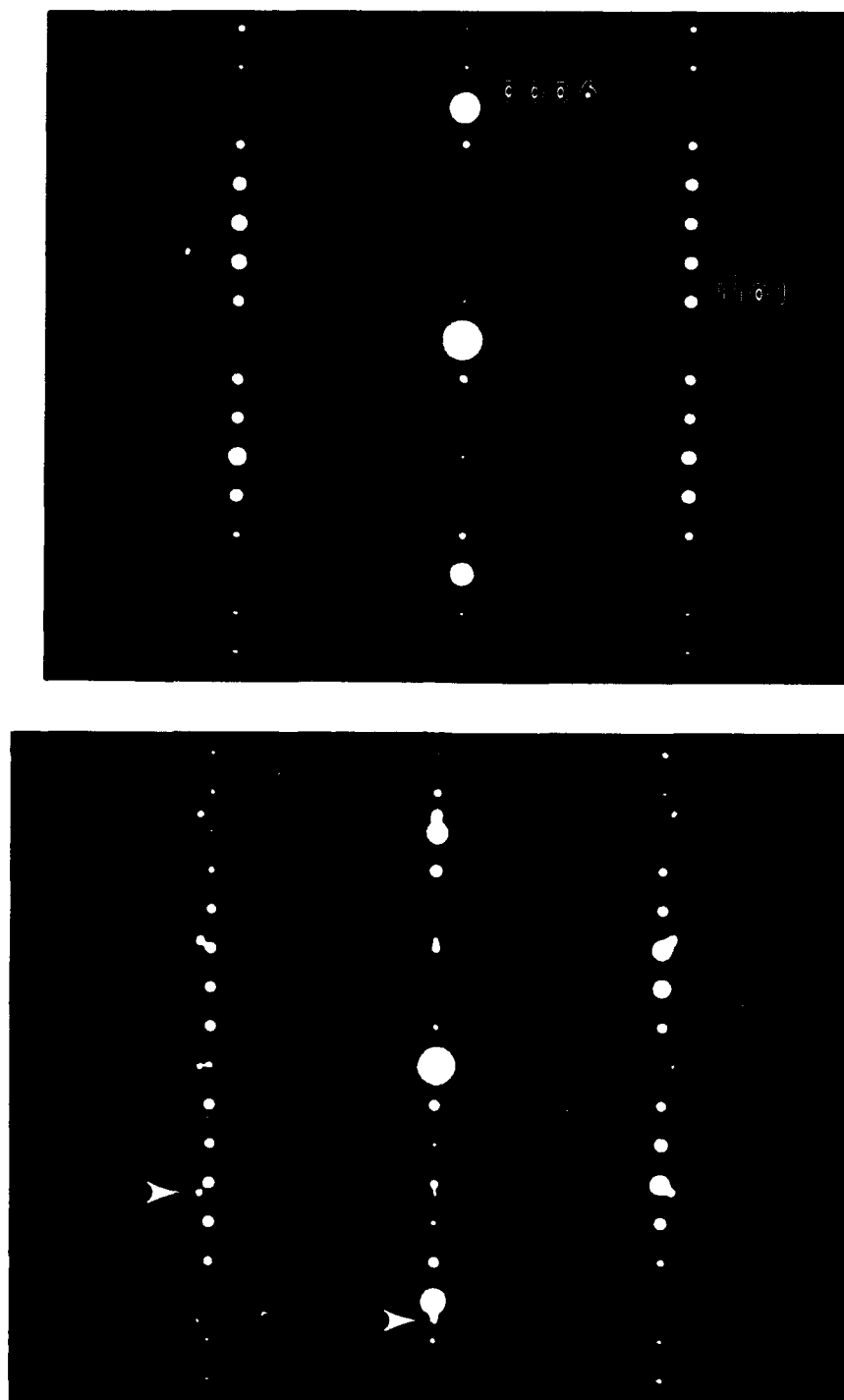


Figure 10. Selected area diffraction patterns of (a) 6H-SiC and (b) Ti/SiC interface in cross-sectional view. Two of the spots due to the Ti film are marked with arrows in (b).  $z = [11\bar{2}0]$ .



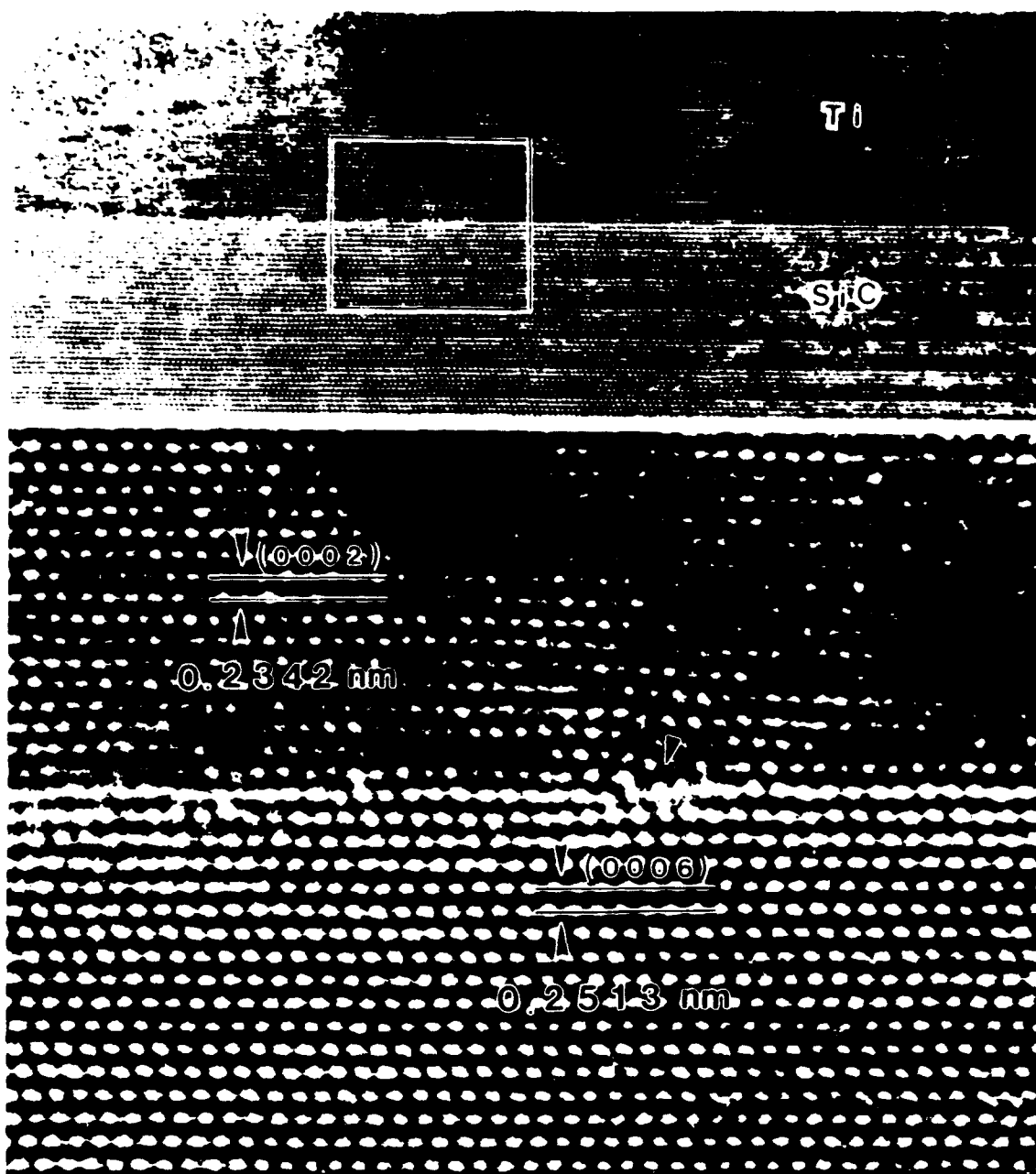


Figure 11. High resolution TEM image of as-deposited Ti/SiC in cross-section. The lower image is a magnification of the boxed-in region. The arrow at the interface marks the position of a misfit dislocation.

Interface Chemistry. After annealing at 700°C for 20 minutes, the interface reaction zone (R.Z.) consisted of a 2 to 3 nm thick, continuous layer of cubic (B1 (NaCl structure))  $\text{TiC}_{1-x}$  in contact with the SiC and a layer of orthorhombic  $\text{Ti}_5\text{Si}_3$  containing discrete  $\text{TiC}_{1-x}$  particles at the Ti side of the interface (Fig. 12). The total width of the R.Z. was 10 to 15 nm. The size of the  $\text{TiC}_{1-x}$  particles was  $5 \pm 2$  nm. The major product phase,  $\text{Ti}_5\text{Si}_3$ , was a continuous layer which contained low angle boundaries.

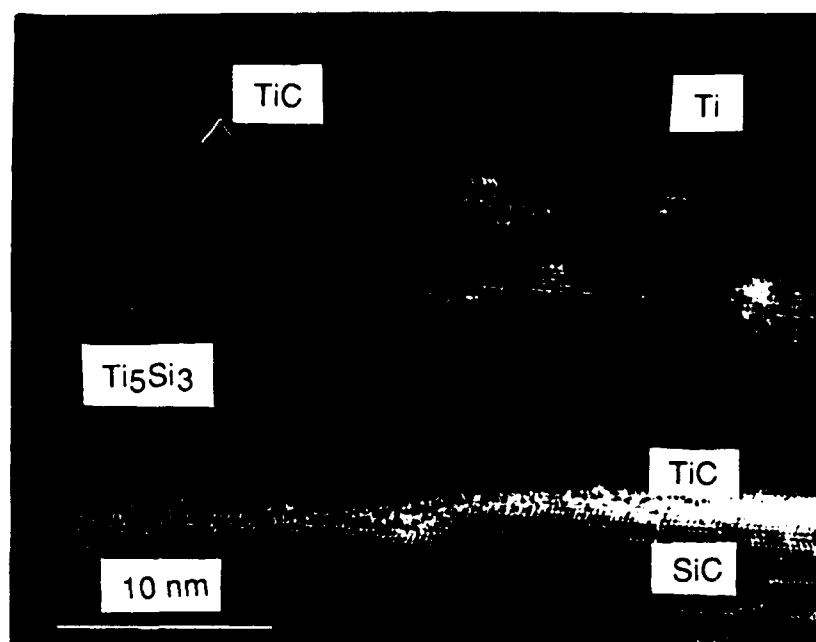


Figure 12. High resolution TEM micrograph of Ti/SiC interface after annealing for 20 min. at 700°C in UHV.

The width of the reaction zone did not change after annealing for 60 minutes (Fig. 13). However, the  $\text{TiC}_{1-x}$  particles disappeared at the interface with Ti. The position of the layers

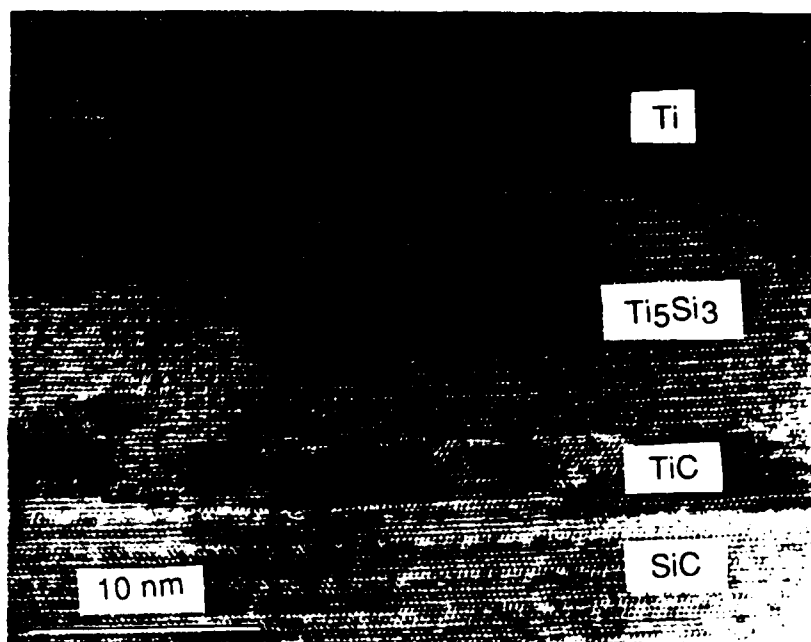


Figure 13. High resolution TEM micrograph of Ti/SiC interface after annealing for 60 min. at 700°C in UHV.

comprising the interface was SiC / TiC<sub>1-x</sub> / Ti<sub>5</sub>Si<sub>3</sub> / Ti. The lattice parameter of TiC<sub>1-x</sub> varied by approximately 2% along the SiC interface. The crystallographic relationships are summarized by the following:

$$\begin{aligned} (0001)_{\text{SiC}} \parallel (11\bar{1})_{\text{TiC}_{1-x}} \parallel (0001)_{\text{Ti}_5\text{Si}_3} \parallel (0001)_{\text{Ti}} \\ [11\bar{2}0]_{\text{SiC}} \parallel [011]_{\text{TiC}_{1-x}} \parallel [4\bar{5}10]_{\text{Ti}_5\text{Si}_3} \parallel [11\bar{2}0]_{\text{Ti}} \end{aligned}$$

Concentration profiles obtained by EDS perpendicular to the interface before annealing and for anneals of 20 min. and 60 min are shown in Figure 14. The resolution is approximately 5 nm as determined by the profile of the as-deposited Ti/SiC interface. After annealing for 20 min., the C concentration showed a high level near the SiC interface in addition to a peak near the interface with Ti. A peak in the Si concentration occurred in the reaction zone (R.Z.) closer to the the SiC. This type of profile occurred because of the faster diffusivity of C than Si in all the reaction products. During the 60 min. anneal, the C near the Ti interface diffused into the Ti, while more of the Si diffused through the reaction zone. These profiles correspond to the reaction phases shown in Figs. 12 and 13.

The  $\alpha$ -Ti hcp phase is stable up to 882°C [15]; therefore, there should be no polymorphic transformation of the Ti phase. At the annealing temperature of 700°C, TiC<sub>1-x</sub> is the only binary phase which exists between the two elements. At this temperature, TiC<sub>1-x</sub> covers a range of stoichiometries from approximately 40.5 to 48.5 atomic percent C, while approximately 1.0% C and < 0.5% Si are soluble in  $\alpha$ -Ti. There are five titanium silicides at this temperature: Ti<sub>3</sub>Si, Ti<sub>5</sub>Si<sub>3</sub>, Ti<sub>5</sub>Si<sub>4</sub>, TiSi, and TiSi<sub>2</sub>.

The free energies of formation of the carbide and silicides with Ti at 700°C are listed in Table III. TiC has by far the lowest free energy of formation at this temperature, while TiSi, Ti<sub>5</sub>Si<sub>4</sub>, and Ti<sub>5</sub>Si<sub>3</sub> have free energies of formation within 10.0 kJ/mol of each other.

Table III. Free energies of formation of binary Ti compounds with Si and C at 700°C.

Compound	$\Delta G$ (kJ/mol)	Reference
Ti <sub>3</sub> Si	-61.3	[15]
Ti <sub>5</sub> Si <sub>3</sub>	-85.6	[15]
Ti <sub>5</sub> Si <sub>4</sub>	-87.7	[15]
TiSi	-95.1	[15]
TiSi <sub>2</sub>	-77.7	[15]
TiC	-172.6	[16]

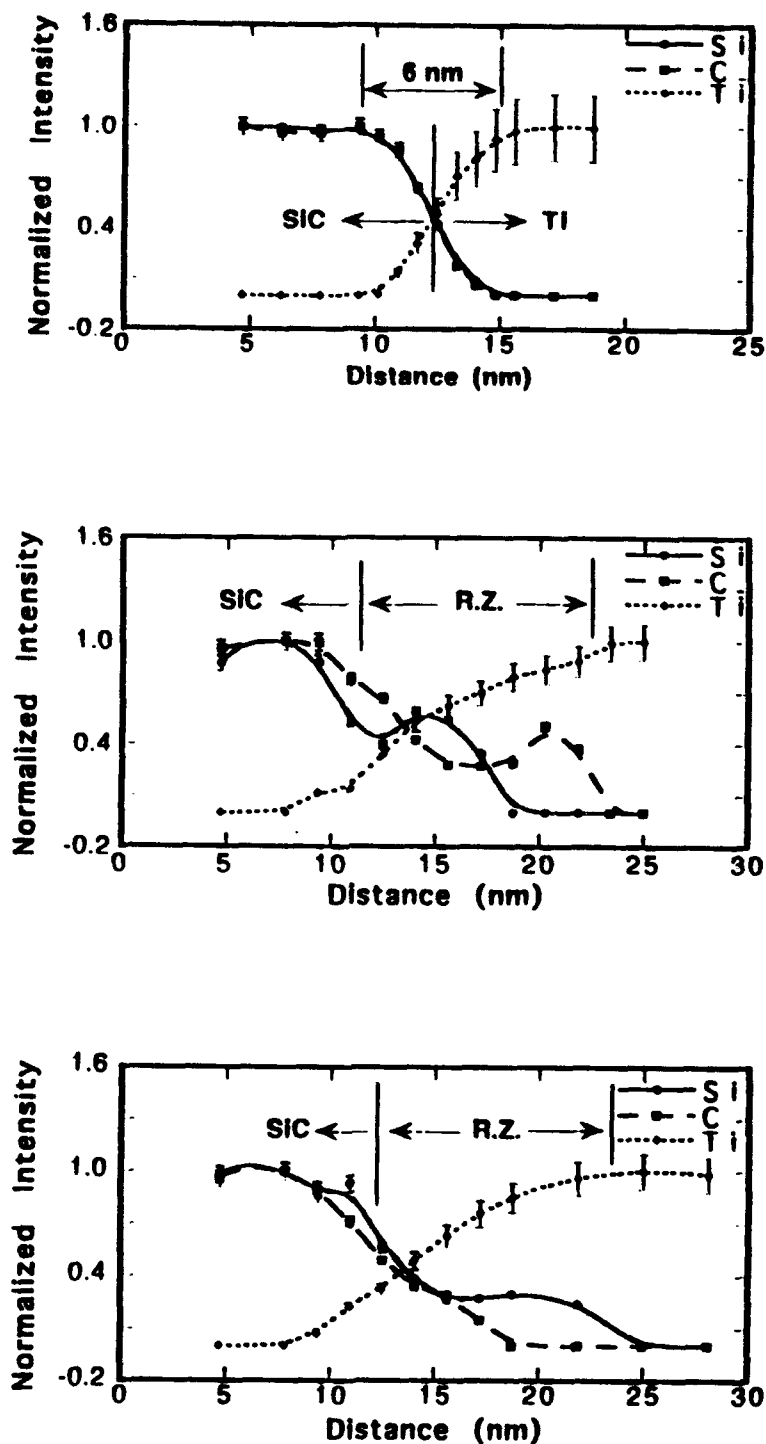


Figure 14. Concentration profiles of Si, C, and Ti perpendicular to the Ti/SiC interface determined by parallel electron energy loss spectroscopy (PEELS) after annealing at 700°C for (a) 20 min. and (b) 60 min.

There seems to be no simple way of predicting the total diffusion path in a material system having three or more components and which is in the process of attaining thermodynamic equilibrium, e.g., Ti and SiC chemically bonded at an interface and heated to

the extent that chemical interdiffusion occurs. Knowledge of all the thermodynamic data is, in general, not sufficient to predict which product phases will form. Thermodynamic data (i.e. temperature, pressure, and free energies) can yield the equilibrium phase fields; however, the diffusion path is controlled by the diffusion coefficients of each component in the pertinent phases. It is the ratio of the diffusivities which determines the interface compositions, and accordingly the diffusion path [17]. Therefore, one must be wary of predictions made for multicomponent systems when only thermodynamic constraints are used. There has been evidence in many metal/SiC systems that the reactions were limited by the dissociation of SiC, resulting in metal-rich silicides.

There have been several extensive studies of the Ti-Si-C system at high temperatures. At temperatures between 570°C and 1200°C and at low or atmospheric pressures, the product phases in Ti/SiC diffusion couples were reported to be TiC [18, 19], Ti<sub>5</sub>Si<sub>3</sub> [20], or both TiC<sub>1-x</sub> and Ti<sub>5</sub>Si<sub>3</sub> [21-24]. At high pressures (10 to 20 kbars) and high temperatures (1200°C to 1500°C) Ti<sub>3</sub>SiC<sub>(1.78-2.00)</sub> was identified along with TiC<sub>1-x</sub> and Ti<sub>5</sub>Si<sub>3</sub> [25]. At the high end of this pressure range Ti<sub>3</sub>Si formed, which exhibited a high solubility for carbon (up to 9 at. %).

Backhaus-Ricoult [22, 23] studied diffusion couples between Ti and polycrystalline SiC at 1200°C. By measuring the concentration profiles of each of the constituents and plotting them on the Ti-Si-C Gibbs phase triangle, the diffusion path was determined. It was stated that because the diffusion of C in Ti is ~10 times faster than Si in Ti, the reaction runs from pure Ti to the Si-rich corner of the Ti phase field, which is connected to the Ti<sub>5</sub>Si<sub>3</sub> phase field. The concentration of the slower diffusing Si quickly increases near the interface and reaches its solubility limit, at which point Ti<sub>5</sub>Si<sub>3</sub> forms. The reaction path then passes through the phase field containing Ti<sub>5</sub>Si<sub>3</sub>, TiC<sub>1-x</sub>, and Ti. Carbon reacts with Ti to form TiC within the Ti<sub>5</sub>Si<sub>3</sub> phase. The morphology of the product layer showed the formation of TiC<sub>1-x</sub> particles throughout a matrix of Ti<sub>5</sub>Si<sub>3</sub>, where the TiC particles contained more C closer to the SiC interface.

It is worthwhile to make some comparisons between our results and those just described. The Ti/SiC samples in the present research were annealed at 700°C; however, the same phases were formed in the reaction as those found at 1200°C. The diffusion paths are apparently very similar if not the same. The faster diffusivity of C in Ti would explain the formation of the TiC particles at the interface with Ti early in the annealing stage. An important difference is that a continuous TiC layer formed along the interface with SiC. It is believed that Backhaus-Ricoult [22, 23] could not have seen this initial TiC layer without the use of high resolution TEM. It is also possible that the TiC layer formed to minimize interface strain between the phases in the reaction zone and the monocrystalline 6H-SiC (0001) used in the present study. A large lattice misfit strain (~8.5%) exists between

(2130) $\text{Ti}_5\text{Si}_3$  and ( $\bar{1}\bar{1}00$ ) $6\text{H-SiC}$ , which were both normal to the (0001) $\text{SiC}$  interface plane and parallel to each other. The resulting morphological sequence, which was described above, is more favorable in terms of strain. Between ( $\bar{1}\bar{1}1$ ) $\text{TiC}$  and ( $1\bar{1}02$ ) $\text{SiC}$  there is only a 0.5% mismatch, while that between (111) $\text{TiC}$  and (21 $\bar{3}0$ ) $\text{Ti}_5\text{Si}_3$  is 2.5%.

Chemical bonding at the interface was studied by XPS after depositing a series of thin Ti films. Figure 15 shows the C 1s and Si 2p peaks after depositing 4, 8, and 12 Å Ti. Each of these peaks has been deconvoluted into a major and a minor peak.

After 4 Å of Ti was deposited, the C 1s peak was composed of a major peak at 283.62 eV and a minor peak at 282.04 eV. With thicker films of Ti, the minor peak grew; after 12 Å of Ti both peaks shifted to slightly lower binding energies of 283.52 eV and 281.94 eV, respectively. The major peak originates from C-bound-to-Si in SiC, and the minor peak is attributed to C-bound-to-Ti [26]. The increasing contribution of the minor peak at the greater film thicknesses is a result of the corresponding reduction in sensitivity to the SiC. Titanium-carbon bonding is expected due to the highly negative free energy of formation of TiC.

Titanium silicide bonding was not detected. Because titanium has a lower electronegativity (1.54) than carbon (2.55), Si-Ti bonding should result in a peak at the low binding energy side of the Si 2p (Si-bound-to-C) peak. Instead, a minor peak at slightly higher binding energy was detected. After 4 Å Ti was deposited, the major and minor peaks were located at 101.40 eV and 102.56 eV, respectively. The minor peak is probably due to  $\text{SiO}_x$ , since the same binding energy difference existed prior to Ti deposition. Si 2p binding energies reported in the literature are  $\sim 103.7$  eV for  $\text{SiO}_2$  [27] and 102.7 eV for SiO [5].

The combination of XPS and TEM analyses shows that interfacial TiC formation begins with an initial two-dimensional coverage of Ti at room temperature and is enhanced after annealing at 700°C. On the other hand, there seems to be some O which remains at the interface bonded to Si. The amount of oxygen does not appear to be sufficiently high to interfere with creating a high quality interface, as indicated by high resolution TEM.

#### D. Conclusions

A comprehensive study of the electrical properties, microstructure, and chemistry of both as-deposited and 700°C annealed thin film Ti/6H-SiC (0001) interfaces was performed with specific regard to the application of contacts in semiconductor devices.

As-received, thermally oxidized, n-type 6H-SiC (0001) substrates were simultaneously cleaned and etched in either an ethanol / hydrofluoric acid / water (10:1:1) or a 10% hydrofluoric acid solution followed by a 15 min. thermal desorption at 700°C in UHV. This procedure resulted in 1x1 unreconstructed surfaces which contained submonolayer residual O and trace amounts of F. X-ray photoelectron spectroscopy analyses revealed that the energy bands bent upwards at the surface. This result indicates that surface states were present,

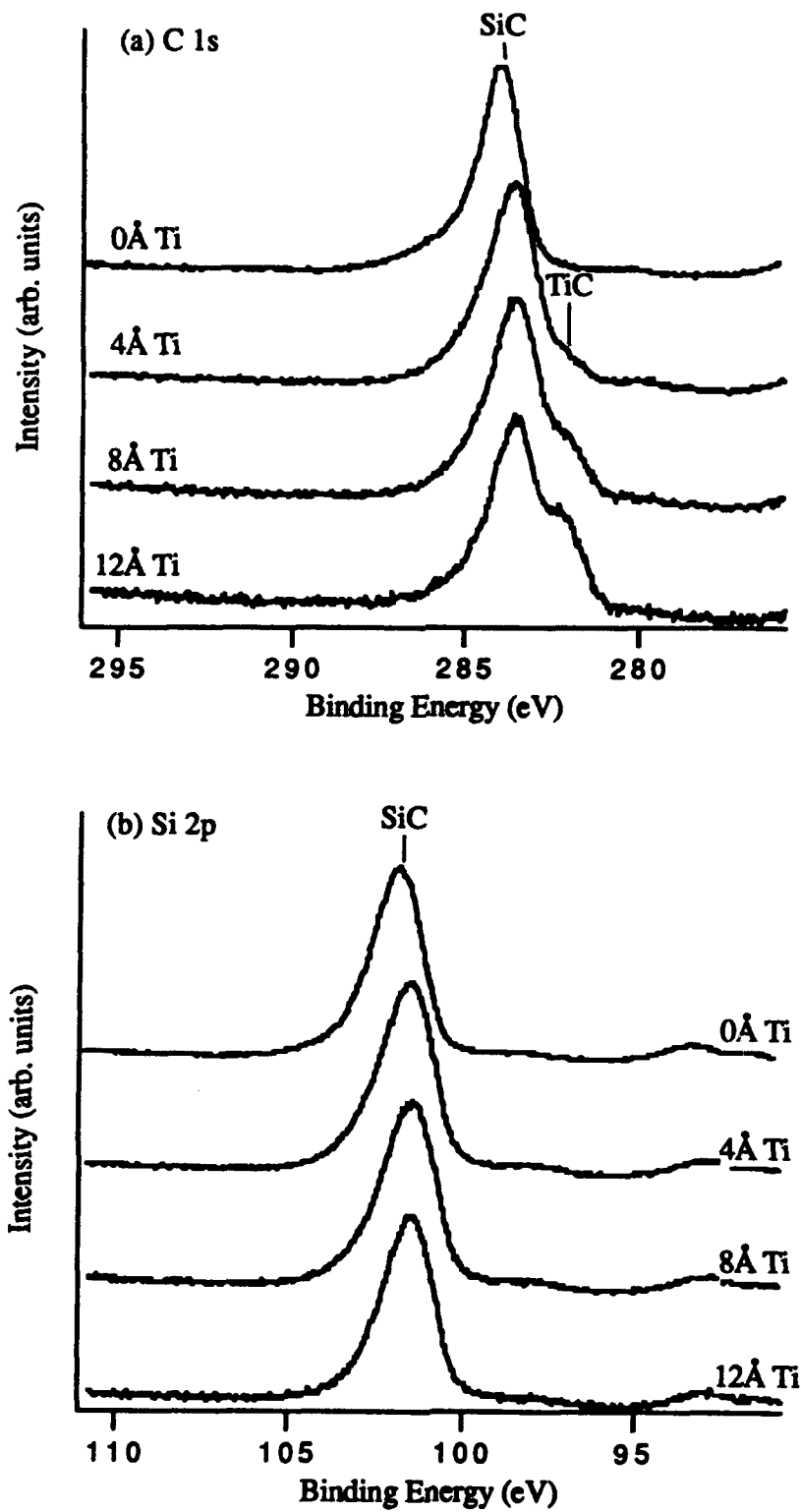


Figure 15. XPS C 1s and Si 2p peaks from SiC after 4, 8, and 12 Å Ti.

which acted as acceptors and which are expected to prohibit an exact correlation between the Schottky barrier heights and metal work functions as predicted by the Schottky-Mott limit for ideal metal-semiconductor contacts.

The deposition of Ti onto these chemically-treated, unheated SiC substrates resulted in epitaxial contacts, which exhibited rectifying behavior, low ideality factors ( $n < 1.09$ ), and typical leakage currents of  $5 \times 10^{-7}$  A/cm<sup>2</sup> at -10V. The SBH's calculated from I-V, C-V, and XPS measurements (0.79–0.88 eV) were somewhat lower than that predicted by the Schottky-Mott limit (1.03 eV). This result may be associated with surface states in the SiC substrates. On the other hand, other metal contacts would need to be examined to understand the relationship of the surface states to the resulting Schottky barrier heights.

The SBH's and electrical properties do not show substantial changes after annealing at 700°C for up to 60 min., except after an initial 20 min. anneal. However, interfacial chemical reactions resulted in the formation of Ti<sub>5</sub>Si<sub>3</sub> and TiC<sub>1-x</sub>, which is in agreement with several previous studies. The fact that the formation of Ti<sub>5</sub>Si<sub>3</sub> and TiC, which are low work function metals [28, 29], did not result in a reduction of the SBH suggests that energy states were also present at the newly-created interface between TiC and SiC.

#### E. Future Research Plans/Goals

The current technology of SiC devices is driving the need for ohmic contacts to p-type SiC which have low contact resistivities at both room and elevated temperatures. Aluminum alloys are currently used because the Al degeneratively dopes the surface of the SiC, which reduces the contact resistance. However, these contacts cause problems at elevated temperatures due to melting and extensive diffusion.

Our plan is to investigate other materials which should be more stable at elevated temperatures. The issues being considered for both choosing the material(s) and conducting the experiments are work function differences, lattice mismatch, thermal properties, and doping profiles/concentrations. After depositing the chosen material(s), the I-V characteristics and the contact resistivities will be measured at room and elevated temperatures.

#### F. References

1. W. O. Saxton, T. J. Pitt, and M. Horner, *Ultramicroscopy*, **4** (1979) 343.
2. *Handbook of X-ray Photoelectron Spectroscopy*, edited by C.D. Wagner, W.M. Riggs, L. E. Davis, and J. F. Moulder (Perkin-Elmer Corp., Eden Prairie, MN, 1979).
3. J. R. Waldrop and R.W. Grant, *Appl. Phys. Lett.*, **62** (1993) 2685.
4. D. B. Fenner, D. K. Biegelsen, and R. D. Bringans, *J. Appl. Phys.*, **66** (1989) 419.
5. J. A. Taylor, G. M. Lancaster, A. Ignatiev, and J. W. Rabalais, *J. Chem. Phys.*, **68** (1978) 1776.
6. K. L. Smith and K. M. Black, *J. Vac. Sci. Technol. A*, **2** (1984) 744.
7. *Auger and X-ray Photoelectron Spectroscopy* 2nd ed. Practical Surface Analysis, Vol. 1 edited by D. Briggs and M. P. Seah (John Wiley & Sons, New York, 1990).



8. R. Kaplan, *Surface Science*, **215** (1989) 111.
9. R. T. Tung, *Phys. Rev. B*, **45** (1992) 13509.
10. J. W. Palmour (Cree Research, Inc., Research Triangle Park, North Carolina, USA, 1992) private communication.
11. S. M. Sze, *Physics of Semiconductor Devices* 2nd ed. (John Wiley & Sons, Inc., New York, 1981).
12. J. R. Waldrop, R. W. Grant, Y. C. Wang, and R. F. Davis, *J. Appl. Phys.*, **72**, 4757 (1992).
13. L. C. Feldman and J. W. Mayer, *Fundamentals of Surface and Thin Film Analysis* (North-Holland, New York, 1986).
14. Z. Sitar, L. L. S. Smith, and R. F. Davis, Submitted to *J. Cryst. Growth*.
15. *Phase Diagrams of Binary Titanium Alloys*, Monograph Series on Alloy Phase Diagrams, edited by J.L. Murray (ASM International, Metals Park, Ohio, 1987).
16. *JANAF Thermochemical Tables*, Journal of Physical and Chemical Reference Data, Vol. 14, edited by M. W. Chase Jr., C. A. Davies, J. R. Downey Jr., D. J. Frurip, R. A. McDonald, and N. A. Syverud (The American Chemical Society and The National Institute of Physics for the National Bureau of Standards, Midland, MI, 1985).
17. G. R. Purdy, D. H. Weidel, and J. S. Kirkaldy, *Trans. Met. Soc.*, **230** (1964) 1025.
18. M. B. Chamberlain, *Thin Solid Films*, **72** (1980) 305.
19. J. J. Bellina Jr. and M. V. Zeller, *Mat. Res. Soc. Symp. Proc.*, **97** (1987) 265.
20. M. Nathan and J. S. Ahearn, *Materials Science and Engineering*, **A126** (1990) 225.
21. C. G. Rhodes and R. A. Spruling in *Recent Advances in Composites in the United States and Japan*, edited by J. R. Vinson and M. Taya, (American Society for Testing and Materials: Philadelphia, 1985).
22. M. Backhaus-Ricoult, *Ber. Bunsenges. Phys. Chem.*, **93** (1989) 1277.
23. M. Backhaus-Ricoult in *Metal-Ceramic Interfaces*, edited by M. Ruhle, *et al.*, (Pergamon Press, New York, 1990).
24. I. Gotman, E. Y. Gutmanas, and P. Mogilevsky, *J. Mater. Res.*, **8** (1993) 2725.
25. S. Sambasivan and W. T. Petuskey, *J. Mater. Res.*, **7** (1992) 1473.
26. L. Ramqvist, K. Hamrin, G. Johansson, A. Fahlman, and C. Nordling, *J. Phys. Chem. Solids*, **30** (1969) 1835.
27. T. L. Barr, *Appl. Surf. Sci.*, **15** (1983) 1.
28. G. V. Samsonov, L. N. Okhremchuk, N. F. Podgrushko, I. A. Podchernyaeva, and V.S. Fomenko, *Inorganic Materials*, **12** (1976) 720.
29. K. Senzaki and Y. Kumashiro, *Bull. Electrotech. Lab. Jpn.*, **41** (1977) 593.

### **XIII. Initial Stage of AlN Film Growth on 6H-SiC by Plasma-Assisted Gas-source Molecular Beam Epitaxy**

#### **A. Introduction**

It is of great importance to obtain atomically smooth surfaces and abrupt interfaces of heterostructural materials. The potential problems in the heteroepitaxial growth are mainly caused from lattice mismatches between the films and substrates [1]. This gives rise to some structural defect in the films such as misfit dislocations and misfit strains. In the case of AlN/SiC which has a 0.9% lattice mismatch, some defects have been reported to be caused by the surface structures of the substrates [2]. Moreover it should be significant to obtain not only defects free films but also atomically smooth films. For the growth of multilayered structures such as SiC/AlN/SiC, the smoothness of each layer would be especially desired. This feature in general is determined by growth modes, i.e. two-dimensional versus three-dimensional growth [3]. To obtain an atomically smooth surface, it should be necessary to grow films with a two-dimensional type of growth mode

In this study the initial stage of growth in terms of defects and surface morphology are investigated. HRTEM was utilized for this purpose.

#### **B. Experimental Procedure**

AlN films were grown on Si-faces of 6H-SiC (0001) substrates. The substrates used in this study were either on-axis or off-axis (3-4° off from (0001) toward  $\langle 11\bar{2}0 \rangle$ ) provided by Cree Research Inc. Films were all grown by a GSMBE method under the same conditions. The typical growth condition is shown in Table I. The details of the deposition can be seen in the accompanying report. In order to observe the initial stage of growth, the thickness of the films was controlled by varying the growth time.

---

Table I. Growth Conditions for the AlN films

---

Temperature	1050 °C
Al evaporation temperature	1260 °C
Nitrogen flow rate	3.5 sccm
Microwave power	100 W
Growth rate	17 Å/min

---

After growing the film, the sample was cut and glued face to face to make a cross-sectional TEM sample, followed by the thinning processes of grinding, dimpling and ion milling. Finally, the sample was examined by a Topcon EM-002B operated at a 200kV acceleration voltage.

### C. Results

Figure 1 shows the cross-sectional image of a deposited AlN film on an on-axis 6H-SiC (0001) substrate. The surface is fairly smooth with only 10–20Å variation in thickness. Strains are periodically observed in the film corresponding mainly to the lattice mismatch between AlN and SiC of ~0.9%. Films grown on off-axis 6H-SiC showed similar features, implying a small affects of substrate orientation on surface morphology. It should, however, be noticed here that the defects observed in the film are strongly related to surface structures such as steps and terraces of the substrates.



Figure 1. Cross sectional TEM image of AlN film grown on 6H-SiC substrate.

Figures 2 (a) and (b) show the high resolution images of the interface regions of the on-axis and off-axis substrates, respectively. Epitaxial 2H AlN films which have an ABAB...stacking sequence can be clearly seen with the presence of some defects at the interface. There are considered to be two types of defects in the films. One is a misfit dislocation perpendicular to the substrate as indicated by arrow 1 in Fig. 2(a), which is produced by the lattice mismatch between AlN and SiC. The other is a planar defect parallel to the (0001) surface (arrow 2). The formation mechanisms will be discussed in the following section.

Figure 3 shows the initial stage of growth of the AlN film whose thickness is ~50Å. The film was grown on an off-axis 6H-SiC substrate. A rough surface texture can be seen, probably indicating island growth.



(a) on-axis substrate



(b) off-axis substrate

Figure 2 HRTEM images of AlN/SiC interfaces of (a) on-axis and (b) off-axis SiC substrates. Arrow 1 and arrow 2 denote the misfit dislocation and the planar defects parallel to the surface, respectively.

#### D. Discussion

It is important to discuss the formation mechanisms of the defects observed in the film as described in the previous section. The initial stage of growth indicated that the film growth



Figure 3. HRTEM image of the initial stage of AlN growth. Island growth features can be observed.

probably commenced in an island growth mechanism. Surface energetic consideration can provide a certain idea of the growth mode thermodynamics [3]. However, one should be careful to apply this approach to this case because the growth is predominantly kinetically controlled.

The planar defects parallel to the surface are probably the results of coalescence between two nucleating islands. Nuclei on the different terrace sites, which are determined by the step heights of 6H-SiC substrate, fail to align with the neighboring nuclei (island) [4]. This misalignment causes the planar defects parallel to the surface. Thus, the existence of surface steps and the subsequent nucleation at these terrace sites can be potential at problem areas. This can explain the results of on-axis substrate because steps were also observed on the surface (Fig. 2(a)).

The formation of misfit dislocations can be understood in conjunction with the lattice mismatch between the film and the substrate. Since the critical thickness of the AlN/SiC system has not been obtained, a study should also be done on this topic. It may be useful to apply the strained super lattice idea [5].

#### E. Conclusion

The nature of the defects in AlN films grown by PAGSMBE was investigated through the observation of the initial stage of growth by cross-sectional HRTEM. Two types of defects were found. One was identified to be a misfit dislocations due to lattice mismatch between

AlN and SiC. The other originated from the coalescence of two islands which nucleated on the different terrace sites.

#### F. Future Research Plans

Attempts will be made to eliminate the density of the defect caused by the surface steps and island morphology. Misfit dislocations may be avoided below critical thickness. Since the critical thickness of AlN on SiC has not yet been obtained experimentally, this would be another goal of this study. Subsequently, a similar investigation should be made for SiC growth on AlN surfaces to complete pseudomorphic heterostructural studies.

#### G. References

1. Jan H. van der Merwe, *Crit. Rev. Solid State Mater. Sci.* 17(3), 187 (1991).
2. L. B. Rowland, R. S. Kern, S. Tanaka, and R. F. Davis, *J. Mater. Res.* 8(9), 2310 (1993).
3. E. Bauer and Jan H. van der Merwe, *Phys. Rev. B* 33, 3657 (1986).
4. H. L. Tsai and R. J. Marty, *Appl. Phys. Lett.* 55, 265 (1989).
5. J. W. Matthews, A. E. Blakeslee, and S. Mader, *Thin Solid Films* 33, 253 (1976).

## **XIV. Growth of Pseudomorphic Heterostructures and Solid Solutions in the AlN-SiC System by Plasma-assisted, Gas-source Molecular Beam Epitaxy**

### **A. Introduction**

A marked increase in the interest in wide band gap semiconductor materials for use in high-temperature, -power, -frequency and -speed microelectronic devices resistant to radiation and short-wavelength optoelectronic devices has recently been demonstrated on a global scale. Two candidate materials that have generated much of this interest are SiC and AlN. Two methods of simultaneously exploiting the favorable characteristics of these materials include the thin film deposition of both pseudomorphic heterostructure and alloys.

Pseudomorphic heterostructures of dissimilar semiconductor materials are the basis for quantum well and laser devices. The physical properties (e.g., lattice parameter, crystal structure, melting point and thermal expansion) as well as the optical and electronic properties (e.g., band gap and index of refraction) of SiC and AlN indicate that stable superlattice structures of these materials having the desired properties are feasible. Theoretical calculations regarding electronic structure and bonding at AlN/SiC interface [1] and critical layer thickness prior to misfit dislocation formation at interfaces in cubic AlN and SiC have been reported [2]. Rowland *et al.* [3] have described the growth of 3C-SiC/2H-AlN pseudomorphic layers on  $\alpha(6H)$ -SiC(0001) substrates by plasma-assisted, gas-source molecular beam epitaxy (PAGSMBE) using solid Al evaporated from a standard effusion cell and the gases of Si<sub>2</sub>H<sub>6</sub>, C<sub>2</sub>H<sub>4</sub> and N<sub>2</sub>. These layers contained a high density of stacking faults and microtwins caused primarily by interfacial stresses and the low stacking fault energy intrinsic to  $\beta$ -SiC.

Solid solutions of AlN and SiC have been achieved by two primary processing routes: reactive sintering of mixtures of powders of a variety of sources and thin film deposition from the vapor phase. Matignon [4] first reported the synthesis of a (AlN)<sub>x</sub>(SiC)<sub>1-x</sub> material. Rafaniello *et al.* [5,6], Ruh and Zangvil [7], Zangvil and Ruh [8,9,10], Kuo and Virkar [11] and Czeka *et al.* [12] have reported 2H solid solutions as well as mixtures of 6H, 4H, and 2H materials and the existence of a miscibility gap as a result of hot pressing and annealing studies with a variety of heat treatment schedules. The tentative phase diagram proposed by Zangvil and Ruh [9] shows a flat miscibility gap at  $\sim 1900$  °C between  $\sim 20$  and 80 wt% AlN. Above this temperature, a 2H solid solution was reported from  $\geq 20$  wt% AlN. For  $\leq 20$  wt% AlN, solutions and two phase mixtures of 6H, 4H, and 2H were observed. Thin film solid solutions have been produced in the Soviet Union by Nurmagomedov *et al.* [13] via sublimation of a sintered SiC/AlN compact at  $\geq 2100$  °C and in the United States by both Jenkins *et al.* [14] using low pressure (10–76 Torr) metalorganic chemical vapor deposition

(MOCVD) between 1200–1250 °C using SiH<sub>4</sub>, C<sub>3</sub>H<sub>8</sub>, NH<sub>3</sub>, and Al(CH<sub>3</sub>)<sub>3</sub> carried in H<sub>2</sub> on  $\alpha$ (6H)-SiC(0001) and Si(100) and by Kern *et al.* [15] by PAGSMBE at 1050 °C using the sources noted previously [3].

## B. Experimental Procedure

In the present research, a specially designed and previously described [16] PAGSMBE system was employed to deposit all AlN-SiC thin films on  $\alpha$ (6H)-SiC(0001) substrates oriented  $3.5 \pm 0.5^\circ$  off (0001) toward [11 $\bar{2}$ 0]. The substrates were chemically cleaned before growth in a 10% HF solution for 5 minutes, and loaded immediately into the UHV growth chamber. Sources of Si and C were disilane (Si<sub>2</sub>H<sub>6</sub>) and ethylene (C<sub>2</sub>H<sub>4</sub>), respectively. Aluminum (99.9999% purity) was evaporated from a standard MBE effusion cell operated in all cases at 1260 °C. A compact electron cyclotron resonance (ECR) plasma source supplied by ASTeX, Inc., operating at 100 W forward power, was used to decompose N<sub>2</sub> (99.9995% purity). Typical gas flow rates employed for heterostructure growth were 0.1–1.0 sccm Si<sub>2</sub>H<sub>6</sub>, 0.2–4.0 sccm C<sub>2</sub>H<sub>4</sub> (Si/C ratio was varied between 1/1 and 1/4) and 3.5 sccm N<sub>2</sub>. Layers of SiC and AlN were grown for 10 and 60 minutes, respectively. For solid solution growth, typical flow rates were 0.5–1.0 sccm Si<sub>2</sub>H<sub>6</sub> and 1.0–4.0 sccm C<sub>2</sub>H<sub>4</sub>. The N<sub>2</sub> (1.0 sccm) was diluted with ultra-high purity Ar (2.5 sccm) to obtain sufficient electron-atom collisions to sustain a plasma. All films were grown between 1050–1300 °C.

Reflection high-energy electron diffraction (RHEED), operating at 10 kV, was used to determine the crystalline quality of the surface of the resulting films. The chemical composition as a function of film thickness was determined using scanning Auger electron spectroscopy (AES). High-resolution transmission electron microscopy (HRTEM) operating at 200 kV was employed to observe the microstructure of the film as well as the film/substrate interfacial region.

## C. Results And Discussion

Figure 1 shows a HRTEM micrograph of a 3C-SiC/2H-AlN bilayer/6H-SiC substrate assembly, the former fabricated at 1050 °C. The AlN layer was grown for 10 minutes using 3.5 sccm N<sub>2</sub> and Al evaporated at 1260 °C. The SiC layer was grown for 60 minutes using 0.25 sccm Si<sub>2</sub>H<sub>6</sub> and 0.33 sccm C<sub>2</sub>H<sub>4</sub>. Each of the interfaces is abrupt and uniform and the layers are identically oriented with continuous atom columns indicating that the layers are epitaxial and pseudomorphic. The strain present in the AlN layer, seen as lattice fringe distortion occurs at the steps present on the SiC substrate. The 3C-SiC layer shows several <111> stacking faults. An AES depth profile of composition versus depth is shown in Fig. 2. RHEED and HRTEM analysis indicated all layers to be monocrystalline.





Figure 1. HRTEM image of an epitaxial 3C-SiC/2H-AlN pseudomorphic multilayer on  $\alpha(6H)$ -SiC(0001). Shown are positions of lattice distortion due to surface steps in the substrate and dislocations in the film.

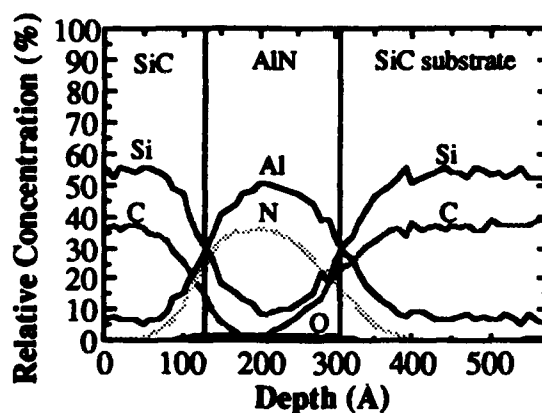


Figure 2. Auger depth profile of SiC/AlN/SiC multilayer.

Figure 3 shows a HRTEM micrograph of a monocrystalline solid solution film grown for 90 minutes at 1275 °C using 0.5 sccm  $\text{Si}_2\text{H}_6$ , 1.0 sccm  $\text{C}_2\text{H}_4$ , 3.5 sccm of Ar-diluted  $\text{N}_2$  and Al evaporated at 1260 °C. The ...ABCABC... stacking sequence indicates that this layer has a cubic crystal structure. RHEED and HRTEM analysis showed the film to be monocrystalline and smooth. The AES depth profile in Fig. 4 indicates the composition to be  $\approx (\text{AlN})_{0.2}(\text{SiC})_{0.8}$ . Previous reports by the authors [15], using the same sources, indicated that solid solutions of the composition  $(\text{AlN})_{0.3}(\text{SiC})_{0.7}$  resulted in 2H solid solutions. This suggests that a cubic to hexagonal structural change occurs between 20 and 30% AlN for alloys in the AlN-SiC system; however, additional research must be conducted to confirm this hypothesis.

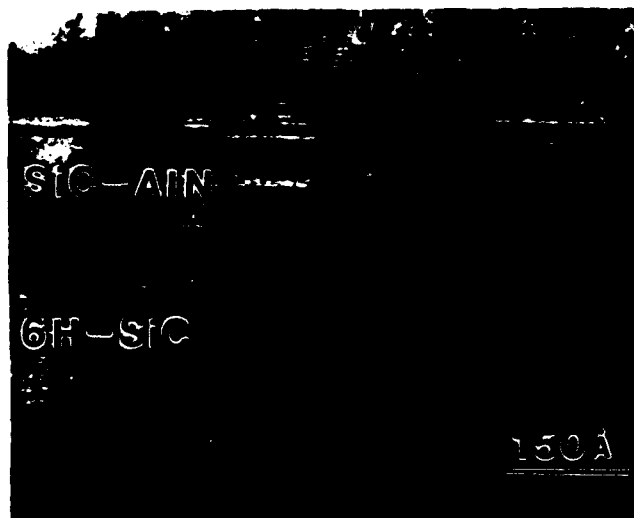


Figure 3. HRTEM image of an epitaxial  $(\text{AlN})_x(\text{SiC})_{1-x}$  solid solution on  $\alpha(6\text{H})\text{-SiC}(0001)$ .

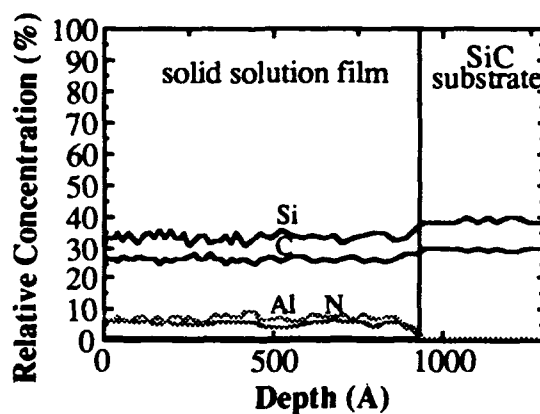


Figure 4. Auger depth profile of an  $(\text{AlN})_x(\text{SiC})_{1-x}$  solid solution containing  $\approx 20\%$  AlN.

#### D. Conclusions

Monocrystalline pseudomorphic heterostructures and solid solutions of AlN and SiC have been grown by PAGSMBE on  $\alpha(6\text{H})\text{-SiC}(0001)$  substrates oriented  $3.5 \pm 0.5^\circ$  off (0001) toward  $[11\bar{2}0]$ . The superlattice materials were pseudomorphic and possessed abrupt interfaces; however, lattice distortion was present in the AlN layers and stacking faults occurred in the 3C-SiC layers. Cubic (zincblende) solid solution films containing 20% AlN were also achieved.

#### E. Future Plans

Studies optimizing growth of SiC on AlN to reduce stacking fault densities and improve crystalline quality are presently underway. Variables such as temperature, flow ratios and pressure are currently being considered. Attempts to grow AlN-rich solid solution films, which would be blue or UV light emitters are also underway.

#### F. References

1. W. R. L. Lambrecht and B. Segall B, Phys. Rev. B **43**, 7070 (1991).
2. M. E. Sherwin and T. J. Drummond, J. Appl. Phys. **69**, 8423 (1991).
3. L. B. Rowland, R. S. Kern, S. Tanaka and R. F. Davis, Appl. Phys. Lett. **62**, 3333 (1993).
4. C. Matignon, Compt. Rend. hu. L' Acad. Sci. **178**, 1615 (1924).
5. W. Rafaniello, K. Cho and A. V. Vikar, J. Mat. Sc. **16**, 3479 (1981).
6. W. Rafaniello, M. R. Plinchta and A. V. Vikar, J. Am. Ceram. Soc. **66**, 272 (1983).
7. R. Ruh and A. Zangvil, J. Am. Ceram. Soc. **65**, 260 (1982).
8. A. Zangvil and R. Ruh, Mat. Sc. Eng. **71**, 159 (1985).
9. A. Zangvil and R. Ruh, J. Am. Ceram. Soc. **71**, 884 (1988).
10. A. Zangvil and R. Ruh in *Silicon Carbide '87*, American Ceramic Society, Westerville, OH, 1989, pp. 63-82.
11. S. Kuo and A. V. Vikar, J. Am. Ceram. Soc. **73**, 2460 (1990).
12. C. L. Czka, M. L. J. Hackney, W. J. Hurley, Jr., L. V. Interrante, G. A. Sigel, P. J. Shields and G. A. Slack, J. Am. Ceram. Soc. **73**, 352 (1990).
13. Sh A. Nurmagomedov, A. N. Pitkin, V. N. Razbegaev, G. K. Safaraliev, Yu M. Tairov and V. F. Tsvetkov, Sov. Phys. Semicond. **23**, 100 (1989).
14. I. Jenkins, K. G. Irvine, M. G. Spencer, V. Dmitriev and N. Chen, J. Cryst. Growth **128**, 375 (1993).
15. R. S. Kern, L. B. Rowland, S. Tanaka and R. F. Davis, J. Mater. Res. **8**, 1477 (1993).
16. L. B. Rowland, R. S. Kern, S. Tanaka, and R. F. Davis, in *Proceedings of the Fourth International Conference on Amorphous and Crystalline Silicon Carbide*, edited by C. Y. Yang, M. M. Rahman, and G. L. Harris (Springer-Verlag, Berlin, 1992), p. 84-89.

## XV. Growth of Aluminum Nitride Crystals by Sublimation

### A. Introduction

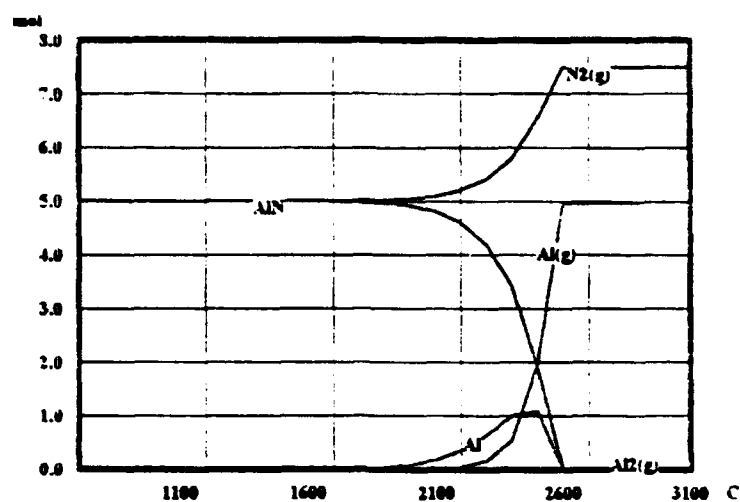
Many high frequency and high temperature electronic and optoelectronic device applications are in strong demand of a suitable material that could perform without deterioration under the conditions required by the application. Aluminum nitride among some other III-V compounds is an excellent choice as a material for active and passive components in electronic circuits for such applications. Also because of its high electrical resistivity ( $>10^{13}$  W-cm) and good thermal conductivity (2W/cm-K) [7] it can be used as a substrate material to carry the Si chips containing these circuits. Due to its large band gap (6.2 eV @ 300K) aluminum nitride is frequently considered for use for optical devices that can operate throughout the entire visible spectrum and into the medium, ultraviolet wavelengths. Having the highest ever reported surface acoustic velocity [1] value AlN is a candidate for many piezoelectric applications. Excellent review articles are available for further information on aluminum nitride [2-5]. However all proposed applications are still waiting for good quality aluminum nitride single crystals. It is the purpose of this research to investigate a suitable method and establish growth conditions for producing bulk aluminum nitride single crystals.

Due to its high melting point and its instability near the melting temperature most AlN single crystal material has been grown from the vapor phase. When the literature is reviewed it can be seen that majority of research on growth of aluminum nitride has been concentrated on chemical vapor transport due its easy integration to the present semiconductor technology. However no researcher has yet reported producing single bulk crystals of AlN.

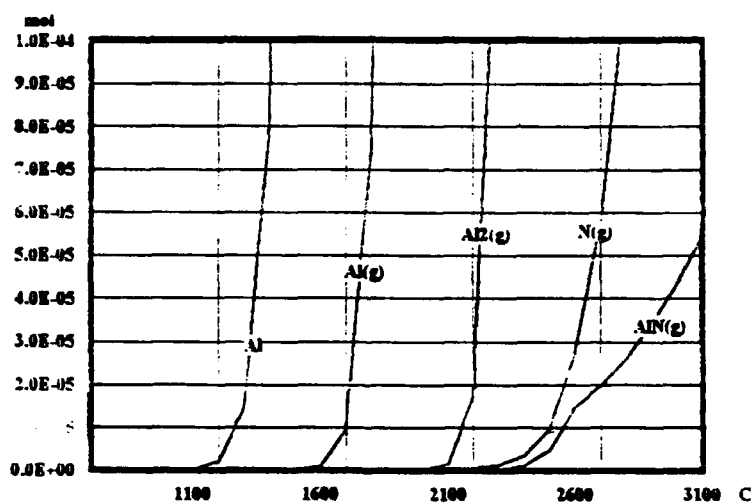
Aluminum nitride evaporates at appreciable rates above 1800°C and under 1 atm pressure. Sublimation takes place according to the following reaction:



Although thermodynamically a very small amount of AlN(g) should exist upon sublimation it has not been detected by any scientist, see Fig. 1. The exact mechanism of sublimation is not known i.e., whether Al and N become adsorbed on the surface prior to evaporation or not, but once nitrogen leaves the surface the existence of N<sub>2</sub> inevitable for experimental conditions employed in this research. It has been calculated that at 2000 °C half time of a nitrogen atom leaving the evaporation surface is  $10^{-4}$ – $10^{-3}$  seconds [11]. From the simple diffusion equation,  $X=(Dt)^{1/2}$  it can be calculated that at any distance greater than 2.5μm from the surface nitrogen will be in its diatomic form.



(a)



(b)

Figure 1. Sublimation behaviour of AlN [12].

### B. Experimental Procedures

As stated in the previous section, the chosen method to grow aluminum nitride crystals in the present study involves the sublimation of a polycrystalline AlN source. The basic idea is to create a 20 to 100 °C temperature difference between the source and the substrate and by this way to recondensate the sublimed AlN on the substrate. For this purpose a vertical graphite furnace was utilized. The furnace used has a natural (built-in) temperature gradient due to its shape. Please see Fig. 2 for a better understanding of the experimental set-up.

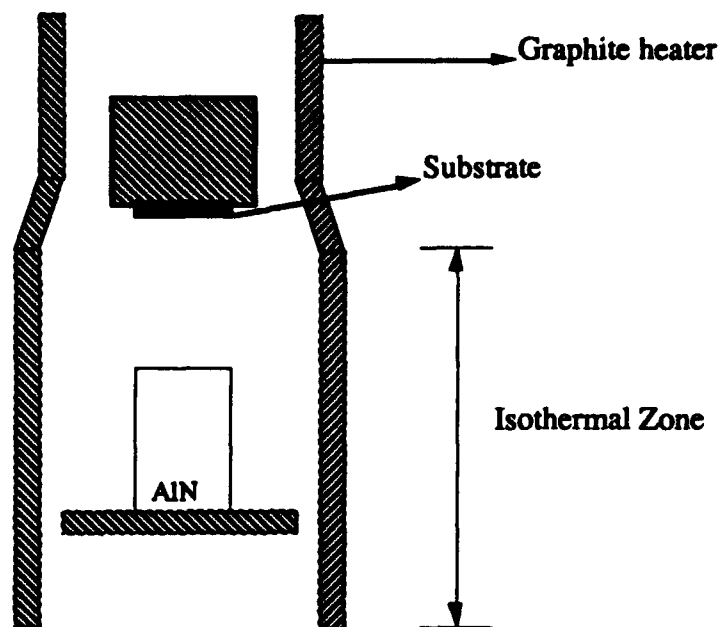


Figure 2. Configuration used for sublimation growth of AlN.

To begin the study, while the pressure is kept at 1 atm, temperatures ranging from 1850°C to 2300°C were experimented for a suitable evaporation rate for the polycrystalline AlN. It was our finding that for an efficient growth process temperature of the polycrystalline source must be between 2000°C and 2200°C at 1 atm. The evaporation rates at this temperature range roughly changes between 30mg and 1000mg/hr. Although temperature gradient was primarily controlled by furnace characteristics, by varying the substrate height with respect to the source a temperature difference of 80 to 100°C was obtained. It is essential to have a smaller difference as the evaporation temperature is lowered. Reason for this is that molecules that are reaching the surface need enough thermal energy or surface mobility to arrange them in an orderly manner to form a solid coating. When this requirement was not met material morphology ranging from loosely bonded powder to individual crystal chunks were obtained.

The substrate to source distance is another crucial parameter in this method. Distances from few mm to 3-4 cm were tested for suitability for the process. One very distinct effect of separation distance on growth is that, as the separation increases the deposition yield drops drastically. As an example the difference in deposition yield 3 mm is roughly 30 times more than the yield at 15 mm separation. Most promising results were obtained at separation distances in the range of 1 to 10 mm.

Due to its small lattice mismatch and stability at the temperatures employed, single crystal SiC wafers were used as substrate. Also SiC substrates coated with thin layers of AlN by molecular beam epitaxy were used in some experiments but no conclusive results have been obtained yet.

Pressure was kept at 1 atm in the majority of the experiments since already there exists a number of parameters that can be varied. The only net effect that was observed by lowering the system pressure was the increased evaporation rate of the source material. All the experiments were carried out under nitrogen atmosphere.

---

Table I. Typical growth parameters

---

Substrate temperature	1950°C–2150°C
Source temperature	2000°C–2200°C
Pressure range	100torr–760 torr
Source - substrate separation	1mm–40mm

---

#### C. Results and Discussion

AlN crystals were grown on SiC substrates. The layers were approximately 0.2 to 0.5 mm in thickness. See Fig. 3. A range of growth parameters were obtained for sublimation growth aluminum nitride. Best results were obtained at 3-4 mm separation at 2200°C source temperature and 2150°C substrate temperature. Resulting deposit was proven to be AlN by X-rays. A major difficulty that was faced was to maintain a constant temperature gradient as crystals grows. It essential to keep the growth conditions constant at the growing surface of the crystal for monocrystalline growth.

#### D. Conclusions

Results obtained from the experiments conducted to date indicates that deposition of single crystal AlN has a high feasibility with a improved design. It has been proven that the idea of creating a temperature gradient and solidifying the sublimed material on cool substrate is indeed an efficient way to grow bulk single crystals of aluminum nitride. Growing longer crystals will require a better equipment design in order to achieve necessary conditions.

#### E. Future Research Plans

Above described method will be further investigated for bulk crystal growth of aluminum nitride. To grow thicker crystals it is necessary to design a new system where the growth conditions could kept constant throughout the growth process. Also effect of reduced pressure on growth will be determined.

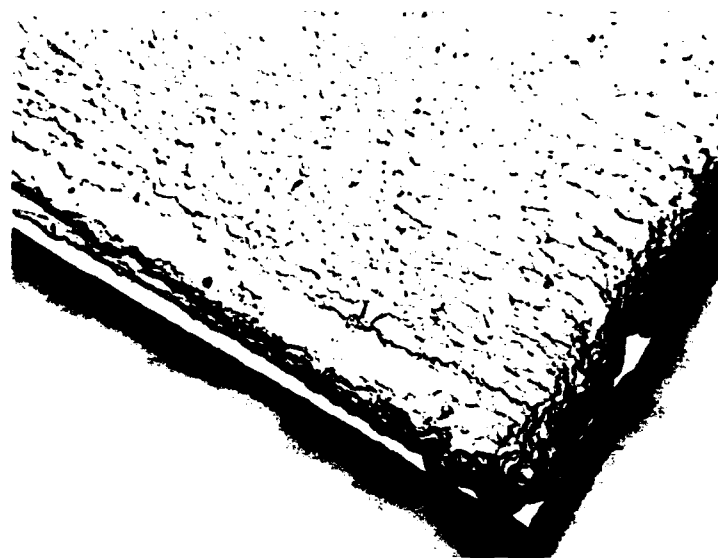


Figure 3. AlN on SiC.

#### F. References

1. G. R. Kline and K. M. Lakin, Proc. IEEE Symp. Ultrasonics **14**, 340 (1983).
2. M. T. Duffy, in Heteroepitaxial Semiconductors for Electronic Devices, G. W. Cullen and C. C. Wang, Eds., Springer Verlag, Berlin (1978), pp.150-181.
3. R. F. Davis, Proc. IEEE **79**, 702 (1991).
4. S. Strite and H. Morkoc, J. Vac. Sci. Technol. B **10**, (1992)
5. J. H. Edgar, J. Mater. Res. **7**, 235 (1992).
6. C. O. Dugger, Mat. Res. Bull. **9**, 331, (1974).
7. G. A. Slack and T. F. McNelly, J. Crys. Gro. **34**, 263, (1976).
8. G. A. Slack and T. F. McNelly, Final technical report, AFOSR Contract F44620-76-C-0039K, March (1978).
9. P. Bhattacharya and D. Bose, Jap. J. Appl. Phys. **10**, L1750, (1991).
10. A. T. Collins, E. C. Lightowers, P. Dean, J. Phys. Rev. **158**, 883, (1960).
11. P. M. Dryburgh, The Ninth International Conference on Crystal Growth, ICCG-9 (1989).
12. HSC Chemisrty, Chemical Reaction and Equilibrium Software. Outokumpu Research, Finland.



## XVI. Application of Epitaxial Aluminum Nitride (AlN) in Metal-Insulator Semiconductor Structures

### A. Introduction

The large band-gap (6.2eV) and good thermal stability (0.05 Torr equilibrium vapor pressure of nitrogen at 1500°C) indicate that AlN films have considerable potential as a dielectric in electronic devices. There are several published papers [1-4] which describe the investigations and the applications of AlN films as insulators in several MIS structures containing Si and GaAs. However, in all these studies the AlN films were polycrystalline.

We have shown in previous reports that AlN films with low defect densities can be epitaxially deposited on SiC substrates by the use of a modified gas source MBE system [5]. In this paper, we have investigated the application of epitaxial AlN films as insulators in SiC MIS structures. The electrical properties of the AlN insulator layers have been studied using current voltage (I-V) and high-frequency capacitance-voltage (hf C-V) measurements.

### B. Experimental Procedure

The MIS structure was fabricated using a commercial Perkin-Elmer 430 MBE system. This system consists of three parts: a load lock (base pressure of  $5 \times 10^{-8}$  Torr), a transfer tube (base pressure of  $1 \times 10^{-10}$  Torr), which also was used for degassing the substrates, and the growth chamber (base pressure of  $5 \times 10^{-11}$  Torr). A Knudson effusion cell with a BN crucible and a Ta wire heater was charged with 6N pure aluminum. Ultra-high purity nitrogen, further purified by a chemical purifier, was used as the sources gas. The nitrogen was excited by an ECR plasma source, which was designed to fit inside the 2.25 inch diameter tube of the source flange cryoshroud.

The substrates were n-type ( $n = 6.4 \times 10^{16} \text{ cm}^{-3}$ ), vicinal  $\alpha(6H)\text{-SiC}(0001)$  wafers oriented  $3\text{-}4^\circ$  towards [1120] and supplied by Cree Research Inc. An ohmic Ni contact was deposited on the backside. Prior to deposition, the substrates were cleaned by a standard degreasing procedure, chemically cleaned in a 10% HF solution for five minutes, mounted on a 3-inch molybdenum block, loaded into the system, heated to 700°C for 30 minutes in the transfer tube under UHV conditions to remove surface hydrocarbons and transferred into the deposition chamber.

A 125 Å thick of epitaxial AlN was deposited on the  $\alpha\text{-SiC}$  wafer at 1100°C, followed by *in situ* deposition of Al-metal layer at room temperature. The details of the epitaxial deposition conditions of AlN film can be found in Ref. [5]. To form MIS diodes, the top Al-layer was patterned by standard lithographic etching techniques as circular dots of radius 50  $\mu\text{m}$  and annealed at 400°C for half hour in the vacuum. The schematic diagram of the MIS structure was shown in Fig. 1.

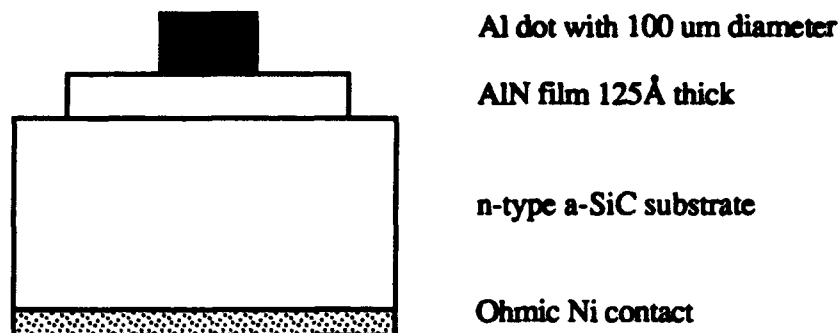


Figure 1. Schematic diagram of AlN MIS diode.

Direct I-V and hf C-V characteristics of the MIS structures at different temperature were characterized using a Hewlett Packard 4145 Semiconductor Parameter Analyzer and a Keithley M590CV Analyzer, respectively.

### C. Experimental Results

The experimental I-V curves of the MIS structure at two different temperatures are shown in Fig. 2. Rectifying behavior was observed. The forward bias current increased with an increase of the forward bias voltage. The breakdown field of the AlN MIS structure was  $\approx 13.4$  MV/cm at room temperature; the value was slightly smaller, 13 MV/cm, at 300°C. The reverse bias currents are very small for both temperatures and no breakdown occurred even for the field larger than 70 MV/cm.

The results of hf C-V measurements of the MIS diode are shown in Fig. 3. These measurements were made using a 100 kHz AC signal. Figure 3 indicates that the diode could be swept from accumulation to inversion. Hysteresis in the C-V trace was observed when the voltage ramp direction was reversed. The diode also exhibited a positive flat band voltage. From the film thickness and accumulation capacitance data, the dielectric constant of AlN insulator layer at 100kHz was estimated as  $\sim 14$ , which is higher than what has been reported [3,6].

### D. Discussion

The recent advances of III-V nitride film quality have resulted in the successful fabrication of a variety of III-V nitride based devices [7-9]. It is expected that it will become important to study and develop the proper insulating material for III-V nitride devices. For many years, the potential of using AlN as dielectric insulator due to its large band gap and good thermal stability has been realized. There were several reported investigations of the use of AlN as an insulator in MIS structures. However most of the work conducted to date has

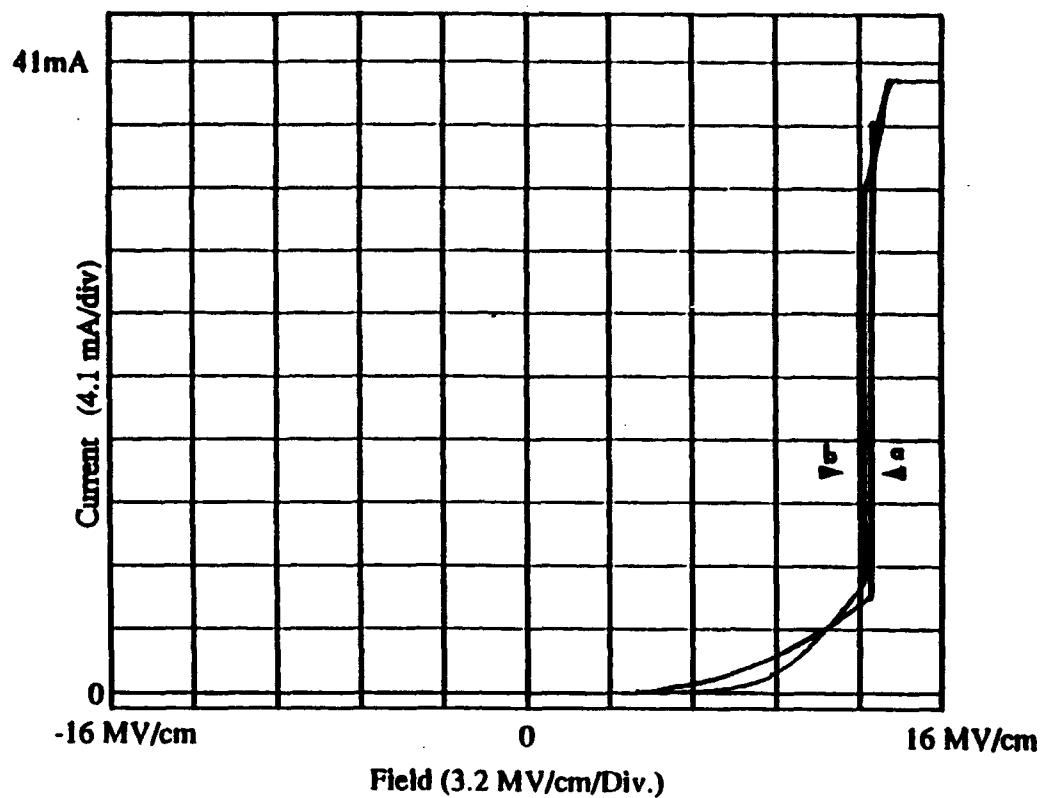


Figure 2. I-V curve for AlN MIS diode measured at (a) room temperature; (b) 300°C.

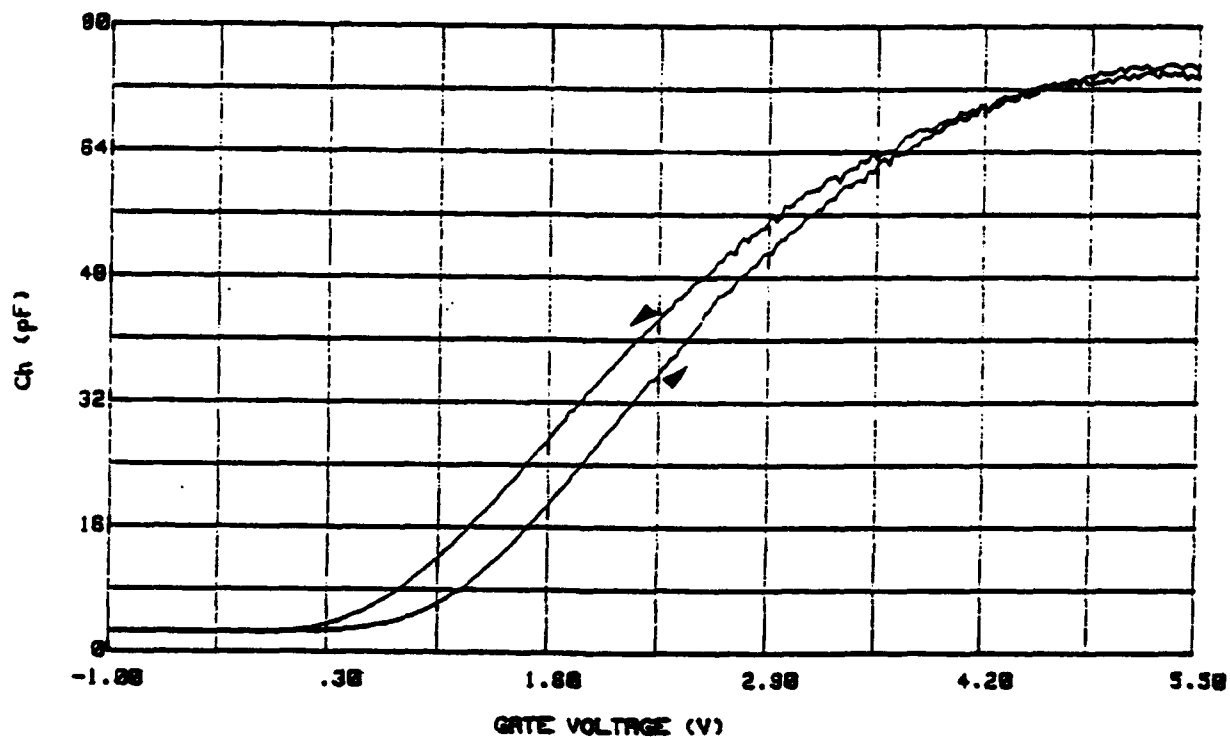


Figure 3. C-V curve of AlN MIS diode measured at 100 kHz of frequency.

been on Si or GaAs substrates, and the AlN film films were polycrystalline. We are for the first time reporting the use of monocrystalline epitaxial AlN films as the insulator in a SiC MIS structure. The dielectric properties of AlN have been studied and the AlN MIS structure has been demonstrated to be operative at high temperature (300°C). The significance of this work is that the application of epitaxial AlN as an insulator can simplify the III-V device process. However, this study is preliminary. More detailed investigations are needed to fully understand the dielectric properties of the AlN films, including the determination of the interface state densities and reducing the methods for the leakage currents before they can be successfully used in device structures.

As we have shown above, the AlN MIS structure exhibited both rectification behavior and unwanted leakage currents. These phenomena may be explained using the band diagram in Fig. 4. Under reverse bias, the SiC semiconductor substrate is in the depletion mode, therefore, the majority of the applied voltage is dropped across the depletion region, as shown in Fig. 4(b). Under forward bias, the semiconductor region is in an accumulation state; therefore, a large part of the voltage is across the barrier, which causes severe band bending at the interface, as shown in Fig. 4(c). This band bending reduces the effective barrier height and increases the probability of tunneling through the thin barrier region. Both of these factors lead to a large leakage currents. It is expected that by increasing the AlN thickness, and using the metals with higher work function, the probability of band bending and tunneling would be suppressed and the leakage current reduced.

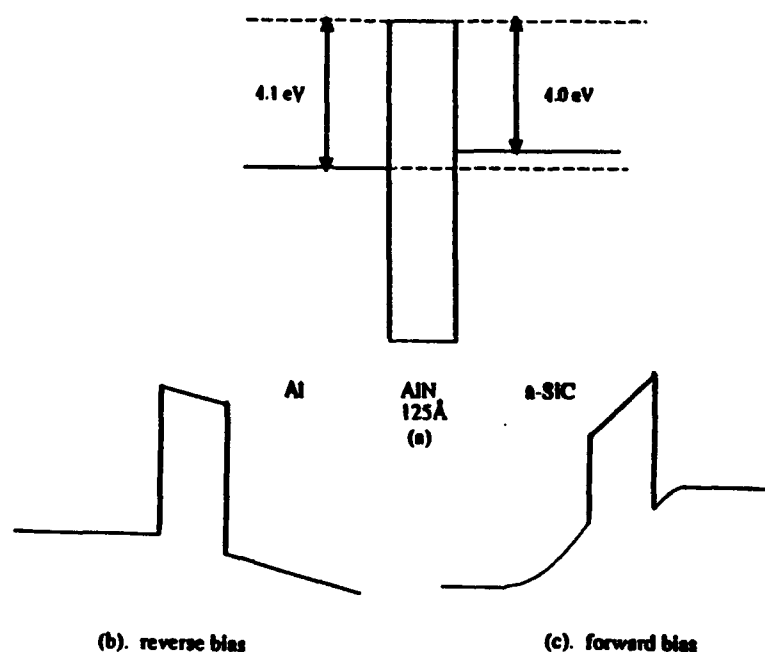


Figure 4. Band diagram of AlN MIS structure under the bias conditions: (a) no bias; (b) reverse bias; (c) forward bias.

#### E. Summary

A preliminary investigation of the use of monocrystalline epitaxial AlN in an SiC MIS structure has been conducted. The breakdown field of AlN was estimated to be 13.4 MV/cm at room temperature. At 300°C, the breakdown decreased slightly to 13 MV/cm. Capacitance-voltage characteristics showed that the diode could be swept from accumulation to inversion. The dielectric constant has been estimated as ~14.

#### F. References

1. S. Mirsch and H. Reimer, *Phys. Stat. Sol.* 11, 631 (1972).
2. E. A. Irene and V. J. Silvestri, *J. of Electronic Materials* Vol.4, 409 (1975).
3. T. L. Chu and R. W. Kelm, *J. Electrochem. Soc.* 122, 995 (1975).
4. Y. Mochizuki, M. Mizuta, S. Fujieda and Y. Matsumoto, *J. Appl. Phys.* 67, 2466 (1990).
5. C. Wang, K. S Ailey, K. L. More and R.F. Davis, in press (1993).
6. A. T. Collins, E. C. Lightowers and P. J. Dean, *Phys. Rev.* 158, 833 (1967).
7. R. F. Davis, *Proc. IEEE* 79, 702 (1991).
8. A. M. Khan, J. K. Kuzina and R. T. Olson, *Appl. Phys. Lett.* 62, 1786 (1993).
9. S. Strite and H. Morkoc, *J. Vac. Sci. Technol.* B10, 1237 (1992).

## **XVII. Metalorganic Chemical Vapor Deposition (MOCVD) of III-V Nitrides**

### **A. Introduction**

The potential semiconductor and optoelectronic applications of the III-V nitrides has prompted significant research in thin film growth and development. The materials of concern in this section are AlN and GaN, specifically, with InN and layered nitrides receiving some attention. Because GaN in the wurtzite structure with a bandgap of 3.4 eV [1] forms continuous solid solutions with both AlN and InN, for example, which have bandgaps of 6.2 eV [2] and 1.9 eV [3], respectively, engineered bandgap materials could result in optoelectronic devices active from the visible to deep UV frequencies [4].

For growing III-V nitrides Metalorganic Chemical Vapor Deposition (MOCVD) has presently gained favor over Atomic Layer Epitaxy (ALE) and layer-by-layer approaches because of the desire to have higher growth rates. CVD also offers higher deposition temperatures beneficial in improving growth characteristics. Thus, a fully operational cold-wall vertical barrel MOCVD reactor system has been built. GaN, AlN, InN, their solid solutions, graded layer structures and heterostructures can be grown. The CVD system also has the capabilities for introducing p- and n-type dopants for incorporation into the growing thin films.

Experimental procedures, results to date, conclusions and plans for future work will be included here.

### **B. Experimental Procedure**

For growing the III-V nitrides the gallium, aluminum and indium sources are triethylgallium (TEG)[Ga(C<sub>2</sub>H<sub>5</sub>)<sub>3</sub>], triethylaluminum (TEA)[Al(C<sub>2</sub>H<sub>5</sub>)<sub>3</sub>] and trimethylindium (TMI)[In(CH<sub>3</sub>)<sub>3</sub>], respectively, installed in the familiar bubbler arrangement with nitrogen used as the carrier gas. TE(G,A) was chosen over TM(G,A) because of its lower decomposition temperature range and a lower carbon incorporation in the growing film during surface decomposition reactions [4]. However, for InN deposition TMI is the organometallic of choice. This results because the TEI precursor is much less thermally stable than its methyl counterpart and undergoes appreciable decomposition starting at 40°C [5] as compared to 270-300°C for TMI [6-9]. Ammonia (NH<sub>3</sub>) is used as the nitrogen source. The system is also equipped with an n-type dopant species, silane (SiH<sub>4</sub>) 8.2 ppm in N<sub>2</sub>, and a p-type dopant organometallic species, bis-cyclopentadienyl magnesium (Cp<sub>2</sub>Mg)[Mg(C<sub>5</sub>H<sub>5</sub>)<sub>2</sub>], with nitrogen as its carrier gas.

Substrates generally used are  $\alpha$ (6H)-SiC (0001) 3° off-axis toward [11 $\bar{2}$ 0]. These SiC wafers are received with a thin (~ 750Å) surface oxide layer. The wafers are cleaned in a 10% HF solution, dried and immediately loaded into the load lock and onto a SiC-coated

graphite susceptor. With the diffusion pump, base pressures near  $1 \times 10^{-5}$  torr are reached before deposition begins. The CVD system schematic is included below to better illustrate the system's features and capabilities, see Fig. 1.

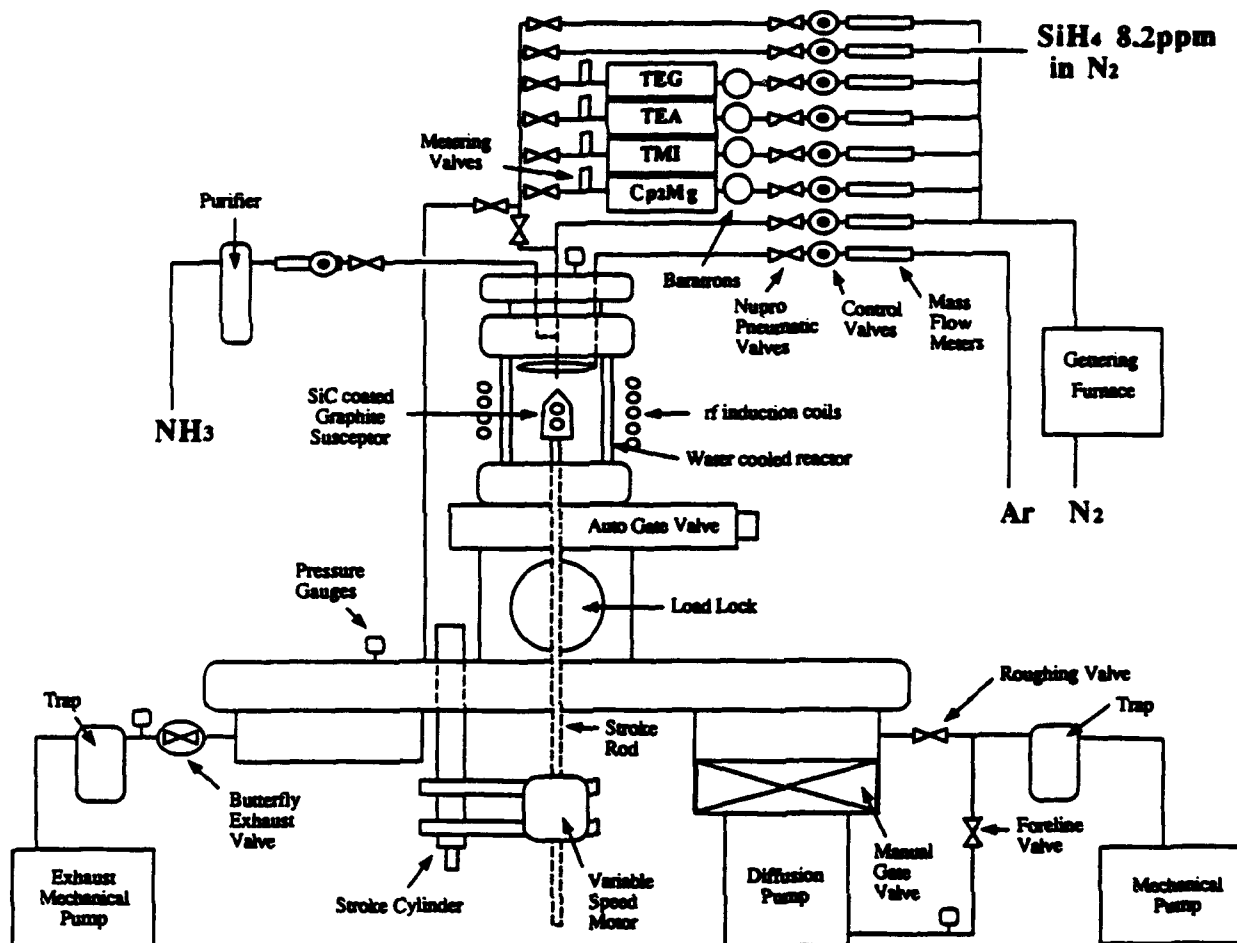


Figure 1. CVD System Schematic.

Once the required base pressure is reached, the manual gate valve to the diffusion pump is closed. With the butterfly exhaust valve controller in the auto mode and the desired run pressure dialed in, the  $N_2$  diluent and Ar curtain-ring gases are ramped up to their preset flow rates. The inert argon curtain-ring is used in an effort to retard unwanted deposition on the water-cooled quartz reactor walls. At this time susceptor rotation of approximately 5 rpm begins. As the pressure is equilibrating at the desired level, the rf induction heating power generator is tuned to the proper power setting. The temperature of the susceptor is monitored using a Leeds & Northrup Optical Pyrometer.

Once the setpoint temperature has been reached, the proper bubbler pressures and carrier gas flow rates are established corresponding to the desired amounts of precursor materials. These gases bypass the reactor and are sent directly to "vent" during equilibration.

Simultaneously, the  $\text{NH}_3$  is ramped up to its setpoint. Generally, the ammonia flows for only a few seconds before the column-III organometallics and dopants, if applicable, are switched from "vent" to "run." Once the MO precursors are diverted into the reactor chamber film deposition begins.

During growth it is imperative to monitor gas flow rates, cooling water flow and susceptor temperature to help improve growth uniformity. Once the desired deposition time has elapsed, the run is terminated in reverse order. The column-III precursors (and dopants) are switched off, as is the rf power supply if no post-growth annealing is necessary. Usually the sample remains under flowing  $\text{NH}_3$ ,  $\text{N}_2$  and Ar until it cools below approximately  $500^\circ\text{C}$ . At this point the  $\text{NH}_3$  is switched off and the sample continues to cool under flowing nitrogen and argon for an additional hour and a half. After this length of time, all the gases and cooling water lines can be closed off. The reactor chamber is then evacuated and refilled with argon at least once before removing the sample.

Reflection high-energy electron diffraction (RHEED) was used to investigate the microstructure and crystallinity of the deposited films. Scanning Electron Microscopy (SEM) was employed for observing the surface morphologies and cross-sectional thicknesses of the deposited films.

### C. Results

*CVD of AlN.* Deposition of AlN and attempts at doping have been an area of vigorous research. The parameters of temperature, pressure and TEA flux have been systematically varied while seeking to optimize AlN growth. TEA flow rates of 6.02, 8.03, 11.95 and 17.54  $\mu\text{mol}/\text{min}$  have been used to grow AlN samples at  $1000^\circ\text{C}$  and a total system pressure of 45 torr. The other variables of interest remained constant throughout the series of these experiments and were as follows:  $\text{NH}_3$  flow rate = 1.5 slm,  $\text{N}_2$  flow rate = 1.5 slm and Ar curtain-ring flow rate = 1.5 slm. The RHEED patterns of the above described samples varied very little. Each pattern revealed streaky spots and Kikuchi lines. The patterns were indicative of the wurtzite structure and apparently a monocrystalline film. Figures 2 and 3 show typical examples of the MOCVD grown AlN on SiC at  $1000^\circ\text{C}$ .

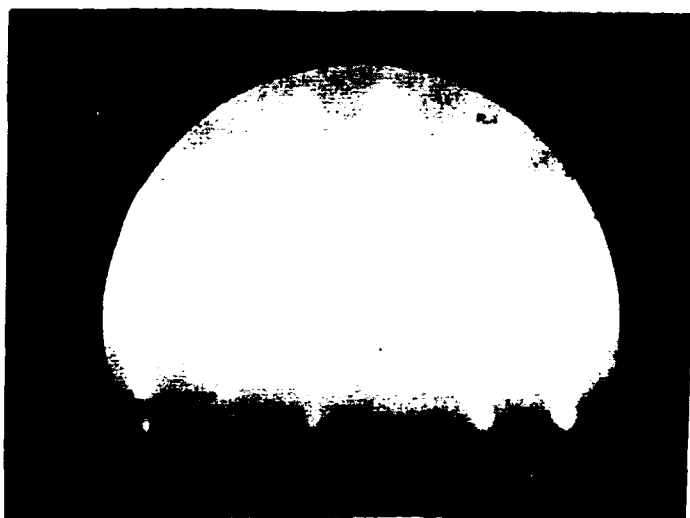
Attempts have been made to p-type dope AlN using the magnesium source,  $\text{Cp}_2\text{Mg}$ . Two samples with TEA flow rates of 8.03  $\mu\text{mol}/\text{min}$  and 17.54  $\mu\text{mol}/\text{min}$ , respectively, with all other variables the same as listed above have been grown at  $1000^\circ\text{C}$  and 45 torr. The  $\text{Cp}_2\text{Mg}$  flow rate was 1.19  $\mu\text{mol}/\text{min}$  for each run. After terminating the TEA and  $\text{Cp}_2\text{Mg}$  flows, the  $\text{NH}_3$  flow was also switched off, but the susceptor was kept at temperature (i.e.  $1000^\circ\text{C}$ ) for an additional ten minutes in flowing  $\text{N}_2$  and Ar. Recall, this is not the same procedure for cooling undoped samples. The samples were annealed in a non-hydrogen environment in an effort to liberate any incorporated hydrogen atoms in the film that may be tying up the p-type





[2 $\bar{1}\bar{1}$ 0] Azimuth

Figure 2. RHEED pattern for AlN deposited on  $\alpha(6H)$ -SiC at 1000°C. TEA flow rate was 8.03  $\mu\text{mol/min}$ .



[2 $\bar{1}\bar{1}$ 0] Azimuth

Figure 3. RHEED pattern for AlN deposited on  $\alpha(6H)$ -SiC at 1000°C. TEA flow rate was 17.54  $\mu\text{mol/min}$ .

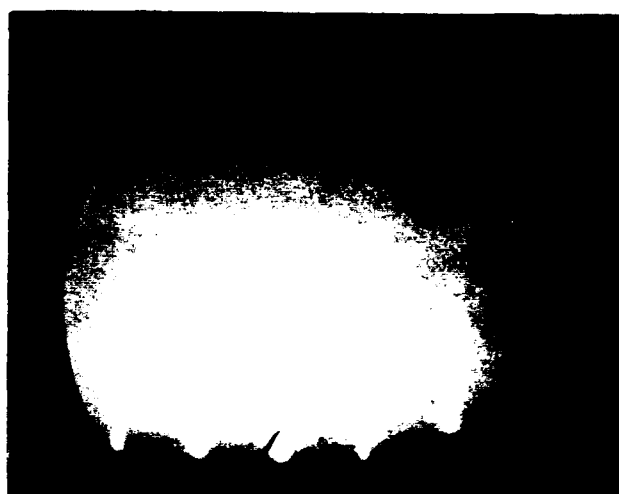
acceptors. In a global effort to minimize the amount of hydrogen entering the growth reactor, nitrogen and not the usual hydrogen is used as the diluent gas, the carrier gases and also as the balance gas in the very dilute concentration of silane. Hall mobility measurements and carrier concentration determinations of these doped films are forthcoming.

Other attempts at growing AlN have been conducted at 1100°C and 45 torr. To date, TEA flow rates of 8.03, 11.95 and 17.54  $\mu\text{mol/min}$  have been used to grow thin films, with all other parameters the same as listed above. Several RHEED images of selected AlN samples grown at 1100°C are shown below, see Figs. 4 and 5.



$[\bar{2}\bar{1}10]$  Azimuth

Figure 4. RHEED pattern for AlN deposited on  $\alpha(6\text{H})\text{-SiC}$  at 1100°C. TEA flow rate was 11.95  $\mu\text{mol/min}$ .



$[\bar{2}\bar{1}10]$  Azimuth

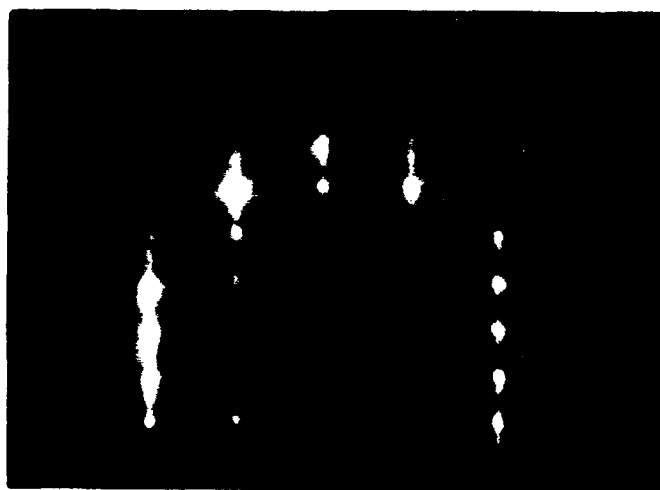
Figure 5. RHEED pattern for AlN deposited on  $\alpha(6\text{H})\text{-SiC}$  at 1100°C. TEA flow rate was 17.54  $\mu\text{mol/min}$ .

*CVD of GaN.* Numerous GaN samples have been grown under a wide range of growth parameters. In short, between a total system pressure of between 30 torr and 57 torr, a TEG flow rate of 10.2  $\mu\text{mol/min}$ ,  $\text{NH}_3$  at 1 slm,  $\text{N}_2$  at 1.5 slm and Ar at 100 sccm has produced the best quality films to date. RHEED images of GaN films grown under the above conditions at 30 torr and 57 torr are shown below, see Figs. 6 and 7.



$[2\bar{1}\bar{1}0]$  Azimuth

Figure 6. RHEED pattern for GaN deposited on  $\alpha(6H)\text{-SiC}$  at  $1000^\circ\text{C}$  and 30 torr. TEG flow rate was 10.2  $\mu\text{mol/min}$ .



$[2\bar{1}\bar{1}0]$  Azimuth

Figure 7. RHEED pattern for GaN deposited on  $\alpha(6H)\text{-SiC}$  at  $1000^\circ\text{C}$  and 57 torr. TEG flow rate was 10.2  $\mu\text{mol/min}$ .

*CVD of InN.* Attempts at growing InN directly on SiC using the layer-by-layer approach described in a previous report has resulted in only "pools" of indium being deposited. Using the CVD system, attempts were made to deposit InN on both GaN and AlN buffer layers. After a GaN buffer layer was grown at 1000°C and 57 torr, the susceptor was cooled to 800°C and the run pressure was increased to 200 torr. Then the TMI flow rate was set to 12.24  $\mu\text{mol/min}$  with  $\text{NH}_3$  and  $\text{N}_2$  both set at 1.5 slm. The InN growth period lasted one hour.

Similarly in another experiment, after a AlN buffer layer was grown at 1000°C and 30 torr, the susceptor temperature was cooled to 650°C and the run pressure was again increased to 200 torr. All other InN deposition parameters, except temperature, remained the same as for the GaN buffered film, including deposition time.

Utilizing EDS and AES, virtually no observable InN grown at 800°C was detected on the GaN buffer layer. SEM of this sample showed only a smooth, featureless surface, presumably that of the GaN buffer layer. However, the InN film grown at 650°C on AlN was easily detectable by EDX and also visible via SEM. The SEM micrograph of InN revealed a uniformly faceted, highly oriented surface texture, not unexpected for a growth temperature of 650°C. The facets were approximately 1200Å in size.

#### D. Discussion

The as-grown AlN films have proven to be very highly resistive. This has caused substantial charging problems when trying to image the surfaces and especially the cross-sectional thicknesses using SEM. Carbon-coating the samples proved to be no help in alleviating the charging problems. Thus, accurate growth rates could not be determined for the various AlN samples grown. Also since cleaving a sample for use in obtaining cross-sectional thickness via SEM is destructive, ellipsometry will begin to be used for determining the thickness of deposited films. Otherwise, using SEM the AlN surfaces appeared uniform and featureless. No faceting was observed.

These high impedance materials, especially AlN, also inhibit the accurate, if any, measuring of Hall mobilities and carrier concentrations. For these reasons, it is imperative that one be able to appreciably dope these materials to improve carrier concentrations, increase mobilities and decrease their resistivities.

For InN growth, two important findings need to be addressed. Firstly, at less than atmospheric pressures it appears that InN can not be grown at temperatures much greater than 650°C. Secondly, at temperatures  $\leq 650^\circ\text{C}$  an AlN buffer layer on SiC (or presumably a GaN buffer layer) is a necessary aid for heteroepitaxy of InN on SiC.

## E. Conclusions

Apparent monocrystalline AlN and GaN thin films have been grown using a vertical MOCVD reactor system. The AlN was grown at both 1000°C and 1100°C. The GaN was deposited at 1000°C. Also, a highly oriented InN film was deposited on an AlN buffer layer on SiC at 650°C.

## F. Future Research Plans/Goals

Investigating the effects on growth upon varying certain deposition parameters such as temperature, pressure, MO flow rate and III/V input ratios will continue in an effort to optimize growth conditions from a microstructural and electrical property point of view.

Deposition of III-V nitride using GaN and/or AlN buffer layers will be attempted. The use of a buffer layer may reduce the effects of lattice mismatch between the SiC substrate and the depositing film and aid in the growth of more desirable, non-faceted, uniformly smooth films.

Because of the highly resistive nature of the nitride films, p- and n-type doping of GaN and especially AlN must be accomplished in order to more accurately measure Hall mobilities and carrier concentrations. Photoluminescence and cathodoluminescence characteristics will also be investigated on future samples. SIMS, in conjunction with Hall measurements, will be used to compare dopant concentrations versus activated majority charge carriers. A grand goal would be to fabricate a simple devices such as a Schottky diode or a pn-junction.

## G. References

1. H. P. Maruska and J. J. Tietjen, Appl. Phys. Lett., **15** (1969) 327.
2. W. M. Yim, E. J. Stofko, P. J. Zanzucchi, J. I. Pankove, M. Ettenberg and S. L. Gilbert, J. Appl. Phys., **44** (1973) 292.
3. J. A. Sajurjo, E. Lopez-Cruz, P. Vogh and M. Cardona, Phys. Rev., **B28** (1983) 4579.
4. J. Sumakeris, Z. Sitar, K. S. Ailey-Trent, K. L. More and R. F. Davis, Thin Solid Films, **225** (1993) 244.
5. *CVD Metalorganics for Vapor Phase Epitaxy: Product Guide and Literature Review II*, Advanced Materials, Morton International, Danvers, MA.
6. D. A. Jackson, Jr., J. Crystal Growth, **94** (1989) 459.
7. R. Karlicek, J. A. Long and V. M Donnelly, J. Crystal Growth, **68** (1984) 123.
8. C. A. Larsen and G. B. Stringfellow, J. Crystal Growth, **75** (1986) 247.
9. N. I. Buchan, C. A. Larsen and G. B. Stringfellow, J. Crystal Growth, **92** (1988) 591.

## **XVIII. Development of a Photo- and Cathodoluminescence System for Optical Studies of III-V Nitride Films**

### **A. Introduction**

Luminescence is the emission of photons due to excited electrons in the conduction band decaying to their original energy levels in the valance band. The wavelength of the emitted light is directly related to the energy of the transition, by  $E=h\nu$ . Thus, the energy levels of a semiconductor, including radiative transitions between the conduction band, valance band, and exciton, donor, and acceptor levels, can be measured.[1,2]

In luminescence spectroscopy, various methods exist to excite the electrons, including photoluminescence (photon excitation), and cathodoluminescence (electron-beam excitation). In each technique, signal intensity is measured at specific wavelength intervals using a monochrometer and a detector. The intensity versus wavelength (or energy) plot can then be used to identify the characteristic energy band gap and exciton levels (intrinsic luminescence) of the semiconductor, and the defect energy levels (extrinsic luminescence) within the gap.[1]

Both photo- and cathodoluminescence analysis has been performed on AlN, GaN, and  $\text{Al}_x\text{Ga}_{1-x}\text{N}$  semiconductors.[3-15] Much of the work has been in measuring the low temperature GaN luminescence peaks. Work on AlN has been limited by the energy gap of 6.2 eV, which corresponds to a wavelength (200 nm) that is lower than most of the optical light sources. An excimer laser using the ArF line (193 nm) could possibly be used, although no one has attempted this to date. Caution must be taken when operating at these wavelengths.

Few time-resolved luminescence measurements have been performed on AlN and GaN. In a time-resolved measurement a pulsed source is used to excite the sample, and the luminescence is measured at short sampling intervals after the pulse. The result is an intensity vs. time plot. Time resolved spectroscopy is useful for separating the emission bands of the investigated samples with different decay times. It is often used to measure donor-acceptor recombination rates and minority carrier lifetimes.

Depth-resolved information can be obtained using cathodoluminescence, since generation depth varies with beam voltage. This technique is particularly useful for studying ion implanted semiconductors and layered structures.

### **B. Experimental Procedures**

A combined photo- and cathodoluminescence system has been assembled and is currently being tested. A schematic view is shown in Fig. 1, and a block diagram is shown in Fig. 2. The sample is in a UHV chamber, and the monochrometer and collection optics are

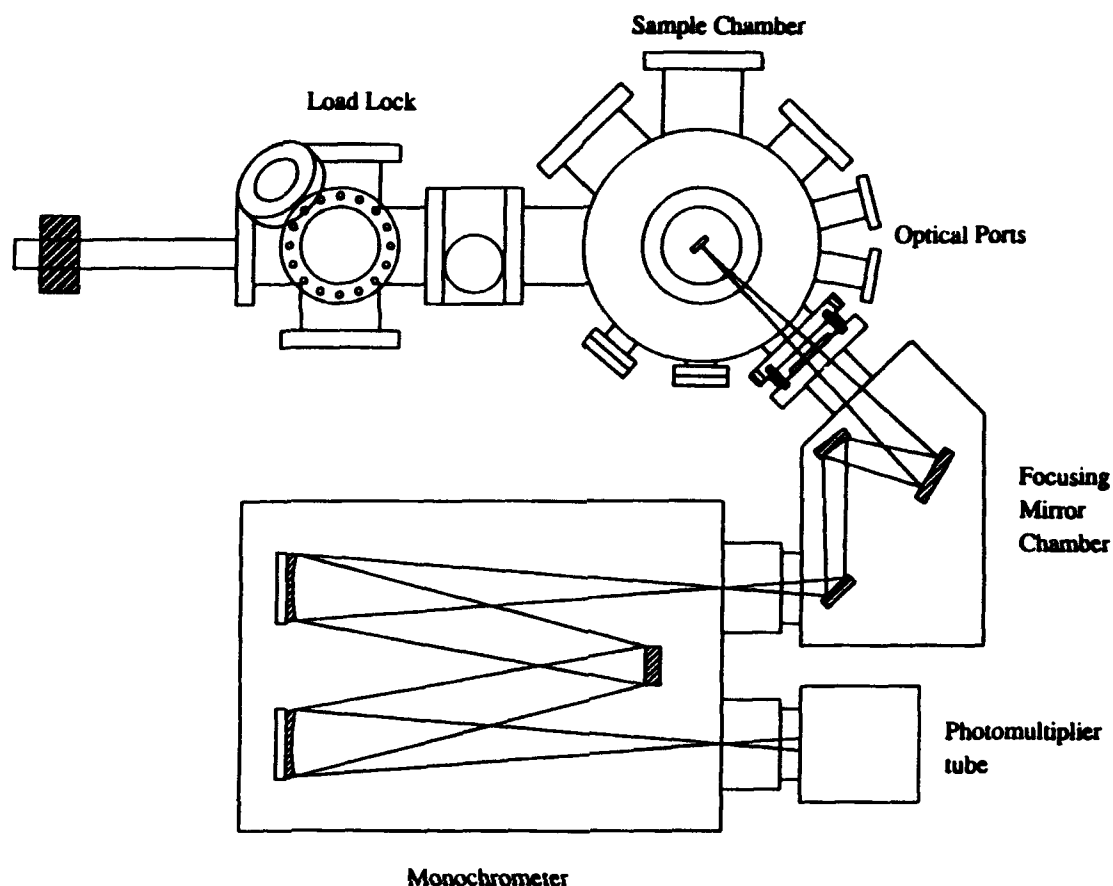


Figure 1. Schematic of the combined photo- and cathodoluminescence system.

in a vacuum environment. The sample is attached to a cryostat from APD cryogenics, which will allow for luminescence measurements at temperatures down to 4.2 K. The monochromator is a McPherson model 219 vacuum monochromator. Its focal length is .5 m, with a wavelength resolution of .04 nm at 313.1 nm. Two optical sources and a beam blanking electron gun will be used as the excitation sources. A Liconix He-Cd laser is currently being used; it is a continuous wavelength laser that operates at wavelengths of 325 nm, with a power of 15 mW. A pulsed excimer laser is the other optical source; it operates at wavelengths of 193 nm (6.4 eV), 248 nm (5.0 eV), and 308 nm (4.0 eV); and so it can be used to measure the luminescence of AlN.

A Kimball Physics electron gun is used for cathodoluminescence measurements. It has maximum beam voltage of 10 keV and a maximum beam current of 450  $\mu$ A. By varying the beam voltage it will be possible to perform depth-resolved spectroscopy.

The beam blanking capability of the electron gun will make it possible to do time-delay studies of the semiconductors.





12. S. Nakamura, T. Mukai, and M. Senoh, *Jpn. J. Appl. Phys.*, **31** (9) 2883-90 (1992).
13. S. Nakamura, N. Iwasa, T. Mukai, and M. Senoh, *Jpn. J. Appl. Phys.*, **31** (5) 107-15 (1992).
14. S. Nakamura, T. Mukai, and M. Senoh, *Jpn. J. Appl. Phys.*, **30** (12A) 1998-2001 (1991).
15. S. Strite, J. Ruan, Z. Li, N Manning, A. Salvador, H. Chen, D. J. Smith, W. J. Choyke, and H. Morkoç, *J. Va. Sci. Technol. B* **9** (4) 1924-29 (1991).

## **XIX. Reactive Ion Etching of GaN and AlN**

### **A. Introduction**

Semiconductor devices are the principle components of electronic and telecommunications systems [1]. In order to densely pack these microscopic components, unidirectional, or anisotropic, etching techniques are required to produce a fine network of lines. Wet etching processes found in many semiconductor manufacturing steps produce a multi-directional, or isotropically, etched material. This is undesirable for microcircuitry since the goal is to produce the smallest devices possible. Therefore, plasma-assisted processes, such as reactive ion etching (RIE), combine the physical characteristics of sputtering with the chemical activity of reactive species to produce a highly directional feature. RIE has the added advantage of providing a more uniform etch and a higher degree of material etch selectivity.

RIE has been employed to etch a wide variety of semiconductor materials including silicon-based materials [2-11], metals, like aluminum [3, 12-18] and III-V compounds, such as GaAs and InP [19-21]. However, plasma-assisted etching of newer III-V compounds, such as GaN and AlN, has been attempted by few investigators [20-24]. There has been wide spread interest in using these nitrides for semiconductor device applications requiring visible light emission, high temperature operation and high electron velocities [20]. Since these materials possess wide bandgaps and optical emissions spectra in the blue to near ultraviolet range, they are prime candidates for ultraviolet detection devices.

The objectives of this report are to discuss recent progress made in the field of reactive ion etching of gallium and aluminum nitride. In the following sections, a brief review of pertinent literature on plasma-assisted etching of gallium and aluminum compounds is provided along with a brief description of the reactive ion etching system and process gases.

### **B. Literature Review**

*Reactive Ion Etching of GaN.* Since GaN is a direct transition material with a bandgap ranging from 3.4-6.2 eV at room temperature, it is an ideal candidate for the fabrication of shortwave length light emitters [20, 25]. High quality GaN films have been successfully grown by MOVPE [25], ECR-MBE [26, 27], MOCVD [28] and a layer-by-layer process [29] on a number of substrate. In order to fabricate complete device structures, reliable etching processes need to be developed. Since GaN is nearly inert to most wet etching solutions, with the exception of highly concentrated hot NaOH and H<sub>2</sub>SO<sub>4</sub> [30], RIE may prove to be an effective method for the production of fine line patterning in semiconductor materials.

There have been a few reports of etching GaN by plasma-assisted processes [20-24]. Foresi [21] investigated fabrication techniques for ohmic contact and Schottky barriers on

GaN. One of the highlights of his work was the successful etching of GaN on sapphire substrate in Freon 12 ( $\text{CCl}_2\text{F}_2$ ) and in hydrogen atmospheres operating at about 10 mTorr and 40 and 60 W of RF power. Results from SEM photographs showed that in the  $\text{CCl}_2\text{F}_2$  plasma, GaN had been completely removed from areas that were not covered by photoresist, and that the sapphire substrate was nearly unetched. Foresi was able to obtain an etch rate of approximately 140 Å/min in the  $\text{CCl}_2\text{F}_2$  plasma at 60 W, while the hydrogen plasma produced insignificant etching results. Etch selectivity between the GaN and photoresist was found to be 3:1. In another investigation, conducted by Tanaka et al. [20], reactive fast atom beam etching was employed to etch GaN on sapphire in a  $\text{Cl}_2$  plasma at substrate temperatures ranging between 80-150°C. Etch rates of 1000-1200 Å/min produced relatively smooth surfaces and a well defined pattern of elongated rectangular bars on the sapphire substrate. More recently, S.J. Pearton et al. [22] have produced smooth, anisotropically etched GaN and AlN in low pressure ECR discharges of  $\text{BCl}_3/\text{Ar}$ ,  $\text{CCl}_2\text{F}_2/\text{Ar}$  and  $\text{CH}_4/\text{H}_2/\text{Ar}$ . The etch rates of these nitrides were highly dependent on the DC bias voltage and ranges of 25-175 Å/min and 0-100 Å/min were reported for GaN and AlN, respectively. It is noted that hydrogen was added to the chlorine plasmas to facilitate removal of hydrogen from the surfaces of the nitride samples, thus producing smoother features. Also, Adesida et al. [23] employed reactive ion etching to produce 4000 Å thick lines in GaN with  $\text{SiCl}_4$  plasmas. They found that the etch rate was independent of pressure but increased with self bias voltage. They obtained slightly overcut features with fairly smooth sidewalls at etch rates up to 500 Å/min. Experimental etching was also conducted with  $\text{SiCl}_4/\text{Ar}$  and  $\text{SiCl}_4/\text{SiF}_4$ , but the addition of Ar and F atoms to the plasma had no effect on the etch rate. In addition, residual Si and Cl were found on the GaN surfaces after etching.

*Reactive Ion Etching of AlN.* Aluminum nitride is a candidate material for optoelectronic devices because it possess a high electrical resistivity, high thermal conductivity, low dielectric constant and has a direct transition bandgap of 6.3 eV [31]. AlN films have been grown by several techniques including CVD, MBE and ALE, and on a variety of substrate materials including sapphire, silicon, spinel, silicon carbide and quartz [32]. Etching fine features in the AlN films is an important step in the fabrication of such devices. Though, only one report of etching of AlN is available in the open literature at this time [22], much work has been conducted on etching of metallic aluminum thin films [3, 12-18]. As a result, analogies to well established data for etching of aluminum are made. Although aluminum and AlN are very different materials, the chemistry and reactions in the plasma may be similar. So, it is proposed that reactive ion etching may also be an effective means for the application of fine line patterning of AlN.

A review of the literature shows that there are two primary methods employed for etching aluminum. Bruce and Malafsky [12] employed a parallel plate configuration (RIE) to

investigate the effects of  $\text{Cl}_2$  on aluminum. They found that two processes are involved, namely, the removal of the oxide layer and etching the metal below it. For those experiments, it was hypothesized that  $\text{BCl}_3$  gas was necessary for the removal of the oxide layer because it was responsible for the initiation of a reduction reaction with the oxide. In the RIE etching configuration, aluminum etched with a chlorinated gas is a purely chemical reaction with little contribution from ion bombardment. This conclusion was made as a result of the insensitivity of RF power to the etch rate [12]. Therefore, anisotropic etching was thought to have been the result of a sidewall passivation mechanism whereby a protective layer is formed on the vertical walls of the trench by reaction of  $\text{H}_2\text{O}$  or carbon containing species with the aluminum. Since ion bombardment is normal to the surface, the walls remained unetched. This mechanism was produced by the addition of  $\text{CHCl}_3$  to the mixture of gases. Feature widths of  $2.25\text{ }\mu\text{m}$  were produced by a gas mixture of  $\text{Cl}_2$ ,  $\text{BCl}_3$ ,  $\text{CHCl}_3$  and He at about 1.2 mTorr. Helium gas was added to the mixture to reduce the amount of erosion of the photoresist.

The combination of an isotropic flux of reactive species with a highly directional beam of energetic ions, so called ion beam assisted etching (IBAE), has been employed for the anisotropic etching of aluminum by many investigators [13-15, 18]. For IBAE, the aluminum oxide layer can be physical removed by sputtering with  $\text{Ar}^+$  or  $\text{Xe}^+$  ions, whereas with RIE the oxide is removed chemically [13]. However, etching takes place again by chemical reaction of  $\text{Cl}_2$  with the aluminum as determined by the lack of dependence of the etch rate on the ion energy and current [14, 15]. From a mechanistic point of view,  $\text{Cl}_2$  adsorbs onto and diffuses into the aluminum resulting in the formation of aluminum chlorides.  $\text{Al}_2\text{Cl}_6$  is the dominant etch product at lower temperatures ( $33^\circ\text{C}$ ), while  $\text{AlCl}_3$  was observed at higher temperatures ( $210^\circ\text{C}$ ) [15]. Saturation of the etched surface with chlorine atoms occurs prior to desorption of  $\text{AlCl}_3$ .

The etch rate is dependent upon several parameters including the presence of residual gases in the chamber, substrate temperature,  $\text{Cl}_2$  flux, ion beam and the presence of carbon containing species. Impurity gases in the chamber (i.e.  $\text{H}_2\text{O}$ ,  $\text{O}_2$ ,  $\text{N}_2$ , etc.) can react with the aluminum films and impede the etching process by leaving a residue on the etched surface. This reduces the amount of  $\text{Cl}_2$  available for reaction and consequently lowers the etch rate [13]. The substrate temperature is another parameter that affects the etch rate of aluminum. Efremow et al. [13] observed a two-fold increase in the etch rate by heating the substrate from  $0^\circ$  to  $100^\circ\text{C}$ . It was hypothesized that the increase in temperature led to a higher evaporation rate of the product  $\text{AlCl}_3$ . In addition, they found that an increase in the  $\text{Cl}_2$  flux produced a significant amount of undercutting due to the nondirectional flow of the  $\text{Cl}_2$  gas. A higher degree of anisotropy was achieved by the combination of ion beam and  $\text{Cl}_2$  flux. Efremow *et al.* suggested that sidewall passivation (by reaction of  $\text{H}_2\text{O}$  with the aluminum)

was partly responsible for the production of the very fine features in their samples. Submicrostructures of 80 nm wide lines were etched into a 100 nm thick aluminum film with 0.3 mTorr  $\text{Cl}_2$  gas and 0.1 mA, 1 keV  $\text{Ar}^+$  beam. Lastly, Park et al. [14] found that chemisorption of the halocarbon gas molecules, such as  $\text{CCl}_4$  and  $\text{CBr}_4$ , onto the aluminum surface formed halogenated aluminum species along with an aluminum carbide. Therefore, a significant reduction in the etch rate was observed due to the difficulty encountered in removing the carbide from the surface.

### C. Proposed Research

**Experimental Apparatus.** A schematic of the RIE system is shown in Fig. 1. The main components of the system include gas handling/storage, etcher, gas scrubber and mass spectrometer. Since toxic gases, such as  $\text{BCl}_3$  and  $\text{Cl}_2$ , may be used to etch GaN and AlN, the system is designed for safe shutdown in the event of a power or water failure and/or inadvertent shutdown of the exhaust systems in the building.

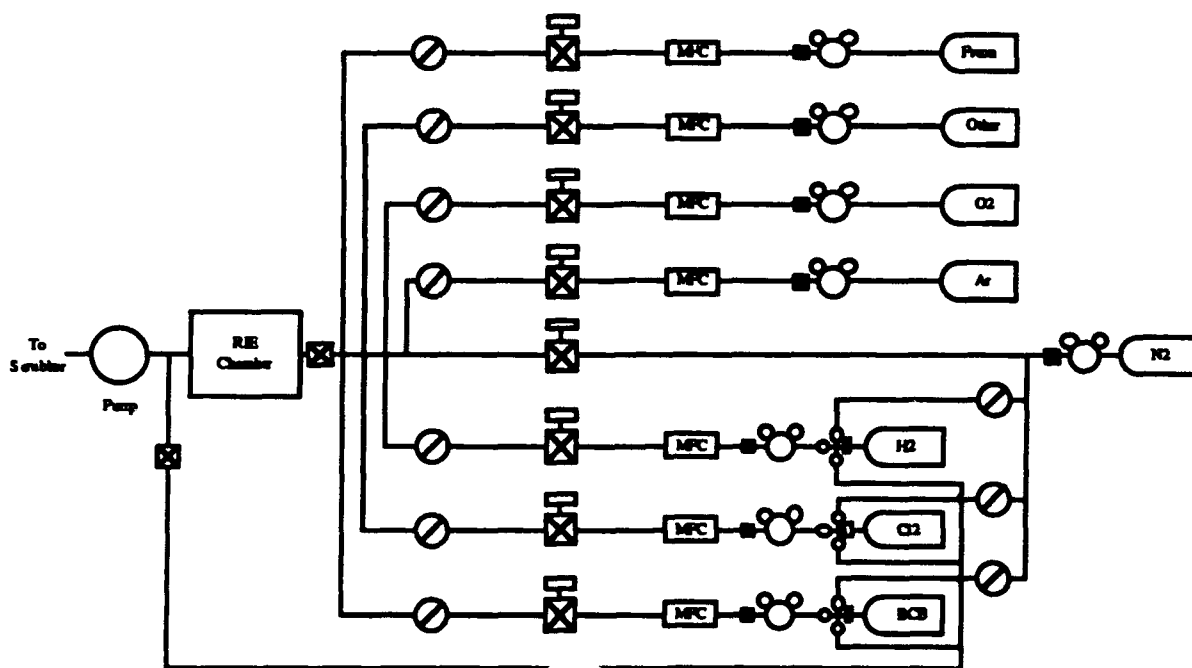


Figure 1. Reactive ion etching system.

The gas handling/storage sub-system consists of the gas storage cabinet(s), gas bottles, bottle regulators and necessary valves and tubing. Dry nitrogen will be used to purge the gas lines before and after every run to remove moisture and chlorine from the lines, thus reducing

the probability of corrosion of the gas lines. Mass flow controllers will be employed for accurate control of the process gases. In addition, pneumatic valves will be installed as a safety precaution. In the event of a power failure, interruption of the water supply or shutdown of the exhaust system, the solenoid actuated pneumatic valves will isolate the gas lines from the etch chamber.

The design of the etcher is based on that of the standard parallel-plate diode configuration in which the bottom electrode is powered by a RF power supply (see for example Ref. vanRoosmalen, 1984 #10). The etcher, a Technics 85 series RIE, consists of an anodized aluminum chamber with an anodized aluminum water-cooled, driven lower electrode. A 350 Watt, 13.56 MHz RF generator with auto impedance matching network produces the power required to maintain a glow discharge in the chamber. Safety interlocks are supplied by Technics to disable the power when the system is vented or a panel is removed. The chamber pressure is measured by a corrosion-resistant capacitance manometer (absolute pressure) which is mounted to the underside of the chamber. The two channels of process gas (made from stainless steel tubing) are isolated from the injection manifold by means of air-operated electrically actuated isolation valves. In addition, an 11 CFM two-stage corrosive-series direct drive rotary vane pump is supplied with the etcher.

Residual process gases and reaction by-products from the etcher will pass through a wet scrubber which is equipped with water inlet and water recirculation lines. These lines are monitored for water flow and exhaust ventilation and are an integral part of the control system. Interruption of the water flow or inadequate ventilation will trip the pneumatic valves and close the gas lines. In addition, the pH level of the scrubber water will be tested and monitored prior to waste disposal.

Lastly, a mass spectrometer may be employed in the future for the detection and characterization of chemical species produced by the etching processes. It could also be used as a kind of end-point detection device. It is further hoped that this analytical instrumentation could provide necessary information for the determination of the success of the etching processes and could provide a basis for an understanding of the etching mechanisms.

*Choice of Process Gases.* There are a number of process gases that can be used to produce anisotropically etched features. For GaN and AlN, fluorine plasmas are impractical because involatile fluorides are formed with Ga and Al at the surfaces, therefore limiting desorption of reaction species from the surface [33]. Chlorine plasmas, on the other hand, have been used extensively for etching these compounds, see Section B above.

In etching GaN, the gases used by Tanaka [20], Foresi [21] and S. J. Pearton *et al.* [22, 24], namely  $\text{CCl}_2\text{F}_2$ ,  $\text{Cl}_2$  and  $\text{BCl}_3$ , will be employed first since those investigators reported successful results. Experimentation with other combinations of gases, such as iodine- and/or bromine-containing gas mixtures) is likely in order to obtain smooth, anisotropic features

with reasonably high etch rates. As for AlN, chlorine containing gases with additions of O<sub>2</sub>, carbon containing gases and or noble gases (i.e. Ar, He, etc.) are likely candidate gases. Though, somewhat of a trial and error methodology will be followed until success is achieved. It is noted that for RIE, sidewall passivation may be an important mechanism for anisotropic etching of AlN and may produce relatively large features. On the other hand, ion beam assisted etching, or similar techniques, are likely to produce smaller features in these nitrides.

#### D. Future Research

The reactive ion etching system has been installed and will be used to etch GaN, AlN, InN and AlGaIn on SiC substrates. In the preliminary stages of this research, several candidate materials (such as photoresist, NiCr, Al and other metals) will be tested in the various process gas streams to determine suitable masks for the etching process. In addition, experimentation with different cathode materials (such as graphite and quartz) is likely in order to minimize the amount of micromasking from the cathode material. Parametric studies will be conducted to determine how the power, pressure, gas load and flow rates affect the etching rate of these nitrides. Lastly, surface analysis techniques such as AES and XPS will be employed to determine the contamination levels and surface condition of the nitrides before and after etching.

#### E. References

1. *Plasma Processing of Materials: Scientific Opportunities and Technological Challenges*, National Research Council—Panel on Plasma Processing of Materials (National Academy Press, Washington, D.C., 1991).
2. J. W. Palmour, R. F. Davis, T. M. Walleit, K. B. Bhasin, *J. Vac. Sci. Technol. A* **4**, 590 (1986).
3. D. L. Smith, P. G. Saviano, *J. Vac. Sci. Technol.* **21**, 768 (1982).
4. D. L. Smith, R. H. Bruce, *J. Electrochem. Soc.* **129**, 2045 (1978).
5. C. J. Mogab, A. C. Adams, D. L. Flamm, *J. Appl. Phys.* **49**, 3796 (1978).
6. S. Matsuo, *J. Vac. Sci. Technol.* **17**, 587 (1980).
7. L. M. Ephrath, *Solid State Technol.*, July 1982, p. 87.
8. Y. H. Lee, M. M. Chen, *J. Appl. Phys.* **54**, 5966 (1983).
9. L. M. Ephrath, *J. Electrochem. Soc.*, August 1979, p. 1419.
10. A. J. vanRoosmalen, *Vacuum* **34**, 429 (1984).
11. M. Zhang, J. Z. Li, I. Adesida, E. D. Wolf, *J. Vac. Sci. Technol. B* **1**, 1037 (1983).
12. R. H. Bruce, G. P. Malafsky, *J. Electrochem. Soc.* **136**, 1369 (1983).
13. N. N. Efremow, M. W. Geis, R. W. Mountain, G.A. Lincoln, J.N. Randall, N.P. Economou, *J. Vac. Sci. Technol. B* **4**, 337 (1986).
14. S. Park, L. C. Rathburn, T. N. Rhodin, *J. Vac. Sci. Technol. A* **3**, 791 (1985).
15. H. F. Winters, *J. Vac. Sci. Technol. B* **3**, 9 (1985).
16. D. A. Danner, D. W. Hess, *J. Appl. Phys.* **59**, 940 (1986).
17. R. J. A. A. Janssen, A. W. Kolfshoten, G. N. A. vanVeen, *Appl. Phys. Lett.* **52**, 98 (1988).

18. Y. Ochiai, K. Shihoyama, T. Shiokawa, K. Toyoda, A. Masuyama, K. Gamu, J. Appl. Phys. **25**, L527 (1986).
19. G. Smolinski, R. P. Chang, T. M. Mayer, J. Vac. Sci. Technol. **18**, 12 (1981).
20. H. Tanaka, Optoelectron. Dev. Technol. **6**, 150 (1991).
21. J. S. Foresi, M.S. Thesis, Boston University, Boston, MA, 1992.
22. S. J. Pearton, C. R. Abernathy, F. Ren, J. R. Lothian, P. W. Wisk, A. Katz, Semiconductor Sci. Technol. **8**, 310 (1993).
23. I. Adesida, A. Mahajan, E. Andideh, M. A. Khan, D. T. Olsen, J. N. Kuznia, Appl. Phys. Lett. **63**, 2777 (1993).
24. S. J. Pearton, J. Vac. Sci. Technol. A **11**, 1772 (1993).
25. I. Akasaki, H. Amano, Physica B **185**, 428 (1992).
26. C. Eddy, Ph.D. Thesis, Boston University, Boston, MA, 1990.
27. T. Lei, T. D. Moustakas, J. Appl. Phys. **71**, 4933 (1992).
28. Z. J. Yu, B. S. Sywe, A. U. Ahmed, J. H. Edger, J. Electr. Mater. **21**, 782 (1992).
29. J. Sumakeris, Z. Sitar, K. S. Ailey-Trent, K. L. Moore, R. F. Davis, "*Layer-by-Layer Epitaxial Growth of GaN at Low Temperatures*" (To be published in Thin Solid Films, 1993).
30. *CRC Handbook of Metal Etchants*, Eds. P. Walker, W. H. Tarn (CRC Press, Boca Raton, LA, 1991).
31. E. S. Dettmer, B. M. Romenesko, H. K. Charles, B. G. Carkhuff, D. J. Merrill, IEEE Trans. Comp. Hybrids Manuf. Technol. **12**, 543 (1989).
32. L. B. Rowland, Ph.D. Thesis, North Carolina State University, Raleigh, NC, 1992.
33. V. M. Donnelly, D. L. Flamm, Solid State Technol., April 1981, p. 161.



## **XX. Contact Formation in GaN and AlN**

### **A. Introduction**

The formation of ohmic contacts with semiconductor materials and devices is a fundamental component of solid state device architecture. As device size has diminished and the scale of integration has increased, the quality of these interfaces has become an increasingly important concern. In addition, the presence of parasitic resistances and capacitances, such as those existing at contact interfaces, becomes more detrimental at higher operating powers and higher oscillation frequencies. The development of adequate and reliable ohmic contacts to the compound semiconductors, particularly those with wider band gaps, has met a number of challenges. The subject of ohmic contacts to p- and n-type III-V compounds, mostly GaAs, AlGaAs, and InP, has received a great deal of attention over the past decade, and significant advances have been made [1-12]. By comparison, the III-V nitrides have received little attention in this regard. However, interest in these materials has been renewed in recent years as thin film growth techniques have improved, p-type doping in GaN and AlGaN solid solutions has been achieved, and p-n junctions have been fabricated.

The majority of successful ohmic contact systems that have so far been implemented with the more conventional compound semiconductors have relied upon alloying (liquid-phase reaction) or sintering (solid-phase reaction) via post-deposition annealing treatments, and/or the presence of high carrier concentrations near the interface [1,2,6,12]. However, many otherwise successful ohmic contact systems have only limited thermal stability and are subject to degradation—usually in the form of extensive interdiffusion, interfacial reaction, and interphase growth, accompanied by increase in contact resistivity—under subsequent thermal processing steps. It is reasonable to suppose that the cleanliness and preparation of the semiconductor surface prior to contact deposition plays a significant role in the behavior of the interface, and there are indications in the recent literature that support this [2,11-13]. Thorough oxide removal is especially important, though it may well prove to be a persistent challenge with Al-containing compounds in particular.

In this study, two main approaches are being taken in the development of ohmic contacts to GaN and AlN. The first approach is similar to that which has resulted in the majority of successful ohmic contacts to the more conventional compound semiconductors such as GaAs: the creation of high carrier concentrations in the semiconductor at the metal interface by means of alloying, sintering, or implantation of dopant species. The so-called pinning of the Fermi level at this surface, particularly with GaAs, results in a more or less fixed potential barrier at the metal interface. In the case of the pinned Fermi level of GaAs, the approach has generally been to shrink the width of the depletion layer by means of increasing the carrier concentration to the point where carrier tunneling through the barrier occurs readily. Even

with optimization of contact composition and annealing times and temperatures, the lowest contact resistivities ( $\rho_c$ ) have been obtained only on the most heavily doped materials. Though there are indications that high doping levels and extensive interfacial reactions through alloying and sintering are not essential for ohmic contact formation in all cases, these processes have proven useful for minimizing  $\rho_c$  [2,11-13].

The other approach toward ohmic contact formation to be taken in this study involves the Schottky-Mott-Bardeen (SMB) model of semiconductor interfaces [14,15]. In this model the relative values of work function of the materials involved determine the band structure of the interface and thus the nature of any potential barriers present. The presence of interfacial states at the semiconductor surface can interfere with the alignment of the Fermi level across the interface and overshadow the effect of the inherent difference in work function between the two materials. The III-V nitride compounds are more ionically bonded than their phosphide and arsenide counterparts, as a result of larger electronegativity differences between the component elements. According to the observations of Kurtin *et al.* [16], this fact indicates that the nitrides should experience less Fermi level stabilization or "pinning" at the surface than do the more covalent compounds. Thus, the barrier heights of contacts to the nitrides should be more dependent on the contact material than is the case with the more conventional and more covalent semiconductors such as Si, GaAs, InP, SiC, etc. With the work of Foresi and Moustakas [17,18], this concept is beginning to be investigated. The SMB model also indicates that the cleanliness of the interface plays an important role in its electrical behavior, particularly in the minimization or elimination of any insulating layers at the interface.

To date, several alloyed and sintered contact strategies, having demonstrated effectiveness with GaAs—and, in the case of Au, with GaN—have been undertaken with GaN and AlN. The tighter bonding of Ga and Al to N, in comparison to As, suggests that higher temperatures and possibly longer times are required for interfacial reactions to take place, and that some reactions may be inhibited or prevented. The behavior of the systems examined so far has been consistent with these suppositions. Contact strategies derived from GaAs technology will continue to be characterized in this study, and an investigation of the roles of work function differences and interfacial cleanliness will be undertaken in the coming weeks.

## B. Experimental Procedure

**Film Deposition.** Doped GaN and AlN films for contact studies were grown on 6H-SiC substrate crystals by means of ECR plasma enhanced molecular beam epitaxy (MBE). Magnesium was grown into the films as the p-type dopant and Ge was used to grow n-type materials, as described in other sections of this report.

Four different contact systems were deposited and examined during this reporting period: single Au layers, Zn/Au, Cr/Au, and AuGe/Ni/Au. The single Au layers were 2500Å thick; the Zn/Au and Cr/Au structures consisted of 350Å layers of Zn or Cr followed by 2300Å of gold. The alloyed AuGe contact consisted of successively deposited layers of AuGe 88:12 eutectic alloy (m.p. 360°C) (1500Å), Ni (420Å), and Au (3000Å). Contact metals were deposited by means of electron beam evaporation using a Thermionics evaporation system having a 3 kW 5-source electron gun. The 5-source capacity of the e-beam hearth allowed the deposition of multiple layers of different metals without breaking vacuum to change sources. Prior to metals deposition, the nitride films were cleaned with a 50:50 HCl:H<sub>2</sub>O dip and rinsed in DI water. A shadow mask was used during deposition to create rectangular-bar TLM (transmission line model) patterns for contact resistivity ( $\rho_c$ ) measurements, as described in the preceding semiannual report of June 1993. Film thicknesses were monitored using a quartz crystal oscillator.

*Contact characterization.* After deposition, I-V measurements were taken between separate pads of the TLM patterns, using tungsten probe tips and an HP 4145C Semiconductor Parameter Analyzer. Annealing treatments were performed in a flowing N<sub>2</sub> atmosphere at successively higher temperatures using a Heatpulse 410 rapid thermal annealing (RTA) furnace. Once the contacts began to show distinctly linear I-V behavior after sufficient annealing, TLM measurements were taken by measuring the total resistance between identical contact pads as a function of separation distance  $l$ . The contact resistivity was obtained from the plot of  $R(l)$  vs.  $l$ , as described by Reeves and Harrison [19]. The simplifications inherent in this model yield values for  $\rho_c$  that represent an upper limit; thus, the measured values are conservative assessments of performance.

### C. Results

*Au contacts on Mg:GaN.* Gold contacts deposited on p-GaN were rectifying as-deposited. Though the as-deposited contacts were rectifying, neither were they close to being ideal Schottky contacts; reverse bias leakage was significant and there was not a clearly linear region in the log I-V plot from which an ideality factor could be calculated. Subsequent annealing steps eventually resulted in linear (ohmic) I-V behavior once sufficiently high temperatures were reached. Figure 1 shows an I-V plot for the p-GaN/Au contact as-deposited (a) and annealed at 800°C for 5 minutes (b). Noticeably linear behavior in the low voltage region was first detected after annealing to 650°C; further annealing at higher temperatures reduced the  $\rho_c$  measurable by TLM. At 700°C the  $\rho_c$  was 3130  $\Omega\cdot\text{cm}^2$ ; after annealing at 800°C for 10 minutes the  $\rho_c$  was reduced to 54  $\Omega\cdot\text{cm}^2$ .

After annealing at 750°C the appearance of the Au contact surface changed; what was originally a shiny, mirrorlike Au surface became somewhat dull to the eye, suggesting

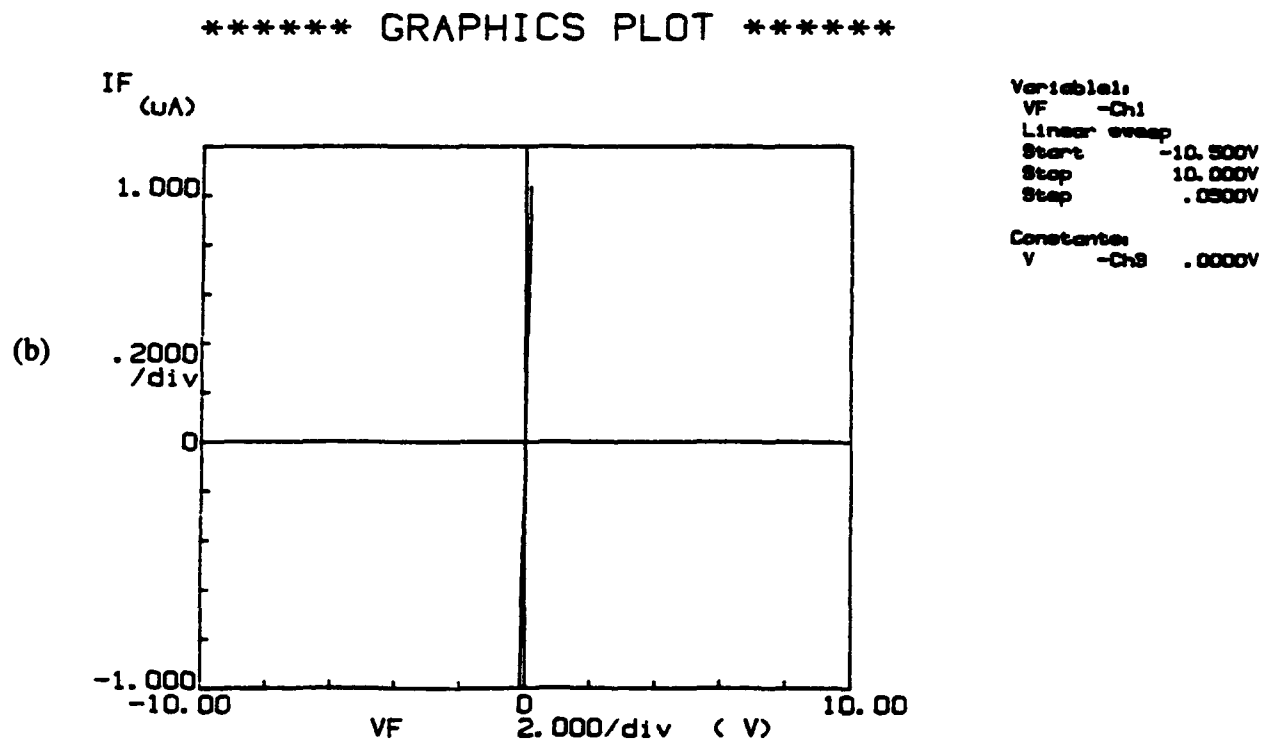
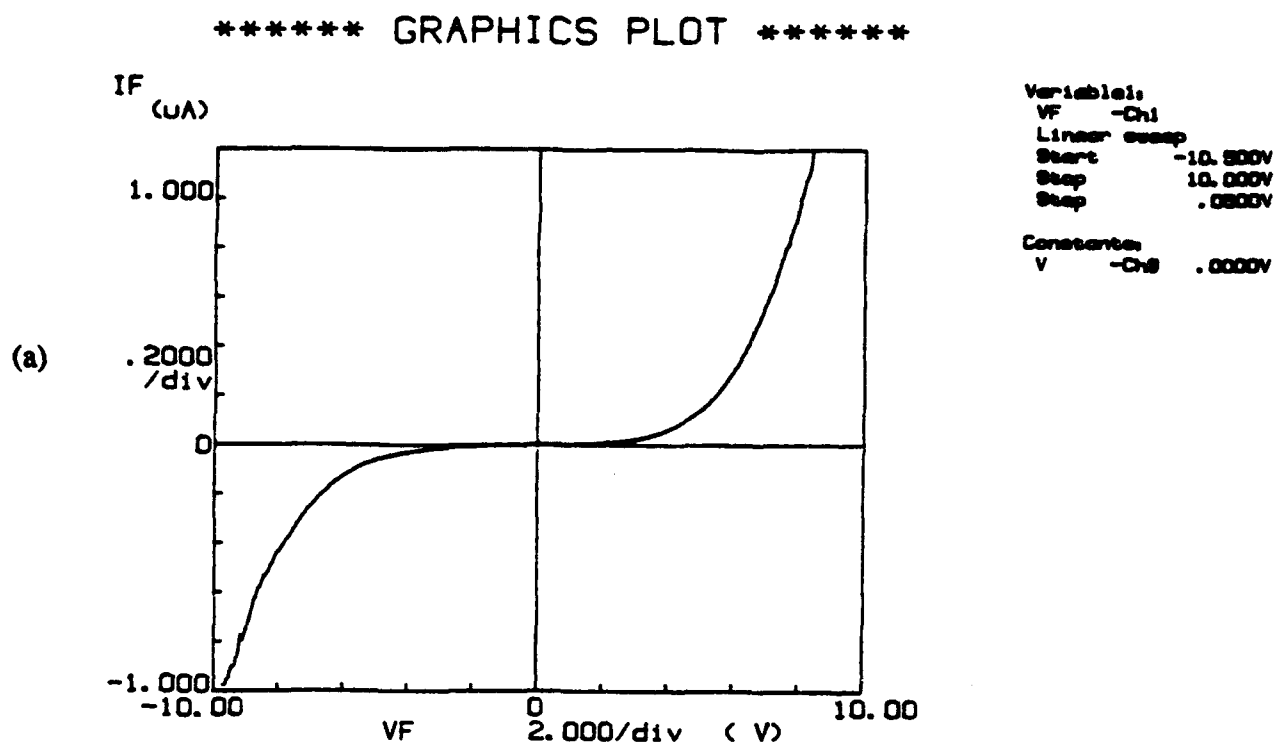


Figure 1. I-V data for Au contacts on Mg-doped GaN: (a) as-deposited (b) annealed to 800°C for 5 min.

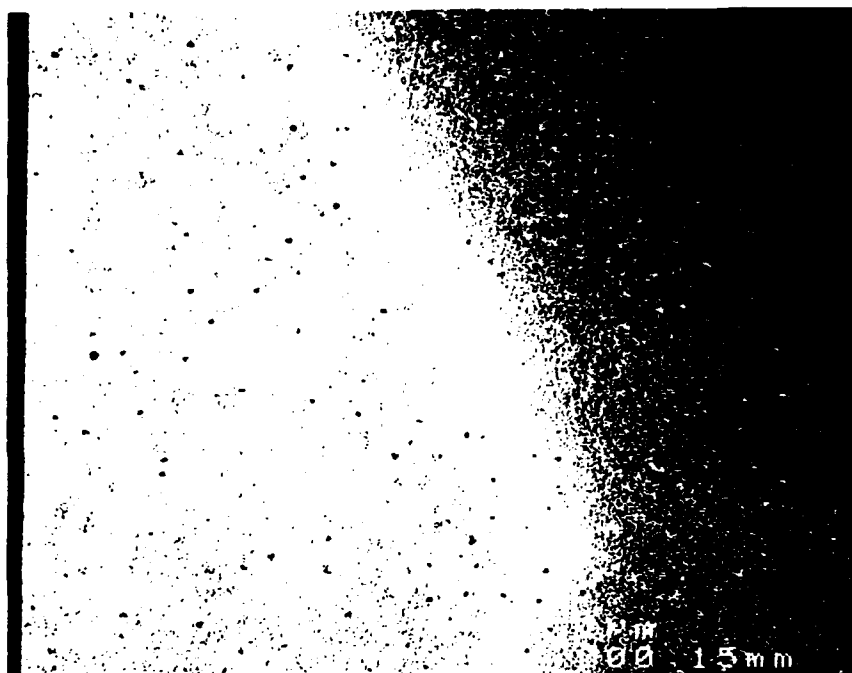
increased roughness. This change in appearance progressed with time upon heating at higher temperatures. An SEM image of the corner of an as-deposited Au contact pad is shown in Figure 2(a). The as-deposited Au surface was similar in texture to the underlying GaN surface. Some shadowing effect from the contact mask was revealed, and this effect was taken into account in the pad spacing for the TLM measurements. After annealing at 800°C for 10 minutes, large lumps developed in the metal film along with tiny specks on the surface. Holes  $>1\text{ }\mu\text{m}$  in size opened up in the Au film, and the metal at the shadowed edge had "balled up" on the GaN surface. At higher magnification, the evidently bare GaN surface could be seen through the holes in the Au layer.

*Zn/Au and Cr/Au contacts on Mg:GaN.* Though chemically different, the Zn/Au and Cr/Au contacts on Mg-doped GaN behaved similarly in many respects. Initially both contacts showed linear I-V behavior in the low-voltage region in the as-deposited state, but in both cases the slope of the I-V trace was so shallow, i.e. the resistance was so high, that reliable contact resistivity values could not be obtained. Figure 3 shows examples of I-V traces of Zn/Au contacts in the as-deposited condition and after annealing at 650°C. Over the wider voltage range of  $\pm 10\text{ V}$  the I-V plots of the Cr/Au contact consistently showed more curvature, but in the range  $\pm 2\text{ V}$  the behavior of both samples was similar. After annealing at 650° both contact systems had become sufficiently conductive for taking TLM measurements, which yielded  $\rho_c$  values of  $3180\text{ }\Omega\text{-cm}^2$  for Cr/Au and  $11850\text{ }\Omega\text{-cm}^2$  for Zn/Au.

The appearance of the Au surface of the Cr/Au contacts changed after annealing at 450°C for 2 minutes. The previously smooth mirror-like surface appeared to roughen on a fine scale, similar to the Au-only contacts described above but slightly lighter in color. Microscopic examination of the surface after annealing at 650°C for 3 minutes, shown in Figure 4, revealed many small pores, shallow crevices, and lumpiness on a very fine scale. The shallow, crater-like depressions in the lower part of the image were left by the probe tips during electrical measurements. The appearance of the Zn/Au contacts remained shiny throughout.

*AuGe/Ni/Au contacts on Ge:AlN.* The AuGe/Ni/Au contacts deposited on Ge:AlN exhibited significant changes as a result of annealing. This contact system was rectifying in the as-deposited condition, but developed linear I-V behavior in the low-voltage region upon annealing. However, annealing through 650°C did not sufficiently reduce the contact resistance enough for reliable TLM measurements. The I-V behavior varied somewhat over different areas of the AlN surface; the I-V plots shown in Figure 5 represent a middle ground of measured behavior that ranged from being more rectifying and more asymmetric than those shown to being more ohmic-like and more symmetrical.

(a)



(b)

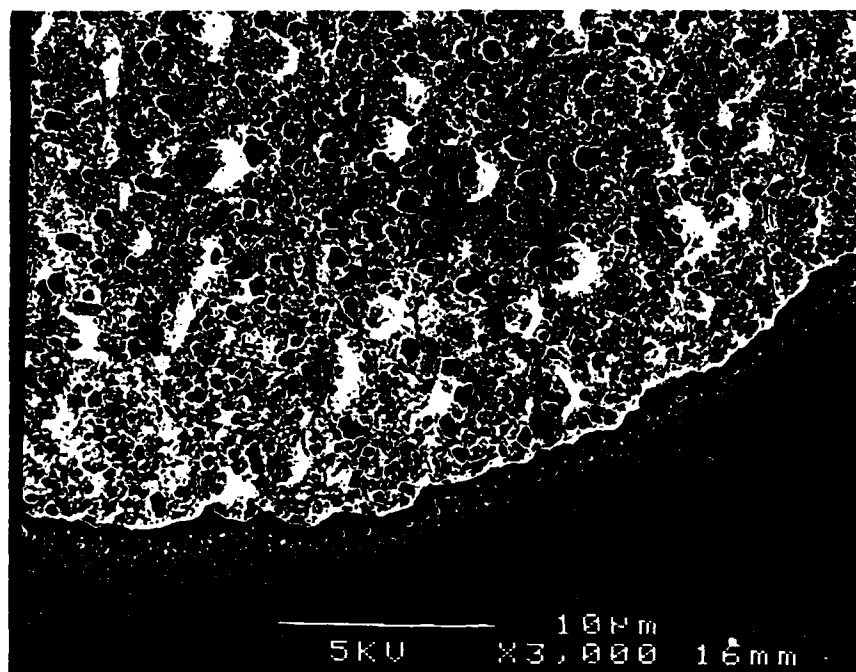


Figure 2. Edge of Au contact pad on Mg:GaN: (a) as-deposited (b) annealed at 800°C for 10 minutes.

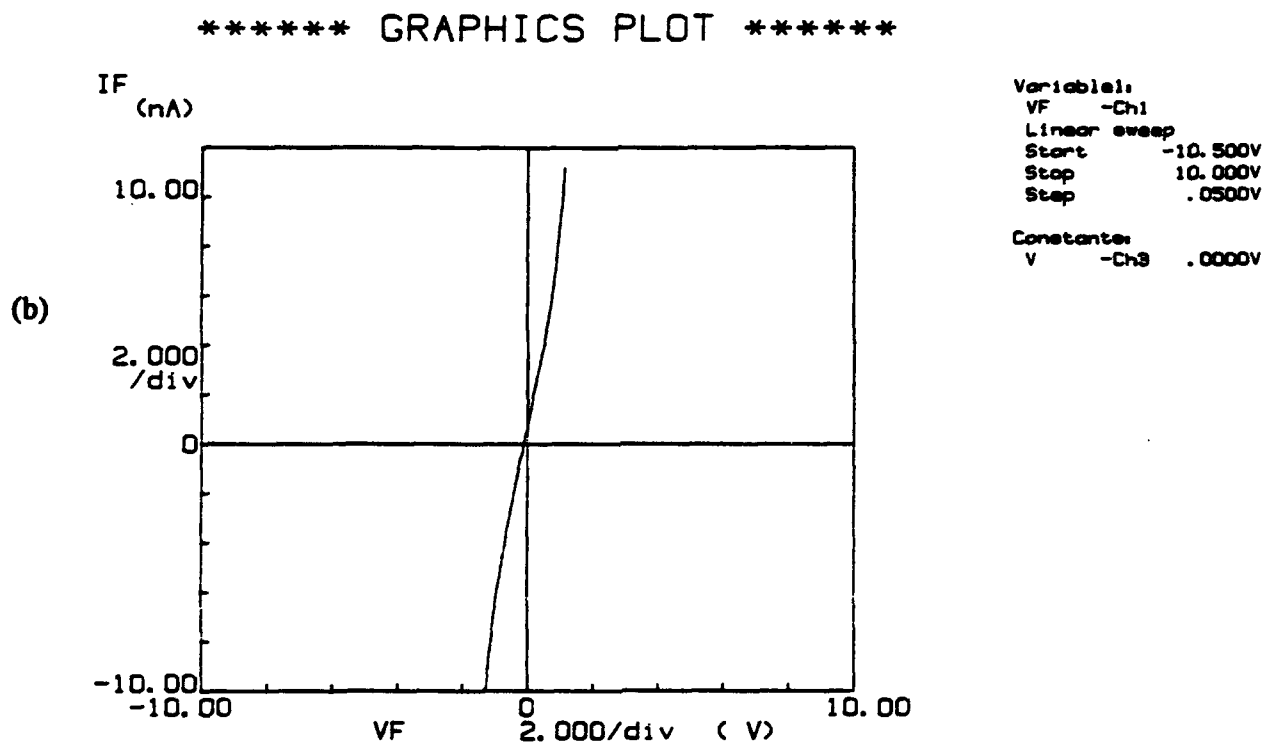
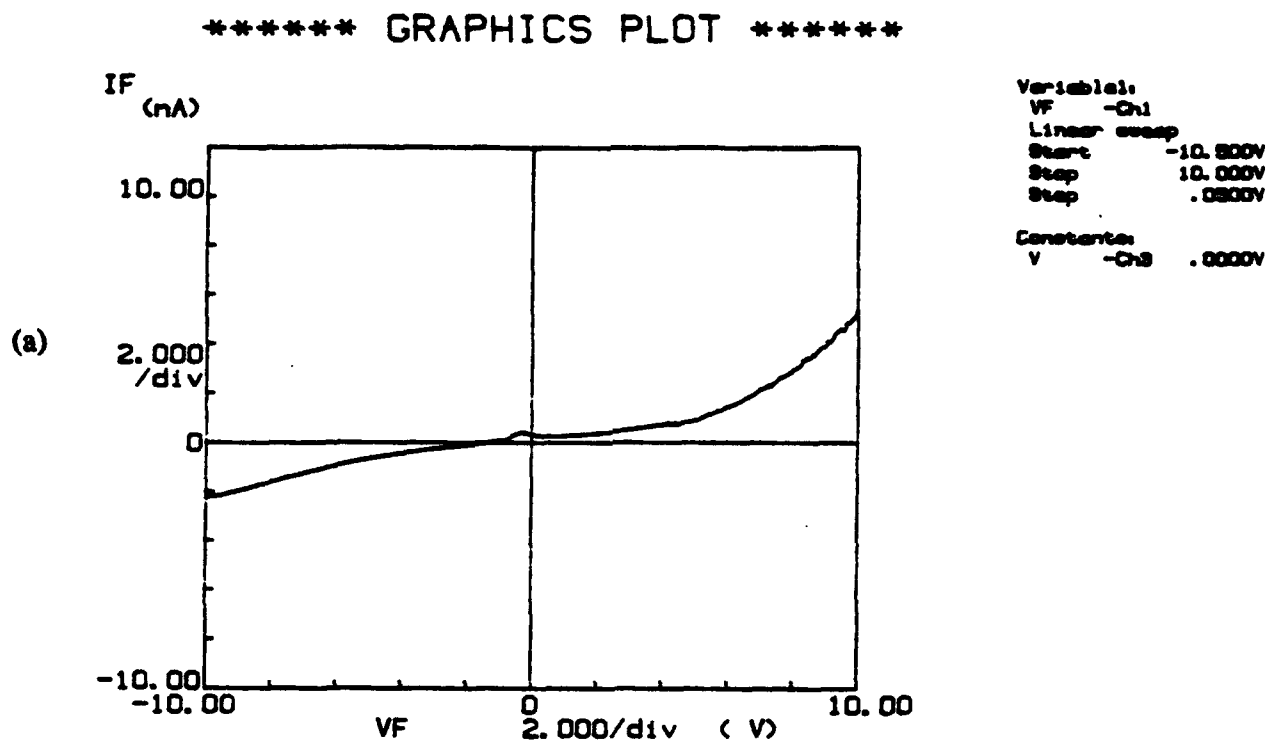


Figure 3. I-V data for Zn/Au contacts on Mg-doped GaN: (a) as-deposited (b) annealed to 650°C for 3 minutes. Data for Cr/Au contacts were similar.



Figure 4. Surface of Cr/Au contact pad on Mg:GaN, annealed at 650°C for 3 minutes.

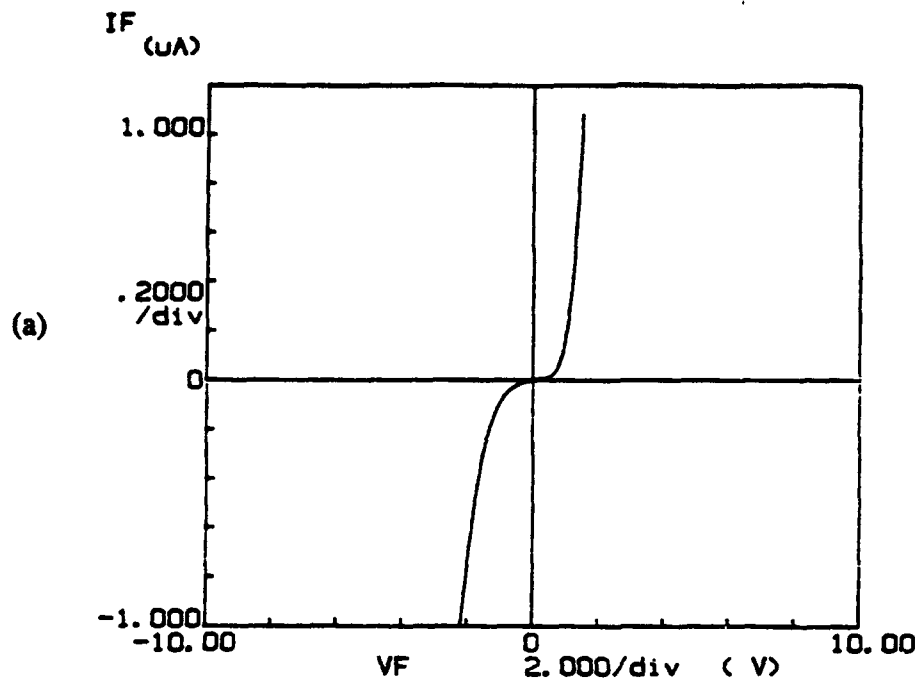
Under the microscope, this contact system revealed yet a different texture than the others. The edge of a AuGe/Ni/Au pad annealed at 650°C for 3 minutes is shown in Figure 6. Like the Au-only film, the metal at the shadowed edge balled up, but to a lesser degree than did Au. The contact surface itself appears to have a fine polycrystalline texture of mixed orientation.

#### D. Discussion

*Au contacts on Mg:AlN.* The rectifying nature of the as-deposited Au contacts on undoped n-GaN was observed by Foresi and Moustakas in their contacts investigation [17,18]. However, the GaN material used by Foresi *et al.* was different than that used in this study; theirs was undoped and inherently n-type, indicative of a high background carrier concentration and defect density. According to the Schottky model, Au should form an ohmic contact on p-type GaN and a rectifying contact on n-type material. However, it should be pointed out that the exact value for the work function and/or electron affinity of GaN and their dependence upon doping levels have not been reproducibly and precisely established as yet. Foresi and Moustakas obtained ohmic contacts with Au on undoped n-GaN after annealing at 575°C for 10 minutes in a reducing atmosphere; according to their TLM measurements they achieved contact resistivities in the range  $1.6\text{--}3.1 \times 10^{-3} \Omega\text{-cm}^2$ .



\*\*\*\*\* GRAPHICS PLOT \*\*\*\*\*



\*\*\*\*\* GRAPHICS PLOT \*\*\*\*\*

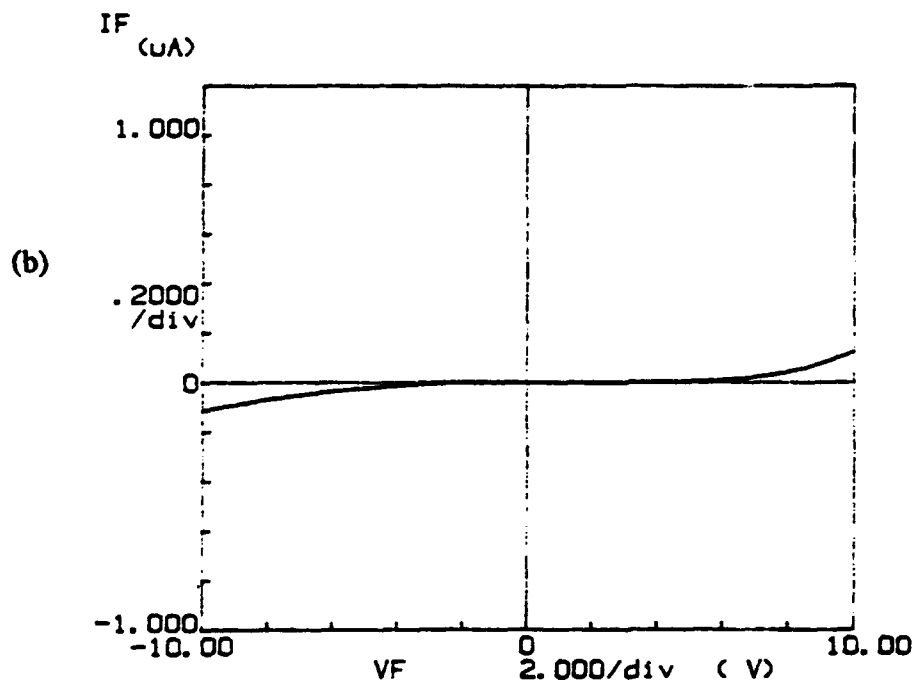


Figure 5. I-V data for AuGe/Ni/Au contacts on Ge-doped AlN: (a) as-deposited (b) annealed at 650°C for 3 minutes.

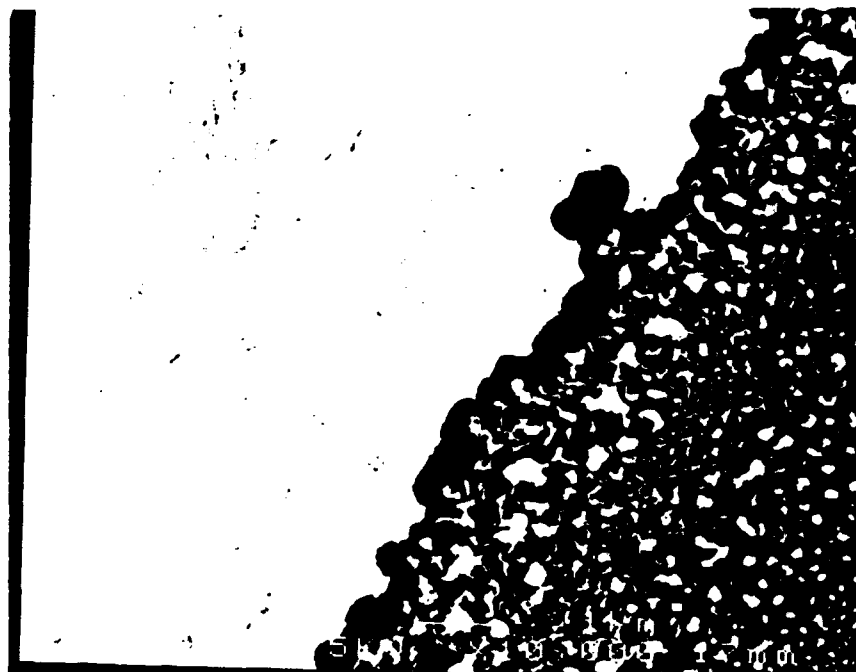


Figure 6. Edge of AuGe/Ni/Au contact pad on Ge:AlN, annealed at 650°C for 3 minutes.

In the present study, the contact resistivities obtained from Au on Mg-doped GaN were higher. The samples were annealed for short periods of time in an RTA furnace under flowing  $N_2$ . The purpose of performing the annealing under  $N_2$  at atmospheric pressure for short times was to reduce the likelihood of generating N vacancies which are believed to be shallow donors that contribute to the background carrier concentration. While increasing the background carrier concentration may contribute to greater current transport in the semiconductor and across the contact interface and apparently reduce the  $\rho_c$ , in general such behavior would be detrimental to overall electronic properties and device performance. More extensive characterization of the electronic properties of our nitride films is needed to better correlate and understand the relationship between dopant concentration, carrier concentration and mobility, Fermi levels, and contact behavior. Improvements in our measurement capabilities, in terms of both equipment and sample preparation techniques, are underway.

The change in appearance and texture of the Au surface after high-temperature annealing is likely due to reactions and/or interdiffusion taking place between the Au and GaN. The lumpiness of the annealed Au film is indicative of metallurgical reaction and phase formation, and the balling-up effect implies a lack of good "wetting" of the GaN surface. Surface characterization and depth profiling by means of Auger electron spectroscopy (AES) will be performed shortly to determine the nature of any chemical changes that took place during annealing. Characterization by means of cross-sectional TEM (X-TEM) will also be

performed to investigate the interfacial structure in detail. A possible scenario is that under sufficient thermal activation Ga diffuses out of the GaN and into the Au layer and reacts to form compounds. Interfacial reactions with contacts on GaAs typically show a significant amount of interphase formation and roughening of the interface. The roughening of the interface due to reaction and phase formation may help to lower  $\rho_c$  by increasing the area of contact between the metal layer(s) and the semiconductor. Gallium nitride lacks the very mobile As species and has stronger interatomic bonding, but sufficiently high temperatures can and favorable chemistry nevertheless free the Ga and N from one another. Depth profiling and cross-sectional examination will allow further clarification of these issues.

*Zn/Au and Cr/Au contacts on Mg:GaN.* The Zn/Au contact system has been used on p-GaAs with some success, but the exact mechanism of its behavior is not yet well understood [2,12]. As Zn acts as an acceptor occupying the Ga site, the Zn is thought to form a highly doped interfacial layer which allows carrier tunneling through the contact interface. Zinc and Cr have approximately similar work functions ( $\phi_{Zn} = 4.33$  eV;  $\phi_{Cr} = 4.5$  eV) and thus, according to the Schottky model, would both be rectifying on a p-type semiconductor having a lower work function ( $\phi_{GaN}$  estimated to be 4.1 eV). Chromium is not used as an acceptor impurity in III-V compounds, but it is capable of assuming a variety of oxidation states between -2 and +6. As indicated on binary phase diagrams, both Zn and Cr have the capability of forming compounds with both Ga and Au, so the potential for interfacial reaction exists given sufficient thermal activation. It is possible that even if a pure contact metal does not have a favorable work function relationship to a semiconductor for ohmic contact formation according to the Schottky model, some of the interfacial compounds that may form could be more favorable. The changes in the Cr/Au contact top surface as a result of thermal treatment suggest interfacial reaction, though whether involving the Cr and Au only or the GaN as well is not clear as yet. The samples will receive further thermal treatment, and upcoming depth profiling and cross-sectional characterization will help determine what has taken place.

*AuGe/Ni/Au contacts on Ge:AlN.* This contact system has become a standard low- $\rho_c$  contact for n-GaAs and the complex nature of its interfacial alloying reactions has received a great deal of study [2,11,12]. Its primary drawback is its relatively poor thermal stability when used with GaAs. After the initial alloying anneal, the electrical properties of AuGe contacts tend to change and degrade significantly upon exposure to subsequent thermal processing steps even at relatively low temperatures (below 500°C). As described above, it is expected that the much stronger interatomic bonding of GaN and AlN in comparison to GaAs will significantly increase the temperatures required for reactions and/or interdiffusion to take place. The other layered contacts, Zn/Au and Cr/Au, have been used with success on p-GaAs,

though the structure and properties of the interfaces have not been as thoroughly studied as has AuGe.

It is evident from SEM examination that the contact system experienced structural changes as a result of annealing treatment. There is no lumpiness as in the other roughened contacts, but rather a fine grain structure that was not apparent in the as-deposited state. However, the degree of interaction between the different layers cannot be determined from the surface texture. As with the other contact systems, further characterization will help to understand the annealed structure of this contact.

This first attempt at ohmic contact formation on doped AlN resulted in a very high contact resistivities. It is likely that the higher interfacial resistance and spatial inhomogeneity of these contacts were largely due to the presence of an insulating oxide layer on the AlN surface. Like the GaN surfaces, the AlN samples were cleaned with a standard HCl dip prior to metal evaporation. However, while HCl removes much of the Ga oxides from GaAs and GaN, it does not remove much of the more stable Al oxides and hydroxides. Since Al oxides have highly negative energies of formation and are very stable compounds, removing them from AlN will likely prove to be a challenge, as has been the experience with AlAs. If the oxide layers can be chemically stabilized and kept very thin, it is possible that the presence of a small amount of oxide can be relatively innocuous in terms of device performance. Atomic cleaning techniques under vacuum, such as plasma or ion etching, prior to contact deposition, are likely to result in substantial improvements of interface properties if structural damage to the semiconductor can be kept to a minimum. In situations where the contact metal can be deposited directly on top of the freshly-grown nitride film without breaking vacuum, such as in MBE growth, oxide formation would be avoided.

#### E. Conclusions

The work conducted in this study so far has shown that it is possible to form metal contacts with ohmic-like linear I-V behavior to doped GaN and AlN films. As yet these contacts exhibit high contact resistivities, but it is reasonable to expect that refinement of contact metals choice, surface cleanliness, and deposition procedures will result in substantial improvements. In the contact systems studied to date, there are indications that interfacial reactions took place during annealing that correlated with the development of linear I-V behavior and reductions in  $\rho_c$ . Further characterization of these contacts, particularly with AES depth profiling and X-TEM analysis, is needed to understand the chemical and structural changes that took place in the contacts as a result of thermal treatment.

#### F. Future Plans/Goals

In addition to chemical and structural characterization of the contact systems described in

this report, the next stage of this study is to investigate more carefully the effects of surface cleaning procedures and to produce more pristine interfaces for electrical characterization. Contacts will be deposited in a UHV e-beam evaporation chamber that has a lower base pressure than the chamber used during this period and has an ion gun to use for surface cleaning as well as metal nitride film formation. Titanium nitride as an ohmic contact candidate for n-type nitride semiconductors was described in the preceding semiannual report, and will be investigated along with the more conventional metal systems.

#### G. References

1. T. C. Shen, G. B. Gao, H. Morkoç, J. Vac. Sci. Technol. B **10**(5), 2113 (1992).
2. R. Williams, *Modern GaAs Processing Techniques* (Artech House, Norwood, MA, 1990).
3. M. Murakami, Materials Science Reports (5), 273 (1990).
4. A. Piotrowska and E. Kaminska, Thin Solid Films **193/194**, 511 (1990).
5. A. Piotrowska, A. Guivarc'h and G. Pelous, Solid-St. Electron. **26**(3), 179 (1983).
6. V. L. Rideout, Solid-St. Electron. **18**, 541 (1975).
7. K. Tanahashi, H. J. Takata, A. Otsuki and M. Murakami, J. Appl. Phys. **72**(9), 4183 (1992).
8. H. J. Takata, K. Tanahashi, A. Otsuki, H. Inui and M. Murakami, J. Appl. Phys. **72**(9), 4191 (1992).
9. M. C. Hugon, B. Agius, F. Varniere, M. Froment and F. Pillier, J. Appl. Phys. **72**(8), 3570 (1992).
10. W. O. Barnard, G. Myburg and F. D. Aurret, Appl. Phys. Lett. **61**(16), 1933 (1992).
11. G. Stareev, Appl. Phys. Lett. **62**(22), 2801 (1993).
12. E. D. Marshall and M. Murakami, in *Contacts to Semiconductors*, edited by L. J. Brillson (Noyes, Park Ridge NJ, 1993).
13. F. W. Ragay, M. R. Leys and J. H. Wolter, Appl. Phys. Lett. **63**(9), 1234 (1993).
14. H. K. Henisch, *Semiconductor Contacts*. (Clarendon Press, Oxford, 1984).
15. E. H. Rhoderick, *Metal-Semiconductor Contacts* (Oxford University Press, New York, 1988).
16. S. Kurtin, T. C. McGill and C. A. Mead, Phys. Rev. Lett. **22**(26), 1433 (1969).
17. J. S. Foresi, *Ohmic Contacts and Schottky Barriers on GaN*, M.S. Thesis, Boston University (1992).
18. J. S. Foresi and T. D. Moustakas, Appl. Phys. Lett. **62**(22), 2859 (1993).
19. G. K. Reeves and H. B. Harrison, IEEE Electron Device Lett. EDL-3 111 (1982).

## **XXI. Growth and Characterization of Cubic Boron Nitride Thin Films\***

**D. J. Kester<sup>a</sup>, K. S. Ailey, D. J. Lichtenwalner and R. F. Davis**

Department of Materials Science and Engineering, North Carolina State University, Box 7907, Raleigh, North Carolina 27695

### **ABSTRACT**

Boron nitride (BN) thin films have been grown on [100] oriented single crystals of Si, diamond, Cu and Ni substrates by ion beam assisted deposition (IBAD) using electron beam evaporation of boron together with simultaneous bombardment by nitrogen and argon ions. Characterization by FTIR and high resolution TEM showed that the films on Si and diamond consisted of initial non-cubic (amorphous and hexagonal BN) layers, followed by the growth of cubic(c)-BN. This growth sequence was attributed primarily to increasing compressive intrinsic stress with increased film thickness. Increasing the substrate temperature above 400°C led to the onset of c-BN at a greater film thickness, while increased ion flux resulted in earlier growth of this phase. These results may be explained by the relaxation of the intrinsic stress in the films at higher temperatures due to increased adatom mobility and to increased intrinsic stress in the films resulting from increased ion bombardment. Lower temperatures led to mixed phase growth. A minimum substrate temperature (200–300°C) is required for nucleation and growth of single phase c-BN by this techniques. It is believed that the interstitial Ar observed in RBS studies is primarily responsible for the stress generation in the films. A combination of h-BN and c-BN were deposited on Ni; only h-BN was obtained on Cu substrates.

### **A. Introduction**

Boron nitride, like carbon, forms with three crystalline structures: a layered hexagonal form (h-BN) which is similar to graphite; cubic boron nitride (c-BN) which corresponds to diamond; and a rarer form, wurtzitic boron nitride (w-BN), which is analogous to Lonsdaleite. The last two phases are metastable at moderate temperatures and pressures.

The interest in c-BN films stems from their potential applications as hard coatings and from their electronic and thermal properties. Cubic BN is the hardest known material other than diamond. Unlike diamond, c-BN does not react with ferrous metals, and it can be used at

---

\*Paper submitted to the Journal of Vacuum Science and Technology.

<sup>a</sup>Present address: Armstrong World Industries, Research and Development, P. O. Box 3511, Lancaster, Pennsylvania 17604

higher temperatures before the onset of structural transformation. These properties make it an excellent cutting tool material. Bulk c-BN crystals formed using high temperature-high pressure techniques are already used in the cutting tool industry. Electronic applications of cubic boron nitride would take advantage of its very wide band gap ( $E_g \approx 6.4$  eV [1]), its ability to be doped both p-type and n-type with Be and Si, respectively [2], and for some applications its very high thermal conductivity.

Cubic boron nitride was first grown in bulk crystal form in 1956 [3]. Reports of c-BN in thin film form appeared as early as 1970 [4], but it was not until about 1987 that thin films conclusively characterized as cubic boron nitride were achieved [5]. Subsequently, many groups have successfully grown c-BN using various techniques including ion beam assisted deposition [6,7] r.f. sputtering [8], ion plating [9], laser ablation [10,11], ECR plasma [12], and chemical vapor deposition (CVD) [13].

Cracking and loss of adhesion of deposited c-BN films are frequently reported phenomena, which have been attributed to a high level of intrinsic compressive stress in the films [14,15]. Murakawa [9] has attempted to overcome this problem using buffer layers between the substrate and the BN film, including a graded B to BN layer and a TiN layer, together with post-deposition annealing of the films. Okamoto *et al.* [16] also used a graded B to BN buffer layer in CVD c-BN films. Both studies produced well adhered films. No reports have appeared of stress-free c-BN films grown directly on a substrate. By contrast, recent research strongly indicates that a high stress level in the film is a necessary condition for the formation of the cubic phase [15, 17].

An additional challenge is growing epitaxial films, which would be essential for the majority of electronic device applications. No reports of reproducible experiments of epitaxial growth of c-BN have appeared. A better understanding of what happens at the substrate-BN interface needs to be developed. In a previous paper [17] we have shown that when BN is deposited on Si, initial amorphous and hexagonal BN layers grow before cubic growth begins. If these interfacial layers are necessary precursors to c-BN growth, then it would appear exceedingly challenging to grow epitaxial c-BN using current PVD methods.

An area of research where significant progress has been made is in determining the deposition conditions necessary for c-BN growth. The work of Kester and Messier [18] established that for a given substrate temperature, the momentum transferred into the growing film by the bombarding ions is the single parameter which controls the formation of c-BN. As long as sufficient N is present, a threshold value of momentum transfer exists for the formation of c-BN. This controlling parameter incorporates the values of ion energy, ion flux, and ion species. As a result of the present study described below we have developed a better understanding of both the conditions required for c-BN growth and of the mechanisms responsible for that growth.

## B. Experiment

**Deposition.** Ion beam assisted deposition (IBAD) has been used successfully for c-BN growth [17,18]. It is particularly useful in that the B deposition rate, bombarding ion energy, ion flux and ion species can be controlled and measured independently. This allows for good quantification of the deposition process. The IBAD configuration in the present study employed electron beam evaporation of boron together with simultaneous bombardment by nitrogen and argon ions from a Kaufman ion source. A schematic of the deposition system is shown in Fig. 1.

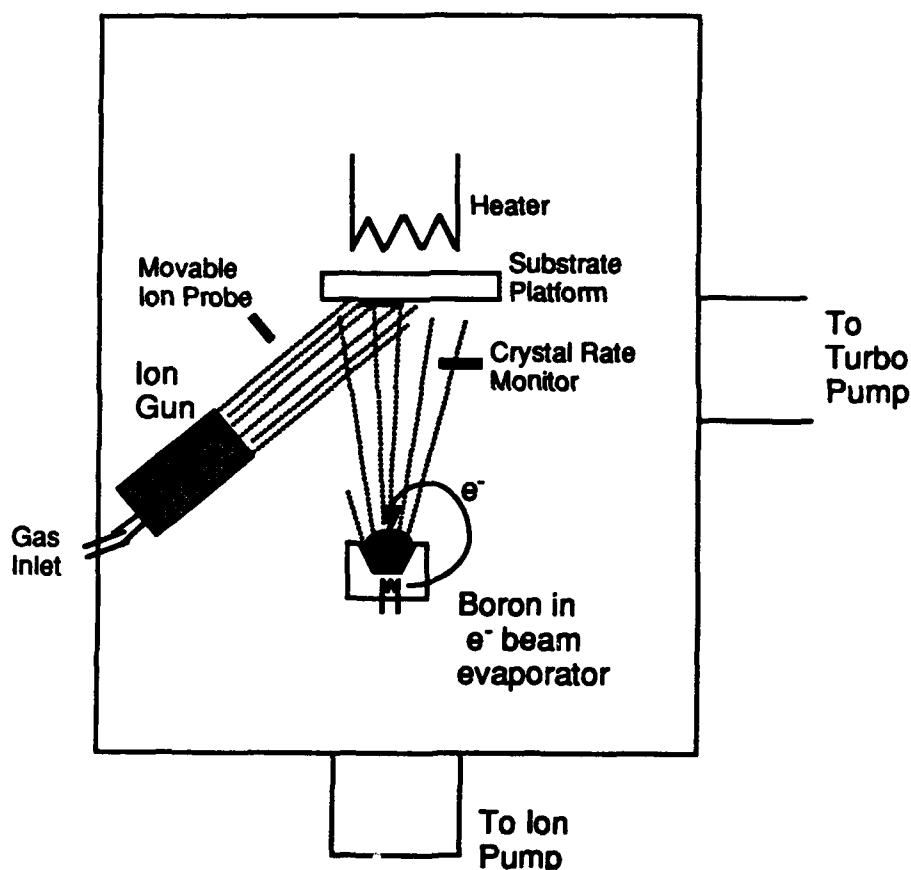


Figure 1. Schematic of UHV electron beam evaporator-based IBAD system used in this research.

The substrates used in this study were (100) single crystal infrared-transparent, high resistivity ( $\rho > 50 \Omega\text{-cm}$ ) on-axis Si; cut and polished single crystal natural diamond; as well as polished single crystal Cu and Ni. The Si substrates were cleaned using a standard RCA procedure [19] of which the final step was a 5 min dip in 10% HF. This left the surface H terminated, as determined by XPS. The diamond substrates were etched in a boiling 3:4:1



H<sub>2</sub>SO<sub>4</sub>:HNO<sub>3</sub>:HClO<sub>4</sub> solution for 45 minutes to remove any graphitic phase, and the Cu and Ni substrates were decreased ultrasonically in a sequence of TCE, acetone, methanol, and DI water. The substrates were attached to Mo holders using Ag paint which acted both as an adhesive and a thermal conductor. This assembly was subsequently loaded through a vacuum load lock into the UHV deposition chamber. Base pressures in the chamber were typically  $5-8 \times 10^{-10}$  Torr.

Each substrate was heated using a W wire coil located behind the Mo substrate holder. They were baked under UHV conditions at 700°C for 20 min to remove residual H<sub>2</sub>O and hydrocarbon species. The substrate temperature during deposition was monitored using thermocouples near the heater, the readings of which had been previously calibrated to several temperatures of the substrate surface. Boron was deposited using a constant deposition rate of 0.5 Å/s, which was monitored using a quartz crystal rate monitor. Fluxes of N and Ar ions were obtained from a 3 cm Ion Tech Kaufman source. Argon and nitrogen gases were used with a gas flow ratio of 1:1. Because of the close ionization potentials of these two gases, the ion ratio was also close to 1:1. The ion source was operated at 500 eV; based on the studies of Hubler *et al.* [20] the N ions were predominantly N<sub>2</sub><sup>+</sup>. The discharge voltage of this source was maintained at a sufficiently low value to prevent double ionization of either species. Since it has been previously shown that c-BN can be successfully deposited using an Ar:N<sub>2</sub> ratio of 1:1 and an ion energy of 500 eV [17,18], these values were maintained constant throughout this study.

Both the ion beam and the boron evaporation were started and allowed to stabilize before deposition. During this period, the substrate was covered by a movable shutter. To eliminate the potential for surface damage, there was no pre-deposition ion bombardment of the substrates.

*Characterization methods.* The primary method of film characterization was Fourier transform infrared spectroscopy (FTIR) due to the ability to distinguish between the cubic and hexagonal or amorphous forms of BN. Cubic BN has a transverse optical mode absorption peak at 1075 cm<sup>-1</sup>, while amorphous and hexagonal BN have a primary absorption peak at 1367 cm<sup>-1</sup> and a secondary peak at 783 cm<sup>-1</sup> [21,22]. The spectra were obtained using an Analect Instruments model fx-6260 spectrometer. The IR beam was passed through the BN coated substrate. A ratio of the resultant spectrum to that obtained from a background scan taken from an uncoated substrate was determined. Reflectance FTIR was employed to characterize the films deposited on the IR opaque Cu and Ni substrates. The latter study was conducted on a Nicolet 620 FTIR equipped with a Spectra Tech IR Plan optical microscope.

The film crystallography and the film-substrate interface were studied via high resolution cross sectional transmission electron microscopy (HRTEM) using a JEOL 4000EX operated at 400kV. The images were recorded using a 1mr convergence semi-angle at a Scherzer defocus of ~ 47nm. Samples were prepared using standard techniques [23].

Rutherford backscattering spectrometry (RBS) was used to measure the compositions and thicknesses of the films due to this techniques ability to give a depth profile of the film, not only information about the surface layer. 2.0 MeV primary  $\text{He}^+$  ions and a  $165^\circ$  scattering angle were used for measuring the energy of the backscattered nuclei. The samples were tilted  $6^\circ$  to prevent channeling.

### C. Results

**FTIR Results.** The results reported in this and the following subsection were obtained using only Si(100) substrates. To study the effect of substrate temperature ( $T_s$ ) on the BN films, depositions were conducted from  $200^\circ\text{C}$  to  $700^\circ\text{C}$ . All other variables were held constant. The results of one of these series of depositions are shown in Fig. 2. There was almost no cubic phase in the  $200^\circ\text{C}$  film. In the temperature range of  $300$ - $400^\circ\text{C}$ , the films

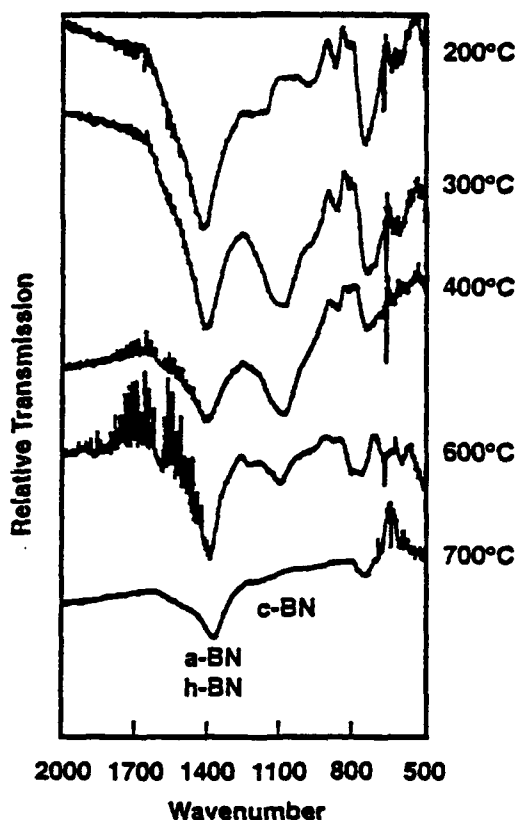


Figure 2. FTIR spectra of BN films deposited on Si(100) at various substrate temperatures. Other deposition conditions were film thickness:  $200\text{\AA}$ ; ion flux:  $0.32\text{ mA/cm}^2$ ; boron deposition rate:  $0.5\text{ \AA/s}$ ; ion energy:  $500\text{ eV}$ ; ion bombardment by 50:50 Ar: $\text{N}_2$ .

were a mixture of the cubic and hexagonal/amorphous phases (IR does not distinguish between the hexagonal and amorphous forms of BN). The relative amount of cubic phase increased with increasing temperature. At some temperature above 400°C the amount of cubic phase began to drop rapidly; it was not observed at all in the film deposited at 700°C. These results correspond well with those of other researchers [24] who have also found that the best temperature for growing cubic boron nitride is at or close to 400°C.

A second significant parameter studied was the ion bombardment flux. As discussed above, it has been previously shown [18] that the critical parameter (at constant temperature) for growing the cubic phase is momentum,  $p$ , transferred from the bombarding ions into the growing film per deposited boron atom,  $p/a$ , where  $a$  is the boron flux measured in atoms  $\text{cm}^{-2} \text{s}^{-1}$ . This critical value is given by

$$\frac{p}{a} = \frac{J}{a} \sqrt{2m \gamma E} \quad (1)$$

where  $J/a$  is the ratio of bombarding ions to depositing boron atoms.  $J$  is the ion flux measured in ions  $\text{cm}^{-2} \text{s}^{-1}$ ,  $m$  is the mass of the bombarding ions and  $E$  is their energy. The maximum energy transfer from the ion to the atom,  $\gamma$ , is given by

$$\gamma = \frac{4mM}{(m+M)^2} \quad (2)$$

with  $M$  being equal to the average mass of the atoms being bombarded. There is a linear relationship between the ion flux,  $J$ , and the momentum transfer value. Therefore a change in the ion flux (while keeping the ion energy and ion species distribution constant) acts directly as a change in momentum transfer. Since changing the ion energy,  $E$ , has less of an effect on the momentum (momentum being proportional to the square root of the energy), the bombardment level in this study was varied by varying the ion flux and keeping the ion energy constant.

Fig. 3(a) shows the effect of changing the ion flux while keeping the temperature constant at 600°C. Essentially no cubic phase is observed until the ion flux reaches 0.30  $\text{mA}/\text{cm}^2$ . The small peaks observed at 1050–1100  $\text{cm}^{-1}$  at the two lower flux values are due to the Si substrate. This confirms that there is a minimum momentum transfer level, and therefore ion flux, necessary to grow the cubic phase at a given temperature. The spectra shown in Fig. 3(b) are from films grown at the same conditions as those in Fig. 3(a), except at 400°C. There is a small cubic peak visible at 0.20  $\text{mA}/\text{cm}^2$ , and the films are predominantly cubic at 0.24 and 0.30  $\text{mA}/\text{cm}^2$ . Comparing Figs. 3(a) and (b) confirms the result seen in Fig. 2 that increasing the substrate temperature above 400°C lowers the proportion of cubic phase in the film.

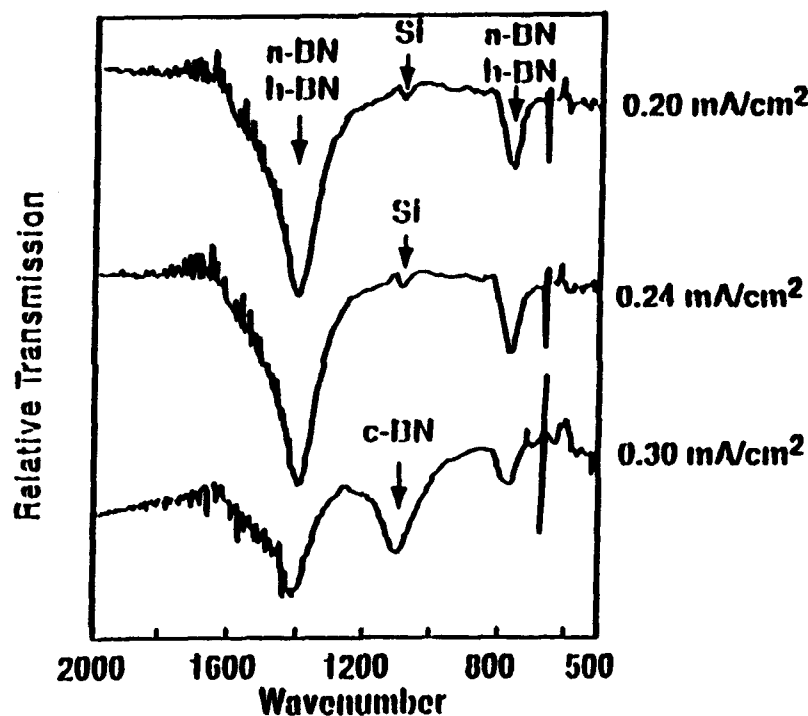


Figure 3 (a). FTIR spectra of a BN film deposited on Si(100) with various ion bombardment fluxes at a substrate temperatures of 600°C. Other deposition conditions were film thickness: 250Å; boron deposition rate: 0.5 Å/s; ion energy: 500 eV; ion bombardment by 50:50 Ar:N<sub>2</sub>.

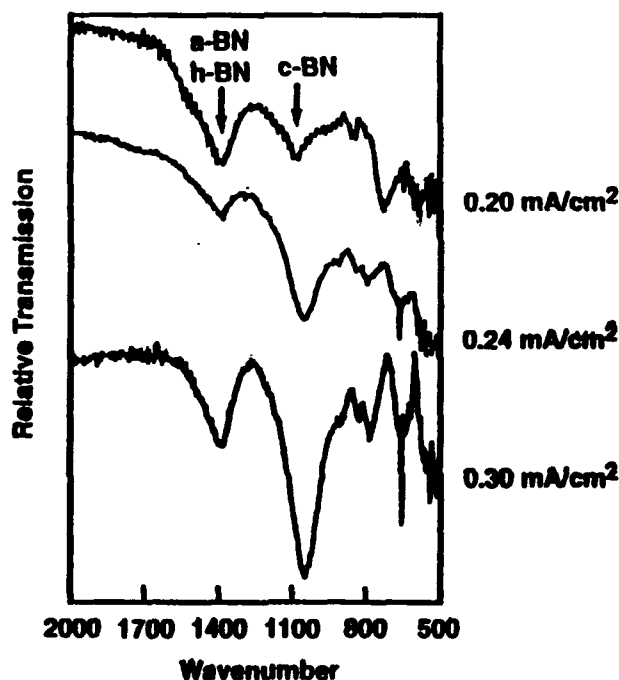


Figure 3 (b). FTIR spectra of a BN film deposited on Si(100) with various ion bombardment fluxes at a substrate temperatures of 400°C. Other deposition conditions were film thickness: 250Å; boron deposition rate: 0.5 Å/s; ion energy: 500 eV; ion bombardment by 50:50 Ar:N<sub>2</sub>.

The data presented above indicated that increasing the ion flux, and thereby the momentum transfer, increases the amount of cubic phase in a film, and that increasing the substrate temperature above 400°C decreases the proportion of cubic phase. However, our previous FTIR and HRTEM results [17] showed that the relative amount of each phase in a 400°C film was also a function of film thickness. These films contained very thin amorphous and hexagonal layers of essentially constant thickness prior to the nucleation and growth of the c-BN layer. Nucleation of the pure cubic phase did not occur until a specific total thickness of the non-cubic phases was achieved.

As such, the FTIR spectra of films of different thicknesses deposited under identical conditions showed that the thicker films had a higher cubic to non-cubic ratio. Examination of films of different thicknesses prepared using the conditions of the 200Å thick 700°C film of Fig. 2, showed the same effect, as demonstrated in Fig. 4. The 100Å film and the 200Å films were completely amorphous/hexagonal, but the 400Å film was predominantly cubic. Similarly, FTIR of a set of films of different thicknesses prepared under the same conditions as the 600°C film of Fig. 2, revealed a growth sequence and layer thicknesses of non-cubic (<200Å), partially cubic (200Å), and predominantly cubic (remainder of film). These results indicate (and the HRTEM results noted below prove) that the different proportions of amorphous/hexagonal and cubic phase found in the different films are not due to different amounts of each phase interspersed through the film, but rather to the transition from single phase hexagonal to single phase cubic occurring at varying thicknesses depending on growth conditions. Specifically, the differences between the 400°C, 600°C, and 700°C films seen in Fig. 2, which ranged from significantly cubic at 400°C to completely non-cubic at 700°C are due to varying thicknesses at which the growth of the cubic phase layer begins. A higher substrate temperature delays the onset of the cubic phase. Increased ion flux enhances the onset of this phase.

**HRTEM results.** High resolution TEM images of films deposited at 200°C, 400°C, and 700°C are shown in Figures 5(a), 5(b), and 5(c). The film deposited at 200°C (Fig. 5(a)) has a 70Å amorphous layer at the Si interface followed by a layer of oriented h-BN. No c-BN is present. The film deposited at 400°C (Fig. 5(b)) has a 20Å amorphous layer followed by 50Å of oriented h-BN followed by c-BN. The film grown at 700°C (Fig. 5(c)) has a 50Å amorphous layer followed by a ~150Å layer of predominantly partially oriented h-BN material with a small amount of c-BN, followed by a c-BN layer.

**RBS Results.** The BN grown for RBS was deposited on the lower atomic number substrate of Be to circumvent overlap of the spectra of the Si substrate with that of the film. The deposition conditions were those which resulted in c-BN growth on Si: a substrate temperature of 400°C, ion energy of 500eV, and an ion flux of 0.24 mA/cm<sup>2</sup>. The film thickness was 500Å. The results are shown in Fig. 6. Rutherford backscattering is more

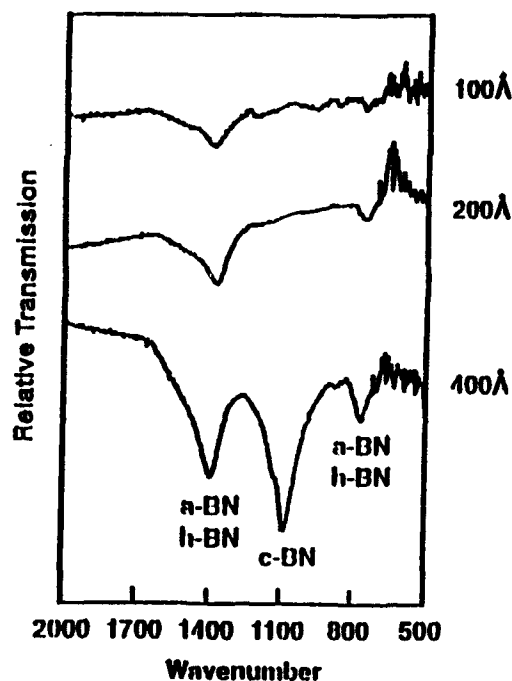


Figure 4. FTIR spectra of BN films deposited on Si(100) with various thicknesses. Other deposition conditions were substrate temperature: 700°C; ion flux: 0.32 mA/cm<sup>2</sup>; boron deposition rate: 0.5 Å/s; ion energy: 500 eV; ion bombardment by 50:50 Ar:N<sub>2</sub>.

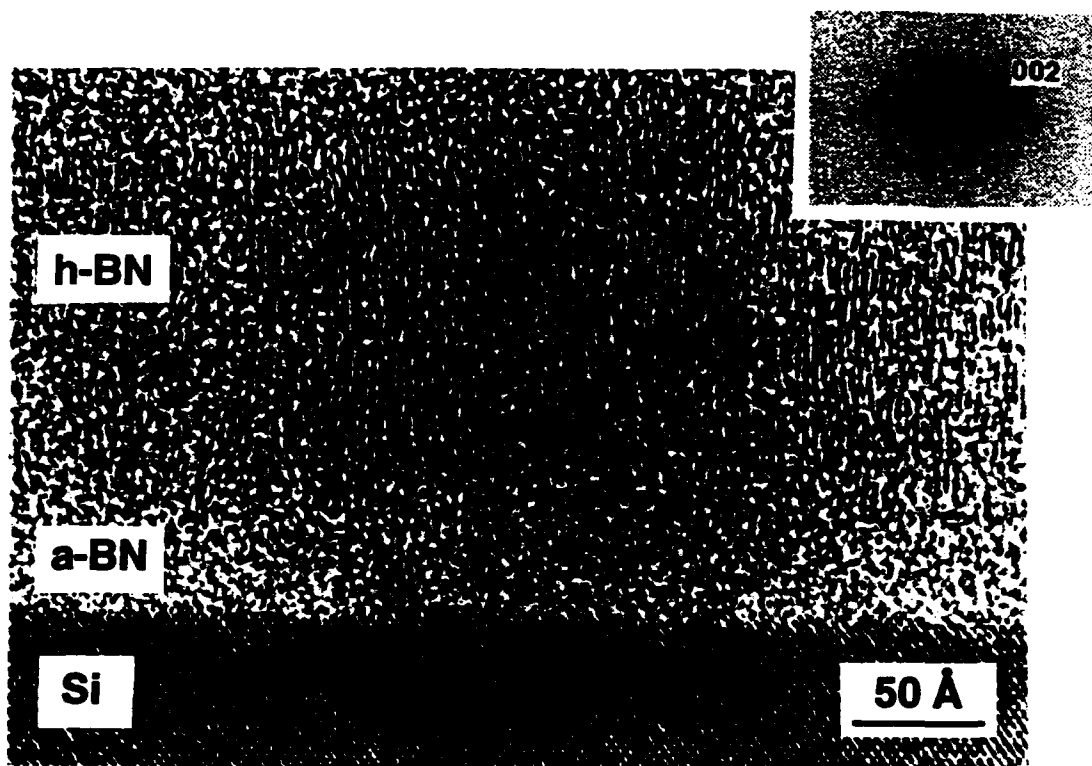


Figure 5(a). HRTEM image of a film deposited on Si(100) at 200°C. Other deposition conditions were ion flux: 0.28 mA/cm<sup>2</sup>; boron deposition rate: 0.5 Å/s; ion energy: 500 eV; ion bombardment by 50: 50 Ar:N<sub>2</sub>.

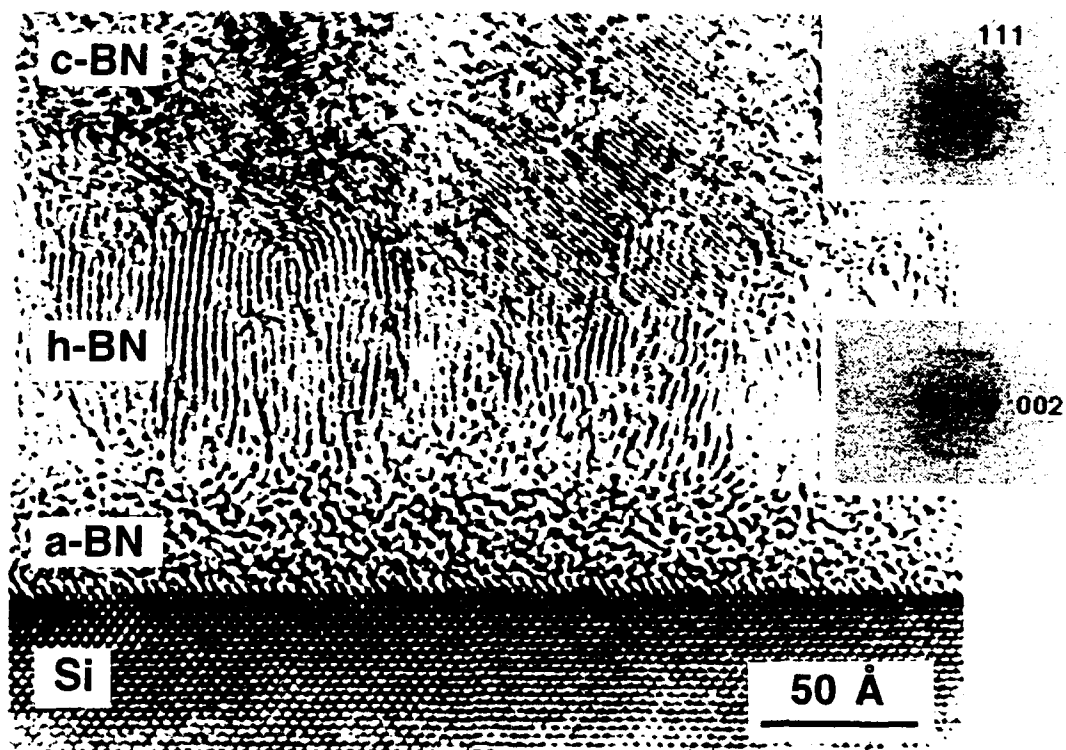


Figure 5(b). HRTEM image of a film deposited on Si(100) at 400°C. Other deposition conditions were ion flux: 0.12 mA/cm<sup>2</sup>; boron deposition rate: 0.25 Å/s; ion energy: 500 eV; ion bombardment by 50: 50 Ar:N<sub>2</sub>.

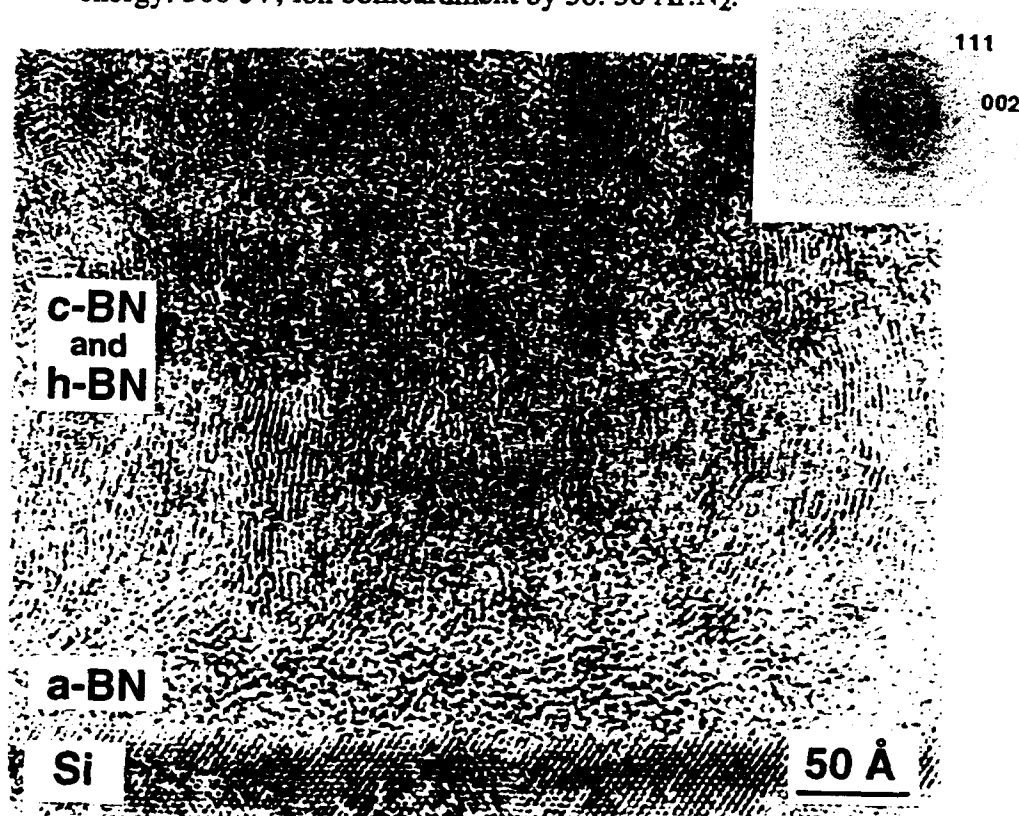


Figure 5(c). HRTEM image of a film deposited on Si(100) at 700°C. Other deposition conditions were ion flux: 0.28 mA/cm<sup>2</sup>; boron deposition rate: 0.5 Å/s; ion energy: 500 eV; ion bombardment by 50: 50 Ar:N<sub>2</sub>.

sensitive to elements of higher atomic number, due to their larger nuclear cross sections. Therefore, the sizes of the original peaks at various channel numbers do not directly show their actual concentration. Computer modeling of the spectra revealed that in addition to the expected Be, B, and N, there was O due to a BeO layer on the substrate as well as Ar, Fe, and Hf in the film having the atomic percentages of  $\sim 1.5\%$ ,  $\sim 0.2\%$ , and  $\sim 0.05\%$ , respectively. The Ar was derived from the ion bombardment during growth; the Fe was probably due to the ion beam bombardment of the stainless steel shutter above the substrates, and the Hf was very likely derived from resputtering of residual amounts previously deposited on the substrate block.

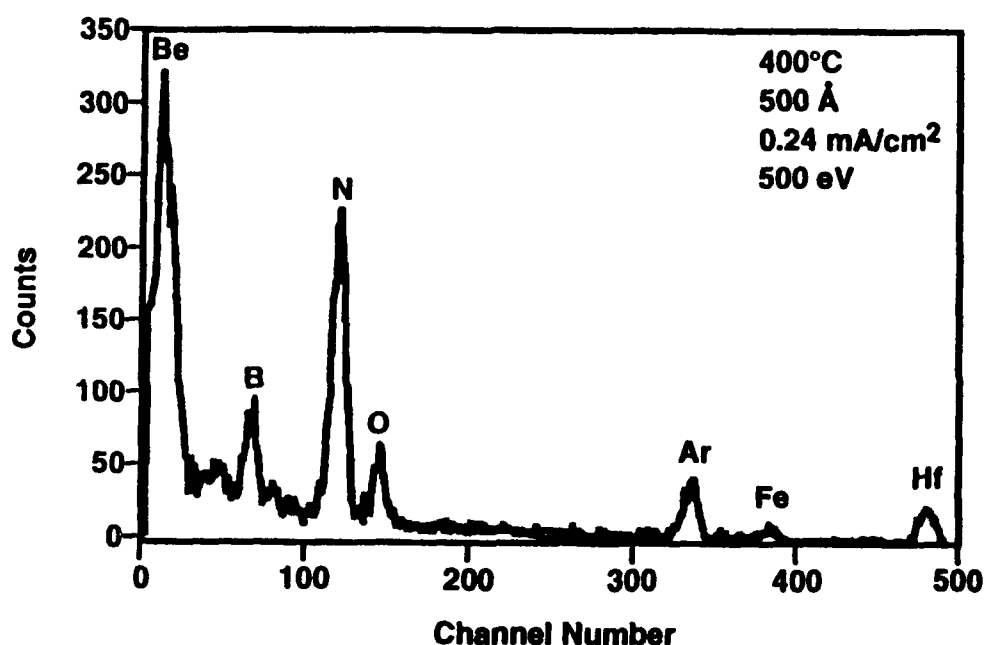


Figure 6. RBS spectra of a BN film on a beryllium substrate. Deposition conditions were film thickness: 500 Å, substrate temperature: 400°C; ion flux: 0.24 mA/cm<sup>2</sup>; boron deposition rate: 0.5 Å/s; ion energy: 500 eV; ion bombardment by 50:50 Ar:N<sub>2</sub>.

*Other Substrates.* Films having a thickness of 1000 Å were grown on diamond at substrate temperatures of 400° and 600°C using an ion energy of 500eV and an ion flux of 0.24 mA/cm<sup>2</sup>. A representative FTIR pattern of one of the films deposited at 400°C is shown in Fig. 7. A sharp c-BN peak is observed at  $\sim 1080$  cm<sup>-1</sup>. The h-BN peak is very small. The spectrum of this relatively thick film has a sharper c-BN peak and a better c-BN to h-BN ratio than any of the films we had previously deposited on Si, and is as good or better than any that have previously appeared in the literature. For the film grown at 600°C the FTIR spectrum was essentially the same.



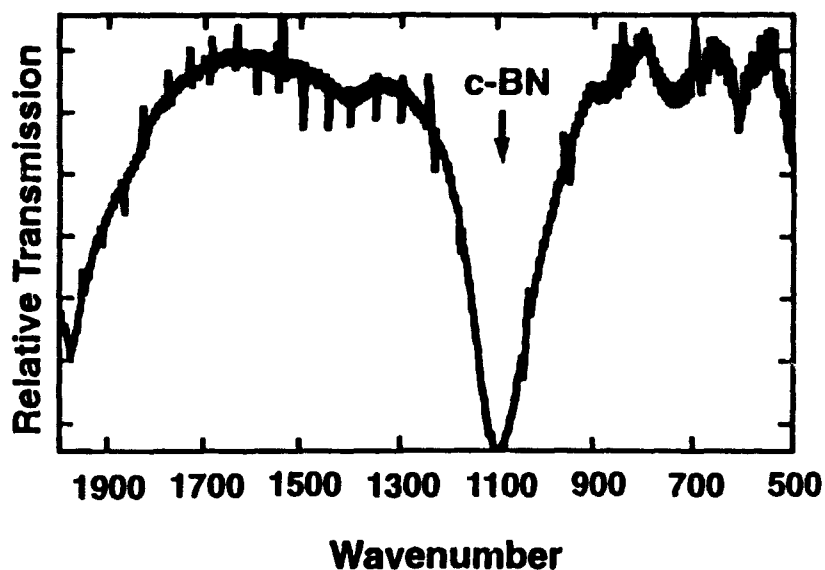


Figure 7. FTIR spectra of BN deposited on a single crystal diamond(100) substrate. Deposition conditions were film thickness: 1000Å, substrate temperature: 400°C; ion flux: 0.24 mA/cm<sup>2</sup>; boron deposition rate: 0.5 Å/s; ion energy: 500 eV; ion bombardment by 50:50 Ar:N<sub>2</sub>.

Observation via SEM of the films deposited at 400°C showed occasional cracking. The films deposited at 600°C showed no cracking or delamination. Films deposited under the same deposition conditions and the same thicknesses on Si exhibited both severe cracking and delamination.

High resolution TEM was performed on the sample grown at 600°C, and an image is shown in Fig. 8. The same type of layered structure observed on BN grown on Si is present, although not as pronounced.

Nickel and Cu also have lattice spacings very close to that of c-BN, with a lattice mismatch for Ni of 2.6% and for Cu of less than 0.05%. Therefore it was thought that like diamond (which has a lattice mismatch of 1.4%) they may be better substrates for c-BN growth than Si which has a lattice mismatch of 33%. Films having a thickness of 500Å were grown at 400°C under the same conditions of ion flux and ion energy employed in the deposition on diamond. As shown in Fig. 9, reflectance FTIR from films grown on the Ni substrate revealed a mixture of h-BN and c-BN; films grown on Cu were h-BN with no evidence of c-BN.

#### D. Discussion

The above results show that the onset of c-BN growth is a function of temperature, ion momentum transfer and deposition period (film thickness). McKenzie *et al.* [14,15] have shown theoretically and experimentally that the effect of deposition period is caused by the build-up of biaxial compressive stresses in the growing film. They observed by FTIR,

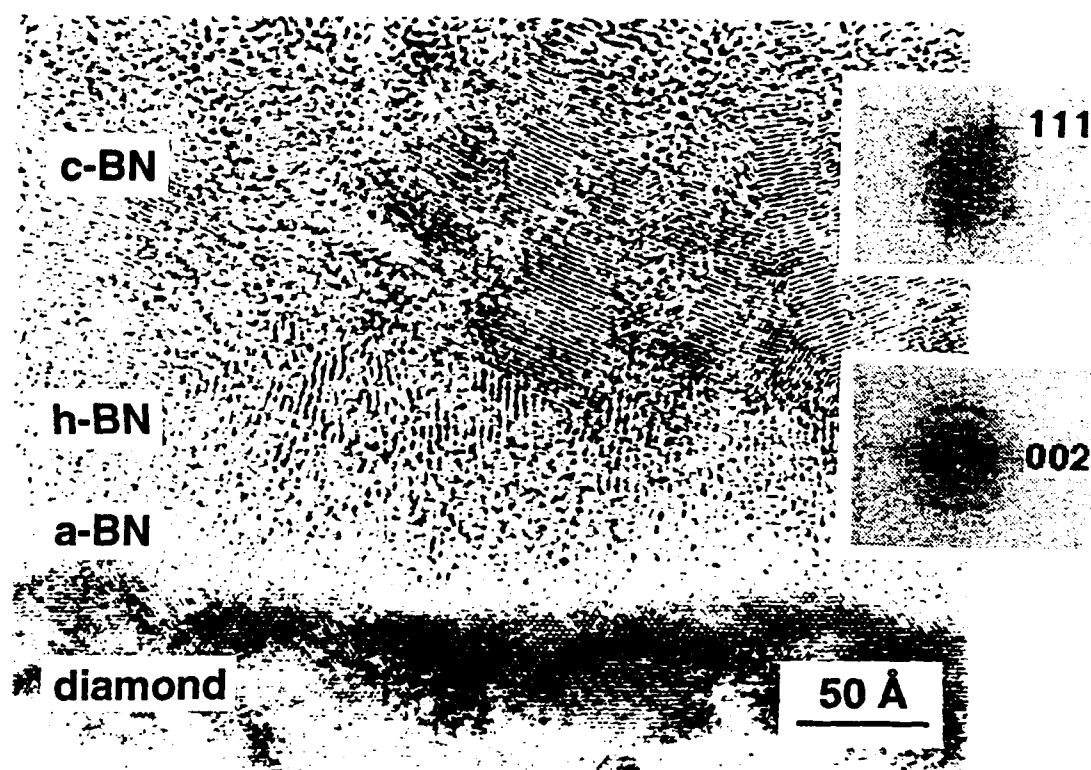


Figure 8. HRTEM image of a 600°C film on a diamond(100) substrate. Other deposition conditions were ion flux: 0.28 mA/cm<sup>2</sup>; boron deposition rate: 0.5 Å/s; ion energy: 500 eV; ion bombardment by 50:50 Ar:N<sub>2</sub>.

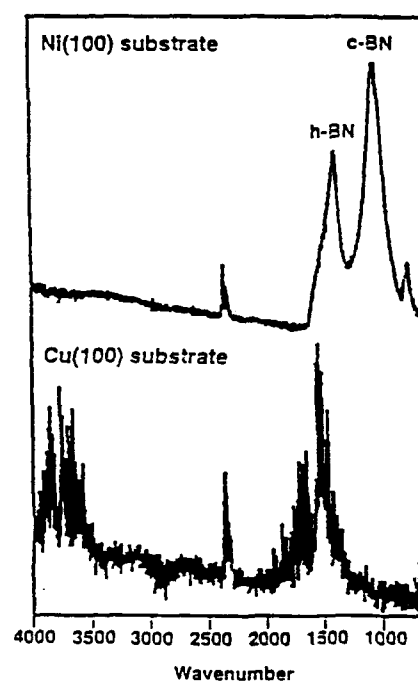


Figure 9. Reflectance FTIR of BN deposited on Cu(100) and Ni(100) substrates. Deposition conditions were film thickness: 500Å, substrate temperature: 400°C; ion flux: 0.24 mA/cm<sup>2</sup>; boron deposition rate: 0.5 Å/s; ion energy: 500 eV; ion bombardment by 50:50 Ar:N<sub>2</sub>.

electron energy loss spectroscopy and TEM an initial layer of h-BN oriented perpendicular to the substrate surface. The nucleation and growth of c-BN occurred as the stress in the film increased. No amorphous phase was reported. The stress at the onset of c-BN growth corresponded to conditions in the high pressure regime where this phase is stable. The present results can be understood using this model. Increasing the substrate temperature from, for example, 400°C to 700°C, results in both a higher surface mobility of the adsorbed species and possibly bulk annealing, which allow stress relaxation. Thus, as shown in Fig. 4, the higher the deposition temperature the greater the film thickness necessary to reach the stress level required for c-BN nucleation and growth, all other conditions being the same. There is a sharp increase in the transition thickness, and therefore a sharp drop in stress, within the 600-700°C temperature range. This corresponds with the results of Windischmann [25] who found in several different materials, that increasing the deposition temperature from room temperature causes a gradual decrease in the intrinsic stress, followed by a sharp drop when the temperature reaches  $T_m/3$ , where  $T_m$  is the melting point. For BN,  $T_m/3$  is ~700°C.

The foregoing explanation does not account for the results of decreasing the temperature below 400°C, for it does not further lower the threshold thickness for initiation of the cubic phase. In fact, at these lower temperatures, growth of the cubic material as a single phase was not observed. The existence of an apparent minimum in substrate temperature for the growth of pure c-BN indicates that the combination of thermal energy and intrinsic stress is insufficient for all the B and N atoms to surmount the activation energy barrier between the layered h-BN and the three-dimensional c-BN structure.

Similarly, an increase in ion flux and momentum transfer into the growing film will lead to a more rapid increase in stress, as shown by Kester and Messier [18] as well as Windischmann [25] and a decrease in the film thickness necessary for the initiation of the cubic phase. The results presented in Figs. 3(a) and (b) show the onset of c-BN to be also a function of ion flux. These correspondences between known effects on stress and the onset of c-BN growth are strong evidence that the cubic phase growth results directly from stress.

The mechanism(s) which cause(s) the increase in stress in the films is not completely understood. It may be densification due to ion bombardment, as reported by [27]. The densification occurs through the collapse of the void structure found in non-bombarded films. Nir [28] and Targove and Macleod [29] have shown experimentally that the magnitude of the compressive stress is a function of the momentum transfer to the growing surface for particle energies <1kV. Theoretical studies by Windischmann [30] support these findings. A second possibility is that the stress is due to the presence of interstitials in the film. In the case of the c-BN films, the relatively high concentration of Ar (1.5 at.%) as shown by RBS would suggest that the compressive stress may be caused by interstitial Ar atoms in the manner observed by McKenzie *et al.* [14].

In the growth of BN films via IBAD by Stambouli *et al.* [31] using bombardment with nitrogen ions, it was found that sufficient bombardment by nitrogen ions resulted in nitrogen-rich (non-cubic)  $\text{BN}_{1+x}$  films with a higher density than stoichiometric BN films. The former also possessed significantly higher compressive stresses than the stoichiometric films. They attributed this to interstitial N. If this is the case, bombardment by the larger Ar ion, and the formation of interstitial Ar at 1.5 at.%, would be expected to also increase the compressive stress in the films. In fact, Fahnline *et al.* [32] showed that 1.5 at.% Ar in Ge films caused a significant increase in compressive intrinsic stress.

Kester and Messier [18] previously showed that the phase of BN films is determined by three factors: substrate temperature, bombardment measured in terms of momentum transfer, and stoichiometry. The stoichiometry factor was a requirement in that at least one bombarding N atom had to be present for each depositing B atom. They plotted the observed phase(s) as a function of temperature and bombardment. In the present study we have shown that these are controlling parameters, but they control not only whether or not cubic growth will occur, but the time of nucleation and growth of this phase. Some of the conditions that they described as leading to mixed cubic and hexagonal growth appear to be conditions leading to layered single phase hexagonal followed by single phase cubic growth.

The problem of adhesion of c-BN on Si was addressed by using substrates with better lattice matching to c-BN including Cu and Ni and diamond. The cubic phase did not grow on the Cu(100) substrate due to its excellent ductility which adsorbed the stresses generated in the growing film; it did grow on the less ductile Ni(100) substrate, but the adhesion was as poor as on Si. These results indicate that the adhesion problem is not simply one of lattice mismatch with the substrate.

Adhesion on the diamond substrates was much better than on the other materials. Although a relatively small number of samples were produced, due to the prohibitive cost, these results suggest that c-BN does not easily grow initially on diamond even though this substrate has a higher surface energy than c-BN. Moreover, these results imply that c-BN will not initially deposit on any material, at least by the methods used in this investigation.

## E. Conclusions

Boron nitride films deposited using ion beam assisted deposition on Si, diamond and Ni substrates grow in a sequence of amorphous, hexagonal and cubic layers. This is believed to be caused primarily by the increased incorporation of intrinsic biaxial compressive stresses in the films. The nucleation of the cubic phase occurs at differing film thicknesses as a function of both substrate temperature and ion flux. There appears to be a minimum substrate temperature (200–300°C) below which single phase growth of c-BN does not occur. At higher temperatures the onset of the cubic phase is a function of temperature, appearing at

greater thicknesses at higher temperatures under the same ion flux. This is attributed to increased adatom mobility and bulk annealing with increasing temperature and a concomitant relaxation of stress. For these reasons the optimum temperature range for the growth of c-BN was determined to be 400-500°C. This range in T is similar to that determined by other investigators. Increased ion bombardment, as measured by momentum transferred into the film, leads to an earlier start of cubic growth, apparently due to the increased stress. It is suggested that the stress in the films may be due to Ar interstitials. The fact that stress is a function of momentum transferred into the film may be due to higher momentum bombardment (higher flux, energy or ion mass) leading to deeper and/or a greater number of interstitials.

We were unable to nucleate c-BN as the initial phase on any substrate; we suspect that this may prove difficult using bombardment based deposition methods due to the requirement of increasing stress generation in the films.

#### E. Acknowledgements

The authors express their appreciation to the Electronic Materials Center of Kobe Steel, USA and the Strategic Defense Initiative via the Office of Naval Research (Contract No. N00014-92-J-1720) for support of this research, to Dr. Nalin Parikh of the University of North Carolina-Chapel Hill for the RBS measurements, to Professor D. R. McKenzie of the University of Sydney and Lisa M. Porter, R. C. Glass and M. J. Paisley of NCSU for helpful discussion.

#### F. References

1. L. Vel, G. Demazeau, and J. Etourneau, *Materials Science and Engineering B10*, 149 (1991).
2. K. Era, O. Mishima, Y. Wada, J. Tanaka, and S. Yamaoka, in *Electroluminescence*, edited by S. Shionoya and H. Kobayashi, *Springer Proceedings in Physics*, Vol. 38, 386 (1989).
3. R. H. Wentorf, Jr., *J. Chem. Phys.* 26, 956 (1957).
4. V. N. Gashtold *et al.*, *Elektronnaya Tekhnika* 12, 58 (1970).
5. K. Inagawa, K. Watanabe, H. Ohson, K. Saitoh, and A. Itoh, *J. Vac. Sci. Technol. A5*, 2696 (1987).
6. D. J. Kester and R. Messier, *Mater. Res. Soc. Symp. Proc.* 235, 721 (1992).
7. T. Wada and N. Yamashita, *J. Vac. Soc. Technol. A10*, 515 (1992).
8. K. Bewilogua, J. Buth, H. Hübsch, and M. Grischke, *Diamond and Related Materials* 2, 1206 (1993).
9. M. Murakawa, S. Watanabe, and S. Miyake, *Diamond Films and Technol.* 1, 55 (1991).
10. G. L. Doll, J. A. Sell, C. A. Taylor II, and R. Clarke, *Phys. Rev. B* 43, 6816 (1991).
11. T. A. Friedmann, K. F. McCarty, and E. J. Klaus, *Applied Physics Letters* 61, 2406 (1992).
12. Y. Osaka, M. Okamoto, and Y. Utsumi, *Mater. Res. Soc. Symp. Proc.* 223, 81 (1991).
13. H. Saitoh and W. Yarborough, *Applied Physics Letters* 58, 2228 (1991).
14. D. R. McKenzie, W. D. McFall, W. G. Sainty, C. A. Davis and R. E. Collins, *Diamond Relat. Mater.* 2, 970 (1993).

15. D. R. McKenzie, J. Vac. Sci. Technol. A11,2758 (1993).
16. M. Okamoto, H. Yokoyama, and Y. Osaka, Japanese Journal of Applied Physics 29, 930 (1990).
17. D. J. Kester, K. S. Ailey, R. F. Davis, and K. L. More, J. Mater. Res. 8, 1213 (1993).
18. D. J. Kester and R. Messier, J. Appl. Phys. 72, 504 (1992).
19. W. Kern and D. A. Puo-tinen, RCA Rev. 31, 187 (1970).
20. D. Van Vechten, G. K. Hubler, and E. P. Donovan, Vacuum 36, 841 (1986).
21. R. Geick and C. H. Perry, Phys. Rev. 146, 543 (1966).
22. P. J. Gielisse, S. S. Mitra, J. N. Plendl, R. D. Griffis, L. C. Mansur, R. Marshall, and E. A. Pascoe, Phys. Rev. 155, 1039 (1967).
23. C. H. Carter, Jr., J. A. Edmond, J. W. Palmour, J. Ryu, H. J. Kim and R. F. Davis in *Microscopic Identification of Electronic Defects in Semiconductors*, edited by N. M. Johnson, S. G. Bishop, and G. Watkins (Mater. Res. Soc. Proc., 46, Pittsburgh, PA 1985) pp. 593 -598.
24. N. Tanabe, T. Hayashi, and M. Iwaki, Diamond and Related Materials 1,151 (1992).
25. H. Windischmann, J. Vac. Sci. Technol. A7, 2247 (1989).
26. H. Windischmann, J. Appl. Phys. 62, 1800 (1987).
27. R. A. Roy and D. S. Yee, in *Handbook of Ion Beam Processing Technology*, edited by J. J. Cuomo, S. M. Rossnagel, and H. R. Kaufman, (Noyes, Park Ridge, NJ, 1989).
28. D. Nir, J. Vac. Sci. Technol. A4, 2954 (1986).
29. J. D. Targove and H. A. Macleod, App. Optics 27, 3779 (1991).
30. H. Windischmann, J. Vac. Sci. Technol. A9, 2431 (1991).
31. V. Stambouli, O. Burat, D. Bouchier, and G. Gautherin, Surface and Coatings Technology 43/44, 137 (1990).
32. D. Fahnlne, B. Yang, K. Vedam, R. Messier, and L. Pilione, Mater. Res. Soc. Symp. Proc. 130, 355 (1989).

## **XXII. Semi-insulating GaP and InGaP Films Grown at Low Temperatures by Gas Source Molecular Beam Epitaxy**

### **A. Introduction**

GaAs buffer layers grown at low temperatures (LT) by molecular beam epitaxy (MBE) have received a great deal of attention as excellent alternative buffer layers to eliminate sidegating (or backgating) effects in the GaAs field-effect-transistor-based integrated circuits [1] and as insulators for high power GaAs metal-insulator-semiconductor field-effect transistors (MISFETs) [2]. These new materials, usually grown at  $\sim 200^\circ\text{C}$ , exhibit good crystalline quality and extremely high resistivity, and thus can provide excellent device isolation. The latter is due to the excess arsenic incorporation ( $\sim 1$  at.%) in the layers leading to densities as high as  $5 \times 10^{18} \text{ cm}^{-3}$  of  $\text{As}_{\text{Ga}}$  antisite defects [3]. Annealing these materials or proceeding with a growth at normal MBE growth temperature ( $600^\circ\text{C}$ ) causes the excess arsenic to form precipitates as indicated from transmission electron microscopy (TEM) studies [4].

Since the success of LT GaAs material, investigations have been extended not only to the LT growth of other As-based III-V compounds such as LT AlGaAs [5] and LT InAlAs [6], but also to the LT growth of P-based materials such as LT InP [7]. However, little work has been reported on LT GaP and InGaP films even though these LT films, all having a wide bandgap, are promising for device applications. In addition, LT GaP and LT InGaP can be extremely useful for some devices since GaP is almost lattice matched to Si and InGaP can be grown lattice matched to GaAs. An immediate question raised on these LT films is whether excess phosphorus and phosphorus precipitates can exist and exhibit the similar properties as their arsenic counterpart. Previous efforts for LT InP did not yield semi-insulating films [8]. In this report, we will discuss the growth and characterizations of LT GaP and LT InGaP films grown by gas source molecular beam epitaxy (GSMBE).

### **B. Experimental Conditions**

All the epilayers presented in this work were grown in a Riber 32RD GSMBE system. Semi-insulating (SI) GaP and GaAs (100) substrates were used for LT GaP and LT InGaP, respectively. The substrates were degreased, etched and then mounted on the Mo blocks with In solder. Elemental Ga and In sources and 100%  $\text{PH}_3$  thermally cracked at  $900\text{--}950^\circ\text{C}$  were used to grow these films. The growth chamber pressure was maintained in the  $10^{-5}$  Torr range using a turbomolecular pump. The growth temperature cannot be accurately determined in our system and was estimated according to our previous calibrations using the oxide desorption temperature of GaAs ( $580^\circ\text{C}$ ) as a reference. The thermocouple reading is  $60\text{--}80^\circ\text{C}$  lower than this reference temperature. Temperatures quoted in this report are the

corrected values rather than the thermocouple readings. The growth rates of all GaP and InGaP epilayers were 1 and 0.5  $\mu\text{m/h}$ , respectively.

The GaP and GaAs substrates were all heated at 630°C for ~5-10 min under  $\text{PH}_3$  or  $\text{AsH}_3$  overpressure for oxide removal before growth of GaP or InGaP films, respectively. In the case of LT GaP, several approaches were applied to the growth of LT films. When films were grown for electrical evaluations, the substrate temperature was lowered directly to the desired low temperature followed by the growth of a GaP layer (~2  $\mu\text{m}$ ). For structural characterization, a GaP buffer layer was grown first at 560°C followed by the LT film. GaP films were also grown at high temperature (560°C) as a reference for both the electrical and structural characterizations.

Reflection high energy electron diffraction (RHEED), cross-sectional transmission electron microscopy (XTEM), and double-crystal x-ray diffraction (DCXRD) were used to assess the crystal quality of the LT GaP and InGaP films. The *in situ* RHEED showed a streaky pattern, indicating crystalline growth of the LT films. The first nonstoichiometry measurements of LT GaP films were carried out using particle-induced x-ray emission (PIXE) technique. The measurements were performed by employing a 0.5 MeV  $\text{H}^+$  beam with samples tilted at 65° with respect to the ion beam. The analytical scanning transmission electron microscopy (STEM) approach was also used to determine the excess phosphorus in LT GaP as well as in LT InGaP films. The analysis was performed in a TOPCON EM-002B ultra-high resolution analytical electron microscope equipped with an electron probe. All the LT samples used in this report had a mirror-like morphology. The resistivities of LT GaP films and GaP substrate were measured with the van der Pauw technique while those of LT InGaP films and GaAs substrate were determined using temperature-dependent Hall effect measurements.

### C. Results and Discussion

**LT GaP. TEM analysis.** LT GaP films grown at temperatures lower than 160°C were polycrystalline as demonstrated by both the RHEED pattern and the TEM diffraction pattern. Increasing the growth temperature by ~30°C resulted in a streaky RHEED pattern and single-crystal films, as confirmed by TEM. Figure 1 shows a cross-sectional TEM dark field micrograph of multilayers of GaP epitaxial films taken under the two beam condition  $g=400$  (g.-g). This structure has a 0.4  $\mu\text{m}$  GaP buffer layer grown at 560°C, followed by a LT GaP layer grown at about 210°C (1  $\mu\text{m}$ ). The growth temperature was then decreased further by ~20°C without interrupting the growth to grow a second LT layer of the same thickness. All layers are single crystalline as indicated from the electron diffraction pattern. The LT films show a contrast from the one grown at high temperature which can be attributed to excess phosphorus in the lattice resulting from a deviation from stoichiometry[9]. One may also



observe in Figure 1 the presence of contrast modulations near the interface between the two LT GaP layers. This can be due to the substrate temperature fluctuations resulting from the 20°C decrease.

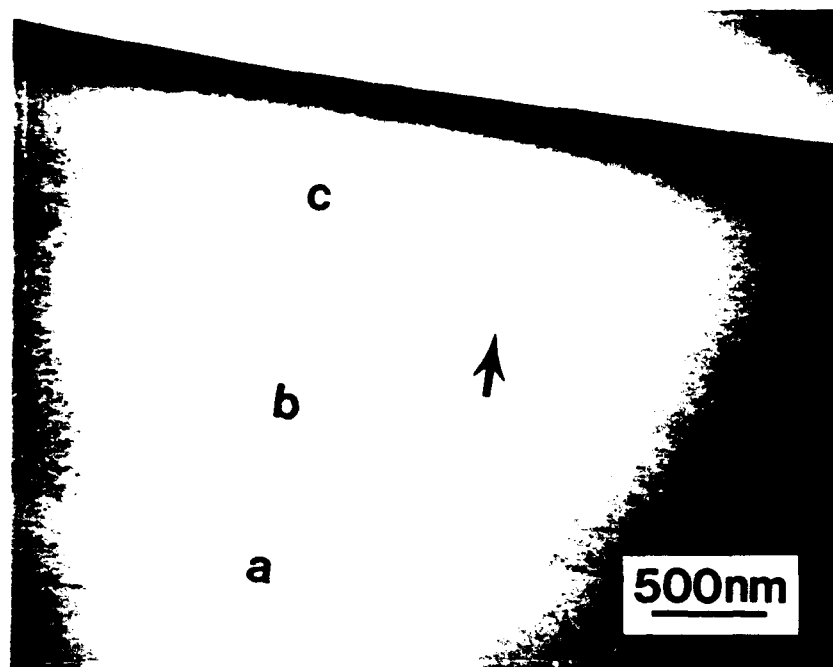


Figure 1. Cross-sectional TEM micrograph of a multilayered structure containing: (a) GaP buffer layer grown at 560°C (HT), (b) LT GaP film (1  $\mu\text{m}$ ) grown at 210°C and, (c) LT GaP layer (1  $\mu\text{m}$ ) grown at 190°C. The arrow indicates the transition region between the two LT GaP films. The contrast between LT GaP films and HT GaP film might be due to the excess phosphorus in LT films.

Using conventional imaging techniques, TEM studies on annealed samples did not show any incoherent phosphorus precipitation with defined boundaries. However, high-resolution TEM on the annealed films revealed the presence of regions having different phase contrast which suggests coherent precipitation. These coherent precipitates, indicated by the arrow in Figure 2(a), may become incoherent and demonstrate a phase boundary after prolonged annealing. To compare the current observations with LT arsenic-based films, a GaAsP film was grown at 200°C. The composition of this ternary alloy was determined by DCXRD to have 20% GaP (after annealing). TEM studies of this annealed LT GaAsP show pronounced incoherent arsenic precipitates as illustrated in Figure 2(b). The precipitates have been segregated to the dislocation lines and microtwin boundaries.

X-ray diffraction. High-resolution x-ray diffraction results were obtained with a Bede 200 double-crystal diffractometer. Films grown at high temperatures show only one diffraction peak from (113) reflection planes [Figure 3(a)]. For the LT growth, two (113) reflections

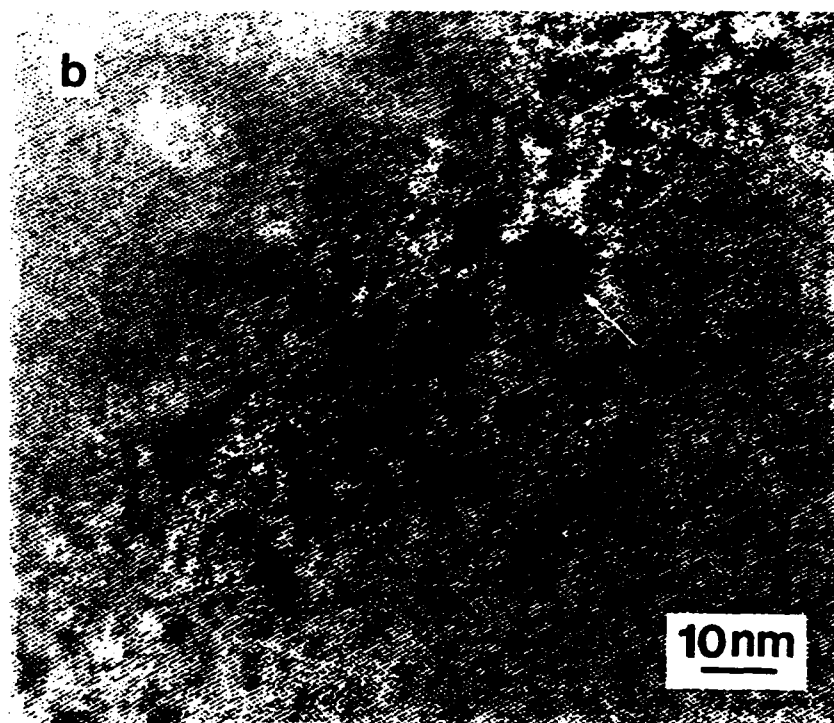
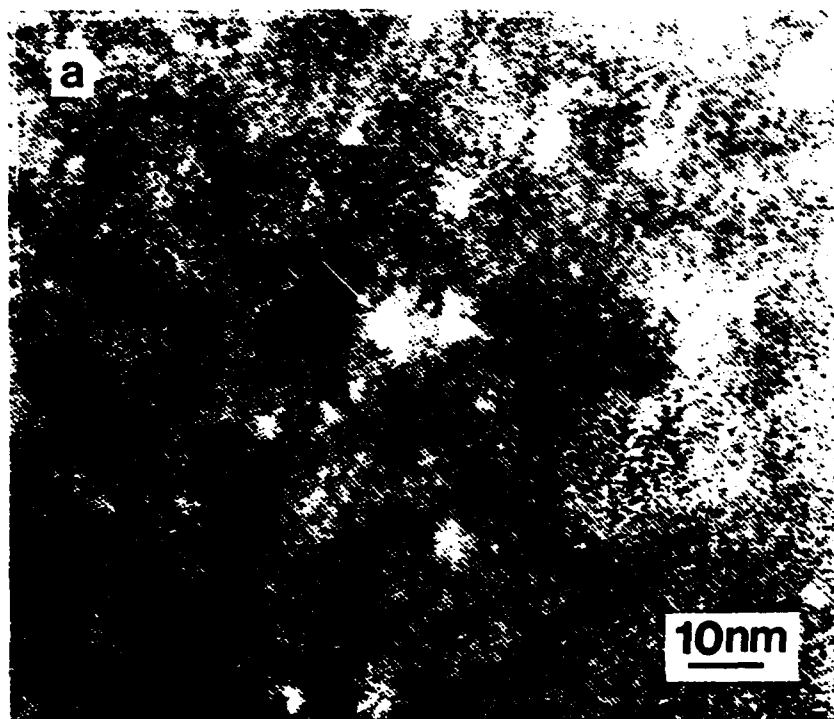


Figure 2. Cross-sectional TEM micrographs of: (a) annealed (at 650°C for 60 min) LT GaP film grown at 190°C on GaP substrate (the arrow indicates one of the coherent precipitates appearing as bright dots), (b) LT GaAsP film grown at 200°C on GaAs substrate and annealed at 650°C for 60 min (the arrow indicates a large arsenic precipitate which is surrounded by small arsenic precipitates appearing as black dots).

were observed: a substrate reflection and an epilayer reflection with a lower intensity at a lower Bragg angle, as indicated in Figure 3(b). The angular separation ( $\Delta\theta$ ) is about 220 arc sec. Splittings as low as 40 arc sec were also observed. The splitting can be attributed to the strain in the epilayer resulting from excess phosphorus, possibly in the interstitial sites of the GaP crystal lattice, causing lattice dilatation. This splitting ( $\Delta\theta$ ) in the DCXRD seems to increase with lower growth temperatures. Both the splitting and the change in the lattice constant in these LT GaP films are not as high as that reported for LT GaAs[10] films. This can be explained by the relative size of the arsenic and phosphorus atoms located at interstitial sites. Annealing of these LT GaP samples was carried out in a metalorganic chemical vapor deposition (MOCVD) reactor with  $\text{PH}_3$  overpressure at 650 and 700 °C for 30-60 min. Annealing did not result in the complete disappearance of the lattice expansion; however, a slight reduction in  $\Delta\theta$  (~30 arc sec) was observed due to the high annealing temperature [Figure 3(c)]. We have not yet detected any consistent pattern of the effect of annealing on the splitting in the DCXRD as related to the growth temperature and the crystallinity. Further studies are currently underway.

**PIXE Analysis.** The nonstoichiometry of LT GaP films has been investigated first by utilizing the PIXE technique. The overall statistical error of this technique was estimated to be about 0.4% on the measurement of  $[\text{P}]/[\text{Ga}]$  atomic ratios. These atomic ratios were used to calculate values of excess phosphorous concentrations defined as  $([\text{P}]-[\text{Ga}])/([\text{P}]+[\text{Ga}])$  by analogy with the calculations of excess arsenic in LT GaAs[10]. The PIXE measurements made on the LT GaP films grown at ~160 and 190°C yielded  $[\text{P}]/[\text{Ga}]$  ratios of 1.045 and 1.025, and thus, corresponding to the excess phosphorus of 2.20 and 1.23 at.%, respectively. Shown in Figure 4 is the superimposed  $\text{P}_{\text{K}\alpha}$  x-ray signals of the as-grown LT GaP film at  $T_s \sim 160^\circ\text{C}$  (outer spectrum) and GaP substrate (inner spectrum). Both spectra were obtained under identical conditions. The other PIXE peaks of the sample were totally overlapped and thus not shown here. It is necessary to point out that the unoverlapped area of the two spectra shown in Figure 4 corresponds to the greater-than-unity  $[\text{P}]/[\text{Ga}]$  ratio and, hence, an increase of phosphorus content of 2.20 at.% in the LT GaP layer. The measured  $[\text{P}]/[\text{Ga}]$  ratios on different LT GaP samples appeared to vary inversely with growth temperatures, implying that a sample grown at a lower temperature may have a larger nonstoichiometric group V deviation in the LT layer.

**STEM Analysis.** Excess phosphorus in LT GaP films were determined also by using the analytical STEM approach. Theoretically, the  $[\text{P}]/[\text{Ga}]$  atomic ratio of a GaP substrate should be unity. Experimentally, however, the atomic ratio is somehow between 0.9 and 1. Therefore, the averaged  $[\text{P}]/[\text{Ga}]$  atomic ratio of a GaP substrate obtained in the experiment served as a normalization factor for that of a LT GaP film. The TEM facility was operated at 120 KV with the probe diameter set at 4.9 nm throughout the analysis. Several data points

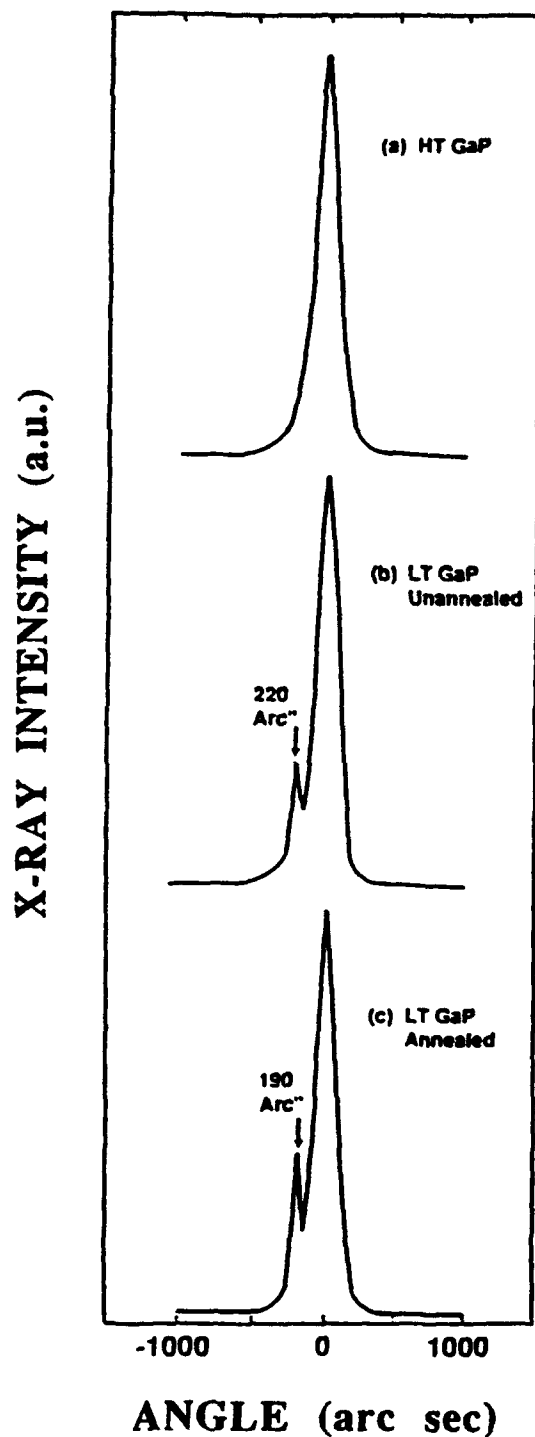


Figure 3. Double crystal x-ray diffraction from the (113) planes of: (a) GaP film grown at 560°C on GaP substrate, (b) LT GaP grown at 200°C and unannealed and, (c) LT GaP grown at 200°C and annealed at 700°C for 60 min.

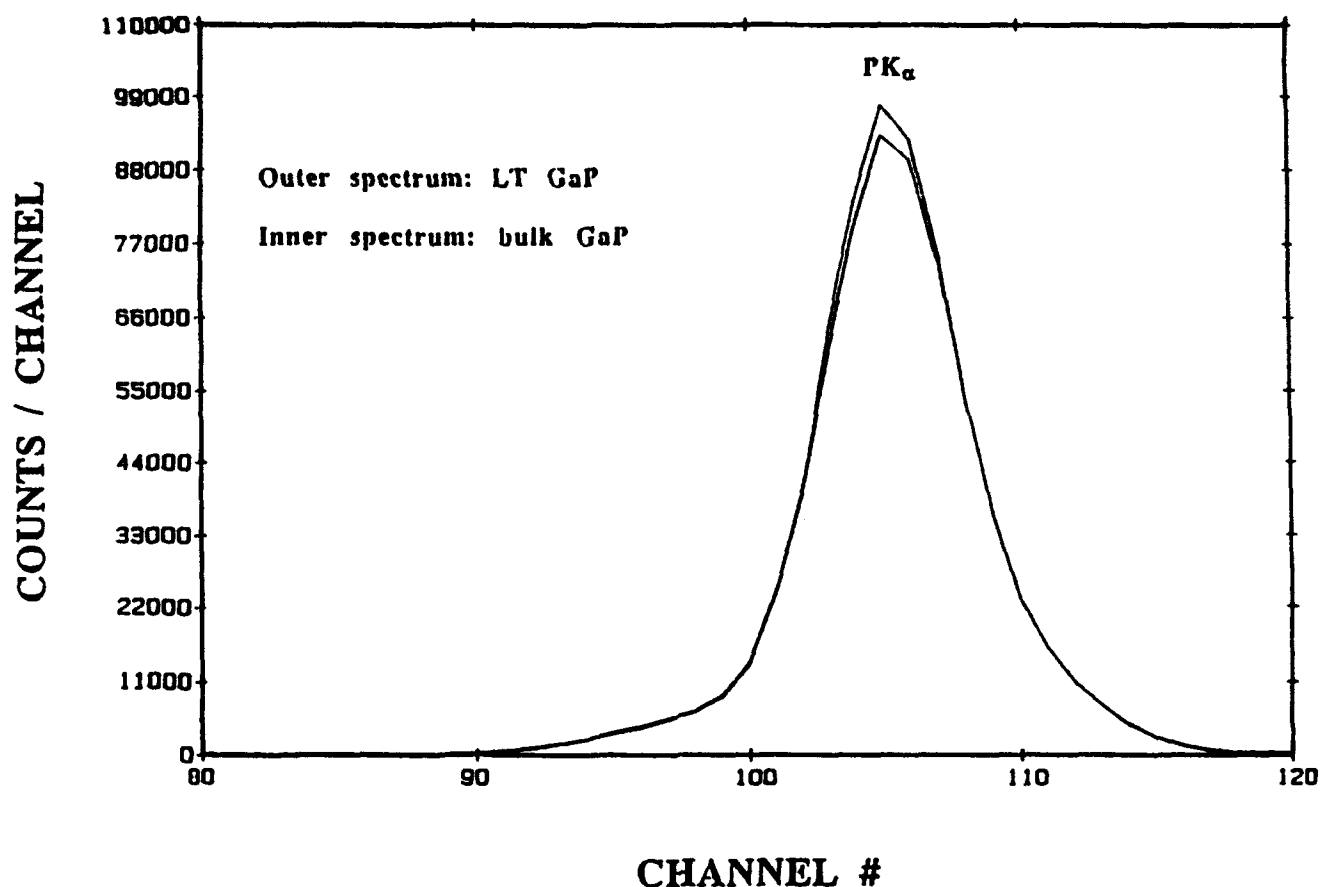


Figure 4. 0.5 MeV  $H^+$  PIXE superimposed  $P_{K\alpha}$  x-ray signals from the as-grown LT GaP epilayer grown at  $\sim 160^\circ\text{C}$  (outer spectrum) and GaP substrate (inner spectrum). Note that the unoverlapped area of the two spectra corresponds to an excess phosphorus of 2.2 at.% incorporated in the epilayer. Other PIXE peaks were totally overlapped and thus not shown here.

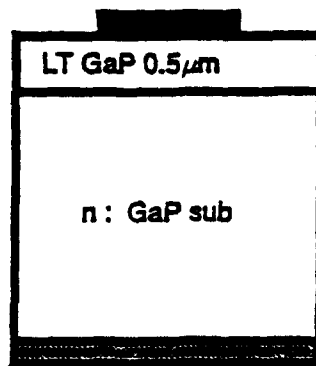
were taken by setting the electron probe at different locations within one layer for the analysis to be statistically accurate. The atomic percentages of phosphorus thus obtained were averaged numerically to obtain the final result for the same epilayer. The analysis yielded that the LT GaP films grown at 180, 190 and  $200^\circ\text{C}$  had about 1.49, 1.38 and 0.74 at.% excess phosphorus, respectively. The amount of excess phosphorus in the film grown at  $190^\circ\text{C}$  is in good agreement with that determined by PIXE technique.

**Resistivity Measurements.** Resistivity measurements were carried out with a high-impedance van der Pauw apparatus. Indium-dots alloyed at  $300^\circ\text{C}$  were used as contacts to the epilayers. The as-grown LT GaP film ( $T_g \sim 190^\circ\text{C}$ ) showed a resistivity of about  $10^8 \Omega \text{ cm}$ . The resistivity of the sample annealed at  $700^\circ\text{C}$  for 60 min could not be measured in darkness, however, with intense light a resistivity of  $10^6 \Omega \text{ cm}$  was obtained. The resistivity of the SI GaP substrate was also too high to be measured in the dark, but had a resistivity about  $10^8 \Omega \text{ cm}$  when measured under intense light. Other samples have shown resistivity in

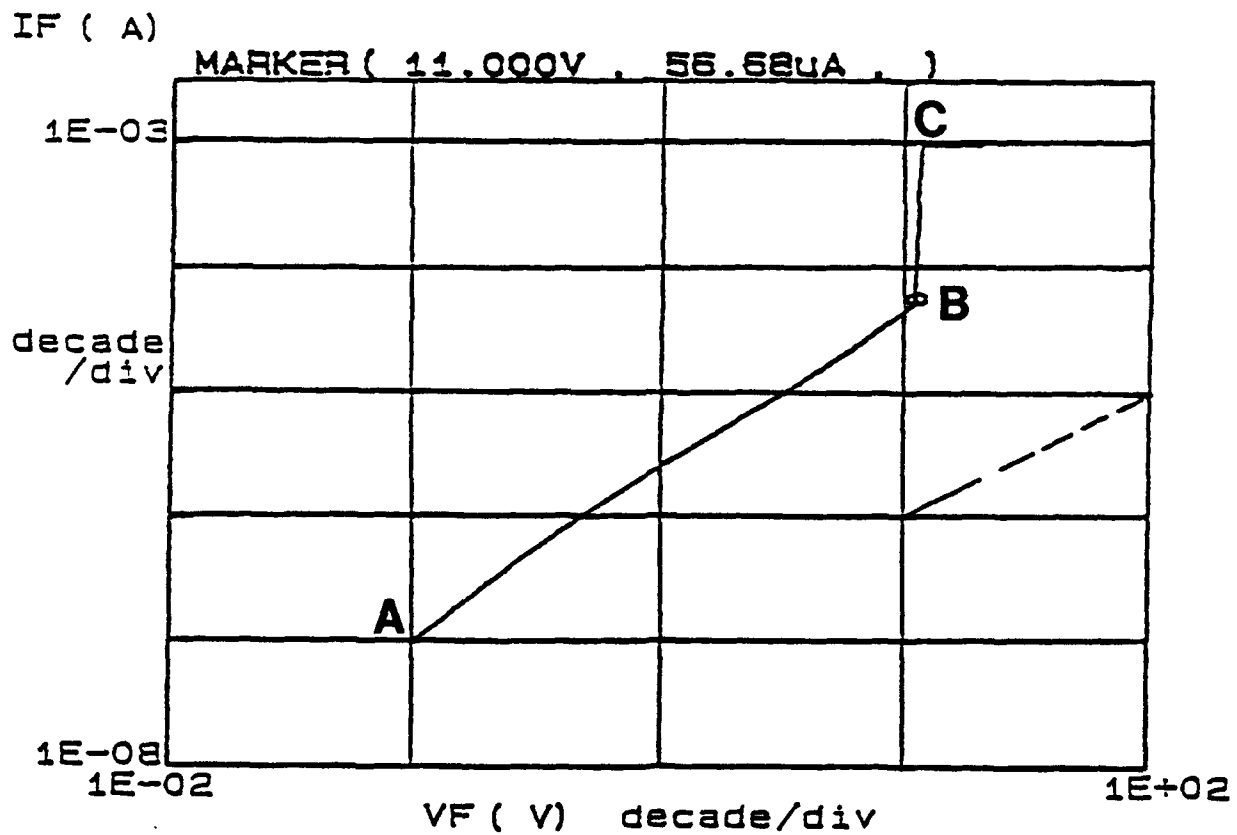
the  $10^6$ - $10^8 \Omega \text{ cm}$  range depending on the growth temperature. GaP films grown at high temperature showed low resistivities. Detailed electrical characterization of these LT GaP films will be reported elsewhere[11]. The semi-insulating property of LT GaP, regardless of annealing, is probably mainly due to the excess-phosphorus-related deep levels.

***LT GaP MIS Diode.*** As mentioned earlier, the semi-insulating property of the as-grown LT GaP can be attributed to the excess-phosphorus-related deep levels in the material. To study these deep levels we have fabricated a GaP metal-insulator-semiconductor (MIS) diode, whose schematic cross section is shown in Figure 5(a). In this device, a 0.5- $\mu\text{m}$ -thick unannealed LT GaP film grown at  $\sim 200^\circ\text{C}$  on n-type GaP substrate was used as an insulating layer. Both contacts are ohmic and the area of the contact to LT GaP film is  $4.5 \times 10^{-3} \text{ cm}^2$ . The current-voltage (I-V) characteristics of the diode are obtained, as shown in Figure 5(b), when variable voltages are applied to the device through the two ohmic contacts. The I-V curve has two distinctive regions as labeled AB and BC, respectively. It is important to note that the large linear region AB of the I-V curve is indicative of a large amount of excess-phosphorus-related deep levels present in the LT GaP layer. Given below are the qualitative explanations for the two different regions of the curve. As the voltage is increased over the two ohmic contacts, more electrons are virtually injected into the LT GaP layer. Since the LT GaP has lots of deep levels which act as deep traps for both electrons and holes, the electrons driven by the voltage are getting trapped. Therefore, the electrical current increases almost linearly with the applied voltage, as illustrated by AB region. At point B where nearly all the available traps are filled, the incoming electrons driven by the voltage have found few vacant traps to fill. In fact, the LT GaP layer is no longer highly resistive as the traps in the layer are all filled. Thus, the driven electrons can go through the diode directly, meeting very low resistance. That is why the current increases sharply with a small increment of voltage, as indicated by region BC. The above explanation is also true for holes. Figure 5(b) shows a typical space-charge-limited current (SCLC) behavior of the diode with a traps-filled limit voltage of  $\sim 11 \text{ V}$ . The energy and concentration of the deep traps involved in the SCLC can be evaluated from the linear region by analogy with the approach adopted for LT InP[12]. However, the quantitative determination is not available at this time and it is left for future investigation.

***LT InGaP. X-ray diffraction.*** DCXRD showed that the LT InGaP films had  $\sim 47\%$  InP. Two LT structures were grown in this work for structural characterization of LT InGaP films. The first structure had only a single LT InGaP layer ( $200^\circ\text{C}$ ,  $1.5 \mu\text{m}$ ) grown on a GaAs buffer layer ( $550^\circ\text{C}$ ,  $80 \text{ \AA}$ ). Two Bragg peaks were observed for the DCXRD (400) reflection with the epilayer peak located at a higher Bragg angle than the substrate peak, as shown in Figure 6(a). This indicates that the LT InGaP film is not lattice matched to the GaAs substrate and its In composition is lower than the InGaP-GaAs lattice-matched composition of  $\sim 49\%$ . The



(a)



(b)

Figure 5. a) Schematic cross section of a GaP MIS diode with LT GaP as an insulating layer; b) Space-charge-limited current behavior of the GaP diode.

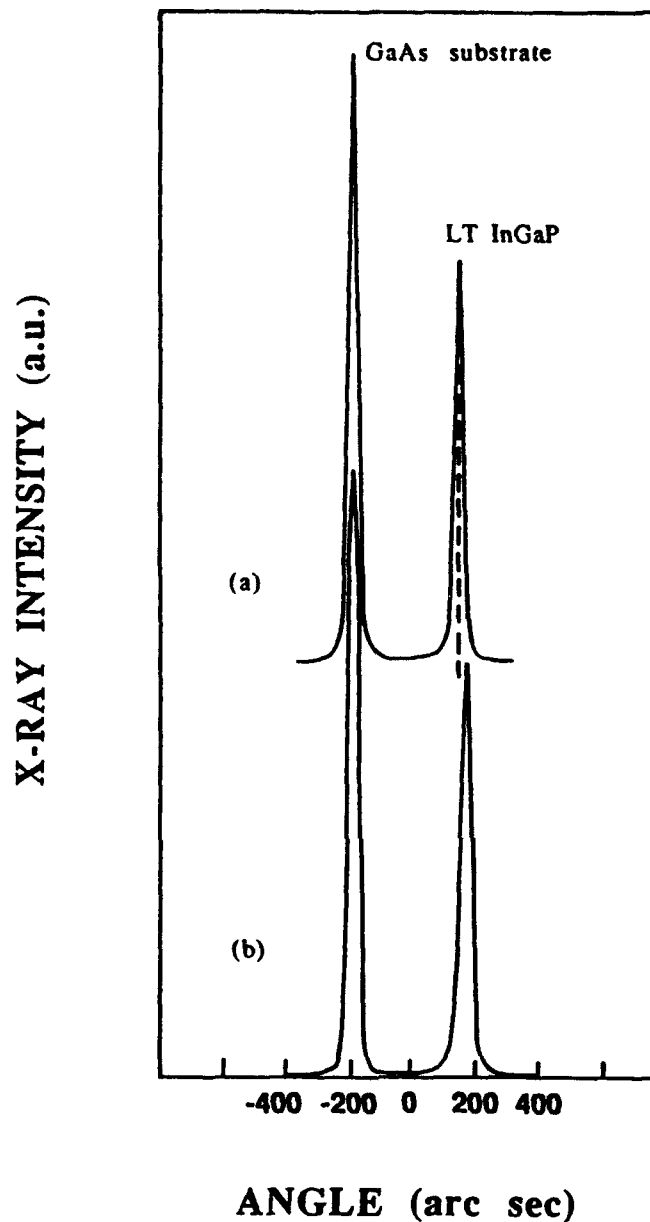


Figure 6. DCXRD from (400) reflection planes of the first structure described in the paper: (a) as-grown and, (b) annealed at 600°C for 1 hr. The LT InGaP peak was shifted to higher Bragg angle by 20 arc sec after annealing.

narrow full width at half maximum (FWHM) of the epilayer peak (20 arc sec) indicates the high quality of the crystalline epilayer. Annealing this sample at 600°C for 1 hr caused the angular separation between the epilayer and the substrate peaks to increase by 20 arc sec, as seen in Figure 6(b). This observation indicates a slight reduction of the lattice parameter of the epilayer after annealing. As to the lattice relaxation as a result of annealing, this is similar to the LT GaAs case. It has been reported that annealing LT GaAs at 600°C for ~10 min



results in a complete removal of the lattice mismatch. Annealing LT InGaP at the same temperature for 1 hr, however, results in only slight relaxation of the expanded lattice. This is manifested by a small peak shift of the annealed film to a higher Bragg angle. In order to compare the structural properties of the LT InGaP and the InGaP epilayers grown at higher temperatures ( $\sim 480^\circ\text{C}$ , hereafter referred to as HT InGaP), a second structure was grown, as shown in Figure 7. During the growth of both HT and LT InGaP epilayers, a fixed  $\text{PH}_3$  flow

LT InGaP	200°C	1 $\mu\text{m}$
HT InGaP	480°C	1 $\mu\text{m}$
GaAs buffer	550°C	1 $\mu\text{m}$
SI LEC GaAs (100) substrate		

Figure 7. Schematic of the multilayer sample with the LT InGaP film grown on top of the HT InGaP film.

rate of  $\sim 4$  sccm was maintained. It should be noted that there was an interruption of the  $\text{PH}_3$  flow into the growth chamber after the HT growth was ended and the substrate temperature was lowered to  $\sim 300^\circ\text{C}$ . The In compositions of the LT and HT InGaP epilayers were assumed to be identical by maintaining the same source temperatures during the layers' growth. DCXRD analyses from (400) reflection planes were performed on both the as-grown and annealed samples. For the as-grown samples, three (400) Bragg peaks were observed: the substrate, LT InGaP and HT InGaP peaks, respectively, as shown in Figure 8(a). Upon annealing at  $600^\circ\text{C}$  for 1 hr the LT peak was found to be the only one shifted, as shown in Figure 8(b). The observation that the annealing did not have any effect on the HT peak position was as expected. The angular separation between the LT and HT InGaP reflections was 70 arc sec before annealing and 50 arc sec after annealing. Therefore, the angular shift of the LT peak towards the HT peak after annealing was 20 arc sec, which was in good agreement with that of the first grown structure previously discussed. This relative shift, corresponding to the incomplete removal of the lattice-mismatch by 0.01%, might be caused by some kind of redistribution of the excess phosphorus in the epilayer lattice due to annealing. The nature of the redistribution is not yet known at this time. Considering the HT InGaP as a "substrate," the LT InGaP/HT InGaP structure was found to have DCXRD

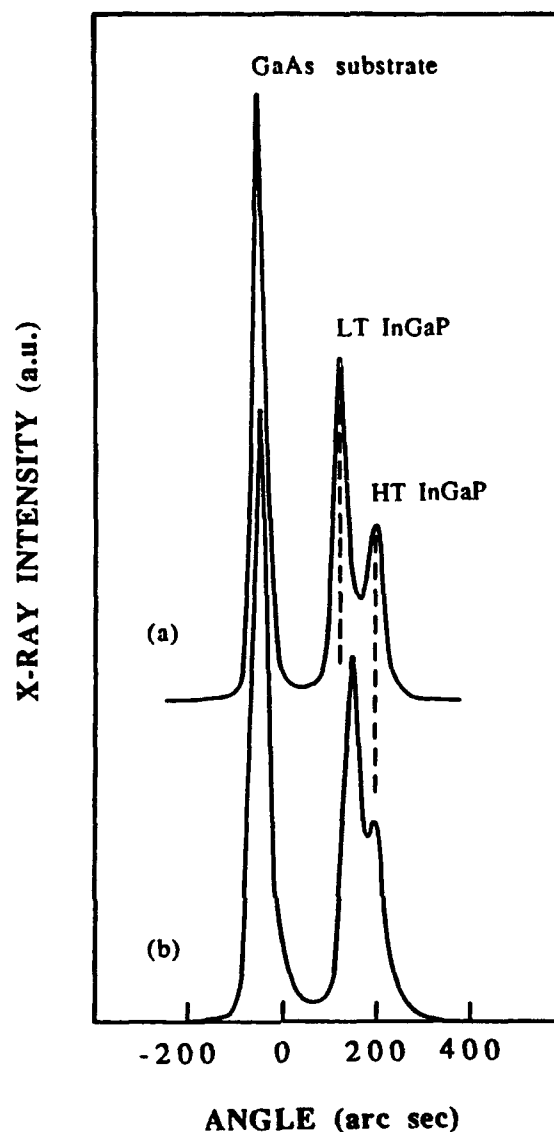


Figure 8. DCXRD from (400) reflection planes of the sample shown in Figure 7: (a) as-grown, the angular separation between the LT InGaP and the HT InGaP reflections is 70 arc sec; (b) annealed at 600°C for 1 hr, the angular separation between the LT InGaP and the HT InGaP reflections is 50 arc sec.

characteristics similar to those of LT GaP/GaP discussed before. The fact that the LT peak was situated on the left side of the HT peak confirmed that the LT InGaP had a slightly larger lattice parameter than that of the HT InGaP (by 0.05% for the as-grown LT epilayer). This lattice expansion can be explained, as in the case of LT GaP, by the presence of the excess phosphorus incorporated into the epilayer.

**TEM analysis.** An XTEM micrograph of the sample described in Figure 7 is shown in Figure 9(a), indicating the presence of phase separation in LT InGaP epilayers. The phase separation is manifested in the form of a "precipitate-like" microstructure. The precipitate-like phase separation ( $\sim 800$  Å in diameter for the layer grown at  $\sim 200^\circ\text{C}$ ) appears to decrease

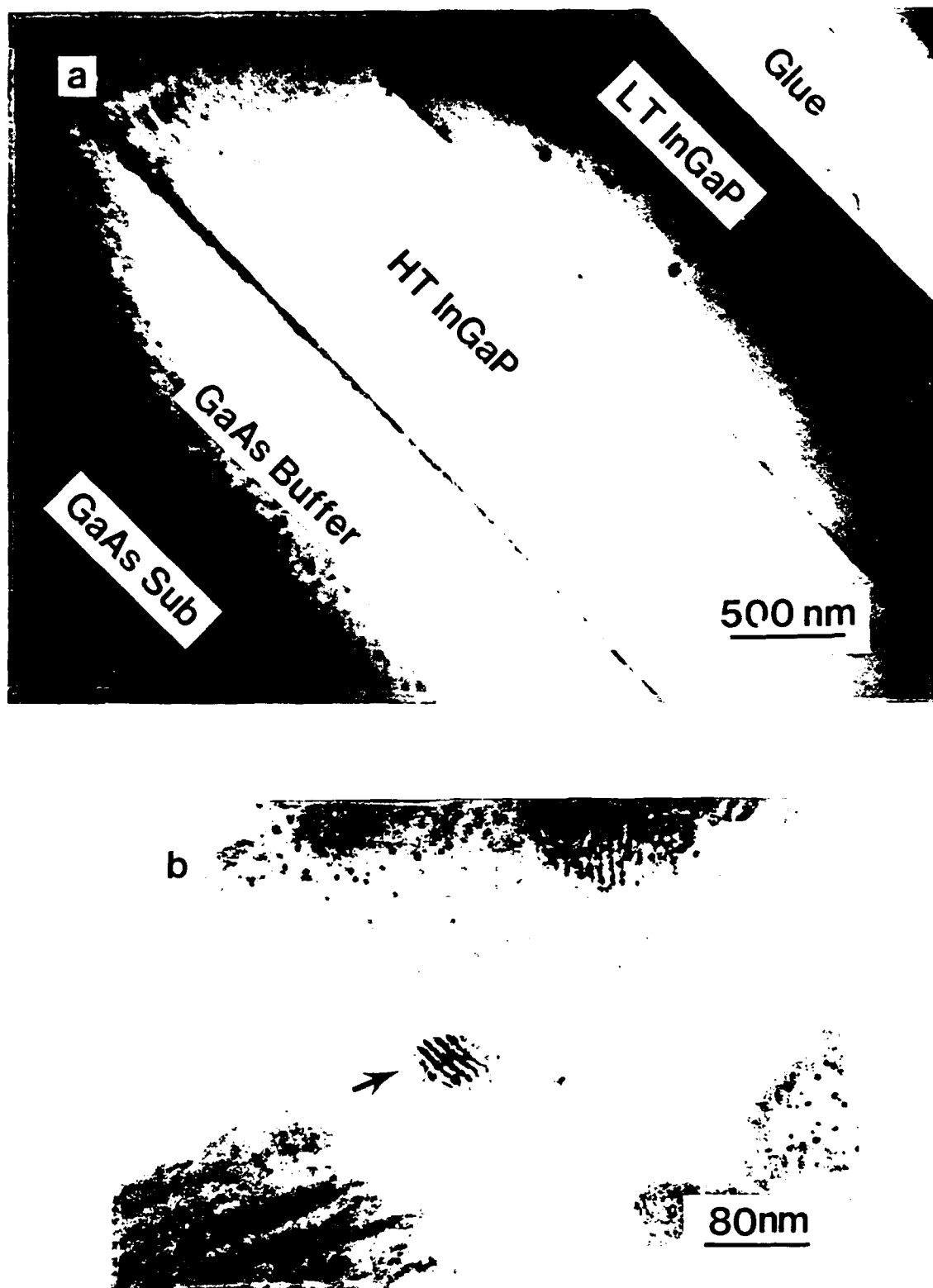


Figure 9. XTEM micrographs obtained from the multilayer sample shown in Figure 7 illustrate: (a) the layer structures and the phase separation, manifested in the form of a "precipitate-like" microstructure, in the LT InGaP layer, and (b) the moiré fringe in one of the phase separated areas, as indicated by the arrow.

in volume as the growth temperature increases. Annealing, however, seems to have a slight influence on the phase separated microstructure. The phase separated areas were crystalline and strained as implied by the moire fringes shown in Figure 9(b). Analytical STEM analyses performed on the LT InGaP indicated a slightly higher In composition in the phase separated areas relative to the matrix. The HT InGaP showed a distinctive feature of slight decomposition. The decomposition in the HT InGaP, as well as the phase separation in the LT InGaP, might be explained by the spinodal decomposition usually observed in liquid phase epitaxy (LPE) and MOCVD growth. Spinodal decomposition causes the appearance of a two-phase microstructure with different In compositions at the growth temperature.

**STEM Analysis.** We have investigated the LT InGaP group-V nonstoichiometry by using the analytical STEM approach. The structure shown in Figure 7 was chosen to measure the small changes of phosphorus concentration in the LT InGaP. The HT InGaP epilayer served as a reference for the LT InGaP epilayer. The TEM facility was operated at 200 KV with the probe diameter set at 5.1 nm throughout the analysis. Several data points were taken within the layer for the statistical accuracy. The phosphorus atomic percentages thus obtained were averaged numerically as the final result. This method was employed for both HT and LT InGaP epilayers. The analysis on the sample chosen above determined that the LT InGaP had 0.5 at.% more phosphorus atoms than the HT InGaP. These excess phosphorus atoms incorporated in the LT epilayer probably caused the lattice mismatch compared to the HT epilayer.

**Calculation of Excess Phosphorus.** For verification of the excess phosphorus results, the lattice mismatch as determined by DCXRD was used to calculate the excess phosphorus incorporated in the lattice. In this approach, the lattice mismatch of the as-grown LT InGaP with respect to the HT InGaP was used to obtain the increase of the volume of the LT InGaP crystal lattice,  $\Delta V$ , assuming the lattice was uniformly elastically distorted. Although this assumption may not be exact, this approach can be a good estimate since the two measured lattice parameters, namely, the perpendicular ( $a_{\perp}$ ) and the parallel ( $a_{\parallel}$ ) referenced to the (100) plane, were fairly close if not identical. We also made the assumption that all the excess phosphorus atoms were incorporated in the interstitial positions of the LT InGaP lattice. Since both Ga and In atoms have larger atomic radii than that of P atom (1.81, 2.0 and 1.23 Å, respectively)[13], the excess phosphorus atoms can be neither on Ga nor on In substitutional positions. If that were not the case, then there would be a lattice contraction instead of the lattice expansion exhibited by the LT InGaP epilayer. The above assumptions led to a simple model in which an excess phosphorus atom acted as a misfitting particle in a uniform matrix. Let  $\epsilon$  be the elastic strain of the LT InGaP lattice induced by the incorporation of the excess phosphorus atoms and  $\delta$  the conventional lattice mismatch between the HT and LT InGaP lattices. The two parameters  $\epsilon$  and  $\delta$  are related by the

Bullough and Newman equation[14]:  $\epsilon = \delta(1+\nu)/[3(1-\nu)]$ , where  $\nu$  is Poisson's ratio. Note that  $\nu=1/3$  for almost all III-V semiconductors. Therefore, the  $\epsilon$ - $\delta$  relation can be simplified as  $\epsilon \approx (2/3)\delta$ . Let  $\delta_{mv}$  denote the measured value of the lattice mismatch by DCXRD, i.e.,  $\delta_{mv} = (a_{LT} - a_{HT})/a_{HT}$  by definition, where  $a_{LT}$  and  $a_{HT}$  are the lattice parameters of the as-grown LT InGaP and HT InGaP epilayers, respectively. In theory, this measured value  $\delta_{mv}$  is composed of the elastic strain  $\epsilon$  and the conventional lattice mismatch  $\delta$ , i.e.,  $\delta_{mv} = \epsilon + \delta$ . Substituting the simplified  $\epsilon$ - $\delta$  relation into the above equation and solving for  $\delta$  gives  $\delta \approx (3/5)\delta_{mv}$ . Given  $a_{LT} = 5.64639 \text{ \AA}$  and  $a_{HT} = 5.64345 \text{ \AA}$  as determined by DCXRD, the equation  $\Delta V = (a_{LT})^3 - (a_{HT})^3$  yields a value of  $0.28105 (\text{\AA})^3$ . The number of the excess phosphorus atoms per unit cell,  $\Delta N_P$ , can be calculated from the equation  $\Delta N_P = \Delta V/v_P$ , where  $v_P$  is the volume of one P atom. Taking in consideration the elastic strain value (the  $\delta$ - $\delta_{mv}$  relation),  $\Delta N_P$  was corrected with the factor of  $3/5$ . The P atom, treated as a hard sphere, has a volume of  $v_P = (4/3)\pi r_0^3$ , where  $r_0$  is the radius of the atom. Since normally there are four P atoms per unit cell, the excess phosphorus atoms per unit cell of LT InGaP can finally be calculated to be  $\sim 0.54 \text{ at. \%}$ . This result is in good agreement with that obtained from the analytical STEM.

**Resistivity Measurements.** The resistivity of a LT material serves as a practical monitor for its device applications. To measure the resistivity of LT InGaP more accurately, a special sample was designed. A  $2\text{-}\mu\text{m}$ -thick LT InGaP film was grown at  $\sim 200^\circ\text{C}$  on a  $500\text{-\AA}$ -thick AlAs layer grown at  $610^\circ\text{C}$ . The LT InGaP film was removed from the substrate by first mounting the sample face-down on a glass slide, then lapping and RIE-etching the substrate off, and finally removing the AlAs layer in HF. Hall effect measurements on the as-grown LT InGaP film revealed n-type conduction with a resistivity of  $9 \times 10^5 \Omega \text{ cm}$  and mobility of  $120 \text{ cm}^2/\text{V s}$  at  $296 \text{ K}$ . The activation energy of the dominant donor[15] was determined from an Arrhenius plot,  $n/T^{3/2}$  vs  $T^{-1}$ , as shown in Figure 10. The slope of this plot, which is just  $-E_{D0}/k$ , leads to  $E_{D0} = 0.48 \text{ eV}$ , within error of what might be expected for the  $(0/+)$  transition of the phosphorus antisites in  $\text{In}_{0.5}\text{Ga}_{0.5}\text{P}$ . After annealing the LT film at  $600^\circ\text{C}$  for 1 hr, the  $296\text{-K}$  resistivity increased to  $10^9 \Omega \text{ cm}$ , but a Hall voltage could no longer be found. Nevertheless, a plot of  $\ln \rho$  vs  $T^{-1}$ , where  $\rho$  is the resistivity, produced an even larger activation energy of  $0.8 \text{ eV}$ . Thus, the material is stable against high-conductivity conversion. It is necessary to point out that the LT InGaP remains semi-insulating before and after annealing.

#### D. Conclusions

In conclusion, we have successfully grown GaP and  $\text{In}_{0.47}\text{Ga}_{0.53}\text{P}$  at a low temperature of  $\sim 200^\circ\text{C}$  for the first time. Both LT GaP and LT InGaP showed a lattice expansion of  $\sim 0.05\%$ , as determined by DCXRD. Unlike LT GaAs, annealing at high temperatures ( $600\text{-}700^\circ\text{C}$  for  $30\text{-}60 \text{ min}$ ) did not result in a total relaxation of the lattice strain, but a slight reduction of the

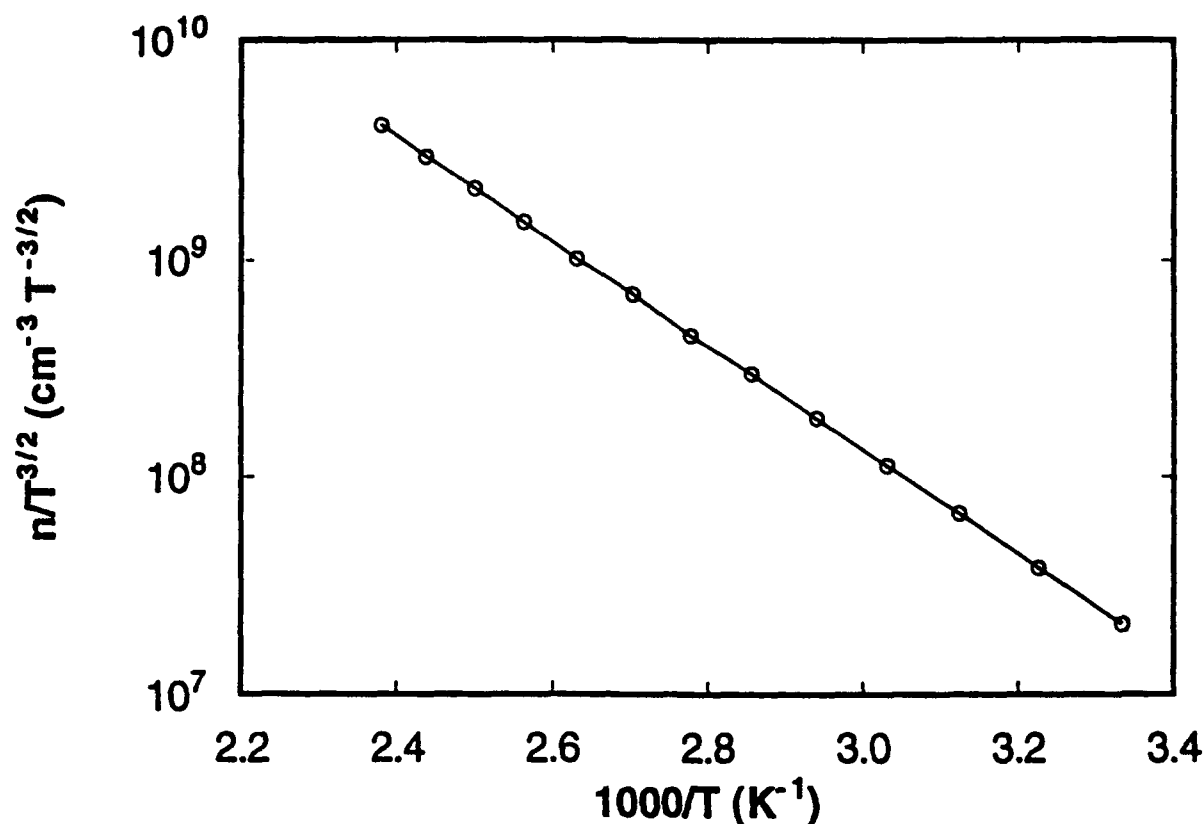


Figure 10. Plot of  $n/T^{3/2}$  vs  $1000/T$  for the as-grown LT InGaP film.

lattice expansion. The lattice expansion can be explained by the incorporation of the excess phosphorus in the order of 1 at.% in the LT GaP epilayer[16] as determined by PIXE and STEM approaches, and of 0.5 at.% in the LT InGaP epilayer as determined by STEM and x-ray approaches. The slight reduction of the lattice expansion after annealing may be caused by redistribution of the excess phosphorus atoms. XTEM showed no formation of incoherent phosphorus precipitates after annealing, but did show coherent precipitation in annealed LT GaP epilayer and phase separation in as-grown LT InGaP epilayer. The latter was manifested in the form of a "precipitate-like" microstructure. This precipitate-like phase separation can be explained by the tendency of the InGaP alloys to spinodally decompose at similar compositions that are close to that which lattice matches GaAs. The HT InGaP film indicated the occurrence of slight spinodal decomposition at the growth temperature. Both as-grown and annealed LT GaP are semi-insulating with  $\rho$  up to  $10^8 \Omega \text{ cm}$ . The resistivity range is  $10^8$ - $10^6 \Omega \text{ cm}$  for LT GaP films grown at  $T_s=190$ - $230^\circ \text{C}$  range. The temperature-dependent resistivity and Hall effect measurements were performed on the LT InGaP film after the substrate was removed. The as-grown LT InGaP film showed a resistivity of  $\sim 10^6 \Omega \text{ cm}$  at room temperature whereas the annealed film at  $600^\circ \text{C}$  for 1 hr exhibited at least three orders

of magnitude higher resistivity. Activation energies of  $\sim 0.5$  and  $0.8$  eV were also obtained from the Hall measurements for the as-grown and annealed LT InGaP films, respectively.

The above preliminary studies show that neither LT GaP nor LT InGaP films exactly follow the observed trends of LT GaAs films. Annealing the LT GaAs films caused lattice strain to disappear and arsenic precipitation accompanied by high resistivity films. However, in LT GaP and LT InGaP, annealing is not necessary to achieve high resistivity. The current LT GaP and LT InGaP results imply that the high resistivity is not a result of the presence of precipitates and the accompanying carriers depletion near the metal phosphorus semiconductor interfaces as in the case of LT GaAs[17]; but, rather is a result of deep levels associated with the excess phosphorus present in these LT films. The high concentration of these excess-phosphorus-related deep levels in LT GaP is indicated qualitatively by the I-V curve of the LT GaP/GaP MIS diode. The properties of LT GaP and LT InGaP films, however, are not consistent with that previously reported on LT InP films, where both phosphorus precipitates and low resistivity were observed[8]. Thus, it seems that more work is needed in the LT growth of phosphorus-based compounds to settle such issues.

#### E. Future Research Goals

*LT GaP.* GaP has a wide bandgap of  $2.27$  eV at room temperature, a high Schottky barrier of  $1.3$  eV for Au/GaP, and no surface Fermi level pinning. These properties are promising for device applications. Since it is semi-insulating, the strained LT GaP film can be an excellent passivating layer for GaAs metal-semiconductor field-effect transistors (MESFETs). Then, the gate-drain breakdown voltage of the MESFETs should be improved greatly. Further investigation on the device application of LT GaP is currently underway. In addition, the critical layer thickness (CLT) of LT GaP on GaAs, which is of importance for the device application, needs to be determined. Raman scattering measurements on LT GaP films are in progress to reveal the presence of  $P_{Ga}$  antisite defects and to calculate the excess phosphorus amount incorporated as the antisites in the LT films.

A variety of Si devices could be made possible if the semi-insulating crystalline LT GaP can be grown on Si substrate successfully. Therefore, growth of LT GaP on Si is worth being given great efforts.

*LT InGaP.* InGaP can be grown lattice-matched to GaAs and has a relatively wide bandgap ( $1.92$  eV) with  $\sim 49\%$  InP composition. Furthermore, InGaP can be selectively etched to the extent of  $100\%$ . Having all these properties, the semi-insulating LT InGaP can have a variety of important device applications with some of the examples given below. It can be used as a gate insulator in GaAs metal-insulator-semiconductor field-effect transistors (MISFETs). It can also be used to make a pico-second photodetector if LT InGaP has very short carrier lifetime of less than  $1$  ps. The carrier lifetime of the LT material can be deduced

from the reflectivity measurements, which are currently planned. Therefore, further investigations are necessary for the fabrication and characterization of LT InGaP/GaAs related devices.

#### G. References

1. F. W. Smith, A. R. Calawa, C.-L. Chen, M. J. Manfra, and L. J. Mahoney, *IEEE Electron Device Lett.* **9**, 77 (1988).
2. L. W. Yin, Y. Hwang, J. H. Lee, R. M. Kolbas, R. J. Trew, and U. K. Mishra, *IEEE Electron Device Lett.* **11**, 12 (1990).
3. M. Kaminska, E. R. Weber, Z. Liliental-Weber, and R. Leon, *J. Vac. Sci. Technol. B* **7**, 710 (1989).
4. M. R. Melloch, K. Mahalingham, N. Otsuka, J. M. Woodall, and A. C. Warren, *J. Cryst. Growth* **111**, 39 (1991).
5. J. N. Miller and T. S. Low, *J. Crystal Growth* **111**, 30 (1991).
6. R. A. Metzger, A. S. Brown, W. E. Stanchina, M. Lui, R. G. Wilson, T. V. Kargodorian, L. G. McCray, and J. A. Henige, *J. Crystal Growth* **111**, 445 (1991).
7. J. Ch. Garcia, J. P. Hirtz, P. Maurel, H. J. Von Bardeleben, and J. C. Bourgoin, *Mat. Res. Soc. Symp. Proc.* **241**, 277 (1992).
8. G. N. Maracas, K. T. Shiralagi, R. A. Puechner, F. Yu, K. T. Choi, J. S. Bow, R. Ramamurty, M. J. Kim, and R. W. Carpenter, *Materials Research Society (MRS) Fall Meeting*, Boston, Dec. 1991.
9. M. Kaminska, Z. Liliental-Weber, E. R. Weber, T. George, J. B. Kortright, F. W. Smith, B. Y. Tsaur, and A. R. Calawa, *Appl. Phys. Lett.* **54**, 1881 (1989).
10. Z. Liliental-Weber, W. Swider, K. M. Yu, J. Kortright, F. W. Smith, and A. R. Calawa, *Appl. Phys. Lett.* **58**, 2153 (1991).
11. J. Ramdani, Y. He, N. A. El-Masry, and S. M. Bedair, to be published.
12. J. W. Roach and H. H. Wieder, *IEEE Electron Device Lett.* **6**, 356 (1985).
13. "Table of periodic properties of the elements" published by Sargent-Welch Scientific Company.
14. R. Bullough and R. C. Newman, *Rep. Prog. Phys.* **33**, 101 (1970).
15. D. C. Look, *Electrical Characterization of GaAs Materials and Devices* (Wiley, New York, 1989), p.117.
16. Y. He, J. Ramdani, N. A. El-Masry, and S. M. Bedair, to be published.
17. A. C. Warren, J. M. Woodall, J. L. Freeouf, D. Grischkowsky, D. T. McInturff, M. R. Melloch, and N. Otsuka, *Appl. Phys. Lett.* **57**, 1331 (1990).



### **XXIII. Distribution List**

Mr. Max Yoder Office of Naval Research Electronics Division, Code: 314 Ballston Tower One 800 N. Quincy Street Arlington, VA 22217-5660	3
Administrative Contracting Officer Office Of Naval Research Resident Representative The Ohio State University Research Center 1960 Kenny Road Columbus, OH 43210-1063	1
Director, Naval Research Laboratory ATTN: Code 2627 Washington, DC 20375	1
Defense Technical Information Center Bldg. 5, Cameron Station Alexandria, VA 22314	2